BENEMÉRITA UNIVERSIDAD AUTÓNOMA DE PUEBLA

INSTITUTO DE FÍSICA “LUIS RIVERA TERRAZAS”

Aplicación de Nanopartículas de $Cu_2ZnSn_{1-x}Ge_xS_4$ como Transportadores de Huecos en Celdas Solares de Perovskita Basadas en Plomo

TESIS

QUE PARA OBTENER EL GRADO

Doctorado en Ciencias (en la Especialidad de Ciencia de Materiales)

PRESENTA

por

M.C. Francisco Enrique Cancino Gordillo

No. de CVU: 784149

ASESORES

Dr. Umapada Pal

Dr. Julio Villanueva Cab

Abril de 2023

El agradecimiento
es la memoria del corazón

Agradecimientos

Agradezco al Dr. Umapada Pal por las enseñanzas, oportunidades, consejos y el tiempo dedicado al trabajo de tesis. Sin duda he recibido un enriquecimiento personal y académico al trabajar con él.

Al Dr. Julio Villanueva Cab por su apoyo brindado en la ejecución de la investigación realizada en esta tesis.

Un agradecimiento especial al Dr. José Luis Ortiz Quiñonez y Dr. Eulises Regalado cuyos comentarios y enseñanzas fuero de gran ayuda para el desarrollo académico y de este trabajo.

Agradezco a mi familia que siempre me otorgan el apoyo para superarme cada día y poder seguir adelante en mi desarrollo profesional.

Extiendo mi agradecimiento a la Dra. Hailin Zhao Hu, Dr. Gregorio Hernández Cocoletzi y Dr. Siva Kumar Krishnan, por sus comentarios y observaciones para mejorar el trabajo de tesis.

Al Instituto de Física "Ing. Luis Rivera Terrazas" por brinda accesibilidad a utilizar la infraestructura.

Al Ing. Horacio Portillo Lozano (encargado del taller de electrónica del Instituto de Física "Ing. Luis Rivera Terrazas"), por la participación en fabricar el sistema de spray pyrolysis.

Finalmente, expreso mi agradecimiento sincero al CONACyT, México por apoyarme con la beca doctoral (CVU # 78149) y fondo por medio del proyecto CB 2017-2018/A1-S-26720*, sin los cuales no será posible a realizar esta investigación.*

Resumen

Los materiales para transportar huecos son muy importantes para desarrollar celdas solares de perovskitas de alta eficiencia y buena estabilidad. Comúnmente, los materiales que se utilizan en las capas transportadoras de huecos (*hole transport layer*, HTL) de celdas solares de perovskita (*perovskite solar cell*, PSC) son materiales orgánicos (spiro-OMeTAD, PEDOT:PSS o PTAA) que presentan una degradación debido a la exposición al ambiente (temperatura, oxigeno o humedad), afectando directamente al rendimiento de los dispositivos. Por lo que se busca utilizar materiales inorgánicos para mejorar la estabilidad de las PSCs y mejorar sus prestaciones. Recientemente, un material que está resaltando por el potencial que tiene para transportar huecos es $Cu_2ZnSn_{1-x}Ge_xS_4$ (CZTGS) en estructura kesterita. El CZTGS es un material ampliamente utilizado como material absorbedor en celdas solares de película delgada. Sin embargo, el CZTGS presenta defectos o formación de impurezas que modifican sus propiedades ópticas y eléctricas, y, en consecuencia, afectando las prestaciones del dispositivo fotovoltaico. En este trabajo de tesis sintetizamos nanopartículas de CZTGS de tamaño promedio entre 12.5 y 11.3 nm, con diferentes fracciones molares de Ge por medio de un proceso hidrotermal. También se presentó una metodología de lavado químico fácil para remover las fases no deseadas (ZnS y Cu_8GeS_6) que se formaron en la síntesis de nanopartículas. Se realizó un estudio sistemático de las propiedades estructurales, morfológicas, ópticas y eléctricas de las nanopartículas sintetizadas antes y después de realizar lavado químico. El lavado químico utilizado convirtió a las nanopartículas de CZTGS a una composición rica en Cu (*Cu-rich*) y pobre en Zn (*Zn-rich*) desde una composición inicial de pobre en Cu (*Cu-poor*) y rica en Zn (*Zn-rich*). La energía de la banda prohibida de las nanopartículas de CZTGS se redujo ~0.1 eV después del lavado químico debido a la formación de un nivel aceptor cerca del máximo de la banda de valencia ocasionado por la oxidación del Cu de Cu^{1+} a Cu^{2+}. Por otro lado, se prepararon películas del CZTGS mediante recubrimiento de centrifugación (*spin-coating*) utilizando tintes de las nanopartículas de CZTGS antes y después del lavado químico para estudiar sus propiedades eléctricas. Las películas de CZTGS preparadas con nanopartículas lavadas químicamente revelaron una mejora (un orden de magnitud) en la conductividad y en la concentración de portadores (huecos) en comparación con las muestras no lavadas. Mientras que el valor de la concentración de portadores más alta ($6.52x10^{18}$ cm^{-3}) se observó para la muestra con mayor contenido de Ge (x= 0.70), la mayor movilidad de los huecos (18.9 $cm^2V^{-1}s^{-1}$) se registró para la muestra x= 0.30. Los efectos de la eliminación de las fases secundarias (Cu_8GeS_6 y ZnS), la variación de la concentración de portadores (~10^{17} a 10^{18} cm^{-3}) y la movilidad fueron discutidos correlacionándolos con la modificación de los defectos y el incremento de la incorporación del Ge. Finalmente, se utilizaron 3 muestras (x= 0.00, 0.30 y 0.60) para ensamblar PSCs utilizando el CZTGS como HTL. La eficiencia de conversión,

estabilidad y parámetros característicos de las celdas fueron evaluadas. La PSC utilizando el CZTGS con el 30% de Ge (x= 0.30) como HTL registró un aumento en la eficiencia en comparación con la PSC usando CZTS desde 5.88 % a 7.48%. El aumento en la eficiencia es debido al incremento de la energía de banda prohibida (de 1.42 a 1.57 eV) y al mejoramiento de las propiedades eléctricas como: la concentración de portadores ($1x10^{18}$ a $2.23x10^{18}$ cm^{-3}) y la movilidad de portadores (3.9 a 18.9 $cm^2V^{-1}s^{-1}$). Por otro lado, la eficiencia para la PSC que utiliza una HTL con mayor contenido de Ge (x= 0.60) decae a 2.56 %, ocasionado por la reducción de la movilidad de los portadores en la capa de HTL. Las PSCs fabricadas usando CZTGS como HTL presentaron una estabilidad más alta a la exposición del ambiente durante 315 h en comparación con las celdas solares de perovskita fabricadas utilizando spiro-OMeTAD como HTL y sin HTL.

Abstract

Hole transport materials are very important for developing efficient perovskite solar cells of good stability. Commonly, the materials used as hole transport layer (HTL) in perovskite solar cell (PSC) are organic materials such as spiro-OMeTAD, PEDOT:PSS or PTAA, which show degradation due to environmental exposure (temperature, oxygen or humidity), affects the performance of the PSC. Therefore, it is necessary to find new hole transport materials, which improve the environmental resistance of PSCs and enhance their performance. Recently, a material that is attracting scientific attention due to its potential as HTL is $Cu_2ZnSn_{1-x}Ge_xS_4$ (CZTGS) in kesterite structure. CZTGS is widely used as an absorber material in thin-film solar cells. However, the CZTGS presents defects and impurities that modify its optical and electrical properties, and consequently, affect the performance of the photovoltaic device. In this thesis, we synthesized CZTGS nanoparticles of average sizes in-between 12.5 and 11.3 nm, with different Ge mol fractions by a hydrothermal process. Also, we presented a simple chemical washing process for removing the undesired phases such as ZnS y Cu_8GeS_6 which form during the synthesis of the nanoparticles. A systematic study was performed to analyze the structural, morphological, optical, and electrical properties of the chemically washed and unwashed nanoparticles. The chemical treatment converted the CZTGS nanoparticles from their initial Cu-poor and Zn-rich to Cu-rich and Zn-rich stoichiometry. The bandgap energies of CZTGS nanoparticles were reduced by about 0.1 eV after chemical treatment due to the formation of energy levels close to the valence band maximum owing to the oxidation of copper from Cu^{1+} to Cu^{2+} state. CZTGS films were prepared by spin-coating using the inks prepared using as-prepared and chemically washed CZTGS nanoparticles to study their electrical properties. CZTGS films prepared with the chemically washed nanoparticles revealed enhanced electrical conductivity (about one order of magnitude) and hole concentration compared to the films fabricated using the ink prepared using untreated nanoparticles. For the chemically washed nanoparticles, while the highest carrier (hole) concentration ($6.52x10^{18}$ cm^{-3}) was observed for the sample prepared with the highest Ge content (x= 0.70), the highest hole mobility (18.9 $cm^2V^{-1}s^{-1}$) was recorded for the sample x= 0.30. Finally, the CZTGS samples (x= 0.00, 0.30, and 0.60) were used as HTL in perovskite solar cells. The efficiency, stability, and characteristic parameters of the fabricated cells were evaluated. The PSC fabricated using CZTGS (x= 0.30) as HTL recorded an enhancement of efficiency from 5.88% (x= 0.00) to 7.48%. The increase in the efficiency was associated with the increment of the band gap energy (from 1.42 to 1.57 eV) and the improvement of electrical properties such as hole concentration (from $1x10^{18}$ to $2.23x10^{18}$ cm^{-3}) and hole mobility (from 3.9 to 18.9 $cm^2V^{-1}s^{-1}$). On the other hand, the efficiency of the PSC fabricated using an HTL with the highest Ge content (x= 0.60) drops to 2.56 % owing to the reduction of the mobility of the carriers in the HTL. The PSCs fabricated using CZTGS as HTL exhibited higher stability to ambient exposure for 315 h compared to the conventional PSC fabricated using spiro-OMeTAD as HTL and without HTL.

Publicaciones relacionadas con la tesis

- Mora-Herrera, D., Silva-González, R., **Cancino-Gordillo, F.E**. and Pal, M. "Development of Cu_2ZnSnS_4 films from a non-toxic molecular precursor ink and theoretical investigation of device performance using experimental outcomes", *Solar Energy*, 199, 246–255 (2020). https://doi.org/10.1016/j.solener.2020.01.077.

- **Cancino-Gordillo, F.E.**, Cab, J.V. and Pal, U. "Structure and transport behavior of hydrothermally grown phase pure $Cu_2ZnSn_{1-x}Ge_xS_4$ (x = 0.0, 0.3) nanoparticles", Applied Surface Science, 571, 151261 (2022). https://doi.org/10.1016/j.apsusc.2021.151261.

- **Cancino-Gordillo F.E.**, Ortiz-Quiñonez J.L., Pal M., Silva González R., Pal U. "Removal of secondary phases and its effect on the transport behavior of $Cu_2ZnSn_{1-x}Ge_xS_4$ kesterite nanoparticles", *Applied Surface Science*, 617, 156617 (2022). https://doi.org/10.1016/j.apsusc.2023.156617.

Publicaciones adicionales

- Ortiz-Quiñonez, J.L., García-González, L., **Cancino-Gordillo, F.E**. and Pal, U. "Particle dispersion and lattice distortion induced magnetic behavior of $La_{1-x}Sr_xMnO_3$ perovskite nanoparticles grown by salt-assisted solid-state synthesis", *Materials Chemistry and Physics* 246 (2020). https://doi.org/10.1016/j.matchemphys.2020.122834.

- Roy, A., **Cancino-Gordillo, F.E**., Saha, S., Pal, U. and Das, S. "Performance of asymmetric supercapacitor fabricated with perovskite-type Sr^{2+}-incorporated $LaMnO_3$ ($La_{0.7}Sr_{0.3}MnO_3$) nanostructures in neutral 1M Na_2SO_4 aqueous electrolyte", *International Journal of Energy Research*, 45(9), 14021–14033 (2021). https://doi.org/10.1002/er.6727.

- Ortiz-Quiñonez, J.L., **Cancino-Gordillo, F.E**. and Pal, U. "Nickel Ferrite Nanoparticle Decorated Graphene Oxide as Efficient Magnetically Separable Adsorbents for Cr(III) Ion Removal from Water", *Chemistry of Materials (2023), under review*.

Participación en eventos

- "Generación y eliminación de fases secundarias en nanoestructuras kesteritas de $Cu_2ZnSn_{1-x}Ge_xS_4$", **Francisco Enrique Cancino-Gordillo**, José-Luis Ortiz-Quiñonez y Umapada Pal, *LXIII Congreso Nacional de Física*, Morelia, Michoacán, México (2020).

- "Aplicación de nanopartículas de $Cu_2ZnSn_{1-x}Ge_xS_4$ (x= 0.0, 0.3 y 1.0) como transportadores de huecos en celdas solares de perovskita basadas en plomo", **Francisco Enrique Cancino-Gordillo**, Umapada Pal y Julio Villanueva Cab, *Simposio estudiantil de posgrado en ciencia de materiales BUAP 2021*, Puebla de Zaragoza, Puebla, México (2021).

- "Transport behavior of Ge incorporated kesterite Cu_2ZnSnS_4 nanoparticles", **Francisco Enrique Cancino-Gordillo**, Julio Villanueva Cab y Umapada Pal, *XXIX International Materials Research Congress*, Cancún, Quintana Roo, México (2021).

- "Eliminating impurity phases in $Cu_2ZnSn_{1-x}Ge_xS_4$ nanoparticles by chemical processing", **Francisco Enrique Cancino-Gordillo**, Jose-Luis Ortiz-Quiñonez, Umapada Pal, *XXX International Materials Research Congress and International Conference on Advanced Materials*, Cancún, Quintana Roo, México (2022).

Índice

Índice de Figuras

Índice de Tablas

Introducción

La población mundial se encuentra en constante crecimiento, ocasionando que la demanda energética aumente de manera considerable año con año para mantener diferentes sectores en operación como: industrias, transporte, hospitales, agricultura, residencial y comercial. En la actualidad, la energía eléctrica que utilizamos, proviene principalmente de recursos no renovables, particularmente de combustibles fósiles (carbón, petróleo y gas), los cuales al ser utilizados liberan dióxido de carbono y otros gases de efecto invernadero, siendo la principal causa del calentamiento global [1], [2]. Debido a esto, surge la necesidad de encontrar un recurso alternativo que permita generar la energía eléctrica de manera benigna para el medio ambiente y que sostiene la demanda energética global. El recurso renovable que ha resaltado por aplicarse en diferentes sectores es la energía solar. De acuerdo con el programa de la organización de las naciones unidas, la energía solar interceptada por la superficie de la tierra es 10 000 veces mayor que la energía consumida por la humanidad [1], [2]. La energía solar puede captarse y transformarse directamente en energía eléctrica por medio de una celda solar, que es un tipo de dispositivo fotoeléctrico, cuyas propiedades eléctricas, como la corriente, el voltaje o la resistencia, cambian una vez que se someten a la radiación solar. Para producir energía eléctrica de manera sustentable usando celdas solares, se han desarrollado diferentes tecnologías a lo largo de las décadas. Considerando la tecnología y materiales utilizadas en fabricación, podemos dividir estos dispositivos en tres generaciones [3]. Las celdas solares de primera generación están integradas por materiales monocristalinos, que permiten una alta eficiencia a un alto costo de fabricación. Dentro de los dispositivos de esta generación se puede encontrar las celdas de silicio (Si) y arseniuro de galio (GaAs) monocristalinos. Las celdas solares de la segunda generación tienen la característica de reducir los costos de fabricación al reducir la cantidad de material que se necesita para fabricarlas. La tecnología que implementan en esta generación es la fabricación de películas delgadas. En esta generación de celdas solares entran los materiales más famosos como: el silicio amorfo (a-Si), teluro de cadmio (CdTe), seleniuro de cobre indio galio

(CIGS) y sulfuro de cobre zinc estaño (Cu_2ZnSnS_4). Por último, las celdas solares de tercera generación se caracterizan por su alta eficiencia cuántica y bajo costos de fabricación. Las celdas de esta generación incluyen las celdas sensibilizadas por tinte y las celdas de perovskitas.

Las celdas solares de tercera generación comenzaron a surgir desde la publicación de Kojima *et al.* [4] sobre la utilización de materiales de perovskita organometálica en celdas solares sensibilizadas. A partir de este punto, un enorme número de investigadores de todo el mundo desarrollaron celdas solares de perovskitas basadas en plomo (Pb), que permitió mejorar la eficiencia de conversión energética desde 3.8% (registrado en el 2009) hasta ≥ 20% (en el 2020) (ver la **Figura I.1**) [5]. Esto demuestra que el avance que ha tenido en la investigación sobre celdas solares de perovskita durante solo 10 años, permitió obtener resultados que tardaron 35 años para obtener en celdas solares de segunda generación [6]. En el capítulo 2.2, se darán detalles de las estructuras comunes y los materiales que conforman las celdas solares de perovskita.

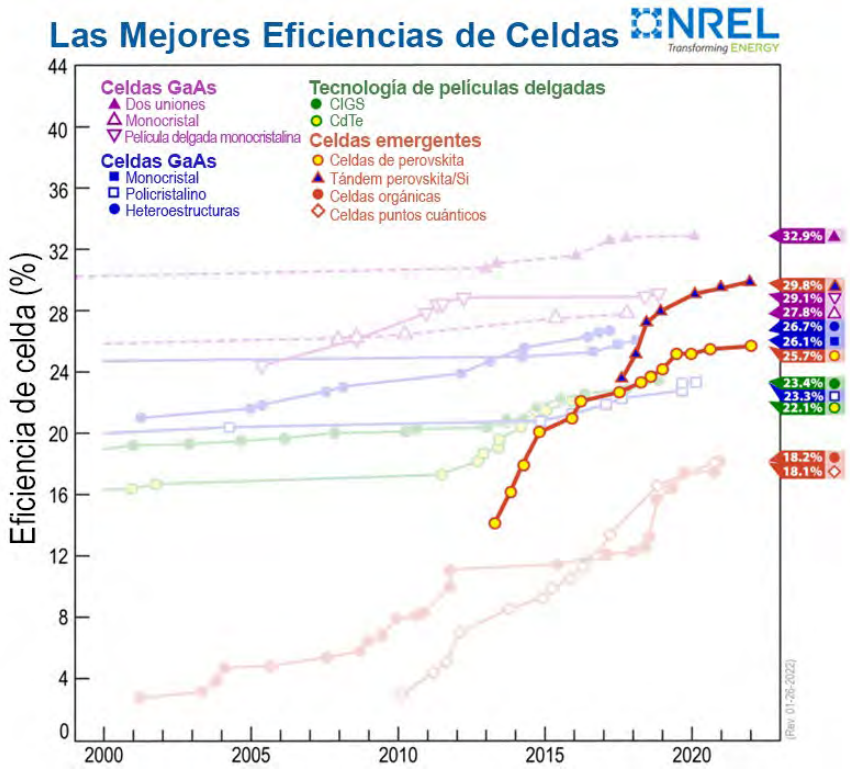

Figura I.1: Evolución de la eficiencia de las celdas solares de perovskita comparado con las tecnologías fotovoltaicas predecesoras (modificada de la referencia [7]).

Actualmente, la investigación en celdas solares de perovskitas se enfoca en la mejorar de la eficiencia de conversión energética, la estabilidad, la toxicidad y los métodos para reducir el costo de su fabricación. Dentro de la investigación que involucra una celda solar de perovskita se resalta encontrar materiales alternativos para la capa transportadora de huecos en los dispositivos. En general, las capas transportadoras de huecos en típicas celdas de perovskita están formadas por materiales orgánicos que presentan una baja estabilidad temporal a condiciones normales de operación (temperatura, radiación solar y humedad), por lo que, se busca remplazar los materiales orgánicos con materiales inorgánicos [8]. En el capítulo 2.3 se presenta una explicación más extensa de los materiales que se usan para fabricar capas transportadoras de huecos en celdas solares de perovskita. Por lo tanto, es considerado una investigación de vanguardia en encontrar nuevos materiales inorgánicos transportadores de huecos que puedan ser aplicados en celdas solares de perovskita. Un material que está comenzando a resaltar para ser un candidato estrella como material transportador de huecos en celdas de perovskita es el semiconductor tipo-p Cu_2ZnSnS_4 (CZTS) [9]–[13]. El semiconductor CZTS es un material de tipo-p, ampliamente investigado como material absorbente en celdas solares de segunda generación [14], [15] y tiene una alta concentración ($\sim 10^{14}$ cm^{-3}) y movilidad de portadores huecos (10 – 30 $cm^2V^{-1}s^{-1}$) [16]–[20]. Además, cumple con los requisitos de ser un material inorgánico con alta estabilidad, síntesis relativamente fácil y de bajo costo, contiene elementos no tóxicos y abundantes. Sin embargo, el semiconductor CZTS es un material del cual las propiedades eléctricas y ópticas dependen de los defectos puntuales como antisitios (Cu_{Zn} o Sn_{Zn}) o vacancias (V_{Cu}) y de los defectos complejos [21]–[23]. En el capítulo 2.1, de la tesis, se presenta las propiedades físicas y los defectos característicos de la estructura cristalina de la kesterita CZTS. Uno de los principales defectos en CZTS con estructura kesterita (tetragonal) es el antisitio de Sn_{Zn}, que produce los defectos complejos como ($2Cu_{Zn} + Sn_{Zn}$) debido a su menor valor de la energía de formación. El defecto complejo de ($2Cu_{Zn} + Sn_{Zn}$) actúa como un centro de recombinación para los pares electrón – hueco o puede causar una trampa energética para los electrones fotogenerados en el material [24]–[26]. Además, el estaño (Sn) es un elemento multivalente y su estado de oxidación puede intercambiar entre Sn^{4+} y Sn^{2+} espontáneamente debido a la perturbación en el balance de carga en la estructura cristalina de la kesterita durante la generación de las cargas por iluminación de luz (cargas fotogeneradas). Con este

contexto, una substitución parcial del Sn por un elemento de mismo grupo con un estado de oxidación estable, como el germanio (Ge), se considera como una solución viable a este problema [27]–[32]. La incorporación de Ge en la estructura del CZTS causa la formación del semiconductor $Cu_2ZnSn_{1-x}Ge_xS_4$ (CZTGS). El Ge, al tener un estado de oxidación estable y radio iónico pequeño, inhibe la formación de defectos no deseados como V_{Sn}, Cu_{Sn}, Sn_{Cu}, Zn_{Sn} y Sn_{Zn} [23], [33]–[35]. Además, la sustitución parcial del Sn por Ge provoca un incremento en la concentración de portadores de 10^{15} a 10^{17} cm^{-3}, y la conductividad del material de 10^{-4} $\Omega^{-1}cm^{-1}$ a 10^{-3} $\Omega^{-1}cm^{-1}$ (temperatura ambiente) [35], [36]. Sin embargo, la obtención del CZTGS en la fase kesterita pura es difícil debido a que las altas fracciones molares de Ge ($x \geq 0.25$) puede generar combinación de las fases tetragonal (kesterita) y ortorrómbica [35], segregación de fases secundarias como ZnS y $Cu_{2-x}S$ ($x \geq 0.8$) [27], o generar defectos con niveles profundos debido a la formación de vacancias de Sn (V_{Sn}) [29], [37]. Por lo que un estudio sistemático del impacto de los defectos y las fases secundarias en las propiedades de transporte del CZTGS se vuelve una tarea esencial para aplicar este material en dispositivos optoelectrónicos como celdas solares.

En este trabajo de tesis se presenta la síntesis de nanopartículas de CZTGS mediante el método hidrotermal, un proceso químico para eliminación de fases secundarias y un estudio sistemático del efecto de eliminación de fases secundarias en sus propiedades ópticas y eléctricas. Las nanopartículas de CZTGS sintetizadas se utilizaron para fabricar la capa transportadora de huecos en un ensamble de celda solar de perovskita con configuración n-i-p y se estudió los parámetros fotovoltaicos y estabilidad del dispositivo al variar la cantidad de Ge en la capa transportadora de huecos.

Capítulo 1 – Antecedentes

1.1 El Cu_2ZnSnS_4 como capa transportadora de huecos

El cuaternario Cu_2ZnSnS_4 (CZTS) es uno de los materiales más atractivos como capa absorbente en las celdas solares de segunda generación (tecnología de película delgada) con un increíble potencial para remplazar las capas absorbentes convencionales que se usan (CdTe y CIGS). El CZTS presenta un alto coeficiente de absorción en el rango espectral visible ($\sim 10^4$ cm^{-1}), una conductividad intrínseca tipo-p y una energía de banda prohibida de transición directa cercana a 1.5 eV [22], [23]. Todas estas propiedades son esenciales para un material que es usado como capa absorbente en las celdas solares de segunda generación. De hecho, la utilización del CZTS como capa absorbente en las celdas solares de segunda generación ha registrado una eficiencia de conversión de poder de 11.8 % [38]. Sin embargo, el valor de la eficiencia se encuentra muy por debajo en comparación con una celda solar de segunda generación utilizando CIGS (> 20 %) [23], [39]. La principal razón de la baja eficiencia del CZTS se debe a la presencia de los defectos electrónicos en este material que afectan directamente sus propiedades eléctricas y ópticas [14].

Por otro lado, debido a la conductividad tipo-p y a la moderada resistividad del CZTS, se está comenzando a utilizar como capa transportadora de huecos (*hole transport layer*, HTL) en celdas solares de perovskita (*perovskite solar cell*, PSC), remplazando a los materiales convencionales como el spiro-OMeTAD o el PEDOT:PSS. Para la utilización como capa absorbente en las celdas de segunda generación, las películas de CZTS deberían presentar un alto coeficiente de absorción, alta estabilidad ambiental, bajo costo de fabricación, bajo contenido de defectos electrónicos y una energía de banda prohibida en el rango de 1.4 – 1.5 eV. Mientras que para utilizar una película de CZTS como HTL en una PSC debe presentar, aparte de una conductividad tipo-p, una baja resistividad, alta concentración de portadores y bajo contenido de defectos [40]. El primer trabajo publicado sobre la utilización del CZTS como HTL es de Wu *et al*. en el año 2015 [9], donde reportaron el usó de nanopartículas sintetizadas por el método de inyección caliente en una PSC con configuración n-i-p. Los autores realizaron un estudio detallado de los parámetros

fotovoltaicos de una PSC usando las nanopartículas de CZTS y compararon los resultados con una PSC de referencia ensamblada con spiro-OMeTAD como HTL. La PSC ensamblada con las nanopartículas de CZTS en la HTL reveló un voltaje a circuito abierto (*open-circuit voltage*, V_{oc}) de 1.06 V, una densidad de corriente a corto circuito (*short-circuit current density*, J_{sc}) de 20.54 mA/cm^2, un factor de llenado (*FF*) de 58.7% y una eficiencia (η) de ~12.75%, mientras que la PSC de referencia ensamblada con spiro-OMeTAD presentó valores de 1.07 V, 18.94 mA/cm^2, 65.0% y 13.23%, respectivamente (ver la **Figura 1.1.1(a)**). Los resultados obtenidos en este trabajo demuestran el potencial que tiene el CZTS para transportar huecos de manera efectiva como los HTLs usados ampliamente como el spiro-OMeTAD. La reducción del *FF* para la PSC fabricada con las nanopartículas de CZTS se le atribuye al aumento en la resistencia en serie (R_s), lo que sugiere un aumento en la corriente de recombinación debido a la menor cobertura del HTL con las nanopartículas de CZTS. Por otro lado, el alto valor del J_{sc} en la PSC fabricada usando las nanopartículas de CZTS como HTL se asocia a la mejora en la absorción de luz en la PSC en el rango espectral de 400–850 nm y, también, a una mejora en la calidad de la interfase entre el contacto de oro y la capa de perovskita; es decir, se redujo la recombinación de los portadores (electrones–huecos). Por otro lado, Yuan *et al*. [41] utilizó puntos cuánticos de CZTS, sintetizados por el método de inyección caliente, como HTL en una PSC con configuración n-i-p. En este caso, los autores estudiaron la variación de la energía de la banda prohibida (desde 1.64 eV a 1.14 eV) realizando una sustitución total del azufre por selenio, para formar $Cu_2ZnSnSe_4$ (CZTSe), y estudiaron los efectos que tenía en los parámetros fotovoltaicos, principalmente en el V_{oc}. El análisis de las curvas de densidad de corriente y voltaje revelaron que las PSCs fabricadas usando puntos cuánticos de CZTS y CZTSe como transportadores de huecos tienen, respectivamente, valores comparables de la J_{sc} (~19 mA/cm^2), pero con una diferencia en sus *FF*s (reducción de 62.1% a 60.5%), V_{oc} (reducción de 0.945 V a 0.808 V) y consecuentemente en la η (reducción de 10.72% a 9.72%). La disminución de V_{oc} en la PSC con HTL de nanopartículas de CZTSe se asoció a un desplazamiento del borde de la banda de valencia hacia mayor energía, el cual induce una alta recombinación de los portadores de carga en la interfaz de la capa de perovskita y el HTL (ver la **Figura 1.1.1(b)**). El estudio realizado por medio de Espectroscopía de impedancia electroquímica (*electrochemical impedance spectroscopy*, EIS) reveló que la PSC fabricada con nanopartículas de CZTSe en

el HTL presenta una baja resistencia a recombinación, es decir, induce una alta velocidad de recombinación. En consecuencia, afecta negativamente los parámetros fotovoltaicos. Adicionalmente, los resultados de voltamperometría cíclica a las nanopartículas de CZTS y CZTSe revelaron que los bordes de la banda de conducción y la banda de valencia se desplazan; reduciendo la energía de la banda prohibida para las nanopartículas de CZTSe, ocasionando que la PSC que utiliza CZTSe como HTL tenga una pérdida de 300 mV en el valor de su V_{oc} (el valor teórico calculado es 1.3 V). Estos resultados demuestran claramente como el valor de la energía de la banda prohibida del HTL afecta a los parámetros fotovoltaicos de la PSC.

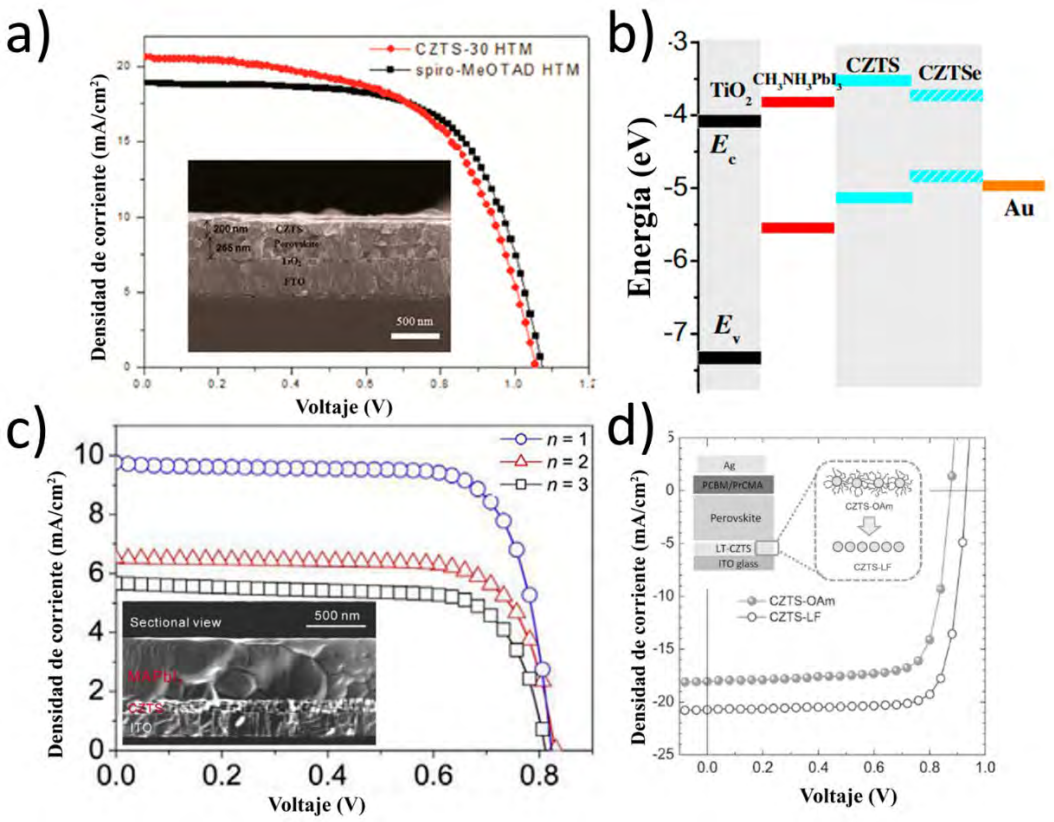

Figura 1.1.1: (a) Curvas J – V de las PSCs usando spiro y CZTS como HTL (modificada de la referencia [9]). El inserto corresponde a la sección transversal de una PSC de configuración n-i-p fabricada usando nanopartículas de CZTS como HTL. (b) Representación esquemática de la alineación de los niveles de energía en una PSC con diferentes tipos de HTLs (modificada de la referencia [41]). (c) Curvas de J–V de una PSC fabricadas con CZTS como HTL de diferentes espesores (desde 97 nm hasta 278 nm). El inserto corresponde a la sección transversal de la celda con configuración p-i-n usando 97 nm de espesor para el HTL (modificada de la referencia [42]). (d) Curvas J–V típicas de una PSC de configuración p-i-n fabricada con nanopartículas de CZTS con ligantes y sin ligantes como HTL (modificada de la referencia [10]).

Ashebir *et al*. [42] fabricaron una película de CZTS utilizando una solución precursora y aplicaron como capa HTL para fabricar una PSC con configuración p-i-n. En la solución precursora se disolvían las sales precursoras de Cu, Zn, Sn y tiourea en N,N-dimetilformamida (DMF). Para fabricar la película utilizaban el método de recubrimiento por centrifugación (*spin-coating*) y posteriormente la película ha sido tratada térmicamente a 300 °C por 5 min. Las imágenes SEM de la sección transversal del CZTS depositado sobre sustrato de vidrio conductor de óxido de estaño dopado con indio (*indium tin oxide*, ITO) muestran que la película es conformada por una capa compacta de 10 – 20 nm de nanopartículas de CZTS. Los autores probaron HTLs de CZTS de diferentes espesores para estudiar el efecto del espesor en los parámetros fotovoltaicos de la PSC. Los resultados obtenidos mostraron que entre más delgada sea la HTL causa un incremento en la J_{sc} y en la η, sin observar cambios significativos en el V_{oc} y *FF* (ver la **Figura 1.1.1(c)**). El valor optimo del espesor del HTL de CZTS que encontraron es alrededor de 97 nm, que presentó los siguientes valores de los parámetros fotovoltaicos: J_{sc} = 9.70 mA/cm^2, V_{oc} = 0.82 V, *FF* = 76.10% y η = 6.02%. La reducción de los valores de estos parámetros fotovoltaicos conforme el incremento del espesor de la capa de CZTS ha sido asociado al alto coeficiente de absorción de la película de CZTS (> 10^4 cm^{-1}, en la región del visible), que causo una atenuación de la intensidad de la iluminación incidente en el paso de su trayectoria cuando atraviesa por la película de CZTS. La atenuación ocasionada por el grosor de la película de CZTS ocasiona que la intensidad de la luz que llega a la capa de la perovskita sea mucho menor y como resultado los parámetros fotovoltaicos se reducen. Adicionalmente, se probaron la estabilidad de la PSC con HTL de CZTS contra una PSC de referencia (usando PEDOT:PSS como HTL), resultando en que la eficiencia se mantiene a un 87% después de 43 días de almacenamiento en la atmosfera de N_2, cuando la celda de referencia se deterioró por completo después de 35 días de almacenamiento en N_2. El trabajo resalta el potencial que tiene el CZTS como HTL en términos de estabilidad comparado con una PSC que usa un compuesto orgánico como HTL. Otro estudio importante sobre la aplicación de nanopartículas de CZTS en PSC como HTL se realizó por Khanzada *et al*. [10], en el cual, reportaron la eliminación de los ligantes en la superficie de las nanopartículas de CZTS para mejorar las propiedades de transporte de la película depositada como HTL. En este trabajo, los autores sintetizaron las nanopartículas de CZTS por el método de inyección caliente,

usando un surfactante (oleilamina) para controlar el crecimiento de las partículas y, posteriormente, remplazaron el ligante (oleilamina) con iones de tetrafluoroborato (BF_4^-) para funcionalizar las nanopartículas con un solvente de coordinación más débil, como la dimetilformamida (DMF). Las nanopartículas sintetizadas fueron utilizadas para HTL de una PSC de configuración p-i-n. Las mediciones de corriente limitada de carga espacial (*space charge limited current*, SCLC) reveló que la movilidad de portadores en las nanopartículas de CZTS sin ligantes ($3.4x10^{-2}$ $cm^2V^{-1}s^{-1}$) es mayor por tres órdenes de magnitud que en las nanopartículas sintetizadas con ligante como oleilamina ($7.7x10^{-5}$ $cm^2V^{-1}s^{-1}$). Además, en la PSC ensamblada usando nanopartículas de CZTS sin ligante presentó un mejoramiento (aumento en sus valores) de los parámetros fotovoltaicos (J_{sc} = 20.7 mA/cm^2, V_{oc} = 0.92 V, *FF* = 81%, η = 15.4%) con una alta reproducibilidad comparados con la PSC ensamblada usando nanopartículas de CZTS con ligante en su superficie (J_{sc} = 18.1 mA/cm^2, V_{oc} = 0.88 V, *FF* = 77%, η = 12.2%) (ver la **Figura 1.1.1(d)**). El aumento en el valor del *FF* se atribuyó al aumento de la movilidad de los portadores y la conductividad de las nanopartículas CZTS al eliminar el ligante orgánico de la superficie. En este estudio los autores demuestran la importancia de mejorar las propiedades del transporte para aumentar el rendimiento de la PSC.

Como fue mencionado en la sección de introducción, el CZTS es un material que tiene muchos defectos puntuales y defectos complejos dependiendo de la estequiometria del material. Entonces es importante explorar la investigación de modificar el CZTS por sustitución de algunos de sus elementos para mejorar sus propiedades de transporte. Recientemente, Wu *et al*. [43] utilizaron el CZTS con una sustitución parcial de los átomos de Zn por átomos de Cd, es decir, utilizó el material $Cu_2Cd_xZn_{1-x}SnS_4$ (CZTS:Cd), para la capa HTL en una PSC con configuración n-i-p. Además, se impurifico la capa HTL por la introducción de nanorodillos de oro. El objetivo del trabajo era realizar la sustitución parcial del Zn por Cd para aumentar la absorbencia óptica del material en la región de 800 a 900 nm (región donde no absorbe la perovskita). Con estas condiciones los autores lograron los siguientes valores de los parámetros fotovoltaicos: J_{sc} = 23.63 mA/cm^2, V_{oc} = 1.15 V, *FF* = 78.0% y η = 21.08%. Por otro lado, Mora-Herrera *et al*. [44] realizaron un estudio teórico (simulación) utilizando una sustitución parcial de los átomos de Sn por átomos de Ge, es decir, utilizaron el material $Cu_2ZnSn_{1-x}Ge_xS_4$ (CZTGS) para la capa HTL en una PSC con

configuración n-i-p. Los resultados de simulación revelaron que la utilización del CZTGS como HTL incrementa la resistencia a la recombinación de portadores en la interfaz de la perovskita y la capa HTL aumentando el valor de V_{oc} (consecuentemente aumenta la η) de la celda. El incremento en la resistencia de recombinación y el valor de V_{oc} ha sido asociado a la reducción de las recombinaciones de portadores fotogenerados en la interfaz del HTL y la perovskita, debido a que el nivel mínimo de la banda de conducción se modifica al sustituir los átomos de Sn por Ge. Los resultados de estos trabajos indican claramente como la modificación del CZTS con la sustitución de los elementos permite mejorar los valores de los parámetros fotovoltaicos. Por lo tanto, para aplicar en PSC como HTL, el material CZTS se debe crecer con las condiciones donde se reduzca la resistencia del material, conservando su propiedad de alta absorción de luz e incremente el valor de la energía de la banda prohibida con un alineamiento favorable de la banda de valencia para evitar recombinaciones en la interfaz de la capa de perovskita y la HTL. En este trabajo de tesis se aborda la síntesis, purificación y estudio de las propiedades físicas (estructurales, ópticas y eléctricas) de las nanopartículas de CZTGS y se correlaciona con los efectos de los parámetros fotovoltaicos y de estabilidad en una PSC con configuración n-i-p al aplicarse como HTL de manera experimental.

1.2 Objetivos

1.2.1 Objetivo

Sintetizar las nanopartículas de $Cu_2ZnSn_{1-x}Ge_xS_4$ por el método hidrotermal en fase pura para su aplicación como material transportador de huecos en celdas solares de perovskita basadas en plomo en configuración n-i-p.

1.2.2 Objetivos específicos

- Sintetizar nanopartículas de $Cu_2ZnSn_{1-x}Ge_xS_4$ mediante un proceso hidrotermal.
- Caracterizar las nanopartículas de $Cu_2ZnSn_{1-x}Ge_xS_4$ por difracción de rayos-x, espectroscopía Raman, microscopia electrónica de barrido junto con espectrometría

de dispersión de energía de rayos-x, microscopia electrónica de transmisión y espectroscopía óptica (UV-Vis).

- Fabricar y optimizar el depósito por *spin-coating* sobre substratos de vidrio empleando tintes de las nanopartículas de $Cu_2ZnSn_{1-x}Ge_xS_4$.
- Evaluar las propiedades de transporte de las películas fabricadas.
- Ensamblar la celda solar de perovskita usando los tintes de nanopartículas de $Cu_2ZnSn_{1-x}Ge_xS_4$.
- Caracterizar las celdas solares fabricadas mediante sus curvas de densidad de corriente – voltaje (curvas J – V) y monitorear su estabilidad para comparar su desempeño con celdas solares de perovskita ensambladas con spiro-MeOTAD (transportador de huecos).

Capítulo 2 – Aspectos Generales

2.1 Propiedades físicas de Cu_2ZnSnS_4 (CZTS) y $Cu_2ZnSn_{1-x}Ge_xS_4$ (CZTGS)

El compuesto Cu_2ZnSnS_4, conocido como CZTS (por sus siglas en inglés *Copper Zinc Tin Sulfide*), es un material que surge para sustituir los compuestos sulfuro de cobre indio (CIS), seleniuro de cobre indio galio (CIGS) y el teluro de cadmio (CdTe) en el sector de los dispositivos fotovoltaicos de segunda generación. Como se sabe los compuestos CIGS y CdTe tienen que enfrentar algunos inconvenientes por contener elementos escasos, tóxicos y con incremento rápido de sus precios [45]. Por lo que la kesterita surge de la familia de los calcogenuros donde su estructura cristalina es derivada del CIGS mediante el remplazo de dos cationes del grupo III con uno del grupo II (Zn) y uno del grupo IV (Sn) [46]. Con este remplazo de cationes se brinda una gran flexibilidad en la selección de elementos, lo que permite la incorporación de elementos abundantes en la tierra, surgiendo los compuestos cuaternarios del grupo I_2-II-IV-VI_4 (**Figura 2.1.1**). Debido a la estructura cristalina y banda de energía similares al CIGS, el compuesto CZTS hereda los méritos de alto coeficiente de absorción ($>10^4$ cm^{-1}) en el rango espectral visible; su energía de banda prohibida ajustable entre 1.0 a 1.5 eV; además de su intrínseca conductividad de tipo-p dentro de un rango adecuado para aplicación en dispositivos fotovoltaicos [46]. Dado a las similitudes, el compuesto CZTS ha sido utilizado con una arquitectura de dispositivo idéntica a la de CIGS (usando la configuración de sustrato de Mo como contacto posterior y una capa CdS como amortiguador de electrones), lo que facilitó el proceso inicial de esta tecnología fotovoltaica de bajo costo [47], [48]. En la actualidad, se han utilizado distintas técnicas para la fabricación de nanoestructuras (películas o nanopartículas) por métodos físicos [49]–[53] y químicos [54]–[59]. A continuación, en el marco de referencia del trabajo se presentan la estructura cristalina, los defectos cristalinos, la sustitución de los cationes del CZTS.

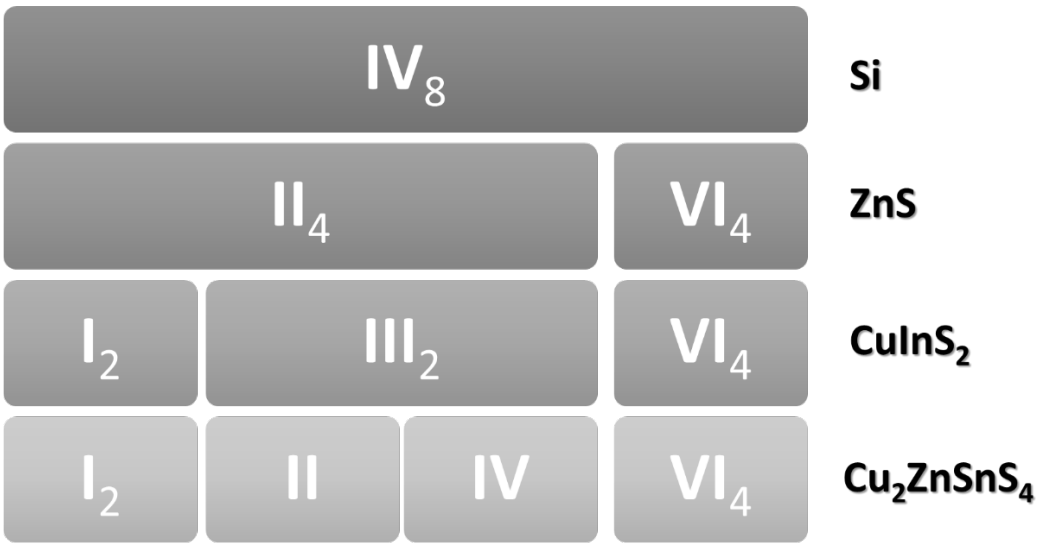

Figura 2.1.1: Diagrama del origen de los compuestos cuaternarios I_2-II-IV-VI_4.

2.1.1 Estructura cristalina del CZTS

Los semiconductores del grupo I_2-II-IV-VI_4 (donde los números romanos corresponden a los grupos de la tabla periódica) son compuestos que presentan dos tipos de estados en equilibrio: la estructura kesterita ($I\bar{4}$) y la estructura estanita ($I42m$). Ambas estructuras cristalinas son muy semejantes excepto que los átomos de Cu y Zn están en diferentes posiciones cristalográficas. Sin embargo, es bien sabido que la estructura kesterita es termodinámicamente más estable en comparación con la estructura estanita; esto se debe principalmente a la diferencia en la energía de formación [60]. De acuerdo con las posiciones de Wyckoff, en la estructura kesterita un átomo de Cu ocupa la posición 2a (0,0,0) y el resto de átomos de Cu se encuentran localizados en la posición 2c (0,½,¼), los átomos de Zn ordenados en las posiciones 2d (0, ¼, ¾), los átomos de Sn localizados en la posición 2b (0,0, ½) y, finalmente, los aniones de S se encuentran ubicados en la posición 8g (*x*,*y*,*z*). El arreglo en las posiciones de los cationes permite que la estructura kesterita se caracteriza por tener capas alternadas a lo largo del eje-c de Cu-Sn, Cu-Zn, Cu-Sn, Cu-Zn y Cu-Sn para z= 0, ¼, ½, ¾ y 1 (ver la **Figura 2.1.2**).

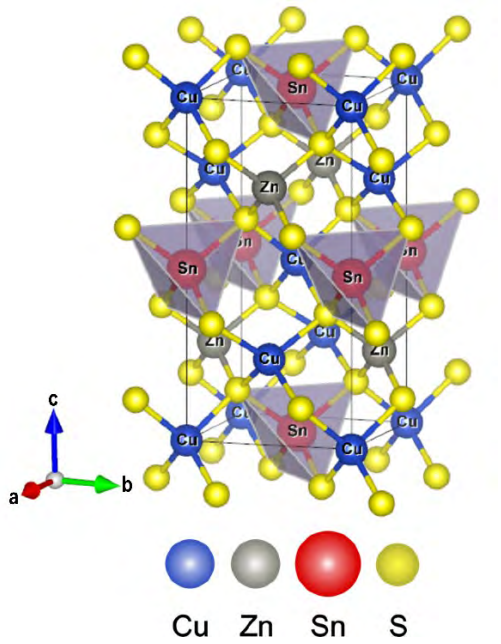

Tabla 2.1.1: Propiedades del Cu_2ZnSnS_4 (CZTS) con estructura kesterita.

Propiedades	Cu_2ZnSnS_4 (kesterita)	
Parámetros de red (Å)	a= 5.4322 c= 10.8434	[61]
Grupo espacial	$I\bar{4}$	
Densidad (g/cm^3)	4.56	[23]
Energía brecha prohibida (eV)	1.4 – 1.5	[22], [62]
Coeficiente de absorción (cm^{-1})	10^4	[22], [62]
Concentración de portadores (cm^{-1})	10^{15} – 10^{20}	[22], [36]
Punto de fusión (°C)	990	[23]

Figura 2.1.2: Estructura kesterita mostrando el poliedro tetragonal de coordinación de los átomos de estaño (Sn) enlazados con 4 átomos de azufre (S). A la derecha se presentan algunas propiedades del Cu_2ZnSnS_4 (CZTS) con estructura kesterita.

Uno de los principales problemas que tiene el semiconductor CZTS es que se ha encontrado experimentalmente mediante difracción de neutrones que existe un desorden en los átomos de Cu y Zn en las capas de z= ¼ y ¾ resultando en un defecto de antisitio de Cu ocupando el lugar del Zn (Cu_{Zn}) o el Zn ocupando el lugar de un Cu (Zn_{Cu}). Cuando existe este desorden de ubicación de los átomos de Cu y Zn la estructura se denomina kesterita desordenada [63]–[69]. El desorden en la posición de los átomos de Cu y/o Zn afecta las propiedades optoelectrónicas del semiconductor como la energía de brecha prohibida y fluctuaciones en la brecha prohibida [64], [65], [67]–[69].

2.1.2 Defectos y fases secundarias del CZTS

El semiconductor CZTS con estructura kesterita es un compuesto de múltiples elementos que conlleva la existencia de diversos defectos y que sea un desafío sintetizarlo estequiométricamente en fase pura. De acuerdo con el estudio de primeros principios, el semiconductor CZTS contiene los siguientes defectos [21], [24], [70], [71]:

- Defectos de antisitio (cuando un átomo se ubica en un lugar cristalográfico diferente) como: Cu_{Zn}, Zn_{Cu}, Zn_{Sn} y Sn_{Zn}.
- Defectos intersticiales (cuando un átomo se encuentra en un espacio que no corresponde a la simetría) como: Cu_i, Zn_i, Sn_i y S_i.
- Defectos de vacancias (cuando un átomo deja un espacio vacío en su posición cristalográfica) como: V_{Cu}, V_{Zn}, V_{Sn} y V_S.
- Defectos de complejos (cuando se forman dos o más defectos) como: (V_{Cu} + Zn_{Cu}), ($2Cu_{Zn}$ + Sn_{Zn}) y (Zn_{Sn} + $2Zn_{Cu}$).

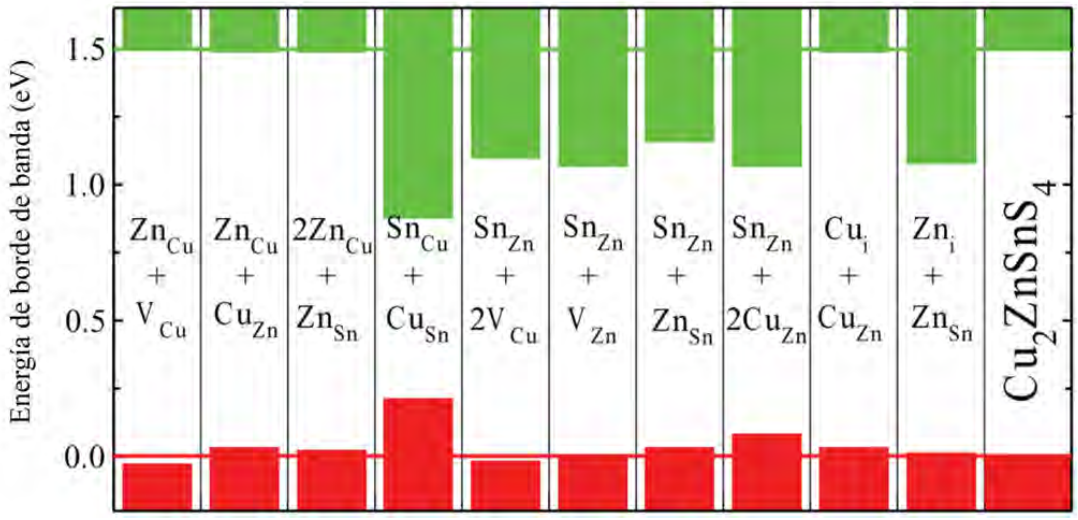

Figura 2.1.3: Corrimientos de banda de conducción y valencia calculados causados por diferentes defectos complejos en Cu_2ZnSnS_4 (CZTS). Las líneas de color rojo y verde representan la posición de la banda de valencia y conducción, respectivamente. La concentración de defectos que se consideró para el cálculo es un defecto complejo por cada 128 átomos en supercelda [25].

Aunque la mayoría de los defectos se han estudiado por cálculos teóricos, la formación de ciertos defectos intrínsecos también fue identificado experimentalmente [14], [72]–[74]. Recordemos que la estructura kesterita contiene iones de Cu^+ y Zn^{2+} con radios iónicos semejantes (~0.74 Å), lo que ocasiona que exista de manera intrínseca una

concentración de defectos de antisitio Cu_{Zn} y Zn_{Cu}. El CZTS es un semiconductor con conducción tipo-p de manera intrínseca y esto se debe a la formación de los defectos de antisitio Cu_{Zn} que forman un nivel aceptor cerca de la banda de valencia y debido a que tiene una energía de formación muy baja se considera un defecto intrínseco del material (**Figura 2.1.3**). Por otra parte, el Sn es un elemento multivalente que tiene dos estados de oxidación estables, el Sn^{2+} y el Sn^{4+}, lo que ocasiona que se forme el defecto complejo de ($2Cu_{Zn}$ + Sn_{Zn}), que tiene una energía de formación muy semejante a los defectos intrínsecos del material. El defecto complejo de ($2Cu_{Zn}$ + Sn_{Zn}) no es favorable para el material, en términos de aplicación en celdas solares de segunda generación, porque forma estados intermedios que puede atrapar huecos o electrones fotogenerados [24], [26]. En la **Figura 2.1.3** se puede observar el corrimiento teórico en la posición del máximo de la banda de valencia y el mínimo de la banda de conducción ocasionado por los defectos complejos que se forman en la estructura kesterita [25].

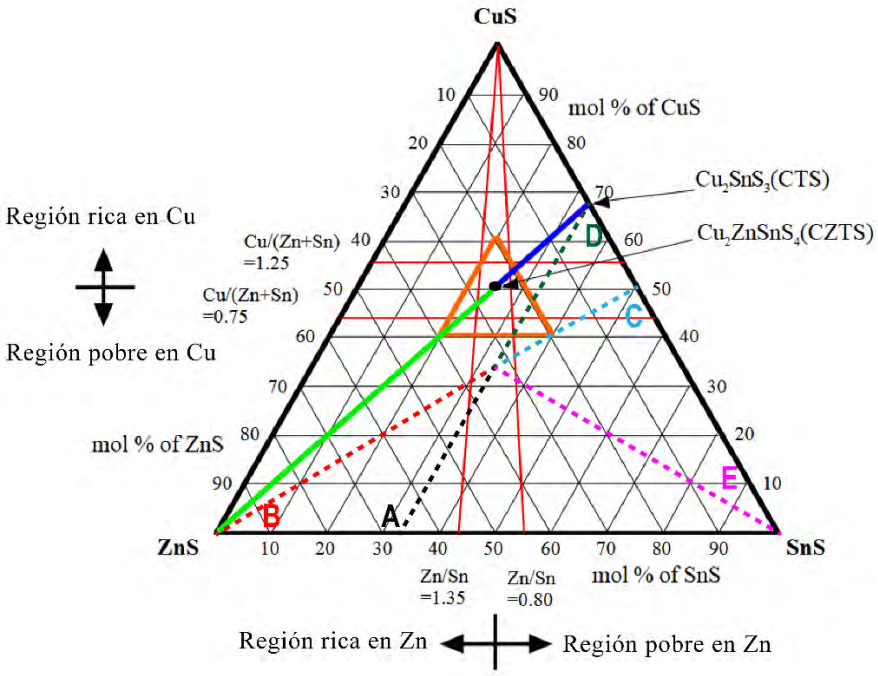

Figura 2.1.4: Diagrama de fase pseudo-ternario CuS-ZnS-SnS. El circulo de color negro representa el punto donde la composición elemental del Cu_2ZnSnS_4 (CZTS) es estequiométrica y el triángulo de color naranja ubicado en el centro representa la región estable fuera de la estequiometria para obtener el CZTS sin fases secundarias. Las líneas punteadas representan las composiciones elementales típicas usadas en la literatura (ver **Tabla 2.1.2**) [70], [75].

El CZTS es un semiconductor que permite variar la composición estequiométrica del compuesto permitiendo modular la concentración de defectos y defectos complejos afectando significativamente las propiedades eléctricas y ópticas del material [22], [70]; es decir, se puede aplicar ingeniería de defectos. Por ejemplo, el defecto complejo ($2Cu_{Zn} + Sn_{Zn}$) tiene una concentración elevada cuando el CZTS tiene composición estequiométrica. Entonces para disminuir la concentración de este defecto se utiliza las condiciones de composición estequiométrica pobre en Cu (*Cu-poor*) y rico en Zn (*Zn-rich*). La composición de *Cu-poor y Zn-rich* en el CZTS se utiliza para la fabricación de capa absorbente de las celdas solares de segunda generación para reducir la concentración del defecto ($2Cu_{Zn} + Sn_{Zn}$) e incrementar la concentración del defecto complejo ($Zn_{Cu} + V_{Cu}$). El defecto complejo ($Zn_{Cu} + V_{Cu}$) no genera niveles de trampas intermedios y no modifica significativamente las posiciones de las bandas de conducción y valencia (**Figura 2.1.3**). Además, los defectos de V_{Cu} generan un aumento en la concentración de portadores de carga. Por lo tanto, para una aplicación en celdas solares de segunda generación se utiliza ampliamente la composición estequiométrica *Cu-poor* y *Zn-rich* [76]–[78]. En la **Tabla 2.1.2** se presentan la predicción del defecto que aumenta su concentración conforme la composición del CZTS se acerca a las líneas punteadas del diagrama de fases de la **Figura 2.1.4** [25], [70].

Tabla 2.1.2: Descripción general de los tipos de defectos en el CZTS con estructura kesterita fuera de la composición estequiométrica [25], [70].

Línea punteada	Composición estequiométrica	Defecto
A	pobre en Cu, rico en Zn, Sn constante	$V_{Cu} + Zn_{Cu}$
B	pobre en Cu, rico en Zn, pobre en Sn	$2Zn_{Cu} + Zn_{Sn}$
C	rico en Cu, pobre en Zn, rico en Sn	$2Cu_{Zn} + Sn_{Zn}$
D	rico en Cu, pobre en Zn, Sn constante	$Cu_{Zn} + Cu_i$
E	pobre en Cu, pobre en Zn, rico en Sn	$2V_{Cu} + Zn_{Sn}$ o $Sn_{Cu} + V_{Cu}$

Por otro lado, el CZTS tiene una región muy pequeña en el diagrama de fases donde se puede obtener en fase pura, es decir, fuera de esta región la composición del CZTS tiene una estequiometria fuera de normal, y se puede generar la formación de fases secundarias (**Figura 2.1.4**) [21], [79], [80]. Consecuentemente, la formación de fases secundarias ocurre durante el crecimiento del CZTS o después de un tratamiento térmico posterior a su

crecimiento [69], [76], [80], [81]. En la **Figura 2.1.4** se puede apreciar dos líneas continuas de color verde y azul. Cuando la composición es *Zn-rich* siguiendo la línea continua de color verde, aumenta la probabilidad de que exista una mezcla de fases de CZTS y sulfuro de zinc (ZnS). Por lo otro lado, cuando la composición es *Zn-poor* siguiendo la línea continua de color azul, tiene la probabilidad de obtener una fase mezcla de CZTS y Cu_2SnS_3 es mayor. En ambos casos la coexistencia de dos fases es perjudicial para la aplicación del CZTS como material absorbedor en una celda solar de película delgada o como material transportador de huecos en una celda solar de perovskita. La región no estequiométrica más estable donde la probabilidad de no generar fases secundarias fue delimitada por el triángulo de color naranja en el diagrama de fase mostrada en la **Figura 2.1.4**. La composición estequiométrica más utilizada en las celdas solares de película delgada es *Cu-poor* y *Zn-rich* [76]–[78], donde es probable que se forme ZnS. El ZnS es considerado como un material aislante por su alta resistencia y su amplia energía de brecha prohibida (3.84 eV) que puede inducir una reducción de área activa de un dispositivo fotovoltaico cuando se utiliza como un material de capas absorbedores [21], [80]. En la **Tabla 2.1.3** se presentan las fases secundarias típicas que se forman en la síntesis del CZTS y cómo puede afectar en términos de celdas solares de segunda generación. Para eliminar algunas fases secundarias que se forman al sintetizar el CZTS se emplea lavados químicos [82]–[85].

Tabla 2.1.3: Algunas propiedades de las fases secundarias reportadas en la síntesis del Cu_2ZnSnS_4 (CZTS) [21].

Propiedades	ZnS	Cu_2S	SnS_2	Cu_2SnS_3
Energía de banda prohibida	3.54 – 3.68 eV	1.21 eV	2.2 eV	0.98 – 1.35 eV
Propiedades eléctricas	Aislante	Conducción de huecos (tipo-p), comportamiento metálico	Conducción de electrones (tipo-n)	Conducción de huecos (tipo-p)

2.1.3 Sustitución de cationes

Como ha sido discutido en las secciones anteriores es necesario buscar alternativas para reducir la concentración de los defectos de antisitio, especialmente los defectos complejos que involucren iones de Sn y que no generé fases secundarias. En este sentido, los investigadores han explorado una sustitución parcial de los cationes Cu, Zn y Sn en la red de

kesterita con otros cationes como plata (Ag^+) [86]–[88], cadmio (Cd^{2+}) [58], [89] y germanio (Ge^{4+}) [30]–[32], [90], [91]. Por ejemplo, una sustitución parcial de los iones de Cu^+ por Ag^+ en la estructura kesterita se ha demostrado teóricamente que disminuye la concentración de defectos de antisitio como el Cu_{Zn} y Zn_{Cu} y los defectos complejos como: (V_{Cu} + Zn_{Cu}), ($2Cu_{Zn}$ + Sn_{Zn}) y (Zn_{Sn} + $2Zn_{Cu}$) [86]–[88]. La formación de los defectos como Ag_{Zn}, (Ag_{Zn} + Zn_{Ag}) y ($2Ag_{Sn}$ + Sn_{Zn}) en la kesterita con la substitución parcial no son esperados porque los átomos de Ag solo pueden tener un estado de oxidación estable (Ag^+) y el radio iónico del Ag^+ (1.14 Å) es substancialmente más grande que el radio iónico del Cu^+ (0.74 Å) y Zn^{2+} (0.74 Å) [92].

Por otro lado, cuando se utiliza el Cd^{2+} para sustituir al catión Zn^{2+} para formar $Cu_2Cd_xZn_{1-x}SnS_4$, se espera que la energía de formación de los defectos de antisitio Cu_{Cd} y Cd_{Cu} se incremente; pero debido a la similitud del radio iónico y al estado de valencia de los átomos esto no ocurre. Además, el Cd es un material tóxico que se considera escaso, por lo que, se busca reducir su utilización en dispositivos fotovoltaicos como se mencionó anteriormente. Entonces, una opción viable es la sustitución parcial de los átomos de Sn por átomos de Ge en la estructura kesterita. De hecho, se ha demostrado que la sustitución parcial de este tipo mejora el rendimiento de las celdas solares de segunda generación fabricadas con CZTS como material absorbente [30]–[32], [90], [91]. La sustitución con los átomos de Ge en el CZTS causa la formación de $Cu_2ZnSn_{1-x}Ge_xS_4$ (CZTGS) que tiene la posibilidad de disminuir la formación indeseada de los defectos antisitio como Sn_{Zn} (especialmente el defecto complejo ($2Cu_{Zn}$ + Sn_{Zn})). La concentración de los defectos de antisitio de Sn_{Zn} decrece en el semiconductor CZTGS porque la energía de formación de estos defectos incrementa debido a que el ion Ge^{4+} no puede ocupar el sitio cristalográfico del Sn, como en el caso de los iones de Cu^+ y Zn^{2+} [29], [93].

El material CZTGS con estructura kesterita en fase pura es un desafío obtenerla porque cuando la substitución de los átomos de Sn por átomos de Ge es alta ($x \geq 0.25$) puede generarse mezcla de fases de tetragonal y ortorrómbica [35], formando subproductos como ZnS y Cu_xS ($x \geq 0.8$) [27] o generando niveles profundos por la formación de defectos de vacancias de Sn (V_{Sn}) [29], [37]. De hecho, en las celdas solares de segunda generación que

utiliza el CZTGS como material absorbedor se ha reportado que la eficiencia de conversión de energía disminuye desde 11% (para x~0.25) a 1% (para x~0.75) [94].

2.2 Celdas de perovskita

Los materiales de perovskita tienen una estructura cristalina especifica con una formula general de ABX_3 (X= oxigeno o halógeno). Como se puede observar en la **Figura 2.2.1** se presenta un esquema de la estructura característica de las perovskitas donde: el catión A ocupa un sitio en un cubo-octaédrico compartido con doce aniones X y el catión B se estabiliza en un sitio octaédrico rodeado con seis aniones X. La formabilidad de la perovskita se estima en función de su factor de tolerancia geométrica (*t*) de acuerdo con la siguiente ecuación [95]:

$$t = \frac{r_A + r_X}{\sqrt{2(r_B + r_X)}} \qquad (2.2.1),$$

donde $r_A, r_B \; y \; r_X$ son los radios iónicos efectivos de cada ion de la estructura, respectivamente. El factor de tolerancia predice si el catión del sitio A puede caber dentro de las cavidades que se forman por los octaedros de BX_6. Generalmente, la estructura cristalina de la perovskita se forma dentro del rango de $0.8 \leq t \leq 1$. Cuando el factor de tolerancia tiene el valor de 1, indica que el ajuste es perfecto y es cuando el grupo espacial es Pm-3m, sin embargo, en el límite inferior (cercano a 0.8) la estructura cristalina de la perovskita comienza a distorsionarse debido a la inclinación de los octaedros de BX_6 y la simetría disminuye, por lo que conduce a que se forme estructuras cristalinas alternas a la perovskita. Entonces para que siempre se conserve la estructura cristalina de la perovskita estable, el radio iónico del catión A tiene que ser más grande que el radio iónico del catión B ($r_A > r_B$).

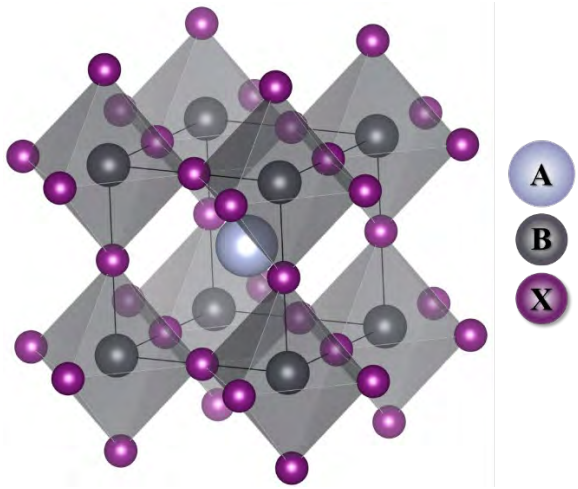

Figura 2.2.1: Esquema de la estructura cristalina general de la perovskita en fase cúbica con formula empírica ABX_3.

Las perovskitas con anión de O^{2-} (ABO_3), los cationes A y B usualmente son divalente (A^{2+}) y tetravalente (B^{4+}), respectivamente, y son denominadas perovskitas de óxidos. Las perovskitas de óxidos (ABO_3) son investigadas debido a sus propiedades eléctricas de ferroelectricidad o superconductividad [96]–[98]. Por otro lado, cuando las perovskitas contienen aniones haluro (X= Cl^-, Br^- o I^-), los cationes A y B son monovalente (A^{1+}) y divalente (B^{2+}), respectivamente, para cumplir con la neutralidad de carga. Las perovskitas de haluro reciben mucha atención debido a la aplicación en celdas solares [99]–[101]. Por lo general, las perovskitas que contiene haluros son basadas en plomo (Pb), es decir, que el catión B corresponde a un ion Pb^{2+}, y dependiendo del elemento que se utilice en la posición del catión A, las perovskitas pueden ser de carácter orgánicas (organometálicas) o totalmente inorgánicas. Algunos ejemplos de la perovskita organometálica es cuando el catión A es un grupo funcional orgánico como: metilamonio (MA, $(CH_3NH_3)^+$) [102], [103], etilamonio (EA, $(CH_3CH_2NH_3)^+$) [104], [105] o formamidinio (FA, $(NH_2CH{=}NH_2)^+$) [106], [107]. Por otro lado, la perovskita es totalmente inorgánica cuando el catión A tiene un elemento como el cesio (Cs) [108]–[110].

Como se mencionó con anterioridad, las perovskitas conformadas con elementos haluros resaltan en la aplicación en celdas solares por las ventajas de baja energía de unión de excitones, alto coeficiente de absorción de luz, y fabricación fácil de bajo costo [99], [100]. La celda solar de perovskita (*perovskite solar cells*, PSC) es conformada por un ensamble de

capas con funciones específicas. En la actualidad existen dos principales configuraciones de fabricación de PSC que consiste en una heterounión de estado sólido mesoporosa o planar [111]. Adicionalmente, dependiendo de la posición de la capa transportadora de electrones (*electron transport layer*, ETL) y la capa transportadora de huecos (*hole transport layer*, HTL), las PSC se puede clasificar en una arquitectura convencional (n-i-p) o en una arquitectura invertida (p-i-n). Cuando se tiene una arquitectura n-i-p, la ETL es depositada sobre un substrato conductor transparente (vidrio recubierto con una película de óxido de estaño dopado con fluor, FTO), donde la luz interacciona primero por esta capa, seguido de la capa de perovskita y finalmente la HTL. Mientras que en la arquitectura p-i-n se deposita la HTL sobre el sustrato conductor transparente, es decir, tiene las capas invertidas en comparación con una PSC con arquitectura n-i-p. En la **Figura 2.2.2** se puede observar una representación esquemática de las opciones que se tiene para fabricar una PSC.

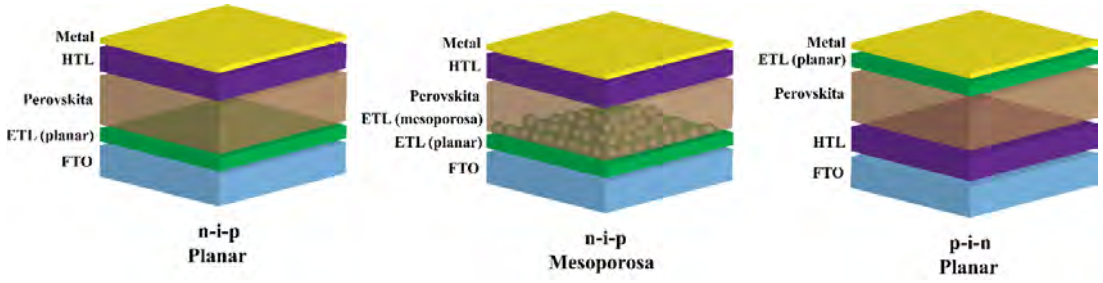

Figura 2.2.2: Esquema de la configuración de las capas que conforman una celda solar de perovskita.

Como se puede ver en la **Figura 2.2.3** se presenta un diagrama de bandas que representa el funcionamiento de una PSC, es importante aclarar que sin importar que arquitectura o configuración se utilice el principio de funcionamiento es el mismo. La capa de perovskita se encuentra entre un sustrato conductor transparente (FTO) y un cátodo con una función de trabajo muy baja (generalmente se emplea oro). Cuando la luz interacciona con la capa de la perovskita se produce un par electrón – hueco que si el contacto directo de la capa de perovskita y el electrodo existiera daría lugar a una grave recombinación no deseada y a una fuga de corriente ocasionando un rendimiento deficiente del dispositivo. Entonces para evitar el problema de la recombinación y la fuga de corriente se emplean las capas ETL y HTL, encargadas de separar el par electrón – hueco mediante un campo eléctrico permitiendo que el electrón sea extraído y transportado a la ETL y el hueco al HTL. Además,

las capas ETL y HTL permiten que el transporte de los portadores sea más eficiente y bloquean las recombinaciones no deseadas.

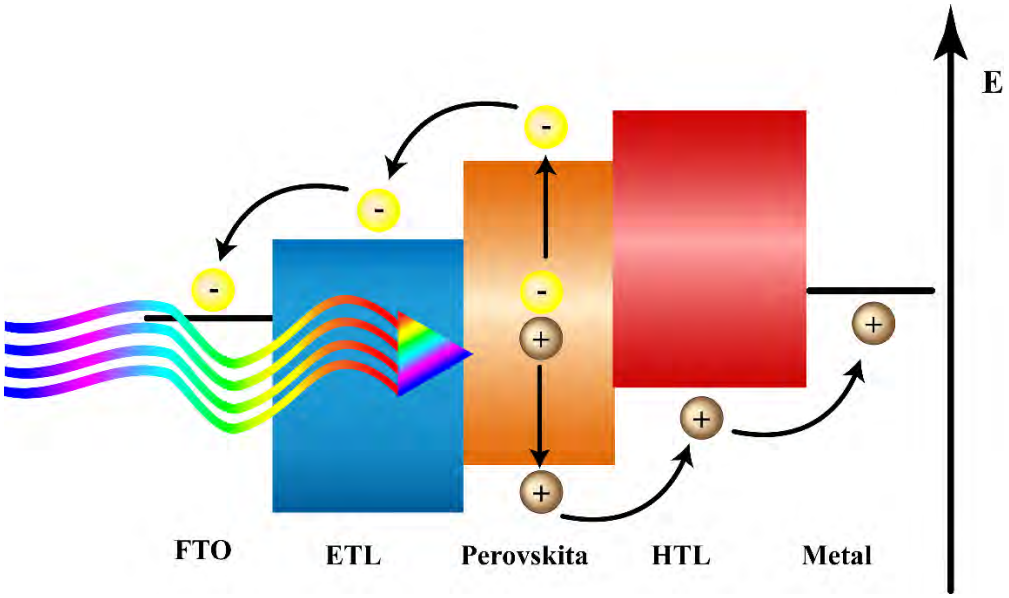

Figura 2.2.3: Diagrama de bandas de los materiales que conforman una celda solar de perovskita y principales procesos que ocurren cuando la capa de perovskita interacciona con la luz.

2.3 Transportador de huecos

Las PSCs comenzaron a aparecer en la comunidad científica en el 2006 con la utilización de la perovskita de $MAPbBr_3$ como sensibilizador liquido en una celda solar sensibilizada por tinte. El dispositivo ensamblado presentó una eficiencia de apenas 2.2 % [112]. Años más tarde el mismo grupo de trabajo reportó una mejora en la eficiencia del 3.8 % y 3.1 % usando dos perovskitas $MAPbI_3$ y $MAPbBr_3$, respectivamente. Ambas perovskitas seguían siendo sensibilizadoras empleando electrolitos líquidos en la celdas solares sensibilizadas por tinte [4]. Los dispositivos que se presentaron en ese trabajo eran muy inestables, en unos cuantos minutos presentaban una degradación que afecta directamente el rendimiento del dispositivo. La degradación del dispositivo era consecuencia de que la perovskita se disolvía en el electrolito líquido utilizado para ensamblar la celda solar sensibilizada por tinte. A pesar de las modificaciones de la celda solar sensibilizada por tinte que reportó Park *et al*. en el 2011, cambio de solvente del electrolito, modifico el depósito

de la perovskita y cambio la superficie del dióxido de titanio (TiO_2), seguían presentando el mismo problema de la inestabilidad del dispositivo [113].

El mayor avance se produjo cuando se remplazó el electrolito líquido con un material transportador de huecos en estado sólido, generalmente denominado capa transportadora de huecos (HTL). Grätzel y Park utilizaron el spiro-OMeTAD (spiro) como el material transportador de huecos en estado sólido de las PSCs fabricadas con la perovskita de $MAPbI_3$ depositada sobre una capa mesoporosa de TiO_2. El dispositivo presentó una mejora en la eficiencia reportando un 9.7 % y un tiempo estable sin degradarse de 500 h [114]. A partir de este punto comenzó la carrera por investigar la aplicación de diferentes materiales de perovskita, técnicas de depósito, arquitecturas diferentes y encontrar materiales alternos para las capas ETL y HTL. Sin embargo, se puede ver con claridad que la HTL tiene un rol importante para cualquier tipo de configuración o arquitectura de ensamble que se utilice en la PSC. La HTL tiene diferentes puntos que lo hacen un elemento critico en la fabricación de un PSC [115], [116]:

- Previene el contacto directo entre la perovskita y el contacto metálico que puede causar una degradación debido a lo corrosivo de los iones haluro o a migración del metal a la perovskita.
- Una extracción y recolección eficiente de los portadores (huecos) generados en la capa de la perovskita después de la absorción de luz.
- Actuar como una barrera energética para bloquear los electrones.

Entonces, para que un material sea exitoso para aplicarse como HTL en una PSC debe de tener una conductividad tipo-p donde la banda del orbital molecular ocupado más alto (*highest occupied molecular orbital*, HOMO) se empareje con el nivel de energía máximo de la banda de valencia (*valence band maximum*, VBM) de la perovskita para tener un transporte de portadores aceptable. Adicionalmente, las propiedades fisicoquímicas el material aplicado como HTL debe ser lo suficientemente estable para no reaccionar con el oxígeno, agua o con la capa de la perovskita y, finalmente, tener en consideración que el costo de fabricación debe ser bajo. En el caso de la arquitectura invertida (p-i-n), el material que sea usado como HTL debe ser totalmente transparente debido a que la luz tiene que pasar primero por esta capa para interaccionar con la perovskita.

Materiales orgánicos e inorgánicos pueden ser utilizados como HTL. Actualmente, el material más usando como HTL en una arquitectura n-i-p es el material orgánico spiro. Sin embargo, es un material orgánico que es sensible a la humedad del ambiente y puede ser fácilmente deteriorar la PSC. Además, el spiro puede reaccionar fácilmente con el ion I^-, el cuál puede migrar desde la perovskita hasta el contacto metálico. Por otro lado, el spiro necesita una oxidación adicional para alcanzar la conductividad ideal, entonces, se ha empleado dopantes de cobalto y litio para acelerar la oxidación y mejorar la movilidad de los portadores (huecos) [115], [116]. En conclusión, las prestaciones de la PSC se ven comprometidas, por estas desventajas, al utilizar el spiro como material en la HTL. Por otro lado, se encuentran los materiales inorgánicos que por su naturaleza son más estables y menos susceptibles a la humedad que su contraparte. Algunos materiales inorgánicos que se han investigado son el CuO, Cu_2O, NiO_x y CuSCN [115], [116]. En consecuencia, la comunidad científica tiene el interés en explorar materiales inorgánicos que solucionen estas desventajas. De hecho, en la actualidad se considera una investigación de vanguardia encontrar nuevos materiales que puedan ser aplicados como HTL en una PSC para aumentar la estabilidad y la eficiencia del dispositivo. En la **Figura 2.3.1**, se presenta un diagrama de bandas de diversos los materiales que son aplicados como HTL en las PSC y que se encuentran en investigación por la comunidad científica.

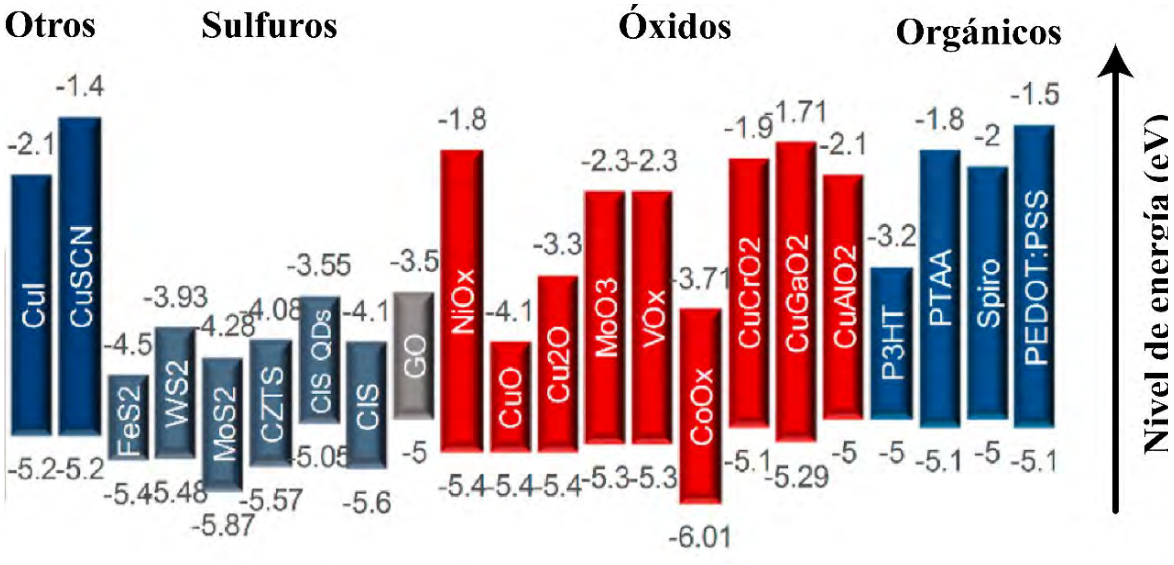

Figura 2.3.1: Diagrama de bandas de los materiales usados como capa transportadora de huecos en celdas solares de perovskita [115].

Capítulo 3 – Métodos de preparación y técnicas de caracterización

En este capítulo se presenta los detalles de la metodología que se utilizó para sintetizar las nanopartículas de $Cu_2ZnSn_{1-x}Ge_xS_4$ (CZTGS), el proceso utilizado para purificación de las nanopartículas de CZTGS, el depósito de las nanopartículas de CZTGS para fabricar películas, el ensamble de las celdas solares de perovskita y las técnicas de caracterizaciones que se emplearon para evaluar las nanopartículas, las películas y las celdas solares.

3.1 Síntesis de nanopartículas de $Cu_2ZnSn_{1-x}Ge_xS_4$

Las muestras de CZTGS estudiadas en este trabajo fueron sintetizadas por un método hidrotermal con diferentes valores nominales de germanio, x = Ge/(Ge+Sn) = 0.0, 0.15, 0.30, 0.40, 0.6 y 0.7. Los reactivos empleados en la síntesis hidrotermal son: acetato de zinc dihidratado ($Zn(CH_3COO)_2 \cdot 2H_2O$, J.T. Baker, 99%), acetato de cobre monohidratado ($Cu(CH_3COO)_2 \cdot H_2O$, Sigma-Aldrich, ≥98%), cloruro de estaño pentahidratado ($SnCl_4 \cdot 5H_2O$, Sigma-Aldrich, 98%), tetracloruro de germanio ($GeCl_4$, Sigma-Aldrich, 99.9999%), etilendiamina ($C_2H_8N_2$, Sigma-Aldrich, ≥98%), azufre en polvo sublimado (S, Fermont, 99.95%), acetona (C_3H_6O, J.T. Baker, ≥99.5%) y agua desionizada (sistema Millipore, $\rho > 10^{18}$ Ω·cm).

Las nanopartículas de CZTGS fueron sintetizadas por un proceso hidrotermal, que consistió en elaborar dos soluciones precursoras. En la primera solución (solución A), se disolvió el acetato de cobre (4 mmol), acetato de zinc (2 mmol), cloruro de estaño y el cloruro de germanio ($GeCl_4$ + $SnCl_4$ = 2.2 mmol) en 10 mL de agua desionizada bajo agitación magnética. Sin embargo, el $GeCl_4$ es altamente reactivo a exponerlo al agua o humedad del ambiente debido a una reacción química donde se forma polvo de óxido de germanio (GeO_2) y vapores de ácido clorhídrico (HCl). Entonces, no es posible utilizar directamente en la solución A. Para poder utilizar el reactivo de $GeCl_4$ se realizó una solución de $GeCl_4$ disuelto en acetona (1:20 v/v) dejando en agitación magnética durante 6 horas en una caja de guantes donde la atmosfera era de Ar. La mezcla de $GeCl_4$ + acetona forma especies organometálicas

estables con enlaces débiles entre Ge^{4+} y oxigeno de la acetona [117]. La solución $GeCl_4$ + acetona se puede utilizar como precursor de $GeCl_4$ en las condiciones normales del experimento (humedad, temperatura y solventes) fuera de la caja de guantes y permite disolverlo en agua junto con los otros reactivos. Por otro lado, la preparación de la segunda solución (solución B) consistió en disolver el azufre (12 mmol) en 10 mL de etilendiamina utilizando agitación magnética. El azufre se disuelve fácilmente a temperatura ambiente en la etilendiamina, presentando un color café oscuro cuando se disolvió por completo. Después de homogenizar las soluciones A y B se procedió a mezclar en un recipiente de teflón de 30 mL. En este paso, se busca que todos los iones metálicos formen un compuesto quelante con la etilendiamina, $[M(-NH_2)]^{n+}$ (donde M es el ion metálico). Posteriormente, las condiciones de temperatura y presión del proceso hidrotermal ocasionarán que la estabilidad de los complejos metálicos quelantes decrezca, dejando el ion metálico (M^{n+}) libre del quelato [118]. Durante el proceso hidrotermal ocurre el ataque nucleofílico de la etilendiamina para reducir al azufre elemental a ion ($S^0 \rightarrow S^{2-}$) y la oxidación del Cu^{2+} a Cu^+ [118]–[120]. Para lograr esa condición el recipiente de teflón con la solución homogénea ha sido introducido en una autoclave de acero inoxidable y calentado a 200 °C durante 24 h (rampa de calentamiento de 3 °C/min) en un horno gravitacional (Lindberg Blue). Con la temperatura y presión alcanzada, una gran cantidad de quelatos se disocia, formando iones metálicos que reaccionan con los iones de azufre disponibles. La reacción de nucleación ocurre de manera rápida, permitiendo que los nanoconglomerados (*nanoclusters*) se formen rápidamente y recristalice en nanopartículas de CZTGS de mayor tamaño [121]. Finalmente, el producto sólido obtenido del proceso hidrotermal se separó y lavó varias veces con acetona empleando centrifugación (7000 rpm, 10 min) y se secó a 60 °C durante 8 h. El procedimiento completo se presenta de manera esquemática en la **Figura 3.1.1**.

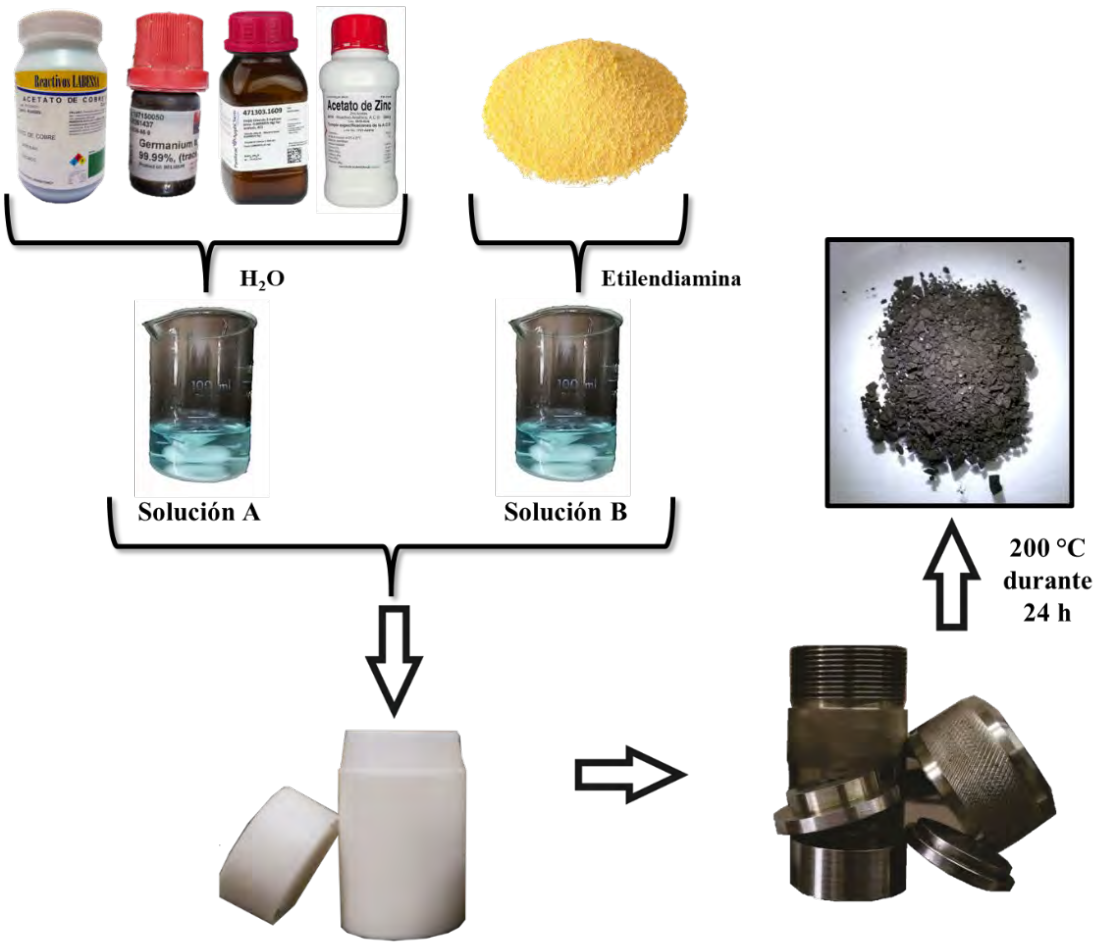

Figura 3.1.1: Representación esquemática del proceso de síntesis utilizado para la reacción hidrotermal de las nanopartículas de $Cu_2ZnSn_{1-x}Ge_xS_4$.

3.2 Lavado químico de las nanopartículas de $Cu_2ZnSn_{1-x}Ge_xS_4$

Como se explicará en la sección 4.1, las muestras de nanopartículas de CZTGS presentaron formaciones de fases adicionales a la kesterita, especialmente para las muestras con altos contenidos de germanio. Para remover las fases no deseadas de las muestras se implementó un procedimiento de lavado químico, que consistía en tomar una fracción de la muestra (~700 mg) y mezclarlo con 90 mL de HCl diluido (10% v/v) por etapas. En un frasco de capacidad 35 mL con tapa sellable se colocó la muestra con 30 mL del HCl diluido para dejar en agitación magnética durante 45 min a una temperatura de 80 °C. Los sólidos eran recuperados mediante centrifugación y el procedimiento se repitió dos veces. Para neutralizar el ácido, al final los sólidos recuperados se agitaron manualmente con 30 mL de solución

acuosa de hidróxido de potasio (KOH) de una concentración 1 M. Finalmente, los sólidos lavados con ácido y neutralizados fueron enjuagados con agua desionizada varias veces y secados a 60 °C para ser almacenados en frascos con tapa hermética y en una atmosfera de nitrógeno (N_2). El procedimiento se repitió para cada muestra que se presenta en esta tesis. El procedimiento completo descrito en esta sección se presenta de manera esquemática en la **Figura 3.2.1**.

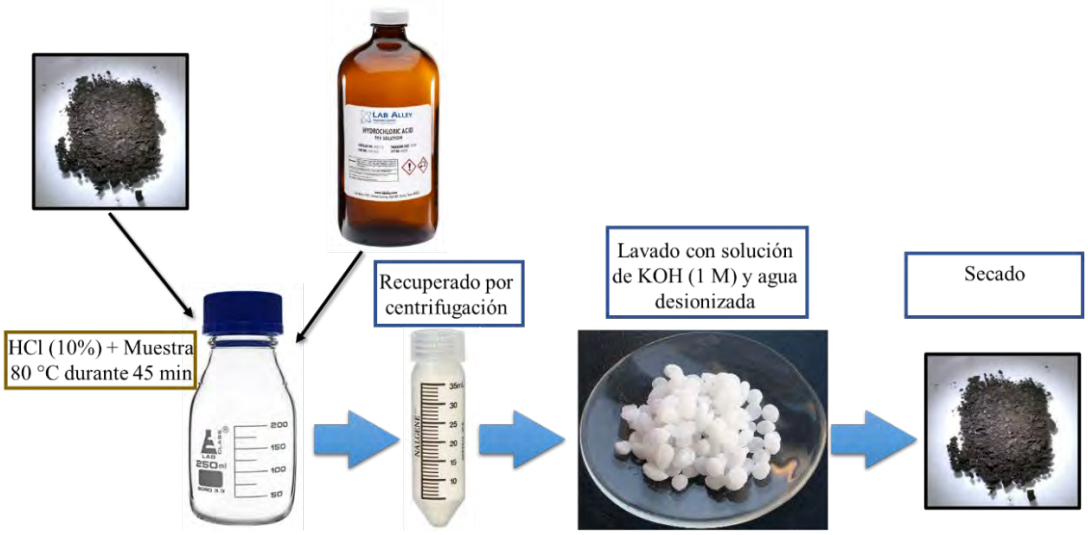

Figura 3.2.1: Representación esquemática del proceso de lavado químico de las muestras de $Cu_2ZnSn_{1-x}Ge_xS_4$ (CZTGS) sintetizadas por el método hidrotermal usando HCl diluido.

3.3 Fabricación de las películas de $Cu_2ZnSn_{1-x}Ge_xS_4$

En la fabricación de las películas de CZTGS se usaron las nanopartículas de CZTGS sin lavado químico y con lavado químico. En la preparación de los tintes de las nanopartículas se utilizó 0.9 mL de hexanotiol por cada 150 mg de muestra. Las mezclas fueron agitadas magnéticamente por 16 h a temperatura del ambiente. Posteriormente, el tinte de las nanopartículas de CZTGS fueron depositadas sobre sustratos de vidrios Corning previamente lavados mediante recubrimiento por centrifugación (*spin-coating*). Alrededor de 25 µL de los tintes de nanopartículas ha sido utilizada para recubrir el sustrato de vidrio Corning (2.5x2.5 cm) usando 2000 rpm durante 30 s. Después del depósito, las películas se calentaban a 100 °C durante 10 min para evaporar el solvente. En la **Figura 3.3.1** se presenta un esquema del proceso de fabricación de las películas de CZTGS.

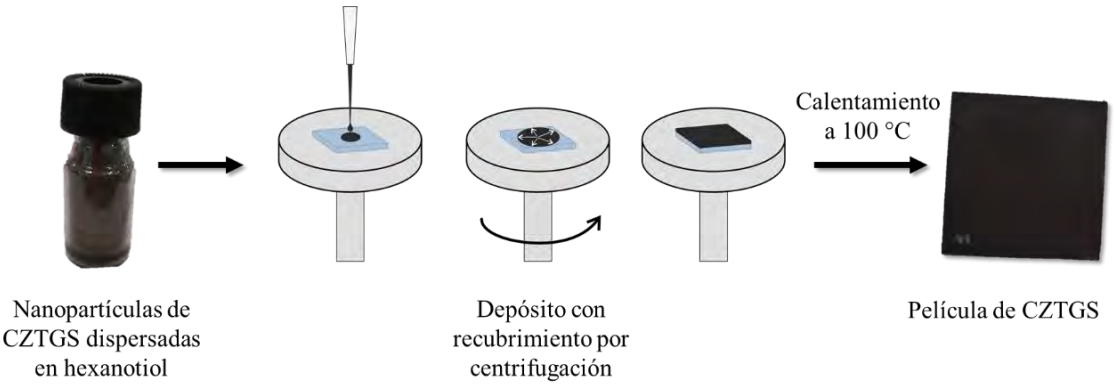

Figura 3.3.1: Representación esquemática del proceso de fabricación de las películas de $Cu_2ZnSn_{1-x}Ge_xS_4$ (CZTGS) por el método de *spin-coating*.

3.4 Ensamble de las celdas de perovskita

3.4.1 Preparación del sustrato

Los sustratos empleados para fabricar las celdas solares de perovskita (PSCs) eran vidrio conductor FTO (Greatcell, TEC15 2.2 mm) con medidas de 2x2 cm. Comenzando con el ensamble de las celdas de perovskita, el vidrio conductor se cubría con una cinta para delimitar la zona que se realizaría un ataque químico para retirar el FTO. El ataque químico consistía en cubrir el FTO (la zona sin recubrimiento) con polvo de zinc (Zn) y usar unas gotas de HCl diluido (1:6 v/v). La zona descubierta con el polvo de Zn y el HCl reacciona removiendo el FTO. El motivo de retirar el FTO en una zona es evitar el corto circuito en el dispositivo ensamblado. En la **Figura 3.4.1(a)** se presenta una fotografía donde se está realizando el proceso de ataque químico de la zona expuesta del FTO recubierta con polvo de Zn. Posteriormente, el vidrio conductor se enjuaga para retirar los residuos del polvo de Zn y se retira el recubrimiento (la cinta Scotch transparente) para proseguir con la metodología del lavado de sustratos de la siguiente manera:

- Tallar vigorosamente la superficie del vidrio FTO sin rayar o dañar usando una solución de jabón Hellmanex diluido en agua desionizada (2:98 v/v).
- Sumergir el vidrio conductor en la solución de Hellmanex para realizar baño ultrasónico durante 15 min. En la **Figura 3.4.1(b)** se muestra una fotografía del soporte que se utilizó para acomodar los sustratos durante el proceso de baño ultrasónico.

- Rociar con grandes cantidades de agua desionizada para retirar los residuos de jabón y posteriormente realizar baño ultrasónico con agua desionizada durante 15 min.
- Tratamiento baño ultrasónico inmersos en isopropanol durante 15 min.
- Tratamiento baño ultrasónico inmersos en acetona durante 15 min.
- Rociar con grandes cantidades de acetona y después isopropanol a los sustratos de vidrio conductor
- Secar rápidamente el isopropanol con un flujo de aire fuerte para evitar marcas de secado.

Adicional al lavado de los sustratos de vidrio conductor se hizo tratamiento con plasma de oxígeno durante 15 min e inmediatamente se comenzó con el depósito de la capa transportadora de electrones. En la **Figura 3.4.1(c)** se muestra una imagen fotográfica del tratamiento de plasma. Es importante mencionar que el tratamiento de plasma fue utilizado para cada etapa de la capa transportadora de electrones y antes de depositar la perovskita. En todos los casos, los depósitos fueron realizados inmediatamente al terminar el tratamiento de plasma.

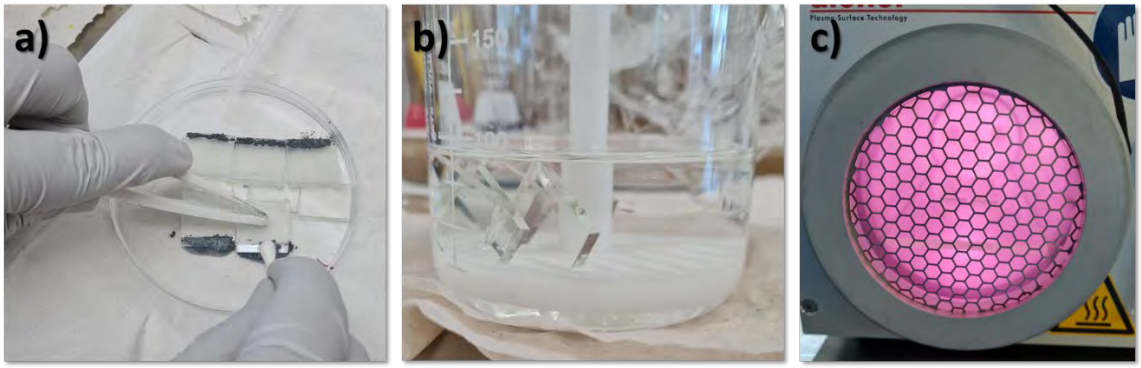

Figura 3.4.1: Imágenes fotográficas del proceso del ataque químico al FTO, lavado y preparación de los sustratos para el ensamble de la celda solar. (a) Ataque químico para remover el FTO usando HCl diluido y polvo de zinc en la zona descubierta del sustrato. (b) Limpieza de los sustratos usando el baño ultrasónico. (c) Los sustratos en limpieza por plasma de oxígeno.

3.4.2 Capa transportadora de electrones (*electron transport layer*, ETL)

La capa transportadora de electrones de una celda solar de perovskita (PSC) es conformada por una capa compacta y una capa mesoporosa de dióxido de titanio (TiO_2). El depósito de la capa compacta de TiO_2 (c-TiO_2) se realizó por el método de rocío pirolítico (*spray pyrolysis*), en el cual se emplea una solución de Titanio(IV)-bis(acetilacetonato) de

diisopropóxido (TiAc, Sigma-Aldrich 75% en isopropanol) disuelto en isopropanol (C_3H_8O, Karal) con una relación 1:24 v/v. Los sustratos de vidrio conductor limpios se colocaron en una plancha de calentamiento y se recubrió una sección del FTO (delimitar la zona del contraelectrodo de la celda). Colocados los sustratos en la plancha, se procedió a elevar la temperatura del sustrato a 350 °C y se esperó 15 min para estabilizar el sistema. Para el rociado, se utilizó un sistema ensamblado en el IFUAP para controlar el desplazamiento del aerógrafo a una distancia de 20 cm con respecto a la plancha. La presión del aire se fijó a 3 bar y en total se utilizó 12 mL de solución para 10 sustratos. El tiempo de un ciclo del recorrido era alrededor de 30 s, es decir, que el aerógrafo tardaba 30 s en recorrer dos veces toda la plancha con los 10 sustratos. Entre ciclo y ciclo se esperó 30 s de reposo. Este procedimiento se repitió hasta acabar 12 mL de solución (10 ciclos; un tiempo total de 10 min). En la **Figura 3.4.2(a)** se muestra una imagen fotográfica del sistema del rocío pirolítico utilizado para el depósito de c-TiO_2 sobre los sustratos de vidrio conductor. Al terminar el proceso de depósito, los sustratos fueron recocidos a 350 °C durante 15 min sobre la plancha. Posteriormente, se apagó la plancha para enfriar los sustratos a la temperatura del ambiente.

El siguiente paso para la fabricación de ETL era depositar la capa mesoporosa de TiO_2 (m-TiO_2) sobre la capa c-TiO_2. Para depositar la capa m-TiO_2 se usó un tinte de nanopartículas de TiO_2, que consistía en dispersar la pasta de nanopartículas (Greatcell, 30 NR-D) en etanol (150 mg/mL). La mezcla fue agitada magnéticamente durante 12 h antes de utilizar en deposición. El método que se empleó para el depósito de la capa m-TiO_2 sobre c-TiO_2 fue el recubrimiento por centrifugación (*spin-coating*) a 4000 rpm durante 30 s, usando una aceleración de 2000 rpm/s. La cantidad de tinte que se usó para fabricar cada capa era de 70 µL. En la **Figura 3.4.2(b)** se muestra una imagen fotográfica del equipo utilizado para depositar la capa m-TiO_2. De la misma forma que el depósito de c-TiO_2, se delimitó la zona del contraelectrodo de la celda de perovskita usando cinta térmica tipo Kapton. Al terminar el depósito, los sustratos fueron colocados sobre una plancha calentada a 100 °C. Después de 5 min en esta temperatura, la cinta térmica ha sido retirada de los sustratos. Los sustratos sin cinta térmica fueron colocados en un horno y calentados a 500 °C por 30 min (con la rampa de calentamiento que se describe en la **Figura 3.4.2(c)**. Con este procedimiento se conseguía una ETL uniforme, de color morado y casi transparente como se puede ver en la **Figura 3.4.2(d)**.

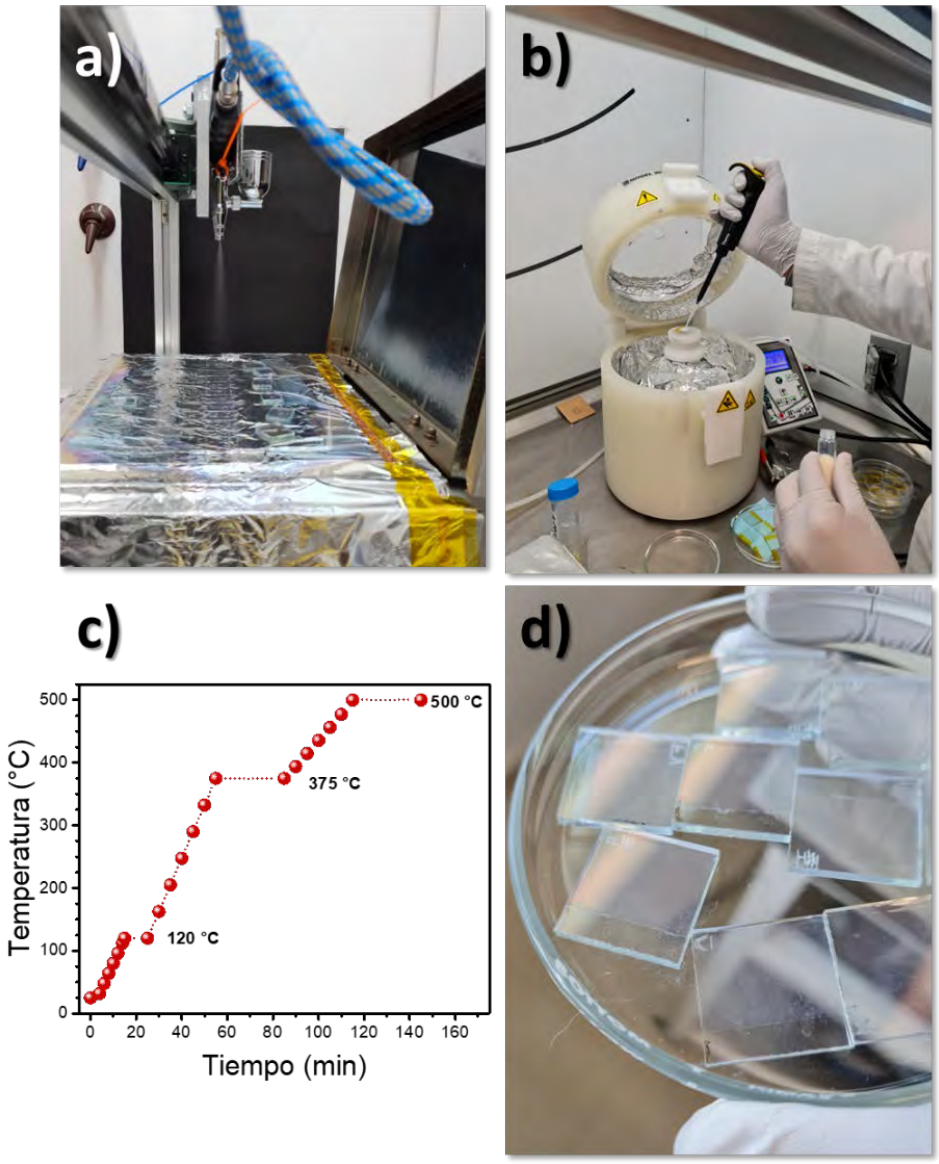

Figura 3.4.2: Algunas imágenes fotográficas de los pasos utilizados en el proceso de fabricación de ETL: (a) Sistema de rocío pirolítico automatizado utilizado para la fabricación de capa compacta de TiO_2, (b) depósito por recubrimiento por centrifugación (*spin-coating*) para fabricación de la capa mesoporosa de TiO_2, (c) rampa de calentamiento utilizada para el tratamiento térmico de los sustratos con la ETL y (d) sustratos con la ETL después del tratamiento térmico.

3.4.3 Capa de perovskita

En esta sección se describe el procedimiento que se usó para el depósito de la perovskita $(FAPbI_3)_{0.83}(MAPbBr_3)_{0.17}$, conocida como FAMA. Todo el procedimiento se realizó en una caja de guantes y siguiendo el procedimiento reportado por Saliba *et al*. [5]. Se preparó una solución FAMA disolviendo $FAPbI_3$ y $MAPbBr_3$ en una relación 5:1 (v/v) usando un solvente mixto anhidro de DMF:DMSO (4:1 v/v). Aproximadamente 70 µL de la solución de la FAMA ha sido utilizado para depositar una capa de perovskita por el método recubrimiento por centrifugación (*spin-coating*). Los depósitos fueron realizados a 3500 rpm durante 30 s. En el depósito se empleó 200 µL de clorobenceno como antisolvente para mejorar la cristalinidad de la capa de perovskita. El antisolvente se aplicó durante el giro del sustrato en el equipo a 10 s antes de que terminara. Posteriormente, las películas se colocaban en una parrilla calentada a 100 °C durante 45 min. Durante este proceso, el color rojizo transparente cambió a un color rojo oscuro (**Figura 3.4.3(b)**).

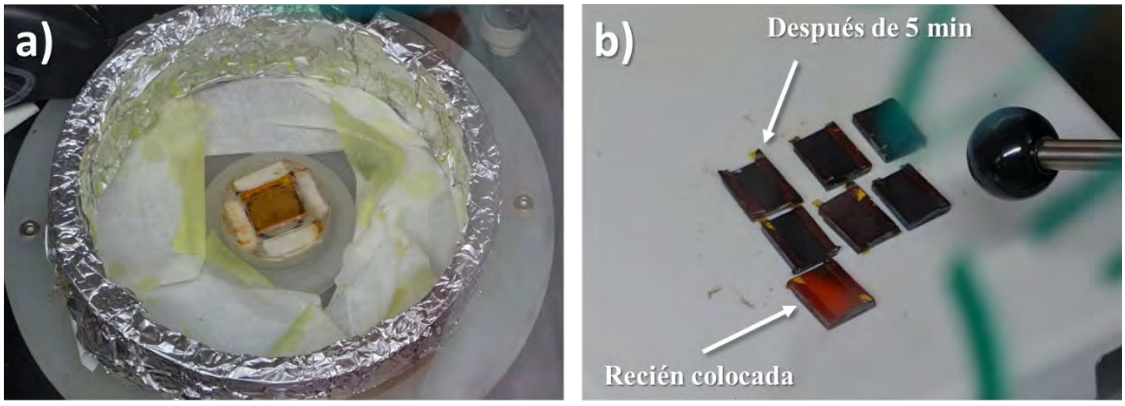

Figura 3.4.3: Imágenes fotográficas del sustrato soportado sobre el porta muestras del *spin*-coating con la capa de FAMA depositada (a) y los sustratos en la parrilla caliente para cristalizar la FAMA (b).

3.4.4 Capa transportadora de huecos (*hole transport layer*, HTL)

El último paso para el ensamble de las celdas de perovskita consiste en depositar el HTL sobre la capa de perovskita. En esta sección se describe el procedimiento que se usó para obtener la celda convencional (celda de perovskita con spiro-OMeTAD) y la celda con CZTGS como transportador de huecos. Para fabricar la película de spiro-OMeTAD se

prepararon dos soluciones: Una solución de sal de litio de bis-(trifluorometano)sulfonimida (LiTFSI; Sigma-Aldrich) y otra solución de tris(2-(1H-pirazol-1-il)-4-terc-butilpiridina)cobalto(III) tri[bis-trifluorometano)sulfonimida] (Co(III); FK209; Sigma-Aldrich), ambos disueltos en acetronitilo con la concentración 1.8 M y 0.25 M, respectivamente. Mientras que la solución de spiro se preparó con spiro-OMeTAD (spiro; Sigma-Aldrich) disuelto en clorobenceno (0.07 M) con 65 µL de 4-terc-butilpiridina (tBP; Sigma-Aldrich) y se agregó 38 µL y 65 µL de las soluciones de Li y Co previamente preparadas. De igual manera que la capa de perovskita, se implementó el recubrimiento por centrifugación (*spin-coating*) en la caja de guantes con las condiciones de 4000 rpm durante 20 s y se utilizó 70 µL de solución de spiro. El depósito de la solución spiro-OMeTAD se realizó de manera dinámica; es decir, después de 7 s que empezó a rotar el sustrato. Por otro lado, para la capa HTL usando CZTGS, se emplearon las nanopartículas de CZTGS con lavado químico dispersadas en tolueno (25 mg/mL). El depósito sobre la perovskita fue realizado en las mismas condiciones que se utilizó para la capa de spiro-OMeTAD. En la **Figura 3.4.4** se muestra una comparación de las celdas de perovskita (sin contactos de oro) usando spiro y CZTGS como transportador de huecos.

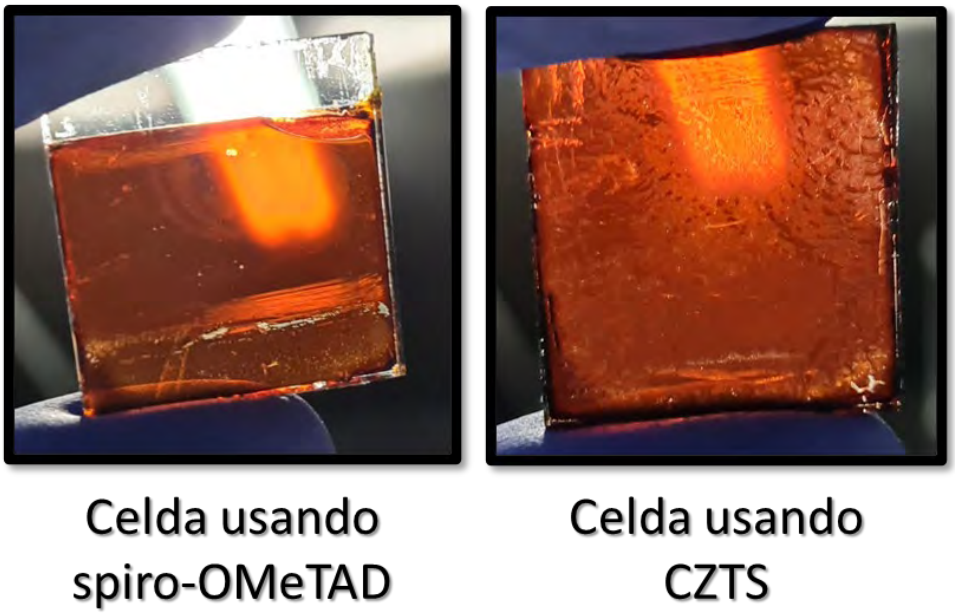

Figura 3.4.4: Imágenes fotográficas comparativas de las celdas (sin contactos de oro) ETL / perovskita FAMA / HTL fabricadas usando spiro-OMeTAD y CZTS como HTL.

3.4.5 Contactos de oro

Después de depositar las capas HTL, se procedió para fabricar los contactos Óhmicos sobre ellas. Para eso se depositaron una capa de Au, aproximadamente de 70 nm espesor sobre la capa HTL por medio de evaporación térmica. Se utilizó una máscara de acero inoxidable grabado químicamente para obtener los contactos en forma de rejilla (ver **Figura 3.4.5**), con longitud de 1.5 cm y 0.3 cm de ancho, para tener un área activa de aproximadamente 0.5 cm^2 de cada contacto. Para todas las mediciones se usó una máscara de un área definida de 0.03 cm^2. Esta máscara se usó para delimitar el área de medición y evitar que se sobreestime el valor de la eficiencia por la luz reflejada de los bordes de los sustratos [122].

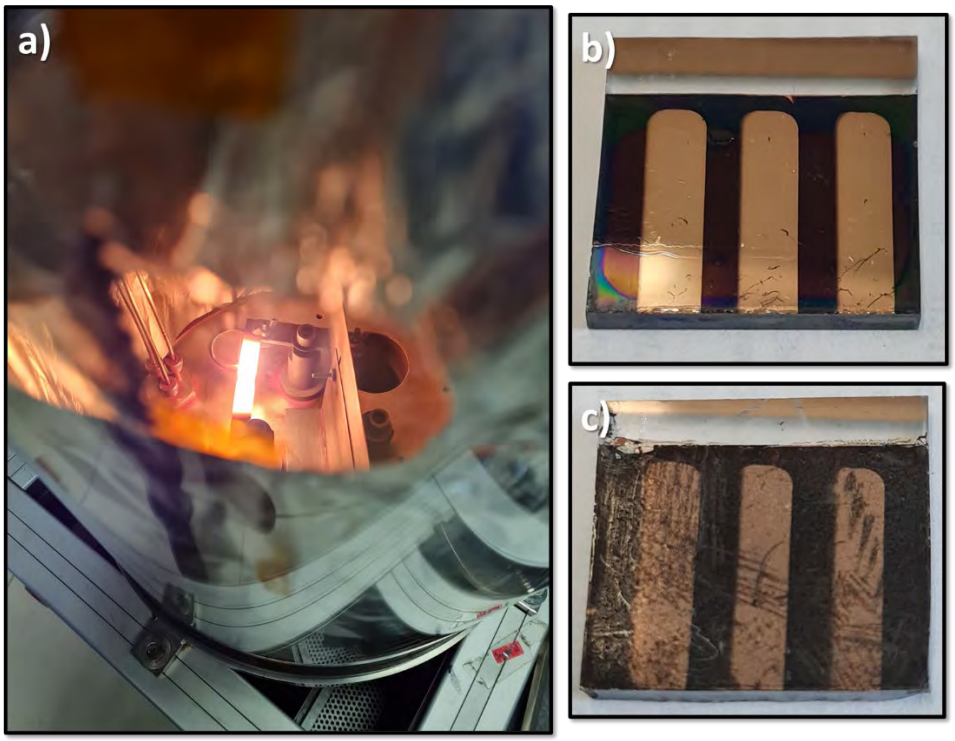

Figura 3.4.5: Imágenes fotográficas de cámara de evaporación del oro (a) utilizada para fabricar los contactos Óhmicos sobre las capas HTL de las celdas solares de perovskita fabricadas usando spiro-OMeTAD (b) y CZTGS (c) como transportador de huecos.

3.5 Técnicas de caracterización

En esta sección se presentan brevemente las técnicas de caracterizaciones utilizadas para analizar las nanoestructuras de CZTGS y las celdas solares de perovskita fabricadas en este trabajo.

3.5.1 Microscopía electrónica de barrido (SEM; *scanning electron microscopy*)

El microscopio electrónico de barrido o transmisión es indispensable para caracterizar los materiales de escala nanométrica. El principio de operación de un microscopio electrónico de barrido es detectar las interacciones de la muestra cuando se incide un haz de electrones enfocado sobre su superficie. La producción del haz de electrones tiene su origen en el efecto termoiónico de un filamento de tungsteno o de hexaboruro de lantano. Posteriormente los electrones son arrancados de la superficie del filamento y acelerados con una diferencia de potencial (~kV). Este proceso se utiliza en los microscopios electrónicos de barrido modernos y es denominado desprendimiento de electrones por efecto de campo (*field – emission*). El haz de electrones se enfoca y se realiza un barrido sobre la muestra utilizando una serie de lentes electromagnéticos. Los componentes comunes de un microscopio electrónico de barrido convencional se presentan en la **Figura 3.5.1**.

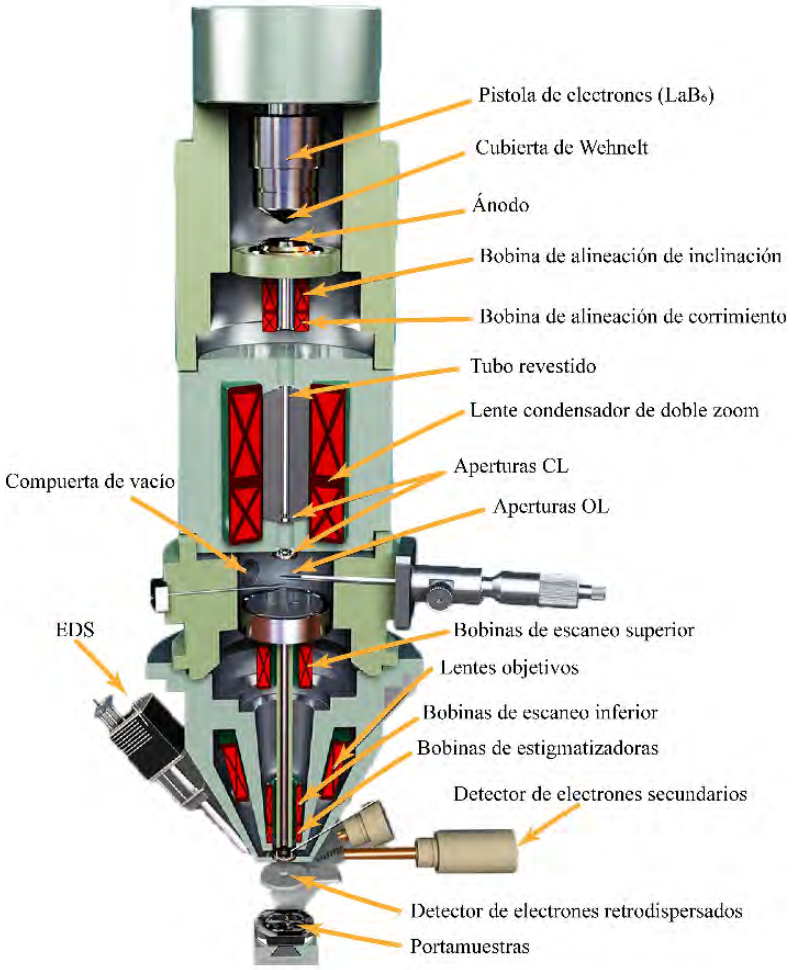

Figura 3.5.1: Representación esquemática de sección transversal de un microscopio electrónico de barrido señalando los componentes típicos [123].

La interacción del haz de electrones con la muestra produce múltiples procesos físicos asociados a la dispersión de los electrones de forma elástica e inelástica, o bien a su absorción por el mismo material. De manera general, los electrones son dispersados al colisionar con un núcleo de un átomo ocurriendo dos efectos. Primero, la dispersión elástica a ángulos pequeños (con respecto al haz incidente) produciendo los electrones denominados retrodispersados. El segundo efecto es cuando la dispersión es inelástica, produciendo electrones de baja energía que son denominados electrones secundarios. Las señales producidas son recolectadas por un centellador, encargado de transformar la señal en una corriente eléctrica; que posteriormente, produce una imagen computarizada en tiempo real. El microscopio electrónico de barrido podrá detectar todas las señales que genere la muestra sólida siempre y cuando se tenga el detector indicado (**Figura 3.5.2**).

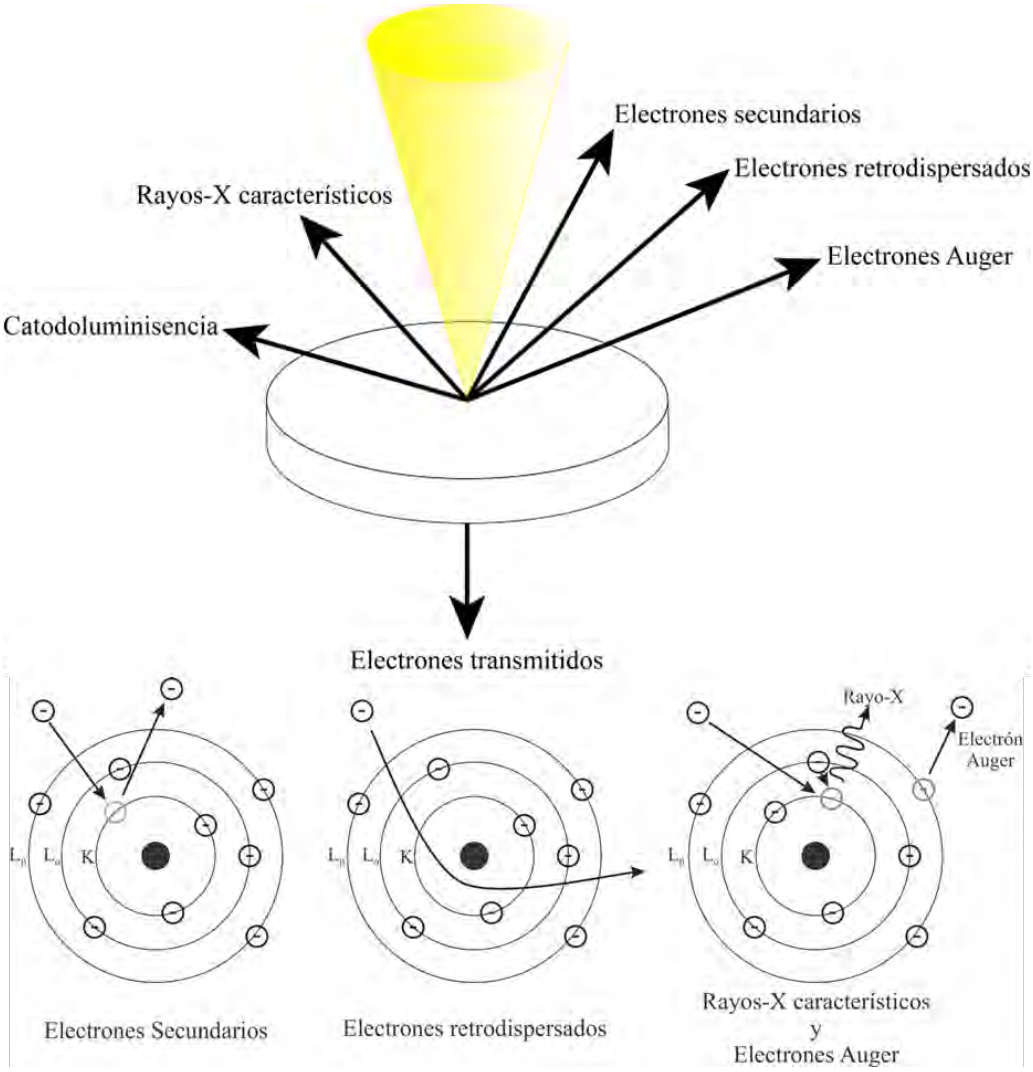

Figura 3.5.2: Señales producidas por la interacción de un haz de electrones con un material sólido en microscopio electrónico de barrido. En la parte inferior se muestra una representación esquemática del origen de la emisión de las algunas señales.

El análisis morfológico de las nanoestructuras de CZTGS y las celdas solares de perovskita fabricadas en este trabajo se realizó en un microscopio electrónico de barrido JEOL JSM-7800F instalado en el laboratorio de análisis superficial del Instituto de Física "Ing. Luis Rivera Terrazas". Para el análisis, se prepararon las muestras dispersando una gota de solución coloidal etanólica de cada muestra de las nanoestructuras de CZTGS sobre sustratos de silicio monocristalino. Por otro lado, las muestras de celdas solares de perovskita se prepararon cortando para analizar la sección transversal de cada celda.

3.5.2 Espectroscopia de energía dispersa de rayos-X (EDS; *energy dispersive spectroscopy*)

Una técnica de microanálisis químico que se emplea en conjunto con el SEM es la espectroscopia de energía dispersa de rayos-X (EDS). En esta técnica, se utilizan los rayos-X característicos emitidos por la muestra sólida durante la incidencia del haz de electrones. Los rayos-X característicos se detectan y cuantifican para conocer la concentración (porcentaje en peso o porcentaje atómico) de cada elemento de la muestra sólida que se analiza en el microscopio electrónico de barrido. Como el detector de rayos-X característicos se encuentra acoplado en el microscopio electrónico de barrido, se puede tener un análisis de morfología y composición elemental en el mismo equipo.

Para explicar el origen del proceso físico donde se generan los rayos-X característicos se acude al modelo atómico de Bohr, el cual es un poco inexacto, pero de gran utilidad para entender el proceso físico de la generación de los rayos-X característicos. En el modelo atómico de Bohr, los electrones se localizan en orbitas definidas, con cantidad conocida y girando en torno al núcleo de carga positiva. En este modelo se designan capas de acuerdo con el orbital que corresponden: La capa K corresponde al orbital más cercano al núcleo, y tiene solo un orbital *s*; por otro lado, la capa L corresponde a los orbitales s y *p*, y así sucesivamente. Los electrones se encuentran ligados a su respectiva capa con una energía específica; esa energía es nombrada como energía de enlace. El haz de electrones de un SEM es capaz de ceder la energía necesaria, es decir, energía mayor a la energía de enlace, para impulsar los electrones de las capas atómicas hacia el vacío, dejando al átomo en un estado excitado. Dado que el estado excitado del átomo no es estable, los electrones de las capas superiores ocuparán el espacio vacío de la capa anterior, y consecuentemente emiten una cantidad de energía en la frecuencia de los rayos-X. La energía emitida por los electrones que ocuparon el espacio vacío emite un fotón característico, que como es en la frecuencia de los rayos-X se nombran rayos-X característicos (ver **Figura 3.5.2**). La separación energética entre capas u orbitales de un átomo es única para cada tipo de elemento, por lo que la energía del fotón emitido permite identificar el elemento. Los análisis de composición de las nanoestructuras de CZTGS sintetizadas en este trabajo se efectuaron en un sistema Oxford

X-Max acoplado al microscopio JSM-7800F. En la **Figura 3.5.1** se muestra un sistema EDS acoplado al SEM.

3.5.3 Microscopía electrónica de transmisión (TEM, *Transmission electron microscopy*)

La microscopía electrónica de transmisión (TEM) junto con transmisión de alta resolución (HRTEM) son técnicas de caracterización indispensables para analizar la calidad, forma, tamaño y cristalinidad de las nanoestructuras. La TEM es un equipo que aprovecha los procesos físicos que se producen cuando un haz de electrones suficientemente acelerados ($\geq$ 50 kV) colisiona con una muestra delgada (convenientemente preparada). Cuando los electrones colisionan con la muestra, en función de su grosor y del tipo de átomos que la conforman, parte de los electrones son dispersados selectivamente, es decir, una parte de todos los electrones que colisionan atraviesan directamente la muestra y otros son desviados. En el caso que la muestra sea un sólido cristalino, los electrones serán difractados por los planos atómicos dentro del material al cumplir la condición de la ley de Bragg, como ocurren en el fenómeno de difracción de rayos-X, pero en este caso un patrón de difracción de electrones transmitidos se forma cuando los electrones pasan a través de una muestra delgada. Todos los electrones dispersados son conducidos y modulados por lentes y campos (eléctricos y magnéticos) para formar una imagen final que puede tener miles de aumentos con alta resolución sobre un detector CCD (*charge coupled device*). La imagen contiene distintas intensidades de gris que corresponden al grado de dispersión de los electrones incidentes [124], [125]. En la **Figura 3.5.3** se demuestra esquemáticamente la sección transversal de un microscopio electrónico de transmisión y algunos de sus principales componentes.

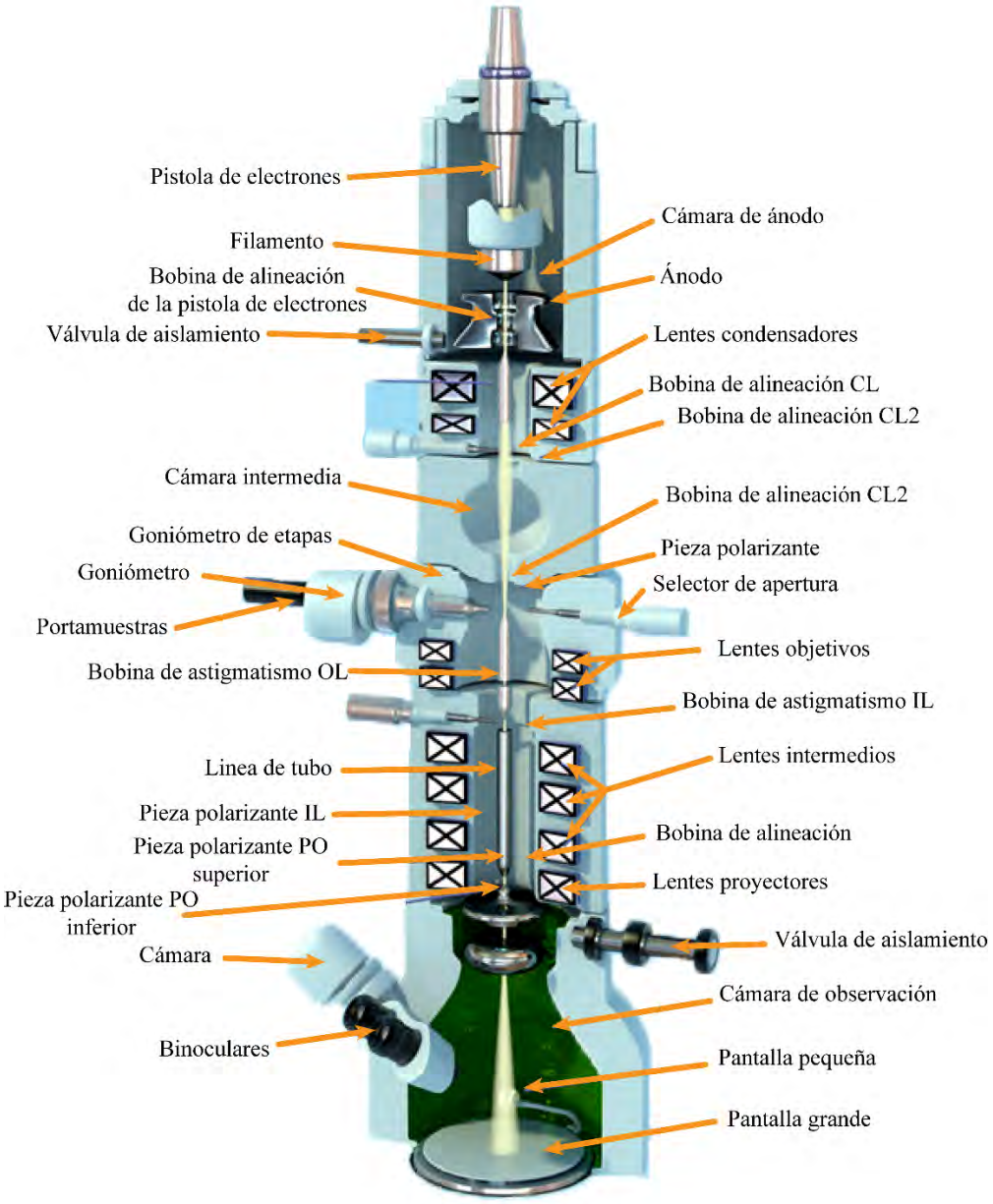

Figura 3.5.3: Representación esquemática de la sección transversal de un microscopio electrónico de transmisión señalando los componentes típicos [123].

En la visualización de las imágenes TEM, zonas oscuras representan las áreas de la muestra donde pocos electrones pudieron ser transmitidos a través de ellas. Mientras que las zonas brillantes representan las áreas donde se permitió la transmisión de los electrones a través de la muestra. Por la cualidad de los electrones acelerados, las imágenes TEM pueden visualizar los planos atómicos de una sola nanoestructura permitiendo no solo analizar la cristalinidad de la nanoestructura sino los defectos en ellos, tamaño y forma de la

nanoestructura. En este trabajo las nanoestructuras de CZTGS se analizaron en un TEM marca JEOL JEM-2100F operando a 200 kV. Para el análisis, se prepararon las muestras dispersando una gota de solución coloidal etanólica de cada muestra de las nanoestructuras de CZTGS en rejillas de cobre cubierta de carbón.

3.5.4 Espectroscopía Raman (*Raman spectroscopy*)

Una de las técnicas no-destructivas que aportan información importante sobre la cristalinidad, fase cristalográfica y composición de un material es la espectroscopía Raman. El efecto Raman se descubrió experimentalmente por el físico Chandrasekhara Venkata Raman, ganador del premio Nobel de física en 1930 [126]. El origen del efecto Raman proviene de la interacción de un haz de luz monocromática que incide sobre un material cristalino. En la interacción de la luz y el material ocurren dos tipos de procesos físicos. El primero es cuando la frecuencia del haz incidente (υ_i) y la dispersada tienen el mismo valor después de interactuar con el material cristalino; esto es una dispersión elástica y recibe el nombre de dispersión Rayleigh. Por otro lado, cuando una pequeña parte del haz incidente es dispersado en forma inelástica, puede ocurrir que la frecuencia inicial (υ_i) reciba la participación vibracional colectiva (fonones) de la red cristalina (υ_f) causando un cambio en la frecuencia del haz incidente. Es importante mencionar que la frecuencia vibracional colectiva de la red cristalina (υ_f) es característica de cada compuesto, porque existe una relación directa con los enlaces y las masas de los iones, y su distribución espacial en la estructura cristalina. La dispersión inelástica puede estar involucrado dos procesos: Cuando la frecuencia del haz incidente (υ_i) disminuye por la dispersión, es decir, pierde energía en la interacción inelástica ($\upsilon_i - \upsilon_f$), recibe el nombre de Stokes. El caso contrario, sería cuando la dispersión del haz tiene una frecuencia mayor ($\upsilon_i + \upsilon_f$), es decir, cuando la vibración colectiva de la red aporta energía a la interacción, este proceso se denomina anti-Stokes. En la **Figura 3.5.4** se presenta un espectro representativo Raman de una muestra cristalina para visualizar la diferencia entre las dispersiones elásticas e inelásticas. Es importante mencionar que la dispersión inelástica lleva la información del material cristalino y es nombrada dispersión Raman y por lo general se monitorea y analiza la señal Stokes por tener mayor intensidad que la señal anti-Stokes.

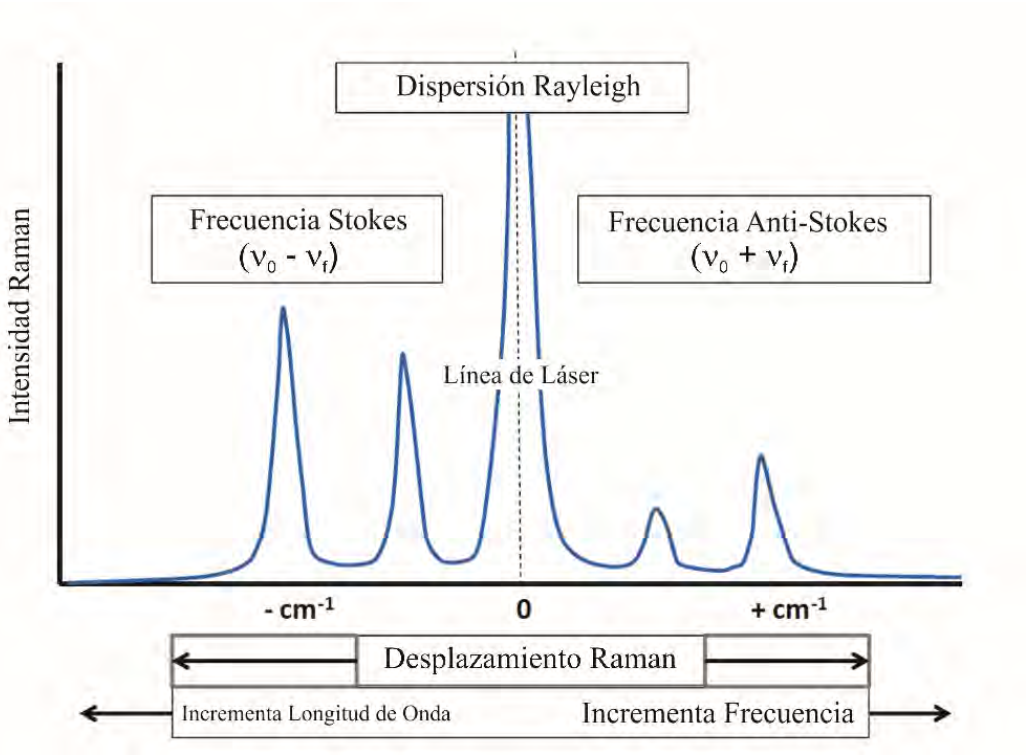

Figura 3.5.4: Espectro Raman típico de una muestra cristalina con señal anti-Stokes, Rayleigh y Stokes [127], [128].

Las nanoestructuras de CZTGS sintetizadas en este trabajo fueron caracterizadas a temperatura ambiente empleando un espectrofotómetro Raman Horiba Lab RAM HR, que cuenta con un láser He-Ne (633 nm) como fuente de excitación y un detecto CCD (*charge coupled device*) enfriada termoeléctricamente. El sistema se encuentra instalado en el laboratorio central del Instituto de Física "Ing. Luis Rivera Terrazas". Para analizar las muestras en forma de polvos fueron colocadas sobre sustratos de vidrio Corning.

3.5.5 Difracción de rayos-X (XRD; *X-ray difraction*)

La técnica de difracción de rayos-X es una técnica no-destructiva que se utiliza para el estudio de la microestructura de los materiales. El fenómeno físico que ocurre en la técnica es la difracción de ondas electromagnéticas cuando interactúan con la materia. La longitud de onda del haz incidente (rayos-X) es comparable con el espacio interatómico del material con el que interactúa, entonces el fenómeno de difracción surge naturalmente en los cristales. En un sólido cristalino, los planos interatómicos tienen átomos dispuestos en orden periódico y ordenado ocasionando que el haz incidente sea dispersado en diferentes fases.

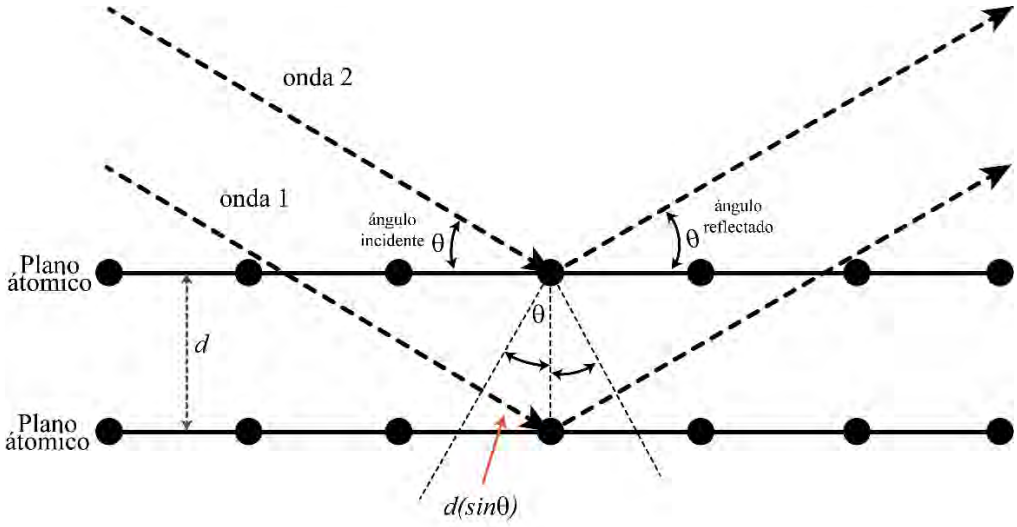

Figura 3.5.5: Representación esquemática del proceso de difracción de ondas electromagnéticas (rayos-X) cuando interacciona con un material cristalino.

Cuando un conjunto de rayos dispersados se refuerza mutuamente, es decir, tuvieron interferencia constructiva, entonces el haz es difractado. La ley que establece la condición esencial para que el fenómeno de difracción ocurra es la ley de Bragg (ecuación (3.5.1)). La ley fue planteada y desarrollada por padre e hijo, William Henry Bragg y William Lawrence Bragg, otorgándoles el premio Nobel de Física en 1915.

$$n\lambda = 2dsen\theta \qquad (3.5.1),$$

donde n es un número entero, λ la longitud de onda de los rayos-X, d la distancia entre los planos de la red cristalina y θ es el ángulo entre los rayos incidentes y los dispersados. En la difracción de polvos, el cristal examinado es reducido a pequeñas partículas (polvo fino), donde cada partícula de la muestra es un pequeño cristal que tiene orientación aleatoria con respecto al haz monocromático de rayos-X incidente. Entonces cada conjunto de planos cristalinos es capaz de producir difracción, es decir, cada pequeño cristal del polvo producirá el fenómeno de difracción y con ello se genera un patrón de difracción de un policristal. Este método es el único utilizable cuando no hay disponibilidad de un espécimen monocristalino.

En este trabajo, las nanoestructuras de CZTGS sintetizadas eran polvos finos, los cuales fueron analizados antes y después de ser tratados en un difractómetro modelo Panalytical – Empyrean usando radiación CuKα (λ= 1.5406 Å) ubicado en el laboratorio de

difracción de rayos-X del Instituto de Física “Ing. Luis Rivera Terrazas”. Los patrones de difracción de las nanoestructuras de CZTGS se adquirieron a temperatura ambiente con pasos de 0.02° en un rango 2θ desde 20° hasta 85°.

3.5.6 Espectroscopía de reflectancia difusa

Espectroscopía de reflectancia difusa es una técnica de caracterización no-destructiva y no-invasiva que es usada para obtener espectros ópticos de materiales no soportados (polvos) con un mínimo de preparación. En general, un espectro de reflectancia es obtenido del análisis de la radiación electromagnética reflejada de la superficie del material en función de la frecuencia o longitud de onda. El espectro de reflectancia contiene información acerca de las propiedades ópticas del material y puede ocurrir dos tipos de reflectancia: (i) la reflectancia especular, asociada a reflexiones provenientes de superficies pulidas y uniformes (como los espejos); (ii) la reflectancia difusa, asociada a reflexiones provenientes de superficies con textura o irregularidades (como polvos). En la **Figura 3.5.5** se presenta un esquema de la diferencia entre la reflectancia difusa y especular.

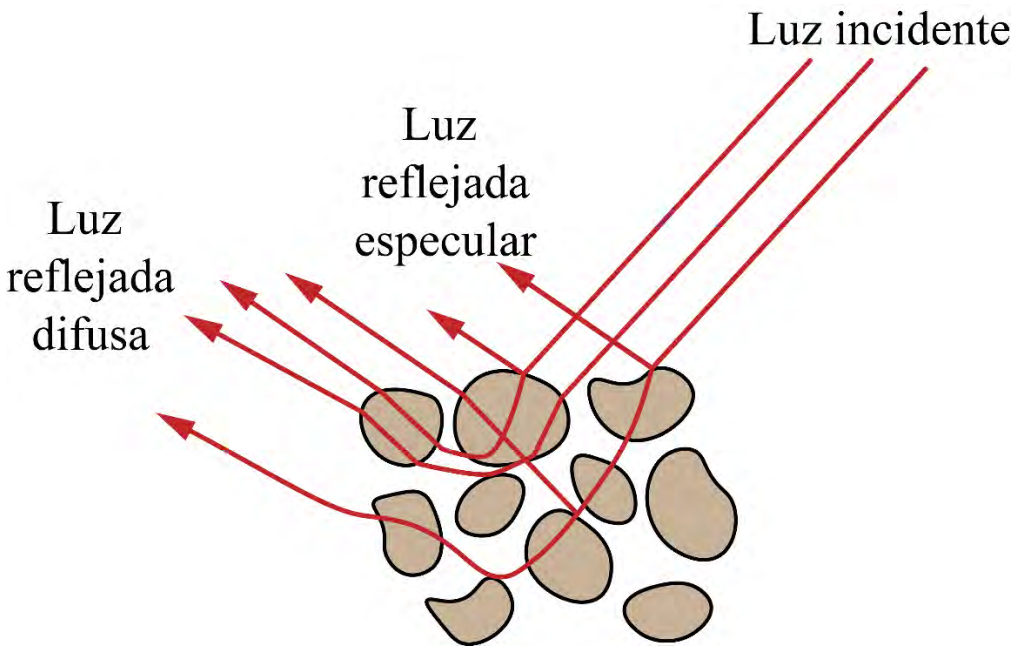

Figura 3.5.6: Representación esquemática del proceso de reflexión difusa y especular sobre la superficie de un material.

Para la captación de toda la luz dispersada a diferentes direcciones es necesario usar una esfera integradora acoplada al espectrofotómetro. Para analizar los espectros de reflectancia difusa se aplica la teoría de Kubelka y Munk [129], [130]. Originalmente, Kubelka y Munk propusieron un modelo que describe cómo la luz viaja dentro de un espécimen dispersor de luz planteando las siguientes ecuaciones diferenciales:

$$-di = -(S+K)idx + Sjdx$$
$$dj = -(S+K)jdx + Sidx \qquad (3.5.2),$$

donde i y j son las intensidades de la luz viajando dentro de la muestra hacia su superficie no iluminada e iluminada, respectivamente; dx es el segmento diferencial a lo largo de la trayectoria de la luz; S y K son los llamados coeficiente Kubelka–Munk (K-M) de dispersión y absorción, respectivamente. El modelo se aplica adecuadamente cuando el tamaño de las partículas es menor que la longitud de onda de la radiación electromagnética incidente y la reflexión difusa ya no permite separar las contribuciones de reflexión, refracción y difracción, es decir, se produce dispersión. Teniendo el caso límite cuando la muestra es infinitamente gruesa, el espesor y el sustrato no influyen en el valor de la reflectancia entonces la ecuación puede expresarse como la ecuación 3.5.3 para cualquier longitud de onda, donde $F(R_\infty)$ es denominada la función K-M que está en función de R_∞ [129], [130].

$$F(R_\infty) = \frac{(1-R_\infty)^2}{2R_\infty} = \frac{K}{S} \qquad (3.5.3),$$

La aplicación de la ecuación 3.5.3 se discute en la sección 4.1 de la tesis, cuando se utiliza para determinar el valor de la energía de banda prohibida de las nanoestructuras de CZTGS sintetizadas para este trabajo. Las mediciones de reflectancia difusa de las muestras de este trabajo se realizaron con un espectrofotómetro Cary 5000 instalado en el laboratorio central del Instituto de Física “Ing. Luis Rivera Terrazas”. Para la calibración de la línea base del equipo se utilizó teflón debido que es un material semejante a la parte interna de la esfera integradora (DRA-CA-30I).

3.5.7 Efecto Hall

Una técnica para estudiar las propiedades de transporte en materiales semiconductores es el efecto Hall. El efecto Hall es un proceso físico en el que se desarrolla un campo eléctrico transversal en un material sólido cuando el material transporta una corriente eléctrica y se aplica un campo magnético que es perpendicular a la corriente. El efecto Hall fue descubierto por Edwin Herbert Hall en 1879 que, entre muchas aplicaciones, contribuyó a establecer el hecho de que las partículas que circulan por un conductor metálico tienen carga negativa, diez años antes del descubrimiento del electrón.

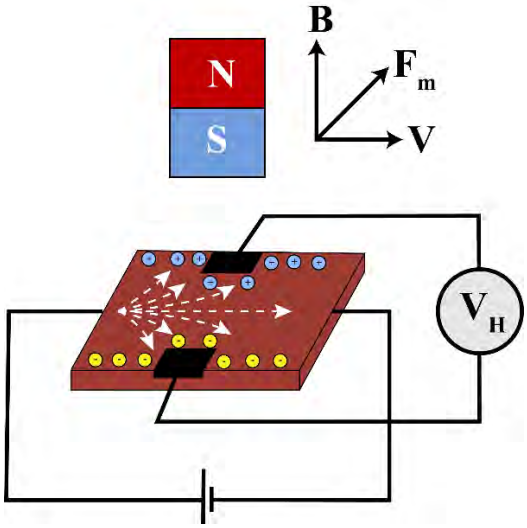

Figura 3.5.7: Representación esquemática del proceso de generación del voltaje Hall mediante el efecto Hall.

En general, el efecto Hall es producido cuando una placa conductora se conecta a un circuito externo y fluye una corriente eléctrica en presencia de un campo magnético transversal (perpendicular a la placa). En ausencia del campo magnético, los portadores de carga seguirán un camino lineal desde un extremo al otro del conductor. Sin embargo, en la presencia del campo magnético, los portadores de carga son desviados debido a una fuerza, alterando su dirección original de flujo. La fuerza que desvía a los portadores de carga es la fuerza de Lorentz. Como resultado, los electrones (carga negativa) serán desviados hacia un lado de la placa y los huecos (carga positiva) hacia el otro lado. Esta separación de cargas genera una diferencia de potencial que es conocida como voltaje Hall. La relación que tiene

el voltaje Hall con el campo magnético y la corriente eléctrica es descrita por la siguiente ecuación:

$$V_H = \frac{IB}{qnd} \quad (3.5.4),$$

donde I es la corriente que fluye a través de la muestra, B es el campo magnético aplicado, q es el valor de la carga del electrón o hueco, n es el número de portadores por unidad de volumen y finalmente d es el espesor de la muestra. El voltaje Hall (V_H) determina el tipo de portador mayoritario de la muestra. Cuando el signo es positivo representa huecos (semiconductor tipo-p), y en caso contrario, cuando el signo es negativo, la conducción es por electrones (semiconductor tipo-n). Las mediciones del voltaje Hall y la aplicación de la ecuación (3.5.4) permiten calcular el número de portadores por unidad de volumen o la densidad de portadores en la muestra. Además, determinando la conductividad del material se puede calcular la movilidad (μ) de los portadores mayoritarios de un semiconductor, usando la ecuación que se presenta a continuación:

$$\mu = \frac{1}{\rho nq} \quad (3.5.5).$$

En este trabajo, las películas de CZTGS fabricadas fueron analizadas por medición de efecto Hall a temperatura del ambiente para estudiar sus propiedades del transporte. Las mediciones fueron realizadas en un equipo de efecto Hall Ecopia 5300, usando la configuración de 4 puntas Van der Pauw, ubicado en el laboratorio central del Instituto de Física “Ing. Luis Rivera Terrazas”. Los contactos de plata que se usaron sobre la película de CZTGS se colocaron con ayuda de una plantilla para que los contactos fueran equidistantes y del mismo tamaño.

3.5.8 Curvas densidad de corriente vs voltaje (J – V)

En las celdas solares, los parámetros fotovoltaicos se obtienen a partir de las curvas de densidad de corriente en función del voltaje (curvas J – V). Para obtener una curva J – V se aplica una diferencia de potencial (voltaje) entre los electrodos de la celda solar y se mide, simultáneamente, la fotocorriente de respuesta bajo iluminación. En las condiciones estándar, la iluminación incidente que se utiliza para obtener una curva J – V debe ser semejante al

espectro de radiación solar con AM1.5G con una intensidad de la luz de 100 mW/cm^2 y a una temperatura de 25 °C. En la **Figura 3.5.8** se presenta una curva J – V característica de una celda solar y los parámetros fotovoltaicos que se puede extraer [131].

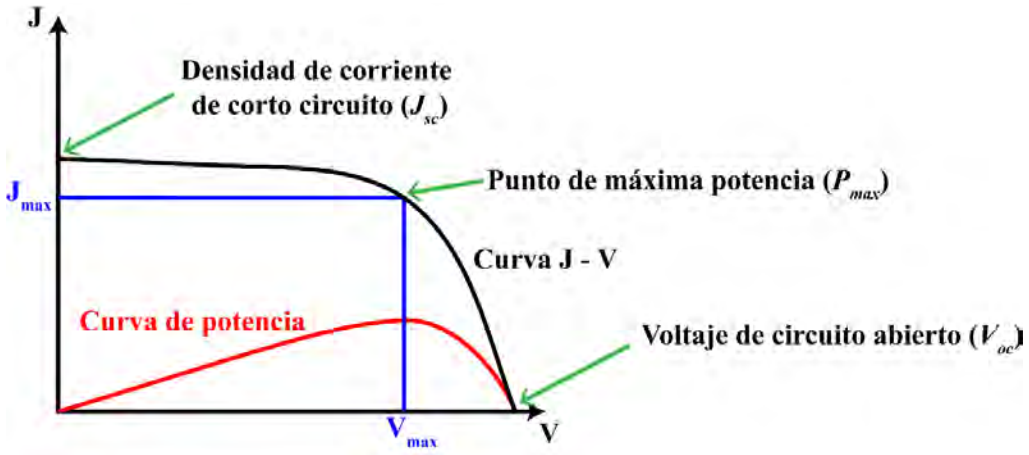

Figura 3.5.8: Curva J – V características de las celdas solares con los parámetros fotovoltaicos.

Como se mencionó anteriormente, a partir de la curva J – V se pueden obtener siguientes parámetros fotovoltaicos característicos del dispositivo:

- Voltaje a circuito abierto (V_{oc}): El valor máximo de voltaje que se registra cuando el dispositivo se encuentra en condiciones de circuito abierto (resistencia = ∞, corriente = 0). El valor de V_{oc} está condicionado por el grado de iluminación y procesos de recombinación del dispositivo, es decir, entre mayor sea la recombinación del dispositivo el valor disminuye.

- Densidad de corriente a cortocircuito (J_{sc}): Determina el valor máximo de densidad de corriente del dispositivo en condiciones de circuito cerrado (voltaje = 0, resistencia = 0). El valor de J_{sc} está condicionado por la absorbancia de la perovskita o del dispositivo, la inyección electrónica en la interfase de la perovskita con la ETL y la capacidad de los electrones y huecos para alcanzar el contacto o contraelectrodo antes de recombinar.

- Potencia máxima (P_{max}): El valor está determinado por el punto donde el producto de la densidad de corriente y el voltaje es máximo.

- Factor de llenado (*Fill Factor*, *FF*): Es el factor que indica la idealidad (una curva cuadrada) de la curva J – V, se calcula por medio de la ecuación (3.5.6) y los valores son menores a la unidad o se expresa en porcentaje.

$$FF = \frac{P_{max}}{J_{sc}V_{oc}} \quad (3.5.6).$$

- Eficiencia de conversión energética (η): El parámetro que relaciona la potencia de entrada con la potencia máxima mediante la ecuación (3.5.7). Es el parámetro más importante de la celda porque indica la eficiencia con la que se convierte la energía solar en energía eléctrica.

$$\eta = \left(\frac{P_{max}}{100\ mW/cm^2}\right) * 100 \quad (3.5.7).$$

La medición de las curvas J – V se llevó a cabo empleando una unidad fuente y de medida (SMU, por sus siglas en inglés "*Source Meter Unit*") marca Kethley 2450 y una lámpara de Xenón calibrada para dar una intensidad de radiación aproximada de 100 mW/cm^2. Es importante mencionar que no se utilizó un simulador solar para realizar las mediciones de las curvas J – V en las celdas fabricadas en este trabajo, por lo cual, los parámetros fotovoltaicos podrían presentar variaciones ocasionadas por la calibración.

3.5.9 Eficiencia cuántica externa (*external quantum efficiency*, EQE)

La eficiencia cuántica externa (EQE) es una técnica de caracterización que permite estimar la relación entre los pares electrón – hueco colectados con el número de fotones de una longitud de onda especifico incididos al dispositivo [132], [133]. Entonces, la EQE contiene la información sobre la eficiencia con la que una celda solar puede absorber un fotón, generar un par electrón–hueco y, finalmente, separar los portadores fotogenerados para ser extraídos en los respectivos contactos. Las mediciones de EQE en una celda solar se realizan en condiciones de corto circuito y aplicando una intensidad de una luz monocromática, donde, se mide la respuesta de la celda solar (fotocorriente de corto circuito). Esta medición se realiza en un rango de longitudes de onda entre 400–800 nm.

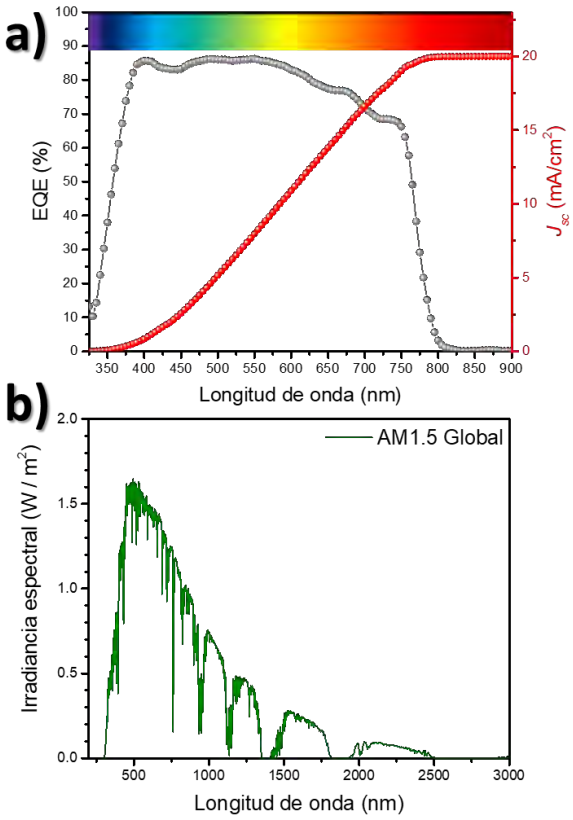

Figura 3.5.9: Curva de eficiencia cuántica característica de una celda solar de perovskita junto con el cálculo de la fotocorriente a partir del EQE (a). Espectro solar global AM 1.5G usado para el cálculo de la fotocorriente (b).

De las mediciones de EQE, se puede calcular la J_{sc} de una celda solar y el análisis de detallado de una curva EQE permite determinar el origen que ocasiona una baja fotocorriente de la celda solar. Una baja fotocorriente en una celda solar puede tener su origen desde un proceso óptico, como reflexión o absorción del sustrato o de algún material que conforma una celda solar, o un proceso electrónico, como perdidas por recombinaciones. En la **Figura 3.5.9(a)** se presenta una curva típica de EQE de una celda solar de perovskita, donde la fotocorriente de la celda solar se calcula integrando el producto de la curva EQE multiplicada por la longitud de onda y la intensidad del espectro solar AM1.5G (**Figura 3.5.9(b)**). Por lo tanto, a partir de las mediciones de EQE se puede determinar el rango espectral en el cual un dispositivo presenta pérdidas de fotocorriente debidas a los procesos antes mencionados.

La EQE de las celdas solares de perovskita fabricadas en este trabajo se midió usando un sistema “Oriel Instruments” ubicado en el laboratorio central del Instituto de Física “Ing. Luis Rivera Terrazas”.

Capítulo 4 – Resultados y discusión

En este capítulo se presentan y discuten los resultados obtenidos de las caracterizaciones realizadas a las nanopartículas CZTGS, las películas de CZTGS y las celdas de perovskita fabricadas usando los dos tipos de HTL.

4.1 Nanopartículas de $Cu_2ZnSn_{1-x}Ge_xS_4$

La composición elemental de las nanopartículas sintetizadas de CZTGS estimada por la técnica de espectroscopía de rayos X por energía dispersa (*energy dispersive X-ray spectroscopy*, EDS) se muestra en la **Tabla 4.1.1**. Como se puede ver en la **Tabla 4.1.1** las relaciones de porcentaje atómico de los cationes Cu/(Zn+Sn+Ge) y Zn/(Sn+Ge) para todas las muestras presentan una composición estequiométrica pobre en cobre (*Cu-poor*, Cu/(Zn+Sn+Ge) ≤ 1) y enriquecido en zinc (*Zn-rich*, Zn/(Sn+Ge) ≥ 1). Por otro lado, los valores de Ge/(Sn+Ge) se encuentra muy cerca de los valores nominales. Mientras que la composición *Cu-poor* y *Zn-rich* de las nanopartículas es ideal para la aplicación en celdas solares de segunda generación, la formación de fases secundarias, como ZnS, $Cu_{2-x}S$ y Cu_2SnS_3, es esperado que ocurra [76]–[78].

Tabla 4.1.1: Composición elemental estimada por EDS y las relaciones de porcentaje atómico de los cationes de las nanopartículas de $Cu_2ZnSn_{1-x}Ge_xS_4$ antes del lavado químico con HCl diluido.

Muestra (valor de "x")	Cu (%at)	Zn (%at)	Sn (%at)	Ge (%at)	S (%at)	Cu/(Zn+Sn+Ge)	Zn/(Sn+Ge)	Ge/(Sn+Ge)
0.0	26.06	14.10	12.31	-	47.54	0.99	1.15	0.0
0.15	25.95	13.45	10.54	1.6	48.27	1.01	1.11	0.13
0.30	27.39	16.34	7.72	3.85	44.71	0.98	1.41	0.33
0.40	26.44	13.68	7.54	4.62	47.72	1.02	1.13	0.38
0.60	27.10	15.64	5.23	6.42	45.61	0.99	1.34	0.55
0.70	27.14	16.93	3.79	8.97	43.17	0.91	1.33	0.70

Para investigar la posible formación de fases secundarias de Cu en las muestras, como $Cu_{2-x}S$ y Cu_2SnS_3, las nanoestructuras sintetizadas fueron analizadas por XRD. Los patrones de difracción a temperatura ambiente de las nanopartículas sintetizadas con diferentes valores nominales de Ge se muestran en la **Figura 4.1.1(a)**. Los patrones de difracción de todas las muestras revelan picos posicionados alrededor de 28.70, 33.23, 47.65, 56.41, 69.52 y 76.77° ángulos de Bragg, que corresponden a los planos cristalinos (112), (200), (220), (312), (400) y (136) del CZTS en fase tetragonal (kesterita), respectivamente. Como se puede observar en la **Figura 4.1.1(a)**, las posiciones de los principales picos de los patrones de difracción (112), (220) y (312) se desplazan gradualmente a mayores ángulos de Bragg conforme se incrementa la cantidad nominal de Ge en las muestras. El desplazamiento en posición de los picos de difracción a mayores ángulos de Bragg en las muestras que contienen Ge se debe a la substitución de los átomos de Sn, con un radio iónico grande Sn^{4+} = 0.69 Å [134] por átomos de Ge de radio iónico menor Ge^{4+} = 0.39 Å [134]. El desplazamiento observado en las posiciones de los picos de difracción con respecto a la muestra libre de Ge indica que la incorporación del Ge en la estructura cristalina se realizó de manera exitosa [27], [135]–[137]. Sin embargo, para las muestras con x = 0.6 y 0.7, los patrones de difracción tienen varios picos de difracción que corresponden a una fase ternaria de Cu_8GeS_6 (PDF # 04-010-4016), cuyas intensidades incrementa conforme aumenta el valor de "*x*" ($x \geq 0.6$). Ninguna otra fase secundaria de Cu, como $Cu_{2-x}S$ o Cu_2SnS_3, se detectó en los patrones de difracción de las muestras.

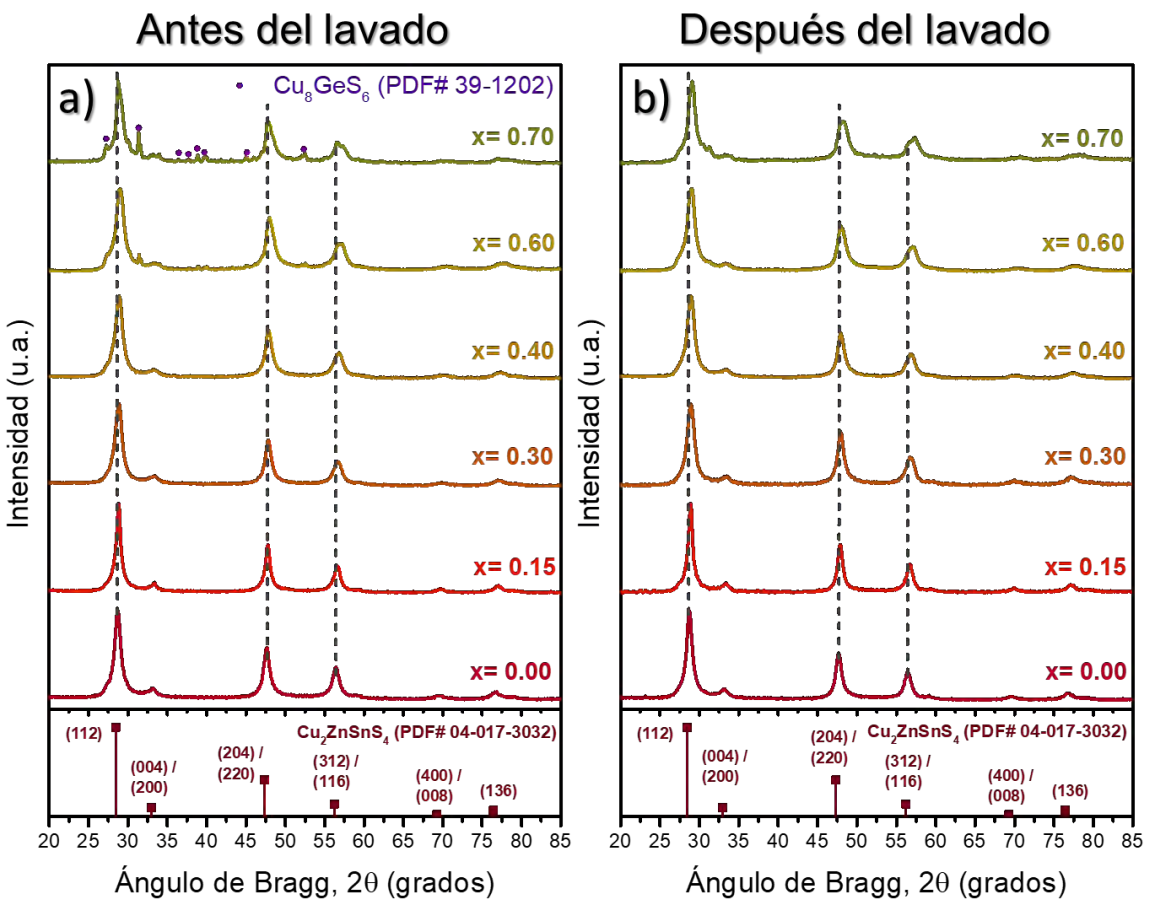

Figura 4.1.1: Patrones de difracción de rayos-X de las nanopartículas de $Cu_2ZnSn_{1-x}Ge_xS_4$ con diferentes fracciones nominales de Ge (a) antes y (b) después del lavado químico con HCl diluido.

La incorporación de los iones de Ge^{4+} en las fases de CuS (covelita) y $Cu_{1.81}S$ (roxbyita) genera los compuestos Cu_2GeS_3 y Cu_8GeS_6, respectivamente [138]. Por lo tanto, es altamente probable que el subproducto obtenido (Cu_8GeS_6) en la síntesis de las nanopartículas con alto contenido de Ge ($x \geq 0.6$) se deba al $Cu_{1.81}S$, que es una fase intermediaria, formada al principio de la reacción hidrotermal. Es importante notar que el estado de oxidación de los iones de Cu en CuS y $Cu_{1.81}S$ son +2 y +1, respectivamente. En la reacción hidrotermal de este trabajo, utilizamos la etilendiamina, que permite la reducción en el estado de oxidación del precursor de cobre (acetato de cobre) de +2 a +1 [120], el cual facilita la formación de $Cu_{1.81}S$ como compuesto intermediario para finalmente producir la fase Cu_8GeS_6 al reaccionar con el precursor de Ge. Una vez que la fase Cu_8GeS_6 se forma, no se puede descomponer durante la reacción hidrotermal, incluso usando mayor temperatura de reacción, debido a la alta estabilidad térmica del compuesto (punto de fusión = 1250 K)

[139]. Además, la fase de Cu_8GeS_6 se ha reportado que comienza a formarse durante una reacción hidrotermal cuando se calienta ~100 °C [138].

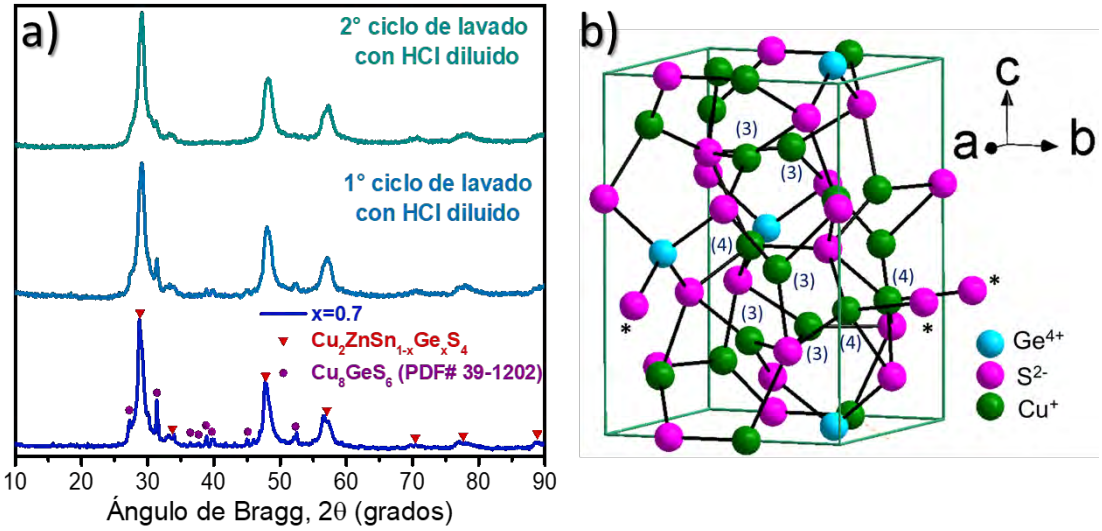

Figura 4.1.2: (a) Patrones de difracción de rayos-X de las nanopartículas de $Cu_2ZnSn_{1-x}Ge_xS_4$ preparadas con la cantidad nominal de x= 0.7, antes y después de 1 y 2 ciclos de lavado con HCl diluido. (b) Representación esquemática de la estructura de Cu_8GeS_6, donde se marcan los iones de Cu que tienen coordinación 3 o 4. Los átomos marcados con el símbolo asterisco (*) corresponden a átomos fuera de la celda unitaria.

Para remover la fase secundaria Cu_8GeS_6, se implementó un proceso de lavado químico con HCl diluido, descrito en la sección 3.2. En la **Figura 4.1.1(b)**, se puede observar que la impureza Cu_8GeS_6 se eliminó exitosamente después de lavado químico con HCl diluido. Para la mayoría de las muestras se necesitó hacer un solo ciclo de lavado químico. Sin embargo, para la muestra con mayor cantidad de Ge y aparentemente mayor presencia de la fase secundaria Cu_8GeS_6, se necesitó realizar dos ciclos de lavado químico con HCl diluido para lograr remover en su totalidad. En la **Figura 4.1.2(a)** se observa como la intensidad de los picos correspondientes a la fase secundaria Cu_8GeS_6 se disminuye progresivamente sin alterar los picos asociados a la fase tetragonal de CZTGS. Por otro lado, la anchura a media altura (*full-width at half máximum*, FWHM) se reduce ligeramente después del lavado químico con HCl. Estos resultados indican que la cristalinidad y el tamaño de grano de las nanopartículas de CZTGS no es afectado significativamente por el lavado químico con HCl.

La fase Cu_8GeS_6 tiene una estructura tipo argirodita. La mayoría de los compuestos con este tipo de estructura son conductores superionicos debido a salto (*hopping*) de los iones Cu^+ a través de la red cristalina [140]–[142]. En la estructura del Cu_8GeS_6, los cationes de Cu^+ tienen una distancia entre vecinos mayor a 2.9 Å y algunos cationes de Cu^+ están enlazados con 3 o 4 aniones de S^{2-} (**Figura 4.1.2(b)**). Entonces, la distancia de los enlaces de Cu–S en Cu_8GeS_6 varía desde 2.219 hasta 2.590 Å [141]–[143]. Mientras que en la estructura kesterita de CZTS (tetragonal), todos los cationes Cu^+ son enlazados con 4 aniones de S^{2-} en un arreglo tetraedro regular (**Figura 4.1.4(b)**) y la variación de la distancia en los enlaces Cu–S es desde 2.26 hasta 2.29 Å [135]. Por lo tanto, la gran distancia de los enlaces Cu–S en Cu_8GeS_6 comparado con las distancias correspondiente en CZTGS hace menos estable el compuesto Cu_8GeS_6, lo cual facilita el lavado químico con HCl diluido para remover el compuesto [144].

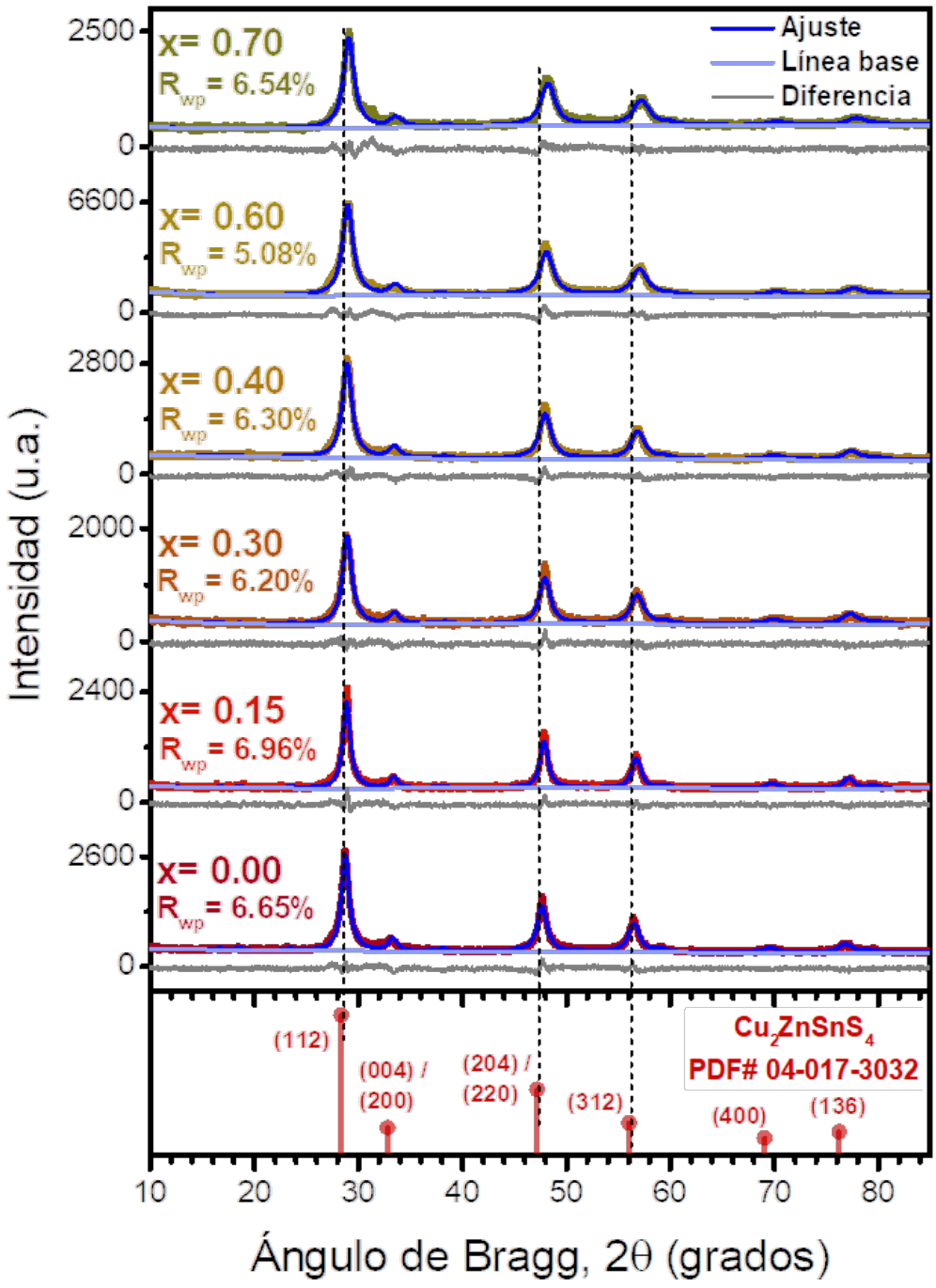

Figura 4.1.3: Perfiles de análisis Rietveld de las nanopartículas de $Cu_2ZnSn_{1-x}Ge_xS_4$ con diferentes fracciones de Ge después del lavado químico con HCl diluido.

La composición elemental estimada por EDS de las muestras después del lavado con HCl diluido se presenta en la **Tabla 4.1.2**. De la composición elemental estimada por EDS de las muestras antes del lavado, la relación de porcentaje atómico Ge/(Sn+Ge) reveló que la cantidad de Ge incrementa conforme el precursor de Ge se aumentaba en la reacción de

síntesis de las nanopartículas. Sin embargo, la relación Ge/(Sn+Ge) para las muestras después de lavado disminuyo, lo cual se asocia a que posiblemente no todos los átomos de Ge presentes en la reacción se incorporaron a la estructura del CZTGS. Por lo que estos átomos de Ge que no participaron en la formación del CZTGS produjeron el ternario Cu_8GeS_6 reaccionando con una fase intermediaria $Cu_{1.81}S$.

Tabla 4.1.2: Composición elemental estimada por EDS y las relaciones de porcentaje atómico de los cationes de las nanopartículas de $Cu_2ZnSn_{1-x}Ge_xS_4$ después del lavado químico con HCl diluido.

Muestra (valor de "x")	Cu (%at)	Zn (%at)	Sn (%at)	Ge (%at)	S (%at)	Cu/(Zn+Sn+Ge)	Zn/(Sn+Ge)	Ge/(Sn+Ge)
0.0	28.92	10.67	10.62	-	49.79	1.36	1.02	0.0
0.15	27.07	10.32	9.38	1.64	51.60	1.27	0.95	0.15
0.30	28.95	10.97	7.55	3.14	49.39	1.34	1.03	0.29
0.40	29.09	10.28	6.86	4.26	49.52	1.36	0.92	0.38
0.60	28.14	12.45	5.08	6.09	48.24	1.20	1.12	0.54
0.70	29.81	9.38	4.48	6.31	50.02	1.48	0.87	0.58

Para monitorear el efecto de la incorporación del Ge en la estructura cristalina de las nanopartículas, los parámetros de la celda unitaria ($a = b, c$), volumen de la celda unitaria y tamaño de grano se estimaron mediante refinamiento Rietveld de los patrones de difracción de las muestras lavadas con HCl diluido. Para el refinamiento Rietveld, se utilizó el programa GSAS-II (versión 4379) [145], la composición elemental estimada por EDS de las muestras, funciones de pseudo-Voigt, estructura kesterita con grupo espacial $I\bar{4}$ (PDF# 04-017-3032) y una línea base construida por polinomios de Chebyshev. Los patrones de difracción del refinamiento Rietveld se presentan en la **Figura 4.1.3**. En la **Figura 4.1.4(a)** se muestran los parámetros estructurales obtenidos del refinamiento Rietveld de las muestras lavadas con HCl diluido. Como se puede observar en la **Figura 4.1.4(a)**, los valores de los parámetros y el volumen de celda unitaria decrece casi linealmente conforme se incrementa el contenido de Ge en las muestras.

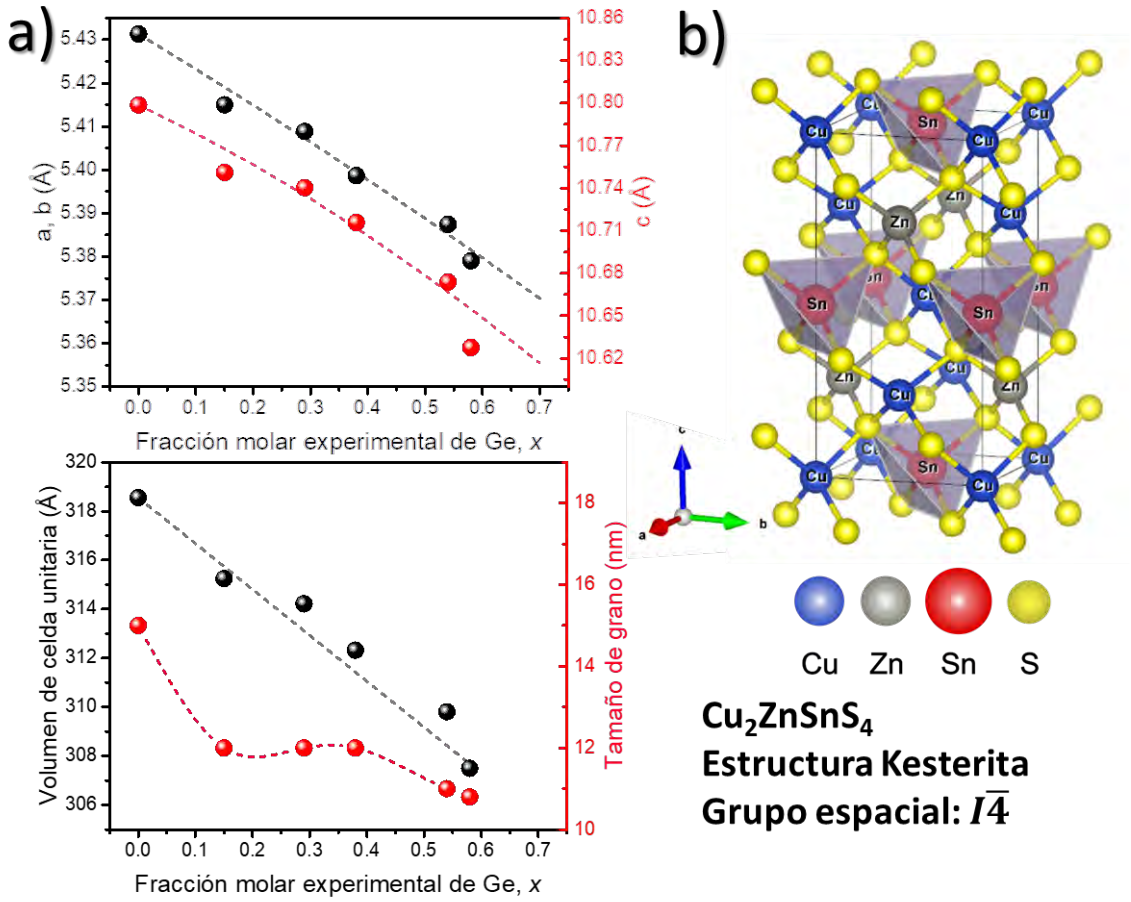

Figura 4.1.4: (a) Parámetros estructurales extraídos del análisis Rietveld de los patrones de difracción de las nanopartículas después del lavado químico. (b) Representación esquemática de la estructura de kesterita.

El decremento linear de los parámetros y volumen de la celda unitaria con valor "*x*" indican que los cambios obedecen la ley de Vegard [137]:

$$\xi(x) = x\xi_{CZGS} + (1-x)\xi_{CZTS} - \delta x(1-x) \qquad (4.1.1),$$

donde $\xi(x)$ es el parámetro de la celda unitaria (a, c) del CZTGS, ξ_{CZTS} es el parámetro de la celda unitaria (a, c) del CZTS, ξ_{CZGS} es el parámetro de red (a, c) del Cu_2ZnGeS_4 (CZGS), δ es el parámetro de desviación del parámetro de red y x es la fracción molar del CZTGS. Para usar la ecuación (4.1.1), los parámetros utilizados de la celda unitaria de CZTS y CZGS son los valores obtenidos desde el refinamiento Rietveld del patrón de difracción de la

muestra sin Ge (x= 0.0) y de los parámetros de celda unitaria reportados en el trabajo de Parasyuk *et al.*, respectivamente [146]. El mejor ajuste de la variación de los parámetros de red, a y c, se obtuvo con parámetro de desviación δ = 0.01 y δ = 0.1 Å, respectivamente.

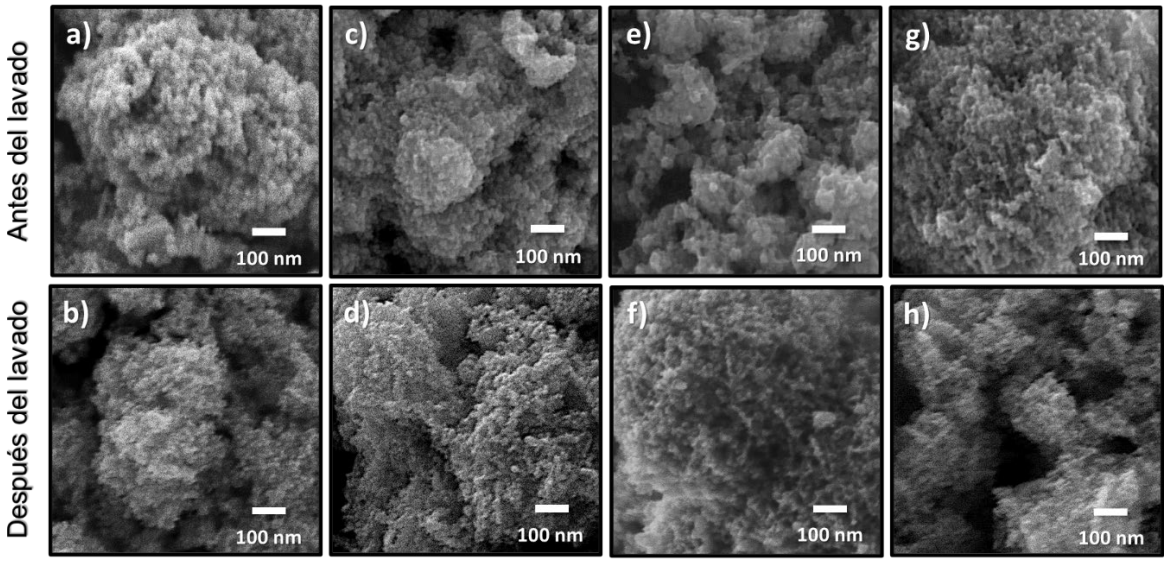

Figura 4.1.5: Imágenes SEM típicas de las nanopartículas de $Cu_2ZnSn_{1-x}Ge_xS_4$ con diferentes fracciones molares nominales de Ge: x = (a,b) 0.00, (c,d) 0.30, (e,f) 0.60 y (g,h) 0.70, para antes (izquierda) y después (derecha) del lavado químico con HCl diluido.

Para estudiar si existe algún efecto del lavado químico en el tamaño, morfología y cristalinidad de las nanopartículas, las muestras fueron analizadas en SEM, TEM y HR-TEM, antes y después del lavado con HCl. En la **Figura 4.1.5** se muestran las imágenes SEM típicas de las nanopartículas de CZTGS con diferentes fracciones nominales de Ge antes y después del lavado con HCl diluido. La formación de partículas cuasi – esféricas de tamaños nanométricos se observa en las imágenes SEM de todas las muestras. Como se puede ver en la **Figura 4.1.5**, las nanopartículas conservan su forma cuasi – esférica incluso después del lavado químico con HCl diluido. La distribución de tamaños se realizó midiendo las dimensiones de cada partícula de las muestras lavadas con HCl diluido revelando que el tamaño promedio de las nanopartículas para las muestras preparadas con un 15% de Ge es de 12.2 ± 3.6 nm (**Figura 4.1.6**). Al incrementar la cantidad de Ge en las muestras el tamaño promedio de las nanopartículas se redujo a 11.3 ± 2.5 nm (para la muestra con x= 0.7). Los planos atómicos en las imágenes de HR-TEM de las nanopartículas lavadas con HCl diluido indican su buena cristalinidad. Además, los puntos intensos en los patrones de la rápida

transformada de Fourier (FFT) de las áreas selectas (marcadas con un recuadro de color rojo) de las imágenes de HR-TEM claramente indican una buena cristalinidad de las nanopartículas. Como se puede observar en las imágenes de HR-TEM presentadas en la **Figura 4.1.6**, la distancia interplanar del plano principal de las nanopartículas con estructura kesterita, es decir (112), decrece desde 3.2 a 2.9 Å, conforme incrementa la cantidad de Ge en la muestra. La reducción del tamaño promedio de las partículas y la distancia interplanar pueden ser asociados a la reducción del volumen de celda unitaria en la estructura del cristal con la incorporación del Ge, como se observó en los parámetros estructurales obtenidos en el análisis Rietveld de los patrones de difracción de las nanopartículas (**Figura 4.1.4(a)**).

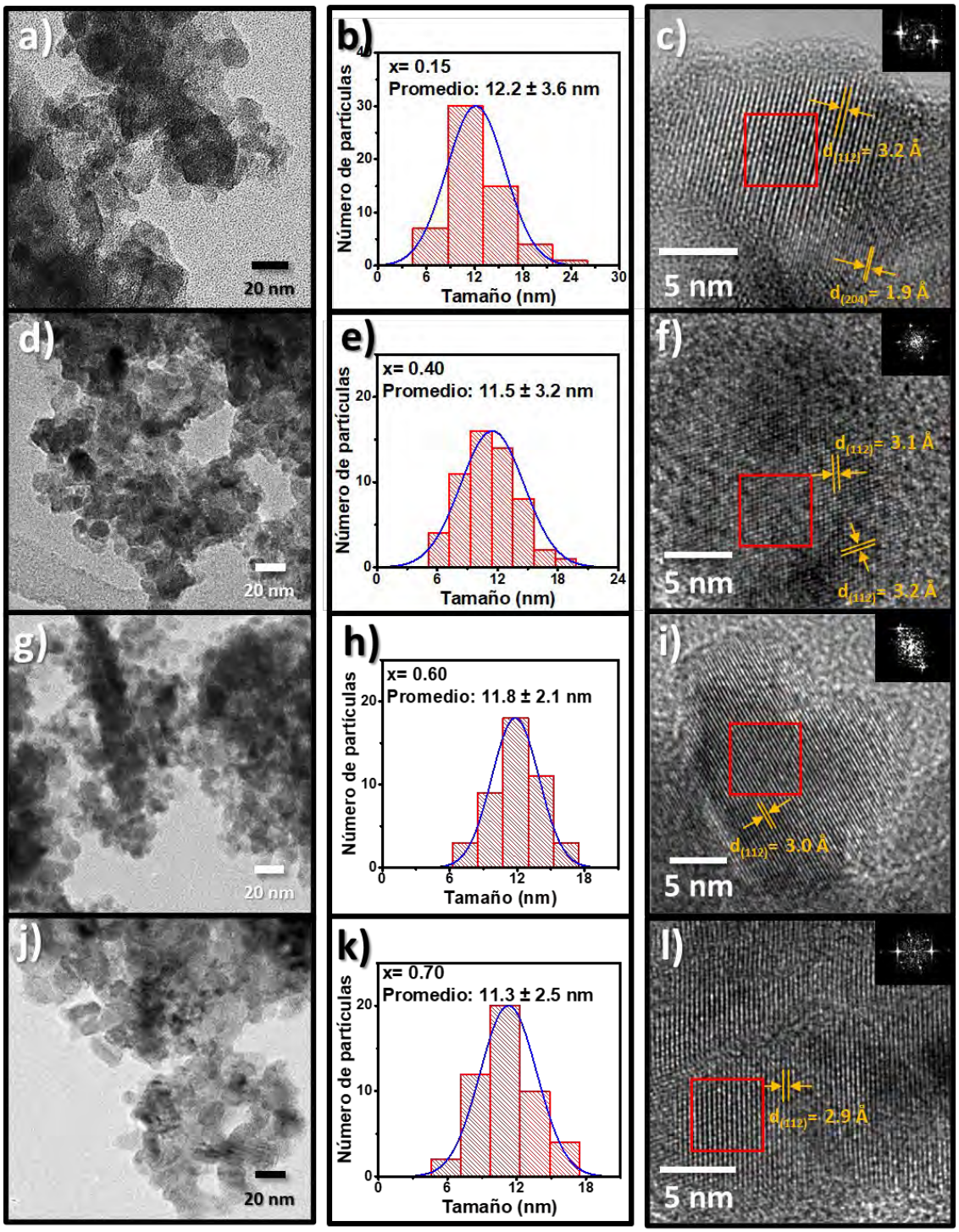

Figura 4.1.6: Imágenes típicas de baja y alta resolución TEM y su correspondiente histograma de distribución de tamaño de las nanopartículas de $Cu_2ZnSn_{1-x}Ge_xS_4$ lavadas con HCl diluido con diferentes fracciones nominales de Ge: x= (a-c) 0.15, (d-f) 0.40, (g-i) 0.60 y (j-l) 0.70. Los insertos en las imágenes de HR-TEM corresponde a los patrones de FFT de las zonas delimitadas por cuadros de color rojo en cada una de ellas.

La pureza y la cristalinidad de las nanopartículas fueron analizadas por la espectroscopia Raman. Los espectros Raman de las nanopartículas fueron adquiridos a temperatura del ambiente antes y después del lavado con HCl diluido. Para las mediciones Raman, se tomó las medidas adecuadas seleccionando los lentes objetivos y filtros de densidad neutral adecuados para evitar la oxidación o quema de las nanopartículas. Los espectros Raman a temperatura ambiente de las nanopartículas de CZTGS antes y después del lavado con HCl diluido se presentan en las **Figura 4.1.7**, respectivamente. Los espectros Raman de todas las muestras revelaron una banda de dispersión intensa posicionada alrededor de 330 cm^{-1}. Sin embargo, esta banda de dispersión es amplia y asimétrica, contiene hombros por ambos lados (en menores y mayores números de onda). Para un análisis detallado, esta banda de dispersión Raman fue deconvolucionada cuidadosamente para todas las muestras usando un ajuste Lorentziano (**Figura 4.1.7**).

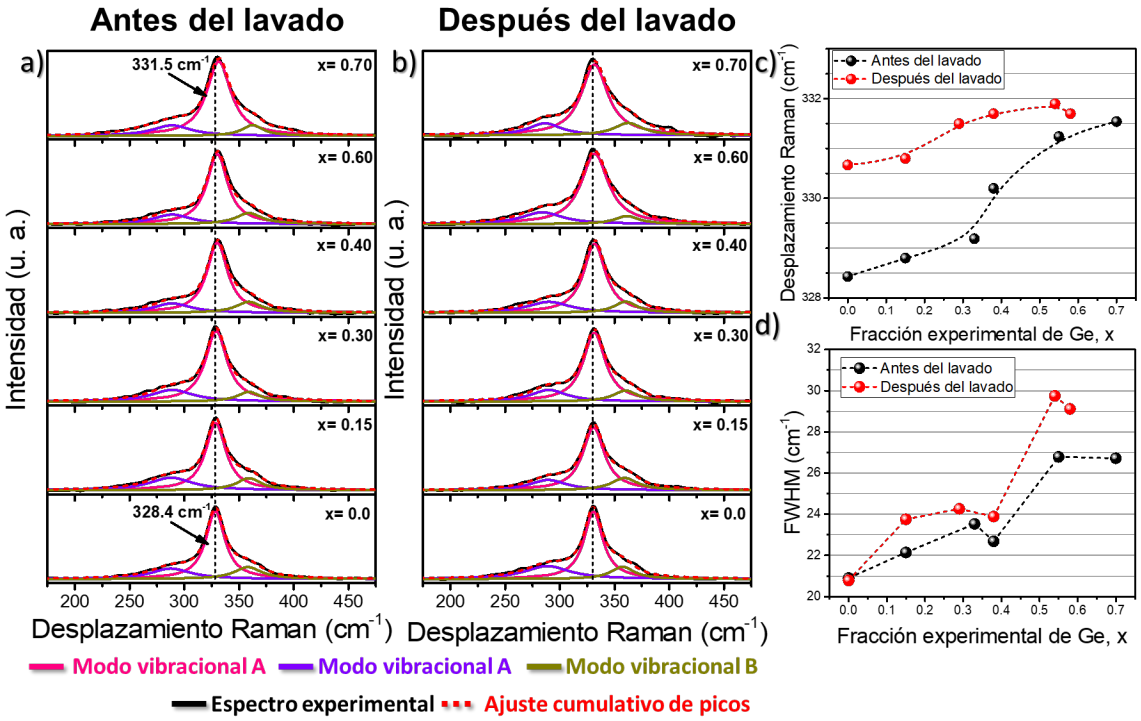

Figura 4.1.7: Espectros Raman a temperatura ambiente y su deconvolución de las nanopartículas de $Cu_2ZnSn_{1-x}Ge_xS_4$ con diferentes fracciones molares de Ge (a) antes y (b) después del lavado químico con HCl diluido. (c) Variación de la posición y (d) su FWHM del pico de dispersión principal (~ 330 cm^{-1}) con el incremento experimental (estimado por EDS) de la fracción molar de Ge.

Como se puede ver en la **Figura 4.1.7**, la banda de dispersión principal de todas las muestras (antes y después del lavado) es compuesta por tres componentes con posiciones de sus picos alrededor de 280, 330 y 350 cm^{-1}. De acuerdo con la literatura, las bandas de dispersión principales para el CZTS estequiométrico, conocidos como modos vibracionales A, están localizadas en 287 y 337 cm^{-1} que corresponden a las vibraciones rotacionales y estiramiento de los enlaces de Sn–S en el tetraedro SnS_4 del CZTS, respectivamente. Mientras que la banda posicionada alrededor de 350 cm^{-1} corresponde a la vibración ocasionada por el desplazamiento de los cationes a lo largo del eje-c, conocidos como modos vibracionales B [147], [148]. Sin embargo, los modos vibracionales A pueden desplazarse a menores números de ondas debido a una composición no estequiométrica [64]. En la **Tabla 4.1.2** se muestra los cambios en los valores de Zn/(Sn+Ge) y Cu/(Zn+Sn+Ge) en las muestras lavadas con HCl diluido en comparación con los valores correspondiente de las muestras sin lavado. El cambio observado en las relaciones de cationes de las muestras lavadas con HCl diluido es probablemente debido a la reducción del Zn (observado en el análisis EDS). La fracción de Zn que no se incorporó a la estructura del $Cu_2ZnSn_{1-x}Ge_xS_4$ probablemente reaccionó con el azufre disponible en la reacción para generar la fase secundaria ZnS. Sin embargo, en los patrones de difracción de las muestras (lavadas y no lavadas) no se detectó ningún pico asociado al ZnS. Además, la fase de ZnS es difícil de detectar en los patrones de difracción de rayos-X (XRD) debido a que la estructura cristalina de ZnS (cubica, a= 5.41 Å) es similar a la estructura kesterita (tetragonal, a= 5.43 Å y c= 10.84 Å) [80], lo cual causa que los picos de difracción estén posicionados en ángulos de Bragg similares. No obstante, en las nanopartículas de CZTGS que se fabricaron no pudimos detectar ninguna señal asociada a la fase de ZnS debido a la utilización del láser de He-Cd (λ = 633 nm) para la excitación, cuya energía está muy por debajo de la energía de la banda prohibida de ZnS (3.6 eV).

Los modos vibracionales de la estructura kesterita son sensibles a la sustitución del Ge. La sustitución del Sn por el Ge en la kesterita CZTS remplaza algunos enlaces de Sn–S por enlaces de Ge–S, modificando la constante de fuerza efectiva de los enlaces atómicos (catión–anión) debido a la diferencia de tamaño y masa de los iones de Sn^{4+} y Ge^{4+}. Por consecuencia, las posiciones de las bandas de dispersión Raman se desplazan a mayores números de onda (*blue–shift*) [27], [137], [149], [150]. El desplazamiento de la banda

complementaria alrededor de 330 cm^{-1} en función de la fracción de Ge (estimado por EDS) en las nanopartículas antes y después de lavado se muestra en la **Figura 4.1.7(c)**. Como se puede observar, la banda complementaria en ambas series de muestras (no lavadas y lavadas) se desplaza a mayores números de onda, indicando claramente que la substitución del Sn por Ge fue exitosa. Sin embargo, en la **Figura 4.1.7(c)** se observa que existe una diferencia entre las posiciones de la banda complementaria de las muestras no lavadas y lavadas. Como se observó en el análisis de EDS (**Tabla 4.1.2**), después de lavado químico con HCl diluido, las nanopartículas de CZTGS se volvieron ricas en Cu (*Cu-rich*) y pobres en Zn (*Zn-poor*), que es estequiometria ideal para su aplicación en dispositivos fotovoltaicos de segunda generación [90]. Los pequeños cambios en las posiciones de las bandas principales de Raman de las muestras lavadas químicamente son probablemente atribuidos al cambio en la composición de las nanopartículas de CZTGS de *Cu-poor* a *Cu-rich*, como se ha reportado previamente por Valakh *et al.* [64].

Por otro lado, la anchura completa a la mitad del máximo (*full width at half máximum*, FWHM) de las bandas Raman es asociado con los defectos en la estructura kesterita cuando tiene un desorden, debido a la formación de los defectos de antisitios como Cu_{Zn} o Zn_{Cu}. El valor del FWHM incrementa cuando la concentración de los defectos de antisitio Cu_{Zn} o Zn_{Cu} aumenta [64]. En general, como se puede ver en la **Figura 4.1.7(d)**, el valor del FWHM de la banda principal ubicada alrededor de 330 cm^{-1}, incrementa con el aumento del contenido de Ge en la estructura kesterita. Las nanopartículas lavadas químicamente tienen la estequiometria *Cu-rich* y *Zn-poor*, en el cual los iones de Cu en exceso pueden ocupar los sitios de los iones de Zn, produciendo los defectos como antisitios Cu_{Zn}. Un desorden en la estructura kesterita ocurre debido a la ocupación aleatoria de los átomos de Cu y Zn, incrementando la concentración del defecto antisitio Cu_{Zn}. Además, en la literatura reportan que el desorden en la estructura kesterita aumenta debido a la sustitución del Sn por Ge [35], [36]. Por lo tanto, el incremento observado en el valor de FWHM (**Figura 4.1.7(d)**) de la banda de dispersión Raman de las nanopartículas CZTGS preparadas es probablemente asociado a un incremento en el desorden de la estructura cristalina debido al aumento de la concentración de los defectos antisitios Cu_{Zn} y la substitución del Sn por Ge en la estructura kesterita. Los resultados obtenidos de análisis EDS y espectroscopía Raman de las nanopartículas fabricadas en condiciones de la síntesis en este trabajo indican que existe un

límite máximo de incorporación de Ge en las nanopartículas de CZTGS. La incorporación del precursor de Ge en la mezcla de reacción más allá de ese límite provoca la formación de la fase secundaria Cu_8GeS_6.

Para determinar los valores de energía de la banda prohibida de las muestras antes y después del lavado químico se adquirieron sus espectros de reflectancia difusa en el rango espectral 300–920 nm (**Figura 4.1.8**). Los espectros de reflectancia difusa fueron procesados con el formalismo de Kubelka–Munk (K-M) para obtener los espectros de absorción equivalentes y determinar los valores de energía de la banda prohibida [129]. La **Figura 4.1.8** muestran los gráficos de K-M de las muestras lavadas y no lavadas, con su extrapolación lineal para determinar respectivos valores de energía de banda prohibida. Los valores de la energía de banda prohibida incrementan desde 1.55 hasta 1.81 eV y 1.42 hasta 1.70 eV conforme aumenta la fracción de Ge en las muestras no lavadas y lavadas, respectivamente. El incremento de los valores de la energía de banda prohibida en las nanoestructuras no lavadas indica claramente que ocurrió la substitución de los átomos de Sn por los átomos de Ge. Además, el incremento de los valores de energía de la banda prohibida en las nanopartículas de kesterita con Ge concuerda con los resultados reportados por varios investigadores [27], [137], [150], [151]. Mientras que la diferencia en los valores de energía de la banda prohibida entre las muestras lavadas y no lavadas corresponde a la eliminación de las fases secundarias en las muestras no lavadas. El HCl diluido tiene la capacidad de romper los enlaces de Zn–S en los materiales con estructura blenda de zinc como ZnS (*Zinc-blende*) [84], [152]. Entonces, existe una posibilidad que el HCl diluido ataqué la kesterita CZTGS (su celda unitaria es equivalente a dos celdas unitarias de blenda de zinc), removiendo selectivamente algunos iones de Zn^{2+} desde la superficie de las nanopartículas. Para mantener la electroneutralidad de la estructura kesterita, el número equivalente de aniones de S^{2-} deben ser removidos y consecuentemente los estados de valencia de los iones Cu de la superficie deben cambiar de Cu^{1+} a Cu^{2+}. Por lo tanto, la eliminación de los iones de Zn^{2+} de la superficie de las nanopartículas kesterita de CZTGS concuerda con la disminución del porcentaje atómico de Zn que fue detectado por el análisis EDS (**Tabla 4.1.2**).

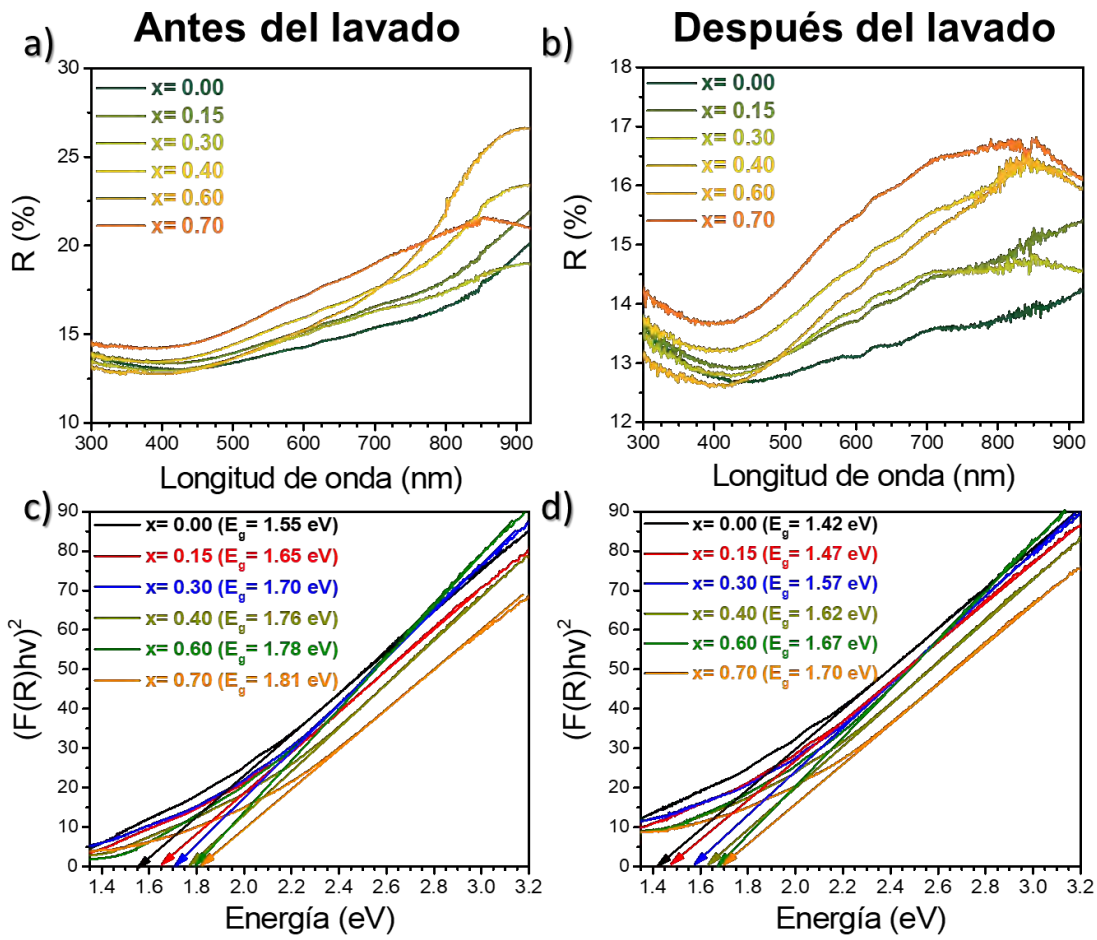

Figura 4.1.8: Espectros de reflectancia difusa y gráficas de Kubelka-Munk usados para estimar el valor de la energía de la banda prohibida de las nanopartículas de $Cu_2ZnSn_{1-x}Ge_xS_4$ antes y después del lavado químico con HCl diluido.

Por otro lado, la diferencia de los valores de energía de la banda prohibida entre las muestras lavadas y no lavadas puede explicarse en términos de la posición del máximo de la banda de valencia (*valence band maximum*, VBM) y el mínimo de la banda de conducción (*conduction band minimum*, CBM). En el CZTS, el VBM es compuesto por los orbitales de antienlace de Cu-3d y S-3p, mientras que el CBM es compuesto por orbitales antienlace de Sn-5s y S-3p [25]. La eliminación selectiva de los iones de Zn^{2+} de la superficie de las nanopartículas de CZTGS por el lavado químico probablemente promueve la formación de un nivel aceptor cerca del VBM debido al cambio del estado de oxidación del Cu desde Cu^{1+} a Cu^{2+}, reduciendo su energía de banda prohibida efectiva [26], [153]–[155].

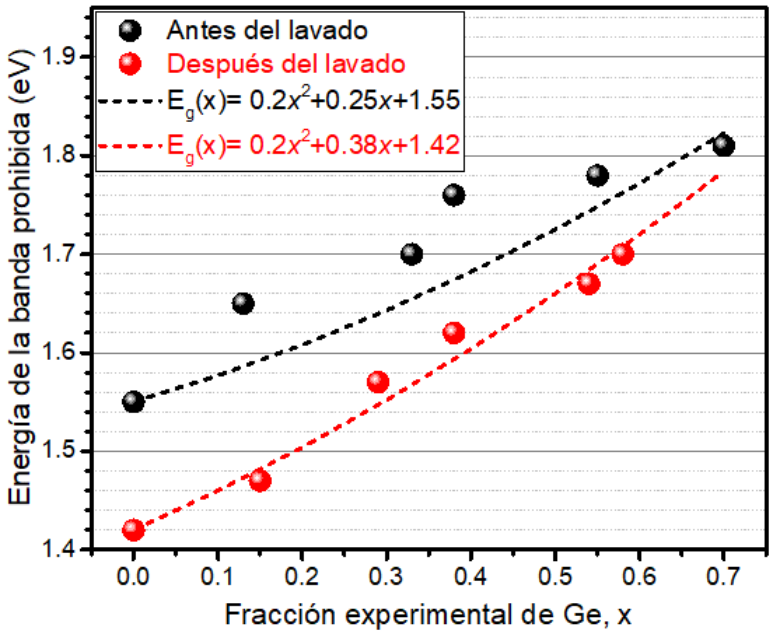

Figura 4.1.9: Variación de los valores de energía de la banda prohibida con la fracción experimental molar de Ge. Las líneas negra y roja corresponden a los valores ideales, de acuerdo con la ley de Vegard, de la energía de la banda prohibida con diferentes cantidades de Ge.

La relación empírica entre los valores de energía de la banda prohibida y la relación Ge/(Ge + Sn) en la kesterita puede ser expresado por la relación de Vegard (ecuación (4.1.2)) [137] con su termino de corrección asociado a la no linealidad (también conocido como parámetro de inclinación):

$$E_g^{CZTGS}(x) = xE_g^{CZGS} + (1-x)E_g^{CZTS} - bx(1-x) \qquad (4.1.2),$$

donde E_g^{CZTS} y E_g^{CZGS} son las energías de la banda prohibida del CZTS y CZGS, respectivamente, x es la fracción molar del Ge y b es el parámetro de inclinación. Los resultados experimentales obtenidos se ajustaron con un parámetro de inclinación constante igual a 0.2 eV, como se reporta en trabajos previos [35], [137]. Además, para el ajuste se consideró los valores de energía de la banda prohibida determinados experimentalmente en este trabajo para el CZTS: 1.55 eV (antes del lavado) y 1.42 eV (después del lavado) y los valores reportados en la literatura para la fase pura de CZGS (2.0 eV)[27], [137]. Como se puede ver en la **Figura 4.1.9**, el valor constante del parámetro de inclinación es pequeño, que implica los valores de energía de la banda prohibida de las nanopartículas de CZTGS incrementan casi linealmente conforme se aumenta la cantidad de Ge en las muestras.

Además, las curvas de color negro y roja muestran que la variación entre los valores experimentales y calculados para diferentes fracciones de Ge están muy es pequeño; en especial para las muestras lavadas químicamente con HCl diluido. La desviación entre la curva calculada y los valores experimentales que se observa para las muestras no lavadas es debido a la presencia de las fases secundarias.

4.2 Películas de $Cu_2ZnSn_{1-x}Ge_xS_4$

El estudio de las propiedades de transporte (resistividad eléctrica ρ, concentración de portadores *p* y movilidad de portadores μ) de las nanopartículas de CZTGS son importantes parámetros que definen sus aplicaciones en dispositivos optoelectrónicos, como celdas solares. Las nanopartículas se depositaron mediante recubrimiento por centrifugación (*spin–coating*), usando el método descrito en la sección 3.3. Para medir la conductividad eléctrica y el coeficiente Hall de las películas a temperatura del ambiente, se utilizó la configuración de 4 puntas van der Pauw. En la **Figura 4.2.1(a)** se puede observar la fotografía de una película de CZTGS depositada sobre vidrio con los contactos equidistantes de plata sobre el portamuestra que fue utilizado para realizar mediciones eléctricas. El espesor promedio de las películas utilizadas para mediciones eléctricas es 2.34 ± 0.44 μm para nanopartículas no lavadas y 2.21 ± 0.66 μm para nanopartículas lavadas químicamente.

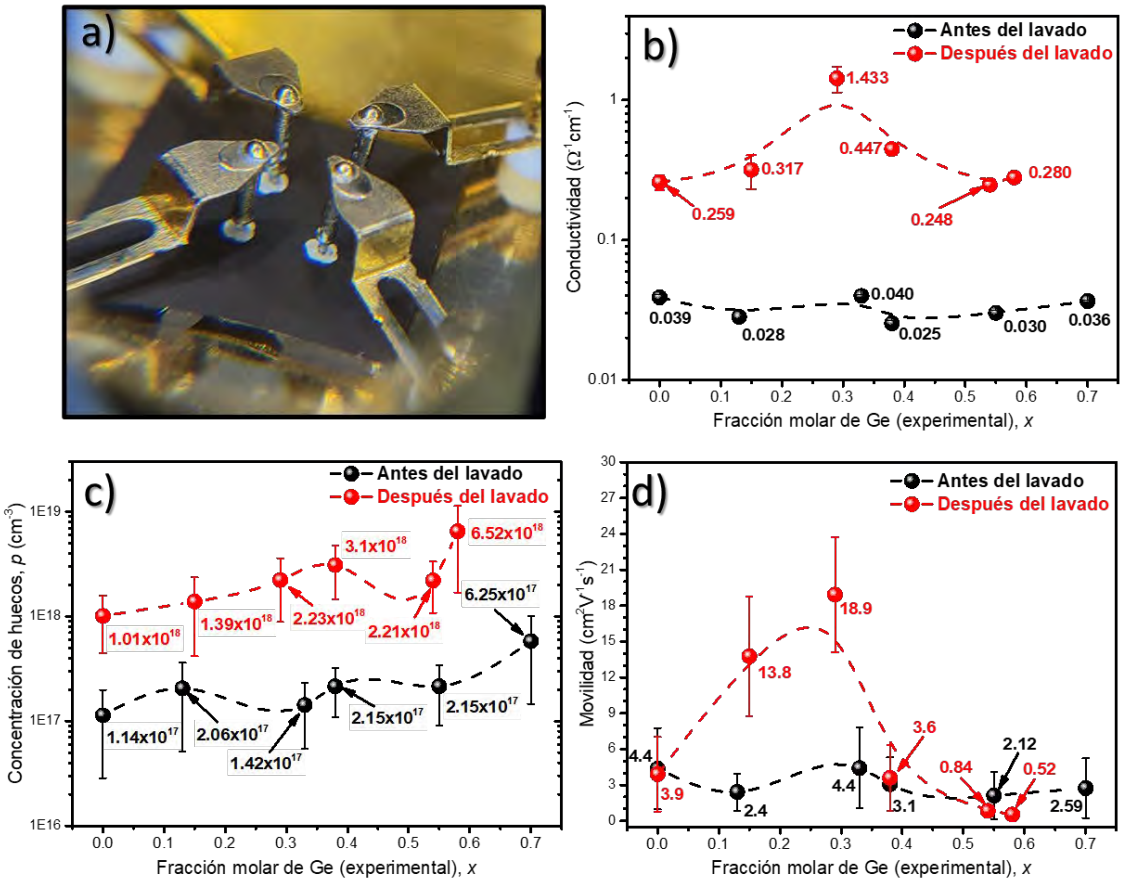

Figura 4.2.1: Imagen fotográfica mostrando una muestra de película de CZTGS con contactos de plata sobre el portamuestras usado para medir coeficiente Hall y resistividad (a). Variación de la conductividad eléctrica (b), concentración de portadores (c) y movilidad de portadores (d) de las películas de CZTGS preparadas con las muestra no lavadas y lavadas con HCl diluido.

Como se puede ver en la **Figura 4.2.1(b)**, la conductividad eléctrica de las películas preparadas con las nanopartículas no lavadas no presenta una variación substancial conforme se incrementa la fracción molar nominal de Ge. Sin embargo, para las películas preparadas con las nanopartículas lavadas químicamente, la conductividad eléctrica es mayor que sus contrapartes no lavadas para todas las concentraciones de Ge. El incremento en la conductividad eléctrica para las películas preparadas con nanopartículas lavadas probablemente se debe a la eliminación de fases secundarias presentes en las muestras no lavadas. Es importante aclarar que para ambos grupos de muestras (lavadas y no lavadas) no se detectó la presencia de ninguna fase secundaria como $Cu_{2-x}S$ o Cu_2SnS_3 en sus patrones difracción de rayos-X o en sus espectros Raman. Por lo tanto, el cambio en la conductividad

debe ser asociado a la remoción de la fase ZnS desde las nanopartículas por lavado con la solución HCl.

Todas las muestras revelaron un voltaje Hall positivo, indicando que a temperatura del ambiente la conductividad es de tipo-p (huecos). En la sección 2.1 se describió que una propiedad intrínseca del CZTS es la conductividad tipo-p debido a la presencia de los defectos de antisitios Cu_{Zn} y vacancias de Cu (V_{Cu}), los cuales forman un nivel aceptor cerca de la VBM [26], [153]–[155]. En la **Figura 4.2.1(c)**, se puede observar que todas las películas preparadas con nanopartículas sin y con lavado, la concentración de huecos incrementa desde $1.14x10^{17}$ hasta $6.25x10^{17}$ cm^{-3} conforme se incrementa la fracción molar de Ge. El incremento en la concentración de huecos en las películas puede ser asociado al aumento en la concentración de defectos de antisitio de Cu_{Zn} en las nanopartículas ocasionado por la incorporación gradual del Ge. El aumento en la concentración de defectos de antisitio Cu_{Zn} se describió en el análisis de espectroscopía Raman de las nanopartículas (**Figura 4.1.7**). Por otro lado, podemos observar que la concentración de huecos de las películas preparadas con nanopartículas con lavado químico es casi un orden mayor (desde 10^{17} hasta 10^{18} cm^{-3}) con respecto de las películas preparadas con nanopartículas sin lavado. El aumento en la concentración de huecos se debe a una alta concentración de defectos antisitios como Cu_{Zn}, que concuerda con los resultados obtenidos por la espectroscopía de reflectancia difusa de las nanoestructuras (**Figura 4.1.8**).

Por otro lado, la movilidad de los portadores en las películas preparadas con nanopartículas no lavadas no tiene una variación significativa con la variación de la fracción molar de Ge (**Figura 4.2.1(d)**). La insensibilidad de la movilidad con la fracción molar de Ge en las películas preparadas con nanopartículas no lavadas es probablemente debido a la formación de la fase ZnS en las partículas conforme el incremento de la cantidad de Ge, el cual es un material aislante. El resultado que se espera es un incremento en la movilidad de portadores cuando la fase de ZnS sea removida. Sin embargo, las películas preparadas con nanopartículas lavadas con HCl diluido mejora la movilidad hasta $x \sim 0.3$. Para mayores contenidos de Ge ($x \geq 0.4$) en las películas, la movilidad de portadores decrece desde 3.6 hasta 0.52 $cm^2V^{-1}s^{-1}$. La reducción observada en la movilidad de portadores para las películas con alto contenido de Ge puede ser debido a la remoción (o eliminación) de la fase Cu_8GeS_6,

el cual se ha sido reportada como un semiconductor tipo-p con alta movilidad de portadores (~16 $cm^2V^{-1}s^{-1}$) cuando el compuesto presenta defectos [156]. Además, el Cu_8GeS_6 formado en las muestras son granos muy grandes debido a que los picos de difracción (alrededor de $2\theta = 43.73°$) asociados a esta fase son estrechos (presenta una pequeña FWHM). Eliminación de estos granos grandes de Cu_8GeS_6 desde las nanopartículas preparadas con altos contenidos de Ge ($x > 0.4$) reduce la movilidad de los portadores, como fue observado en las películas preparadas con nanopartículas kesteritas lavadas con HCl diluido (**Figura 4.2.1(d)**). Por otro lado, la reducción en la movilidad de los portadores para las muestras con altos valores de "x" ($x > 0.3$) probablemente debido a su alta concentración de portadores, el cual induce un esparcimiento de portadores (*carrier scattering*) en la muestra, incluso a la temperatura del ambiente.

4.3 Celdas de perovskita

En esta sección de la tesis se presentan los resultados obtenidos del ensamble de las celdas solares de perovskita usando el material convencional spiro-OMeTAD y las nanopartículas de CZTGS como HTL. Para las celdas solares de perovskita fabricadas usando CZTGS como HTL se utilizaron 3 muestras con diferentes concentraciones de Ge (x= 0.0, 0.30 y 0.60) y lavadas químicamente con HCl diluido para estudiar el comportamiento de los parámetros fotovoltaicos y la estabilidad de la celda. Por conveniencia, la capa de perovskita $(FAPbI_3)_{0.83}(MAPbBr_3)_{0.17}$ se nombrará FAMA, y las celdas fabricadas utilizando spiro-OMeTAD como HTL se llamará como spiro. Las celdas fabricadas con HTL de CZTGS con diferentes contenidos de Ge se representarán como celdas x= 0.00, 0.30 y 0.60.

4.3.1 Caracterización de las capas ETL, perovskita FAMA y HTL

En esta sección se presenta una serie de caracterizaciones que se hicieron a las capas que conforman la celda solar de perovskita (PSC) fabricada en este trabajo. Para estudiar la estructura cristalina de la perovskita FAMA se realizó mediciones de difracción de rayos-X de las películas depositas en las diferentes etapas de ensamblado de la PSC. En la **Figura 4.3.1** se observa que en la capa ETL se tiene la formación del TiO_2 al presentar un pico de difracción posicionado en 25.47°. La siguiente capa en el ensamble es la perovskita FAMA.

Su patrón de difracción reveló picos bien definidos ubicados en 14.28, 20.11, 24.63, 28.56, 31.98, 35.13, 40.73 y 43.30°, los cuales corresponden a la formación de la perovskita combinada $(FAPbI_3)_{1-x}(MAPbBr_3)_x$ (cuando x > 0.10) [157]. Sin embargo, se detectó el pico característico atribuido a la presencia residual de PbI_2 al 12.77º. El impacto de la formación PbI_2 residual en la perovskita de doble catión se encuentra bajo discusión debido a la dificultad de determinar exactamente cuál es su efecto sobre las prestaciones del dispositivo [158]–[160]. Es importante aclarar que la estabilidad de las celdas que se reportan en este trabajo podría mejorar eliminando este PbI_2 residual. Por otro lado, en los patrones de difracción de las películas de spiro y CZTS depositadas sobre FAMA, los picos asociados a la perovskita FAMA no presentan ningún cambio en la posición o en la anchura media altura (*full width at half maximum*, FWHM), lo que indica que la perovskita no presentó ningún cambio estructural.

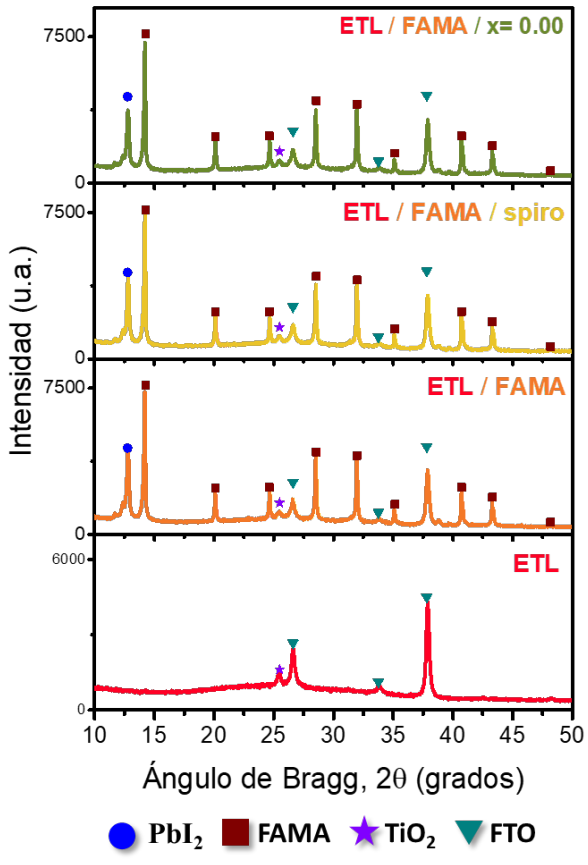

Figura 4.3.1: Patrones de difracción de rayos-X de las películas que conforman a una celda solar de perovskita FAMA.

En la **Figura 4.3.2** se presenta los espectros de absorción de las películas que conforman a una PSC junto con el espectro de fotoluminiscencia de la película de perovskita FAMA. En todos los espectros de absorción se observa un borde de absorción posicionado en ~754 nm (1.64 eV), el cual, corresponde a la FAMA para todas las muestras. Por otro lado, se puede observar que el borde de absorción coincide con la banda de fotoluminiscencia de la perovskita correspondiente a la transición banda – banda [157]. Adicionalmente, se puede apreciar que existe una mayor absorción de la muestra que tiene el x= 0.00. Esto se debe principalmente a que la película de CZTS contribuye a la absorción de la luz incidente. Sin embargo, no se aprecia el borde de absorción del CZTS (1.42 eV) debido a que la capa del CZTS puede tener un espesor muy delgado en comparación con la perovskita FAMA [9].

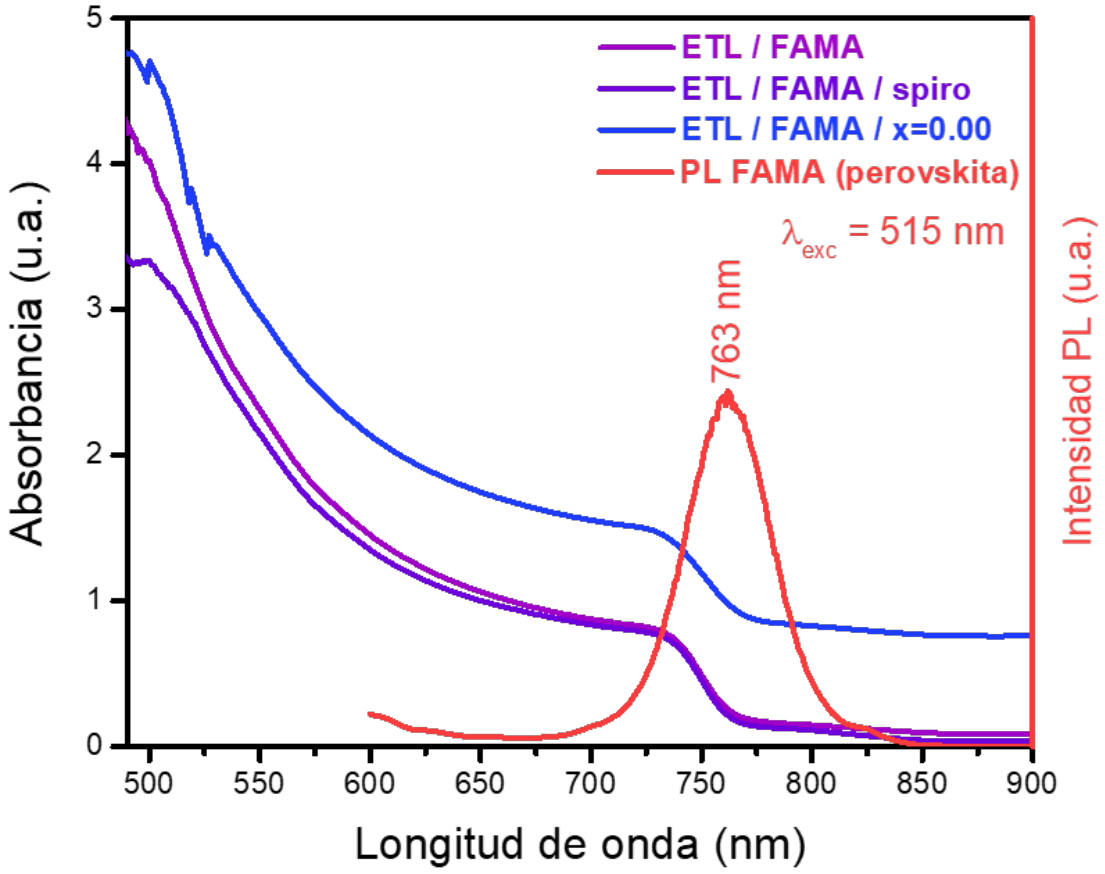

Figura 4.3.2: Espectro de absorción de las películas que conforman a una celda solar de perovskita junto con el espectro de fotoluminiscencia de una película de perovskita FAMA.

De los resultados obtenidos de la caracterización de difracción de rayos-X y de espectroscopía óptica, se puede decir que la formación de la perovskita FAMA sobre la ETL es exitosa y no tiene ninguna modificación estructural al depositar la capa HTL. En la **Figura 4.3.3** se presenta una imagen SEM típica de la sección transversal de las capas ensambladas utilizando CZTS (x= 0.00) como HTL. La formación de la capa c-TiO_2 sobre el FTO se aprecia homogénea con un espesor de 57.76 ± 4.2 nm. Por otro lado, la capa de m-TiO_2 depositada sobre la capa de c-TiO_2 se observa uniformidad y que la perovskita se encuentra inmersa en la capa. Las capas de m-TiO_2 y perovskita FAMA tienen espesores aproximados de 233.54 ± 12.8 nm y 404.04 ± 26.1 nm, respectivamente. Sin embargo, en la capa de perovskita FAMA no se alcanza a visualizar los granos grandes debido a un problema de acumulación de carga que no se pudo solucionar. Encima de la perovskita FAMA se observa la capa de CZTS fabricada con los tintes de nanopartículas. El espesor aproximado de la HTL es de 160.37 ± 16.6 nm, que encuentra por arriba de lo óptimo reportado para una capa de CZTS como HTL (~100 nm) [42]. Adicionalmente, en esta capa se alcanza a observar que las nanopartículas de CZTS conservan la misma morfología que se presentó en la **Figura 4.1.5**.

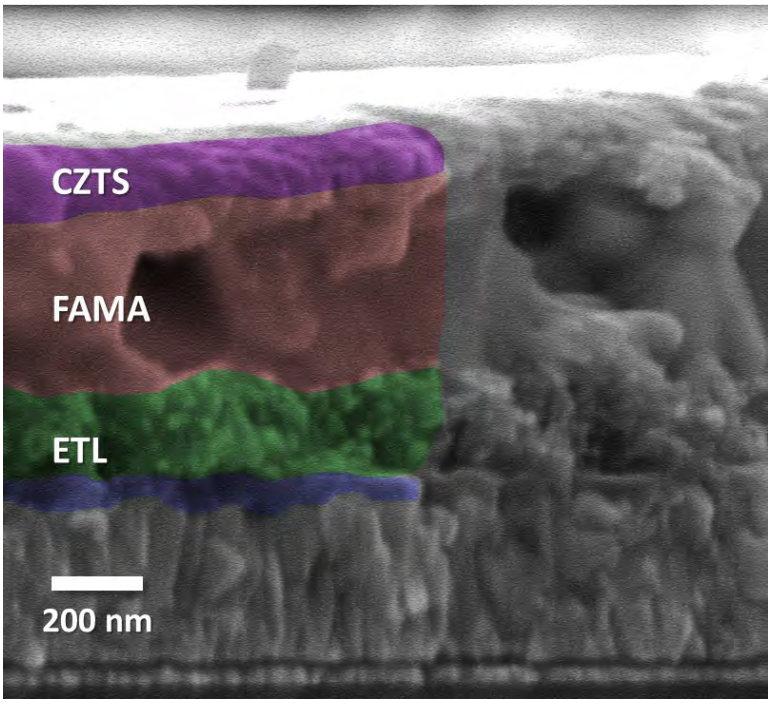

Figura 4.3.3: Imagen SEM típica de la sección transversal del ensamble de películas que conforman a una celda solar de perovskita utilizando CZTS (x= 0.00) como HTL.

4.3.2 Eficiencia y reproducibilidad de la celda de perovskita

La medición de las curvas J – V para las PSCs fabricadas y la obtención de los parámetros fotovoltaicos se realizaron aplicando la metodología descrita en la sección **3.5.8.** Primeramente, se ensamblaron PSCs utilizando spiro como HTL para optimizar el proceso de fabricación y revisar la reproducibilidad de la metodología implementada. En la **Figura 4.3.4(a)**, se presentan los parámetros fotovoltaicos promedio obtenidos de las mediciones de 6 celdas. En los valores presentados se puede visualizar que la dispersión es baja, indicando una alta reproducibilidad de la metodología utilizada para la fabricación de las PSCs. Por otro lado, en la **Figura 4.3.4(b)** se presenta una curva J – V representativa, junto con sus valores de parámetros fotovoltaicos, de una PSC utilizando spiro como HTL.

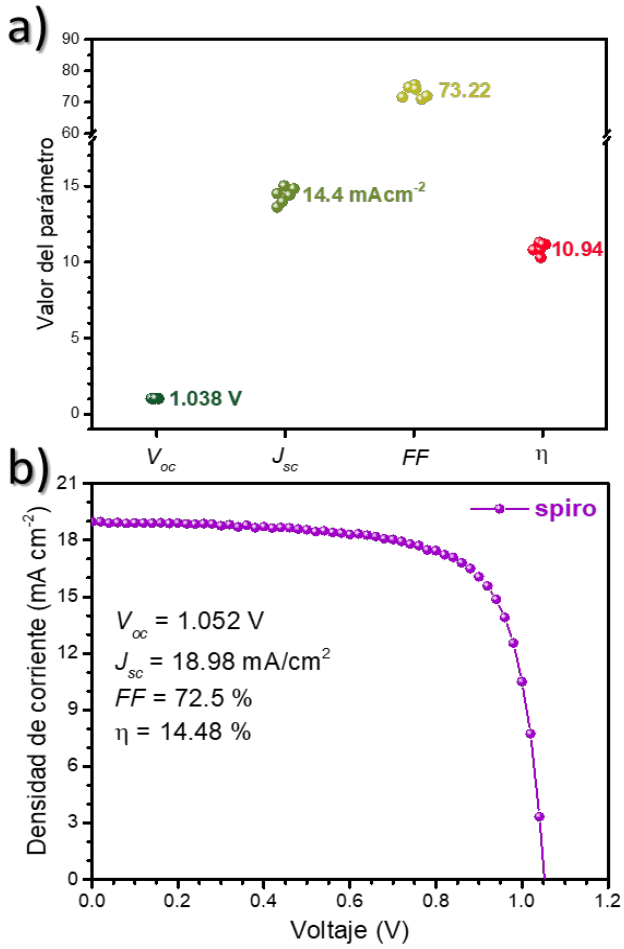

Figura 4.3.4: Parámetros fotovoltaicos obtenidos de las PSCs utilizando spiro como HTL (a) y una curva típica de densidad de corriente – voltaje para una PSC (b).

4.3.3 Celdas de perovskita utilizando $Cu_2ZnSn_{1-x}Ge_xS_4$ como HTL

En la **Figura 4.3.5**, se presenta los parámetros fotovoltaicos promedio obtenidos para las mediciones de 3 celdas por cada grupo de celdas. Como se puede ver en **Figura 4.3.5,** los valores de los parámetros fotovoltaicos presentan una dispersión baja, indicando que la reproducibilidad de la metodología utilizando CZTGS como HTL para fabricar las PSCs se encuentra dentro de un rango aceptable. En la **Tabla 4.3.1** se presentan los valores fotovoltaicos promedio de las celdas fabricadas en este trabajo junto con los trabajos experimentales publicados usando el CZTS como HTL para PSC. En la **Figura 4.3.6(a)** se presenta las curvas J – V de las PSCs fabricadas utilizando $Cu_2ZnSn_{1-x}Ge_xS_4$ (x= 0.00, 0.30

y 0.60) como HTL. Los parámetros fotovoltaicos obtenidos de las curvas J – V se resumen en la **Tabla 4.3.2**. En las curvas J – V de las celdas que contiene Ge en su HTL se puede observar una deflexión (en el rango de 0.0 – 0.4 V) que puede deberse a que la extracción de la corriente fotogenerada es limitada. Este efecto se observa solo en las celdas que contiene Ge en la HTL, por lo que posiblemente se deba al aumento de los defectos de antisitio Cu_{Zn} (recordando que el Cu en esa posición cristalográfica tiene estado de oxidación 2+) en la superficie de las nanopartículas, limitando el movimiento de las cargas fotogeneradas; lo cual concuerda con los resultados discutidos en la sección anterior sobre las nanopartículas de CZTGS. Esto puede generar una extracción de carga más lenta que limita la corriente colectada, como se ha observado cuando existe desplazamiento de carga como consecuencia de barridos de voltaje lentos en las celdas solares de perovskita [161].

Tabla 4.3.1: Resumen de investigaciones experimentales realizadas sobre CZTS como HTL en PSC.

Año	HTL	Perovskita	Configuración	V_{oc} (V)	J_{sc} (mA/cm^2)	*FF* (%)	η (%)	Estabilidad	Ref.
2023	NPs CZTGS kesterita x= 0.00	FAMA	n-i-p mesoporosa	0.888	10.92	60.9	5.88	**360 h pierde 20%**	**Este trabajo**
	NPs CZTGS kesterita x= 0.30			0.948	13.21	60.1	7.48		
	NPs CZTGS kesterita x= 0.60			0.770	4.83	69.1	2.56		
2015	NPs CZTS kesterita	$MAPbI_3$	n-i-p planar	1.06	20.5	59	12.8	No reporta	[9]
2016	NPs CZTS kesterita	$MAPbI_3$	n-i-p mesoporosa	0.95	18.8	61	10.7	No reporta	[41]
	NPs CZTSe kesterita			0.81	19.4	62	9.7		
	NPs CZTS kesterita con ligante		n-i-p planar	0.92	20.7	81	15.4		[10]
	NPs CZTS kesterita sin ligante			0.88	18.1	77	12.2		

2018	NPs CZTS kesterita	$MAPb_{1-x}Sn_xI_{3-y}Cl_y$	n-i-p planar	0.76	19.2	63	9.2	360 h pierde 95%[a]	[11]
2019	NPs CZTS kesterita	$MAPbI_3$	p-i-n planar	0.82	9.7	76	6	43 días pierde 20%[a]	[42]
	NPs CZTS kesterita	$CsPbBr_3$	n-i-p mesoporosa	0.94	7.36	70	4.84	2500 h pierde 5%	[12]
2020	NPs CZTS kesterita	$MAPbI_3$	n-i-p mesoporosa	0.91	19.4	53	9.3	96 días pierde 40%[c]	[162]
	NPs CZTS kesterita			0.938	21.72	63	12.9	60 días pierde 2%	[13]
	NPs CZTS kesterita			0.98	18.31	61	10.9	30 días pierde 15%	[163]
	CZTS:Cd[b]		n-i-p planar	1.14	23.04	77	20.2	500 h pierde 10%	[43]
2021	CZTSe[d]	$MAPbI_3$	p-i-n planar	1.03	17.9	73	13.5	350 h pierde 20%	[164]

[a] Almacenada en atmosfera de N_2

[b] Película delgada

[c] Almacenada en oscuridad

[d] Película delgada y doble HTL

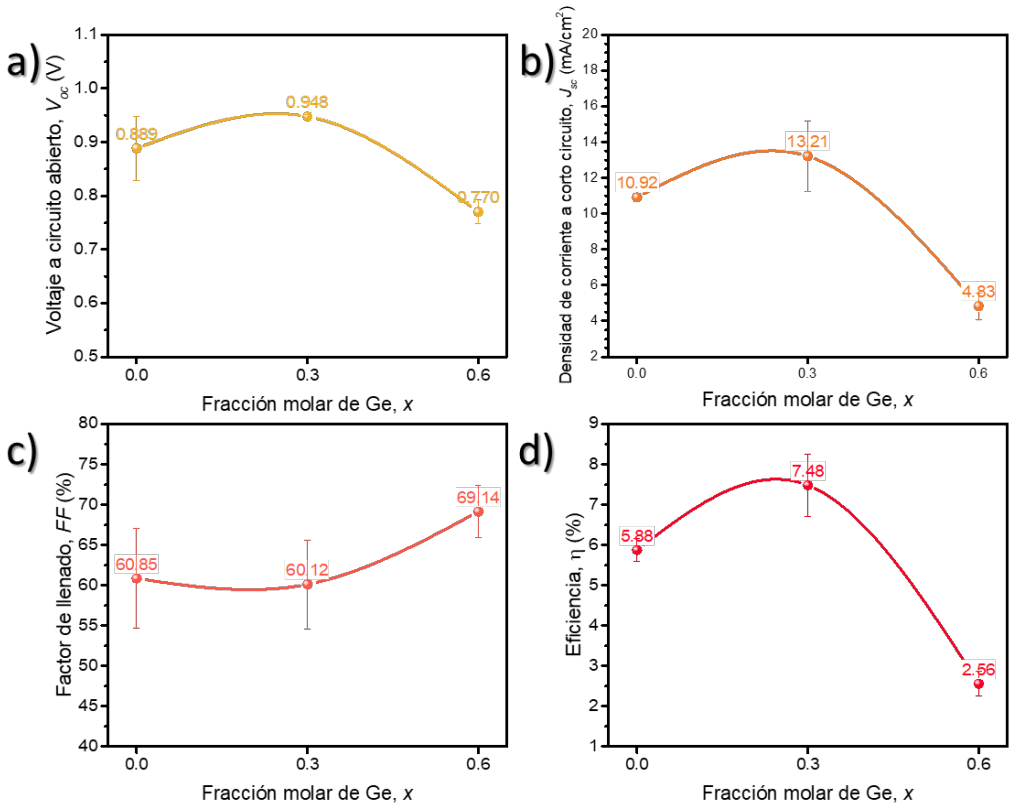

Figura 4.3.5: Parámetros fotovoltaicos obtenidos de las PSCs utilizando $Cu_2ZnSn_{1-x}Ge_xS_4$ como HTL usando diferentes concentraciones de Ge: x= 0.00, 0.30 y 0.60.

Como se puede ver en la **Tabla 4.3.2**, la PSC fabricada utilizando x=0.00 presenta V_{oc} de 0.821 V, una J_{sc} de 10.64 mA/cm^2, un FF de 67.62 % y una eficiencia de 5.91 %, los cuales son comparables con los valores reportados (ver **Tabla 4.3.1**). Todos los valores de los parámetros fotovoltaicos de la PSC con x= 0.30 incrementaron en comparación con la PSC que no tiene Ge en la capa HTL. Como se observó en la **Figura 4.1.8**, el valor de la energía de banda prohibida de las nanopartículas incrementó conforme aumentaba la concentración de Ge en la muestra. Además, se abordó la explicación de que los bordes de la banda de valencia y la banda de conducción están conformados por los orbitales Cu-3d y Sn-5s, respectivamente. Por lo tanto, se espera que conforme se incorpora el Ge en la muestra, el mínimo de la banda de conducción (*conduction band mínimum*, CBM) tenga un corrimiento que a consecuencia incremente el valor de la energía de banda prohibida del material. El incremento en el valor de la energía de la banda prohibida se observa claramente en la sección 4.1 cuando se discute los resultados de reflectancia difusa de las nanopartículas.

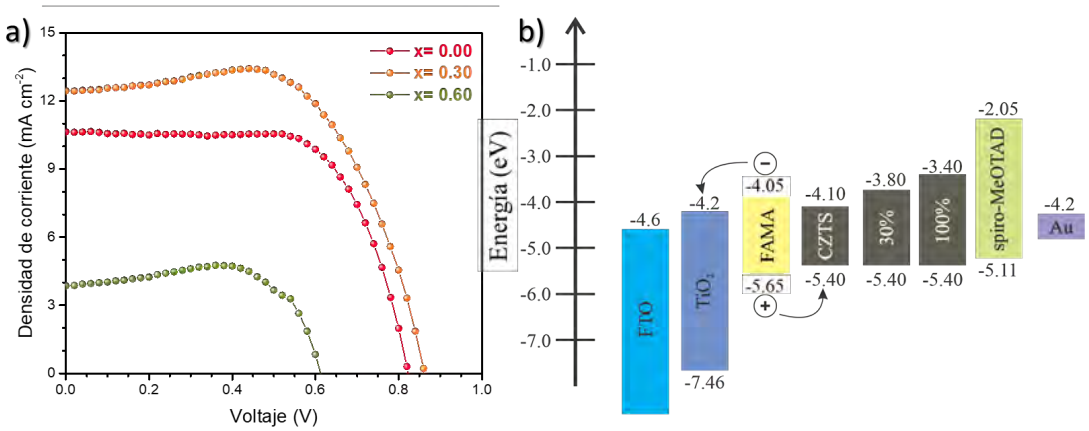

Figura 4.3.6: Curvas J – V típicas de las PSC utilizando CZTGS como HTL (a). Representación esquemática de los diagramas de bandas de los materiales que conforman a la PSC (b) [115].

En la **Figura 4.3.6(b)** se presenta una representación esquemática de la alineación de las bandas de los materiales que conforman a una PSC. En el diagrama de alineación de las bandas podemos observar que la interfaz de la perovskita y la capa HTL de CZTS favorece a la existencia de posibles recombinaciones de los portadores. Entonces, con el incremento de la energía de la banda prohibida esperamos reducir la recombinación de portadores y aumentar las prestaciones de la PSC [44]. Por lo tanto, el ligero aumento en el V_{oc} que se observa para la muestra x= 0.30, se debe a reducir las recombinaciones en la interfaz de la perovskita y el HTL. Mientras que la J_{sc} presenta una mejora debido a incrementar el valor de la energía de banda prohibida del CZTS de 1.42 eV (x= 0.00) a 1.57 eV (x= 0.30). Sin embargo, para la PSC con x= 0.60 se observa que los valores disminuyen abruptamente, debido a que la película fabricada con estas nanopartículas presenta una movilidad de portadores muy baja debido una alta concentración de defectos. La explicación de la baja movilidad de portadores y el aumento de los defectos se discutió en las propiedades eléctricas de la sección 4.2 (**Figura 4.2.1**).

Tabla 4.3.2: Parámetros fotovoltaicos de las mejores PSC fabricadas con $Cu_2ZnSn_{1-x}Ge_xS_4$ (x= 0.00, 0.30 y 0.60) como HTL.

Muestra (valor de "*x*")	V_{oc} (V)	J_{sc} (mA/cm2)	P_{max} (mW)	*FF* (%)	η (%)
0.00	0.821	10.64	0.186	67.62	5.91
0.30	0.861	12.42	0.223	66.33	7.10
0.60	0.611	3.86	0.059	78.73	1.86

En la **Figura 4.3.7** se presenta la eficiencia cuántica de las celdas fabricadas. En todos los casos, para una mejor comparación, las curvas fueron normalizadas a su punto máximo. La celda de perovskita fabricada usando spiro presenta una EQE típica para este tipo de celdas. Esto es indicativo que la celda de perovskita fabricada usando spiro presenta una buena colección y extracción de carga, y una baja recombinación de portadores. Por otro lado, la celda que utiliza CZTGS como HTL presenta perdidas a longitudes de onda mayores a 500 nm en comparación con la celda convencional (spiro). La pérdida puede deberse a una extracción de carga deficiente ocasionado por la HTL en la frontera con la perovskita y una recombinación de portadores muy rápida en comparación con la celda de spiro como HTL. Sin embargo, se puede observar que en la región de 400 – 800 nm para la celda que usa CZTGS con x= 0.30 incrementa el valor de la EQE, en comparación con las celdas x= 0.00 y 0.60. El aumento en la EQE de la celda x= 0.30 se debe al incremento en la banda prohibida del CZTGS (**Figura 4.1.8**) desde 1.42 eV (x= 0.00) a 1.57 eV (x= 0.30) y consecuentemente se aumenta el J_{sc} (ver **Tabla 4.3.2**). Adicionalmente, la celda con x= 0.30 presenta una recombinación más lenta debido a la reducida recombinación en la interfaz de la perovskita y la HTL, como se describió en los resultados de las curvas J – V.

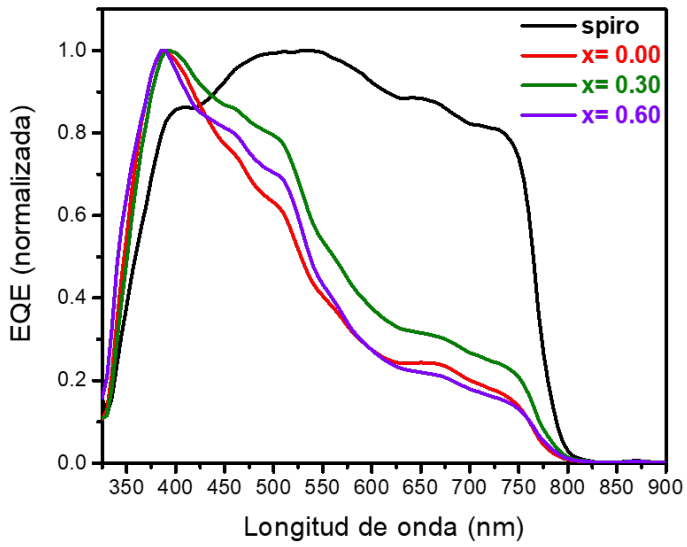

Figura 4.3.7: Espectro de eficiencia cuántica externa para las celdas solares fabricadas con diferentes HTL medidos bajo condiciones ambientales normales (humedad relativa de 35% a temperatura del ambiente) junto con la fotocorriente calculada a partir de la curva EQE de cada celda.

Adicionalmente, se investigó la estabilidad de los dispositivos fabricados, exponiéndolos a las condiciones ambientales del laboratorio (21 °C con 35% de humedad relativa). En la **Figura 4.3.8** se presenta el añejamiento prologando de las PSCs fabricadas utilizando spiro, x= 0.00, x= 0.30 y x= 0.60 como HTL y compararlo con el añejamiento de una celda convencional (spiro) y sin HTL. La eficiencia de la PSC sin HTL decae hasta un 80 % en las primeras 45 h y posterior a ese periodo el dispositivo degradado presenta una eficiencia cercana a cero. Mientras que la PSC fabricada con spiro durante las primeras 45 h únicamente pierde el 20 % de su eficiencia inicial y lentamente se degrada hasta perder el 50 % de su eficiencia inicial después de 315 h transcurridas. Por otro lado, las celdas fabricadas con CZTGS permanecen estables durante todo el proceso de añejamiento después de 315 h de exposición a las condiciones del ambiente. En la prueba de estabilidad de las celdas se puede observar que la eficiencia aumenta ligeramente al transcurso de ~80 h. De acuerdo con el trabajo de Zhu *et al*. [159], el aumento en la eficiencia de las celdas al transcurrir el tiempo es debido a la presencia del PbI_2 residual en las celdas. El PbI_2 se encuentra en la superficie de los granos de la perovskita FAMA ocasionando que los defectos superficiales sean pasivados, como consecuencia se registra un ligero aumento en la eficiencia de la celda y posteriormente continua con el comportamiento de degradación. En la **Figura 4.3.8**, se puede apreciar las imágenes fotográficas de las PSCs después del tiempo de añejamiento (315 h), donde se ve claramente como la celda fabricada con spiro presenta una coloración diferente por los bordes y en el centro, asociada a la degradación de la perovskita.

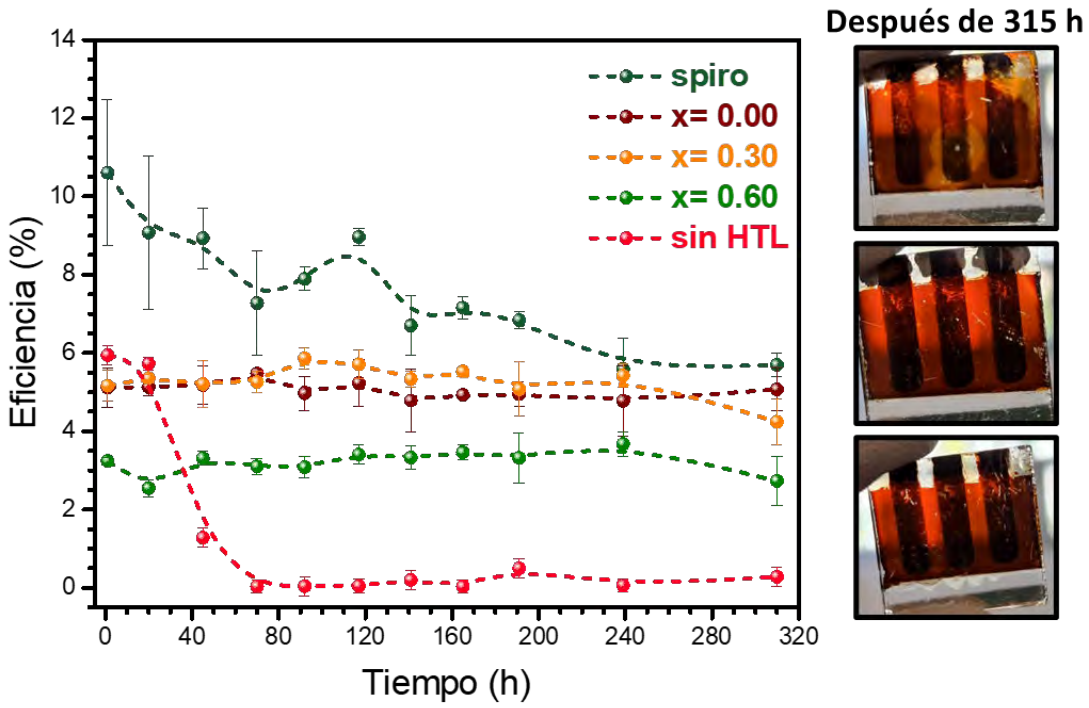

Figura 4.3.8: Añejamiento de las PSCs durante 315 h expuestas a las condiciones ambientales del laboratorio (21 °C y 35% de humedad relativa. A la derecha se presenta imágenes fotográficas de las PSCs después del periodo de añejamiento.

La perovskita $FAPbI_3$ tiene una transición espontanea a temperatura ambiente de la fase perovskita α-$FAPbI_3$ (color negro) a la no-perovskita δ-$FAPbI_3$ (color amarillo). La transición de fase induce una caía rápida en la prestación de los dispositivos [157]. Entonces para mitigar esta transición de fase se fabrica la perovskita FAMA, que está compuesta de la incorporación de la perovskita $MAPbBr_3$ en la perovskita $FAPbI_3$. Entonces, la coloración del color rojizo a un color amarillo (ver **Figura 4.3.8**) representa que la perovskita FAMA se está degradando lentamente a la fase δ-$FAPbI_3$. Esta degradación ocurre debido a que el spiro también se oxida y degrada lentamente al exponerse al ambiente, efecto que no ocurre con la película de CZTGS. Por lo tanto, con estos resultados podemos decir que las PSCs fabricadas con CZTGS, como HTL, mejoran los valores fotovoltaicos cuando se incorpora únicamente 30 % de Ge (x= 0.30), mientras que la estabilidad a la exposición ambiental es superior debido a que no reacciona con el ambiente y forma una capa protectora para la perovskita.

Capítulo 5 – Conclusiones

La metodología implementada en el trabajo de investigación de la tesis doctoral llevó a la obtención nanopartículas de CZTGS sintetizadas mediante el método de hidrotermal que se caracterizaron por las técnicas de SEM, TEM, EDS, XRD, espectroscopía Raman y espectroscopía UV-Vis. Además, se presenta un proceso de purificación para obtener fase kesterita pura de las nanopartículas de CZTGS y cómo cambian las propiedades eléctricas del CZTGS. Con los resultados obtenidos de la caracterización de las nanopartículas permitieron la aplicación como HTL en una celda solar de perovskita. Las celdas solares de perovskita presentaron una mejora en los parámetros fotovoltaicos cuando el HTL contenía un 30% de Ge en las nanopartículas (x= 0.30). Las celdas de perovskita fabricadas usando CZTGS como HTL presentaron mayor estabilidad a las condiciones ambientales que las celdas convencionales. A partir de los resultados obtenidos en este trabajo de investigación se puede concluir lo siguiente:

- Por un método hidrotermal de temperatura relativamente baja, se puede fabricar nanopartículas cuasi-esféricas de $Cu_2ZnSn_{1-x}Ge_xS_4$ (CZTGS), con tamaño promedio entre 12.5 y 11.3 nm con fase predominante kesterita.
- La alta incorporación de Ge en la estructura kesterita de las nanopartículas de CZTGS induce a la formación de las fases secundarias de ZnS y Cu_8GeS_6, presentando un límite de incorporación (~x= 0.5).
- Las fases secundarias formadas en las nanopartículas de CZTGS se puede removerse de manera exitosa por un tratamiento químico sencillo, como tratamiento con una solución HCl diluido a 80 °C.
- El lavado químico propuesto no afecta la estructura de la kesterita, ni la morfología y el tamaño de las nanopartículas de CZTGS.
- La incorporación del Ge en las nanopartículas de CZTGS aumenta la concentración del defecto de antisitio Cu_{Zn}, el cual, reduce la energía de la banda prohibida y aumenta la concentración de los portadores (huecos).

- La incorporación de Ge (x= 0.30) en la capa transportadora de huecos mejora las prestaciones de la celda de perovskita debido a aumentos de la movilidad de portadores, el ancho de banda prohibida y a la disminución de la recombinación en la interfaz perovskita/CZTGS.

- Las celdas solares de perovskita ensambladas con CZTGS como capa transportadora de huecos presentan una mayor estabilidad a la exposición ambiental (temperatura, oxígeno y humedad) que la celda de perovskita convencional (spiro).

Sin embargo, es necesario investigar más la interfaz entre el material CZTGS y la perovskita para comprender los mecanismos de transferencia de carga y la razón por la limitada extracción de los portadores fotogenerados, el cual afecta la corriente a corto circuito de los dispositivos fotovoltaicos. Adicionalmente, es necesario seguir optimizando el espesor y la homogeneidad de la película de CZTGS sobre la perovskita para mejorar la eficiencia de la celda solar de perovskita.

Referencias

[1] International Energy Agency, "World energy balances: an overview of global trends", 2017. Consultado: el 7 de enero de 2018. [En línea]. Disponible en: http://www.iea.org/t&c/

[2] L. F. Cabeza, K. G. Terry Hollands, A. Jäger-Waldau, M. Kondo, C. Konseibo, V. Meleshko, W. Stein, Y. Tamaura, H. Xu, y R. Zilles, "Direct Solar Energy", en *IPCC Special Report on Renewable Energy Sources and Climate Change Mitigation*, E. Calvo y J. Schmid, Eds. United Kingdom and New York, 2011, pp. 337–391. Consultado: el 1 de enero de 2023. [En línea]. Disponible en: http://www.ipcc.ch/pdf/special-reports/srren/Chapter 3 Direct Solar Energy.pdf

[3] M. A. Iqbal, M. Malik, W. Shahid, S. Z. U. Din, N. Anwar, M. Ikram, F. Idrees, M. A. Iqbal, M. Malik, W. Shahid, *et al.*, "Materials for Photovoltaics: Overview, Generations, Recent Advancements and Future Prospects", *Thin Films Photovoltaics*, ene. 2022, doi: 10.5772/INTECHOPEN.101449.

[4] A. Kojima, K. Teshima, Y. Shirai, y T. Miyasaka, "Organometal Halide Perovskites as Visible-Light Sensitizers for Photovoltaic Cells", *J Am Chem Soc*, vol. 131, núm. 17, pp. 6050–6051, may 2009, doi: 10.1021/ja809598r.

[5] M. Saliba, J. P. Correa-Baena, C. M. Wolff, M. Stolterfoht, N. Phung, S. Albrecht, D. Neher, y A. Abate, "How to Make over 20% Efficient Perovskite Solar Cells in Regular (n-i-p) and Inverted (p-i-n) Architectures", *Chemistry of Materials*, vol. 30, núm. 13, pp. 4193–4201, jul. 2018, doi: 10.1021/acs.chemmater.8b00136.

[6] T. Salim, S. Sun, Y. Abe, A. Krishna, A. C. Grimsdale, y Y. M. Lam, "Perovskite-based solar cells: impact of morphology and device architecture on device performance", *J Mater Chem A Mater*, vol. 3, núm. 17, pp. 8943–8969, may 2015, doi: 10.1039/C4TA05226A.

[7] National Renewable Energy Laboratory, "Best Research-Cell Efficiency Chart", 2022. https://www.nrel.gov/pv/cell-efficiency.html (consultado el 10 de noviembre de 2022).

[8] Y. Yang, N. D. Pham, D. Yao, H. Zhu, P. Yarlagadda, y H. Wang, "Inorganic p-type semiconductors and carbon materials based hole transport materials for perovskite solar cells", *Chinese Chemical Letters*, vol. 29, núm. 8, pp. 1242–1250, ago. 2018, doi: 10.1016/j.cclet.2018.05.008.

[9] Q. Wu, C. Xue, Y. Li, P. Zhou, W. Liu, J. Zhu, S. Dai, C. Zhu, y S. Yang, "Kesterite Cu_2ZnSnS_4 as a Low-Cost Inorganic Hole-Transporting Material for High-Efficiency Perovskite Solar Cells", *ACS Appl Mater Interfaces*, vol. 7, núm. 51, pp. 28466–28473, dic. 2015, doi: 10.1021/acsami.5b09572.

[10] L. S. Khanzada, I. Levchuk, Y. Hou, H. Azimi, A. Osvet, R. Ahmad, M. Brandl, P. Herre, M. Distaso, R. Hock, *et al.*, "Effective Ligand Engineering of the Cu_2ZnSnS_4 Nanocrystal Surface for Increasing Hole Transport Efficiency in Perovskite Solar Cells", *Adv Funct Mater*, vol. 26, núm. 45, pp. 8300–8306, dic. 2016, doi: 10.1002/adfm.201603441.

[11] S. B. Patel, A. H. Patel, y J. V. Gohel, "A novel and cost effective CZTS hole transport material applied in perovskite solar cells", *CrystEngComm*, vol. 20, núm. 47, pp. 7677–7687, 2018, doi: 10.1039/C8CE01337C.

[12] Z. Zhou, Y. Deng, P. Zhang, D. Kou, W. Zhou, Y. Meng, S. Yuan, y S. Wu, "Cu_2ZnSnS_4 Quantum Dots as Hole Transport Material for Enhanced Charge Extraction and Stability in All-Inorganic $CsPbBr_3$ Perovskite Solar Cells", *Solar RRL*, vol. 3, núm. 4, p. 1800354, abr. 2019, doi: 10.1002/solr.201800354.

[13] Y. Cao, H. Wu, W. Li, Z. Zhao, Z. Xiao, W. Zi, N. Cheng, J. Liu, y Y. Tu, "Cu_2ZnSnS_4 as an efficient hole transporting material for low temperature paintable carbon electrode based perovskite solar cells", *Org Electron*, vol. 76, p. 105455, ene. 2020, doi: 10.1016/j.orgel.2019.105455.

[14] M. H. Sharif, T. Enkhbat, E. Enkhbayar, y J. Kim, "Control of Defect States of Kesterite Solar Cells to Achieve More Than 11% Power Conversion Efficiency", *ACS Appl Energy Mater*, vol. 3, núm. 9, pp. 8500–8508, sep. 2020, doi: 10.1021/acsaem.0c01141.

[15] C. Platzer-Björkman, "Kesterite compound semiconductors for thin film solar cells", *Current Opinion in Green and Sustainable Chemistry*. 2017. doi: 10.1016/j.cogsc.2017.02.010.

[16] Y. Cao, M. S. Denny, J. v Caspar, W. E. Farneth, Q. Guo, A. S. Ionkin, L. K. Johnson, M. Lu, I. Malajovich, D. Radu, *et al.*, "High-Efficiency Solution-Processed $Cu_2ZnSn(S,Se)_4$ Thin-Film Solar Cells Prepared from Binary and Ternary Nanoparticles", *J Am Chem Soc*, vol. 134, núm. 38, pp. 15644–15647, sep. 2012, doi: 10.1021/ja3057985.

[17] S.-Y. Wei, Y.-C. Liao, C.-H. Hsu, C.-H. Cai, W.-C. Huang, M.-C. Huang, y C.-H. Lai, "Achieving high efficiency $Cu_2ZnSn(S,Se)_4$ solar cells by non-toxic aqueous ink: Defect analysis and electrical modeling", *Nano Energy*, vol. 26, pp. 74–82, ago. 2016, doi: 10.1016/j.nanoen.2016.04.059.

[18] D. Mora-Herrera, R. Silva-González, F. E. Cancino-Gordillo, y M. Pal, "Development of Cu_2ZnSnS_4 films from a non-toxic molecular precursor ink and theoretical investigation of device performance using experimental outcomes", *Solar Energy*, vol. 199, pp. 246–255, mar. 2020, doi: 10.1016/j.solener.2020.01.077.

[19] Y.-P. Lin, T.-E. Hsieh, Y.-C. Chen, y K.-P. Huang, "Characteristics of $Cu_2ZnSn(S_xSe_{1-x})_4$ thin-film solar cells prepared by sputtering deposition using single quaternary Cu_2ZnSnS_4 target followed by selenization/sulfurization treatment", *Solar Energy Materials and Solar Cells*, vol. 162, pp. 55–61, abr. 2017, doi: 10.1016/j.solmat.2016.12.042.

[20] I. G. Orletskyi, M. M. Solovan, V. v. Brus, F. Pinna, G. Cicero, P. D. Maryanchuk, E. v. Maistruk, M. I. Ilashchuk, T. I. Boichuk, y E. Tresso, "Structural, optical and electrical properties of Cu_2ZnSnS_4 films prepared from a non-toxic DMSO-based sol-gel and synthesized in low vacuum", *Journal of Physics and Chemistry of Solids*, vol. 100, núm. September 2016, pp. 154–160, 2017, doi: 10.1016/j.jpcs.2016.09.015.

[21] M. Kumar, A. Dubey, N. Adhikari, S. Venkatesan, y Q. Qiao, "Strategic review of secondary phases, defects and defect-complexes in kesterite CZTS–Se solar cells", *Energy Environ Sci*, vol. 8, núm. 11, pp. 3134–3159, 2015, doi: 10.1039/C5EE02153G.

[22] M. Grossberg, J. Krustok, C. J. Hages, D. M. Bishop, O. Gunawan, R. Scheer, S. M. Lyam, H. Hempel, S. Levcenco, y T. Unold, "The electrical and optical properties of kesterites", *Journal of Physics: Energy*, vol. 1, núm. 4, p. 044002, ago. 2019, doi: 10.1088/2515-7655/ab29a0.

[23] K. Pal, P. Singh, A. Bhaduri, y K. B. Thapa, "Current challenges and future prospects for a highly efficient (20%) kesterite CZTS solar cell: A review", *Solar Energy Materials and Solar Cells*, vol. 196, pp. 138–156, jul. 2019, doi: 10.1016/j.solmat.2019.03.001.

[24] S. Chen, L.-W. Wang, A. Walsh, X. G. Gong, y S.-H. Wei, "Abundance of Cu_{Zn} + Sn_{Zn} and $2Cu_{Zn}$ + Sn_{Zn} defect clusters in kesterite solar cells", *Appl Phys Lett*, vol. 101, núm. 22, p. 223901, nov. 2012, doi: 10.1063/1.4768215.

[25] S. Chen, A. Walsh, X.-G. Gong, y S.-H. Wei, "Classification of Lattice Defects in the Kesterite Cu_2ZnSnS_4 and $Cu_2ZnSnSe_4$ Earth-Abundant Solar Cell Absorbers", *Advanced Materials*, vol. 25, núm. 11, pp. 1522–1539, mar. 2013, doi: 10.1002/adma.201203146.

[26] D. Han, Y. Y. Sun, J. Bang, Y. Y. Zhang, H.-B. Sun, X.-B. Li, y S. B. Zhang, "Deep electron traps and origin of p-type conductivity in the earth-abundant solar-cell material Cu_2ZnSnS_4", *Phys Rev B*, vol. 87, núm. 15, p. 155206, abr. 2013, doi: 10.1103/PhysRevB.87.155206.

[27] X. Lv, C. Zhu, H. Hao, R. Liu, Y. Wang, y J. Wang, "Improving the performance of low-cost water-based solution-synthesised $Cu_2ZnSn_{1-x}Ge_x(S,Se)_4$ absorber thin films by germanium doping", *Ceram Int*, vol. 46, núm. 16, pp. 25638–25645, nov. 2020, doi: 10.1016/j.ceramint.2020.07.039.

[28] S. Kim, K. M. Kim, H. Tampo, H. Shibata, K. Matsubara, y S. Niki, "Ge-incorporated $Cu_2ZnSnSe_4$ thin-film solar cells with efficiency greater than 10%", *Solar Energy Materials and Solar Cells*, vol. 144, pp. 488–492, 2016, doi: 10.1016/j.solmat.2015.09.039.

[29] M. Neuschitzer, M. E. Rodriguez, M. Guc, J. A. Marquez, S. Giraldo, I. Forbes, A. Perez-Rodriguez, y E. Saucedo, "Revealing the beneficial effects of Ge doping on $Cu_2ZnSnSe_4$ thin film solar cells", *J Mater Chem A Mater*, vol. 6, núm. 25, pp. 11759–11772, 2018, doi: 10.1039/C8TA02551G.

[30] C. J. Hages, S. Levcenco, C. K. Miskin, J. H. Alsmeier, D. Abou-Ras, R. G. Wilks, M. Bär, T. Unold, y R. Agrawal, "Improved performance of Ge-alloyed CZTGeSSe thin-film solar cells through control of elemental losses", *Progress in Photovoltaics: Research and Applications*, vol. 23, núm. 3, pp. 376–384, mar. 2015, doi: 10.1002/pip.2442.

[31] S. Giraldo, M. Neuschitzer, T. Thersleff, S. López-Marino, Y. Sánchez, H. Xie, M. Colina, M. Placidi, P. Pistor, V. Izquierdo-Roca, *et al.*, "Large Efficiency Improvement in $Cu_2ZnSnSe_4$ Solar Cells by Introducing a Superficial Ge Nanolayer", *Adv Energy Mater*, vol. 5, núm. 21, p. 1501070, nov. 2015, doi: 10.1002/aenm.201501070.

[32] S. Kim, K. M. Kim, H. Tampo, H. Shibata, y S. Niki, "Improvement of voltage deficit of Ge-incorporated kesterite solar cell with 12.3% conversion efficiency", *Applied Physics Express*, vol. 9, núm. 10, p. 102301, oct. 2016, doi: 10.7567/APEX.9.102301.

[33] K. Biswas, S. Lany, y A. Zunger, "The electronic consequences of multivalent elements in inorganic solar absorbers: Multivalency of Sn in Cu_2ZnSnS_4", *Appl Phys Lett*, vol. 96, núm. 20, p. 201902, may 2010, doi: 10.1063/1.3427433.

[34] Y. Li, W. Ling, Q. Han, y W. Shi, "Colloidal $Cu_2Zn(Sn_{1-x}Ge_x)S_4$ nanocrystals: electrical properties and comparison between their wurtzite and kesterite structures", *RSC Adv.*, vol. 4, núm. 98, pp. 55016–55022, oct. 2014, doi: 10.1039/C4RA10780B.

[35] D. Mora-Herrera, M. Pal, y F. Paraguay-Delgado, "Facile solvothermal synthesis of $Cu_2ZnSn_{1-x}Ge_xS_4$ nanocrystals: Effect of Ge content on optical and electrical properties", *Mater Chem Phys*, vol. 257, p. 123764, ene. 2021, doi: 10.1016/j.matchemphys.2020.123764.

[36] F. E. Cancino-Gordillo, J. V. Cab, y U. Pal, "Structure and transport behavior of hydrothermally grown phase pure $Cu_2ZnSn_{1-x}Ge_xS_4$ (x = 0.0, 0.3) nanoparticles", *Appl Surf Sci*, vol. 571, p. 151261, ene. 2022, doi: 10.1016/j.apsusc.2021.151261.

[37] M. Neuschitzer, J. Marquez, S. Giraldo, M. Dimitrievska, M. Placidi, I. Forbes, V. Izquierdo-Roca, A. Pérez-Rodriguez, y E. Saucedo, "V_{oc} Boosting and Grain Growth Enhancing Ge-Doping Strategy for $Cu_2ZnSnSe_4$ Photovoltaic Absorbers", *The Journal of Physical Chemistry C*, vol. 120, núm. 18, pp. 9661–9670, may 2016, doi: 10.1021/acs.jpcc.6b02315.

[38] C. Yan, J. Huang, K. Sun, S. Johnston, Y. Zhang, H. Sun, A. Pu, M. He, F. Liu, K. Eder, *et al.*, "Cu_2ZnSnS_4 solar cells with over 10% power conversion efficiency enabled by heterojunction heat treatment", *Nat Energy*, vol. 3, núm. 9, pp. 764–772, sep. 2018, doi: 10.1038/s41560-018-0206-0.

[39] M. A. Green, E. D. Dunlop, J. Hohl-Ebinger, M. Yoshita, N. Kopidakis, y X. Hao, "Solar cell efficiency tables (Version 58)", *Progress in Photovoltaics: Research and Applications*, vol. 29, núm. 7, pp. 657–667, jul. 2021, doi: 10.1002/pip.3444.

[40] U. Syafiq, N. Ataollahi, y P. Scardi, "Progress in CZTS as hole transport layer in perovskite solar cell", *Solar Energy*, vol. 196, pp. 399–408, ene. 2020, doi: 10.1016/j.solener.2019.12.016.

[41] M. Yuan, X. Zhang, J. Kong, W. Zhou, Z. Zhou, Q. Tian, Y. Meng, S. Wu, y D. Kou, "Controlling the Band Gap to Improve Open-Circuit Voltage in Metal Chalcogenide based Perovskite Solar Cells", *Electrochim Acta*, vol. 215, pp. 374–379, oct. 2016, doi: 10.1016/j.electacta.2016.08.130.

[42] G. Y. Ashebir, C. Dong, Z. Wan, J. Qi, J. Chen, Q. Zhao, W. Chen, y M. Wang, "Solution-processed Cu_2ZnSnS_4 nanoparticle film as efficient hole transporting layer for stable perovskite solar cells", *Journal of Physics and Chemistry of Solids*, vol. 129, pp. 204–208, jun. 2019, doi: 10.1016/j.jpcs.2019.01.008.

[43] Y. Wu, W. Bi, Z. Shi, X. Zhuang, Z. Song, S. Liu, C. Chen, L. Xu, Q. Dai, y H. Song, "Unraveling the Dual-Functional Mechanism of Light Absorption and Hole Transport of $Cu_2Cd_xZn_{1-x}SnS_4$ for Achieving Efficient and Stable Perovskite Solar Cells", *ACS Appl Mater Interfaces*, vol. 12, núm. 15, pp. 17509–17518, abr. 2020, doi: 10.1021/acsami.0c00607.

[44] D. Mora-Herrera y M. Pal, "Path toward the Performance Upgrade of Lead-Free Perovskite Solar Cells Using $Cu_2ZnSn_{1-x}Ge_xS_4$ as a Hole Transport Layer: A Theoretical Simulation Approach", *J. Phys. Chem. C*, vol. 2022, p. 5862, 2022, doi: 10.1021/acs.jpcc.2c01445.

[45] S. I. Swati, R. Matin, S. Bashar, y Z. H. Mahmood, "Experimental study of the optical properties of Cu_2ZnSnS_4 thin film absorber layer for solar cell application", *J Phys Conf Ser*, vol. 1086, núm. 1, p. 012010, sep. 2018, doi: 10.1088/1742-6596/1086/1/012010.

[46] K. S. Gour, V. Karade, P. Babar, J. Park, D. M. Lee, V. N. Singh, y J. H. Kim, "Potential Role of Kesterites in Development of Earth-Abundant Elements-Based Next Generation Technology", *Solar RRL*, vol. 5, núm. 4, p. 2000815, abr. 2021, doi: 10.1002/solr.202000815.

[47] M. He, C. Yan, J. Li, M. P. Suryawanshi, J. Kim, M. A. Green, y X. Hao, "Kesterite Solar Cells: Insights into Current Strategies and Challenges", *Advanced Science*, vol. 8, núm. 9, p. 2004313, may 2021, doi: 10.1002/ADVS.202004313.

[48] A. Wang, M. He, M. A. Green, K. Sun, y X. Hao, "A Critical Review on the Progress of Kesterite Solar Cells: Current Strategies and Insights", *Adv Energy Mater*, p. 2203046, 2022, doi: 10.1002/AENM.202203046.

[49] T. Tanaka, T. Nagatomo, D. Kawasaki, M. Nishio, Q. Guo, A. Wakahara, A. Yoshida, y H. Ogawa, "Preparation of Cu_2ZnSnS_4 thin films by hybrid sputtering", *Journal of Physics and Chemistry of Solids*, vol. 66, núm. 11, pp. 1978–1981, nov. 2005, doi: 10.1016/j.jpcs.2005.09.037.

[50] M. Xie, D. Zhuang, M. Zhao, Z. Zhuang, L. Ouyang, X. Li, y J. Song, "Preparation and Characterization of Cu_2ZnSnS_4 Thin Films and Solar Cells Fabricated from Quaternary Cu-Zn-Sn-S Target", *International Journal of Photoenergy*, vol. 2013, pp. 1–9, 2013, doi: 10.1155/2013/929454.

[51] R. A. Wibowo, W. S. Kim, E. S. Lee, B. Munir, y K. H. Kim, "Single step preparation of quaternary $Cu_2ZnSnSe_4$ thin films by RF magnetron sputtering from binary chalcogenide targets", *Journal of Physics and Chemistry of Solids*, vol. 68, núm. 10, pp. 1908–1913, oct. 2007, doi: 10.1016/j.jpcs.2007.05.022.

[52] T. Tanaka, D. Kawasaki, M. Nishio, Q. Guo, y H. Ogawa, "Fabrication of Cu_2ZnSnS_4 thin films by co-evaporation", *physica status solidi (c)*, vol. 3, núm. 8, pp. 2844–2847, sep. 2006, doi: 10.1002/pssc.200669631.

[53] T. Unold, J. Just, y H.-W. Schock, "Coevaporation of CZTS Films and Solar Cells", en *Copper Zinc Tin Sulfide-Based Thin-Film Solar Cells*, Chichester, UK: John Wiley & Sons Ltd, 2015, pp. 221–238. doi: 10.1002/9781118437865.ch10.

[54] M. Zhou, Y. Gong, J. Xu, G. Fang, Q. Xu, y J. Dong, "Colloidal CZTS nanoparticles and films: Preparation and characterization", *J Alloys Compd*, vol. 574, pp. 272–277, oct. 2013, doi: 10.1016/j.jallcom.2013.05.143.

[55] X. Yan, X. Hu, y S. Komarneni, "Solvothermal synthesis of CZTS nanoparticles in ethanol: Preparation and characterization", *Journal of the Korean Physical Society*, vol. 66, núm. 10, pp. 1511–1515, may 2015, doi: 10.3938/jkps.66.1511.

[56] K. Tanaka, N. Moritake, y H. Uchiki, "Preparation of Cu_2ZnSnS_4 thin films by sulfurizing sol–gel deposited precursors", *Solar Energy Materials and Solar Cells*, vol. 91, núm. 13, pp. 1199–1201, ago. 2007, doi: 10.1016/j.solmat.2007.04.012.

[57] M. Pal, N. R. Mathews, R. S. Gonzalez, y X. Mathew, "Synthesis of Cu_2ZnSnS_4 nanocrystals by solvothermal method", *Thin Solid Films*, vol. 535, núm. 1, pp. 78–82, 2013, doi: 10.1016/j.tsf.2012.11.043.

[58] M. Cao, L. Li, W. Z. Fan, X. Y. Liu, Y. Sun, y Y. Shen, "Quaternary Cu_2CdSnS_4 nanoparticles synthesized by a simple solvothermal method", *Chem Phys Lett*, vol. 534, pp. 34–37, may 2012, doi: 10.1016/j.cplett.2012.03.016.

[59] M. Cao y Y. Shen, "A mild solvothermal route to kesterite quaternary Cu_2ZnSnS_4 nanoparticles", *J Cryst Growth*, vol. 318, núm. 1, pp. 1117–1120, mar. 2011, doi: 10.1016/j.jcrysgro.2010.10.071.

[60] B. Wang, H. Xiang, T. Nakayama, J. Zhou, y B. Li, "Theoretical investigation on thermoelectric properties of Cu-based chalcopyrite compounds", *Phys Rev B*, 2017, doi: 10.1103/PhysRevB.95.035201.

[61] A. Fischereder, T. Rath, W. Haas, H. Amenitsch, J. Albering, D. Meischler, S. Larissegger, M. Edler, R. Saf, F. Hofer, *et al.*, "Investigation of Cu_2ZnSnS_4 formation from metal salts and thioacetamide", *Chemistry of Materials*, 2010, doi: 10.1021/cm100058q.

[62] M. Y. Valakh, A. P. Litvinchuk, V. M. Dzhagan, V. O. Yukhymchuk, Y. O. Havryliuk, M. Guc, I. v Bodnar, V. Izquierdo-Roca, A. Pérez-Rodríguez, y D. R. T. Zahn, "Optical properties of quaternary kesterite-type $Cu_2Zn(Sn_{1-x}Ge_x)S_4$ crystalline alloys: Raman scattering, photoluminescence and first-principle calculations", *RSC Adv*, vol. 6, núm. 72, pp. 67756–67763, 2016, doi: 10.1039/C6RA13608G.

[63] S. Schorr, "The crystal structure of kesterite type compounds: A neutron and X-ray diffraction study", *Solar Energy Materials and Solar Cells*, vol. 95, núm. 6, pp. 1482–1488, jun. 2011, doi: 10.1016/j.solmat.2011.01.002.

[64] M. Y. Valakh, O. F. Kolomys, S. S. Ponomaryov, V. O. Yukhymchuk, I. S. Babichuk, V. Izquierdo-Roca, E. Saucedo, A. Perez-Rodriguez, J. R. Morante, S. Schorr, *et al.*, "Raman scattering and disorder effect in Cu_2ZnSnS_4", *physica status solidi (RRL) - Rapid Research Letters*, vol. 7, núm. 4, pp. 258–261, abr. 2013, doi: 10.1002/pssr.201307073.

[65] J. K. Larsen, J. J. S. Scragg, N. Ross, y C. Platzer-Björkman, "Band Tails and Cu–Zn Disorder in Cu_2ZnSnS_4 Solar Cells", *ACS Appl Energy Mater*, vol. 3, núm. 8, pp. 7520–7526, ago. 2020, doi: 10.1021/acsaem.0c00926.

[66] M. Quennet, A. Ritscher, M. Lerch, y B. Paulus, "The order-disorder transition in Cu_2ZnSnS_4: A theoretical and experimental study", *J Solid State Chem*, 2017, doi: 10.1016/j.jssc.2017.03.018.

[67] M. Valentini, C. Malerba, F. Menchini, D. Tedeschi, A. Polimeni, M. Capizzi, y A. Mittiga, "Effect of the order-disorder transition on the optical properties of Cu_2ZnSnS_4", *Appl Phys Lett*, vol. 108, núm. 21, p. 211909, may 2016, doi: 10.1063/1.4952973.

[68] S. Bourdais, C. Choné, B. Delatouche, A. Jacob, G. Larramona, C. Moisan, A. Lafond, F. Donatini, G. Rey, S. Siebentritt, *et al.*, "Is the Cu/Zn Disorder the Main Culprit for the Voltage Deficit in Kesterite Solar Cells?", *Adv Energy Mater*, vol. 6, núm. 12, p. 1502276, jun. 2016, doi: 10.1002/aenm.201502276.

[69] I. S. Babichuk, M. O. Semenenko, S. Golovynskyi, R. Caballero, O. I. Datsenko, I. V. Babichuk, J. Li, G. Xu, R. Qiu, C. Huang, *et al.*, "Control of secondary phases and disorder degree in Cu_2ZnSnS_4 films by sulfurization at varied subatmospheric pressures", *Solar Energy Materials and Solar Cells*, vol. 200, p. 109915, sep. 2019, doi: 10.1016/j.solmat.2019.109915.

[70] S. Schorr, G. Gurieva, M. Guc, M. Dimitrievska, A. Pérez-Rodríguez, V. Izquierdo-Roca, C. S. Schnohr, J. Kim, W. Jo, y J. M. Merino, "Point defects, compositional fluctuations, and secondary phases in non-stoichiometric kesterites", *Journal of Physics: Energy*, vol. 2, núm. 1, p. 012002, dic. 2019, doi: 10.1088/2515-7655/ab4a25.

[71] T. Maeda, S. Nakamura, y T. Wada, "First Principles Calculations of Defect Formation in In-Free Photovoltaic Semiconductors Cu_2ZnSnS_4 and $Cu_2ZnSnSe_4$", *Jpn J Appl Phys*, vol. 50, núm. 4, p. 04DP07, abr. 2011, doi: 10.1143/JJAP.50.04DP07.

[72] N. Kattan, B. Hou, D. J. Fermín, y D. Cherns, "Crystal structure and defects visualization of Cu_2ZnSnS_4 nanoparticles employing transmission electron microscopy and electron diffraction", *Appl Mater Today*, vol. 1, núm. 1, pp. 52–59, nov. 2015, doi: 10.1016/j.apmt.2015.08.004.

[73] A. Nagaoka, H. Miyake, T. Taniyama, K. Kakimoto, y K. Yoshino, "Correlation between intrinsic defects and electrical properties in the high-quality Cu_2ZnSnS_4 single crystal", *Appl Phys Lett*, vol. 103, núm. 11, p. 112107, sep. 2013, doi: 10.1063/1.4821279.

[74] M. Dimitrievska, A. Fairbrother, E. Saucedo, A. Pérez-Rodríguez, y V. Izquierdo-Roca, "Influence of compositionally induced defects on the vibrational properties of device grade $Cu_2ZnSnSe_4$ absorbers for kesterite based solar cells", *Appl Phys Lett*, vol. 106, núm. 7, p. 073903, feb. 2015, doi: 10.1063/1.4913262.

[75] H. Katagiri, K. Jimbo, M. Tahara, H. Araki, y K. Oishi, "The influence of the composition ratio on CZTS-based thin film solar cells", 2009.

[76] W.-S. Liu, S.-Y. Chen, C.-S. Huang, M.-Y. Lee, y H.-C. Kuo, "Investigation of Zn/Sn ratio for improving the material quality of CZTS thin films with the reduction of $Cu_{2-x}S$ secondary phase", *J Alloys Compd*, vol. 853, p. 157237, feb. 2021, doi: 10.1016/j.jallcom.2020.157237.

[77] A. Fairbrother, X. Fontané, V. Izquierdo-Roca, M. Espíndola-Rodríguez, S. López-Marino, M. Placidi, L. Calvo-Barrio, A. Pérez-Rodríguez, y E. Saucedo, "On the formation mechanisms of Zn-rich Cu_2ZnSnS_4 films prepared by sulfurization of metallic stacks", *Solar Energy Materials and Solar Cells*, vol. 112, pp. 97–105, may 2013, doi: 10.1016/j.solmat.2013.01.015.

[78] A. Fairbrother, X. Fontané, V. Izquierdo-Roca, M. Placidi, D. Sylla, M. Espindola-Rodriguez, S. Lõpez-Mariño, F. A. Pulgarín, O. Vigil-Galán, A. Pérez-Rodríguez, *et al.*, "Secondary phase formation in Zn-rich $Cu_2ZnSnSe_4$-based solar cells annealed in low pressure and temperature conditions", *Progress in Photovoltaics: Research and Applications*, vol. 22, núm. 4, pp. 479–487, abr. 2014, doi: 10.1002/pip.2473.

[79] H. Du, F. Yan, M. Young, B. To, C.-S. Jiang, P. Dippo, D. Kuciauskas, Z. Chi, E. A. Lund, C. Hancock, *et al.*, "Investigation of combinatorial coevaporated thin film Cu_2ZnSnS_4. I. Temperature effect, crystalline phases, morphology, and photoluminescence", *J Appl Phys*, vol. 115, núm. 17, p. 173502, may 2014, doi: 10.1063/1.4871664.

[80] G. Altamura y J. Vidal, "Impact of Minor Phases on the Performances of CZTSSe Thin-Film Solar Cells", *Chemistry of Materials*, vol. 28, núm. 11, pp. 3540–3563, jun. 2016, doi: 10.1021/acs.chemmater.6b00069.

[81] J. Xu, J. Yang, S. Jiang, y S. Shang, "Secondary phases and disorder degree investigation of Cu_2ZnSnS_4 films", *Ceram Int*, vol. 47, núm. 3, pp. 4135–4142, feb. 2021, doi: 10.1016/j.ceramint.2020.09.290.

[82] M. Buffière, G. Brammertz, S. Sahayaraj, M. Batuk, S. Khelifi, D. Mangin, A.-A. el Mel, L. Arzel, J. Hadermann, M. Meuris, *et al.*, "KCN Chemical Etch for Interface Engineering in $Cu_2ZnSnSe_4$ Solar Cells", *ACS Appl Mater Interfaces*, vol. 7, núm. 27, pp. 14690–14698, jul. 2015, doi: 10.1021/acsami.5b02122.

[83] S. Sahayaraj, G. Brammertz, B. Vermang, S. Ranjbar, M. Meuris, J. Vleugels, y J. Poortmans, "Effect of the duration of a wet KCN etching step and post deposition annealing on the efficiency of $Cu_2ZnSnSe_4$ solar cells", *Thin Solid Films*, vol. 633, pp. 166–171, jul. 2017, doi: 10.1016/j.tsf.2016.09.055.

[84] A. Fairbrother, E. García-Hemme, V. Izquierdo-Roca, X. Fontané, F. A. Pulgarín-Agudelo, O. Vigil-Galán, A. Pérez-Rodríguez, y E. Saucedo, "Development of a Selective Chemical Etch To Improve the Conversion Efficiency of Zn-Rich Cu_2ZnSnS_4 Solar Cells", *J Am Chem Soc*, vol. 134, núm. 19, pp. 8018–8021, may 2012, doi: 10.1021/ja301373e.

[85] M. Mousel, A. Redinger, R. Djemour, M. Arasimowicz, N. Valle, P. Dale, y S. Siebentritt, "HCl and Br_2-MeOH etching of $Cu_2ZnSnSe_4$ polycrystalline absorbers", *Thin Solid Films*, vol. 535, núm. 1, pp. 83–87, may 2013, doi: 10.1016/j.tsf.2012.12.095.

[86] M. G. Gang, V. C. Karade, M. P. Suryawanshi, H. Yoo, M. He, X. Hao, I. J. Lee, B. H. Lee, S. W. Shin, y J. H. Kim, "A Facile Process for Partial Ag Substitution in Kesterite $Cu_2ZnSn(S,Se)_4$ Solar Cells Enabling a Device Efficiency of over 12%", *ACS Appl Mater Interfaces*, vol. 13, núm. 3, pp. 3959–3968, ene. 2021, doi: 10.1021/acsami.0c19373.

[87] C. Ma, H. Guo, K. Zhang, N. Yuan, y J. Ding, "Fabrication of p-type kesterite Ag_2ZnSnS_4 thin films with a high hole mobility", *Mater Lett*, vol. 186, pp. 390–393, ene. 2017, doi: 10.1016/j.matlet.2016.10.013.

[88] H. Guo, C. Ma, K. Zhang, X. Jia, Y. Li, N. Yuan, y J. Ding, "The fabrication of Cd-free Cu_2ZnSnS_4-Ag_2ZnSnS_4 heterojunction photovoltaic devices", *Solar Energy Materials and Solar Cells*, vol. 178, pp. 146–153, may 2018, doi: 10.1016/j.solmat.2018.01.022.

[89] S. Hadke, S. Levcenko, G. Sai Gautam, C. J. Hages, J. A. Márquez, V. Izquierdo-Roca, E. A. Carter, T. Unold, y L. H. Wong, "Suppressed Deep Traps and Bandgap Fluctuations in Cu_2CdSnS_4 Solar Cells with ≈8% Efficiency", *Adv Energy Mater*, vol. 9, núm. 45, p. 1902509, dic. 2019, doi: 10.1002/aenm.201902509.

[90] K.-S. Lim, S.-M. Yu, S. Seo, H. Shin, T.-S. Oh, y J.-B. Yoo, "Incorporation of Ge in Cu_2ZnSnS_4 thin film in a Zn-poor composition range", *Mater Sci Semicond Process*, vol. 89, pp. 194–200, ene. 2019, doi: 10.1016/j.mssp.2018.09.020.

[91] L. Choubrac, M. Bär, X. Kozina, R. Félix, R. G. Wilks, G. Brammertz, S. Levcenko, L. Arzel, N. Barreau, S. Harel, *et al.*, "Sn Substitution by Ge: Strategies to Overcome the Open-Circuit Voltage Deficit of Kesterite Solar Cells", *ACS Appl Energy Mater*, vol. 3, núm. 6, pp. 5830–5839, jun. 2020, doi: 10.1021/acsaem.0c00763.

[92] J. Li, D. Wang, X. Li, Y. Zeng, y Y. Zhang, "Cation Substitution in Earth-Abundant Kesterite Photovoltaic Materials", *Advanced Science*, vol. 5, núm. 4. Wiley-VCH Verlag, el 1 de abril de 2018. doi: 10.1002/advs.201700744.

[93] M. Ritzer, S. Schönherr, P. Schöppe, W. Wisniewski, S. Giraldo, G. Gurieva, A. Johannes, C. T. Plass, K. Ritter, G. Martínez-Criado, *et al.*, "On the Germanium Incorporation in $Cu_2ZnSnSe_4$ Kesterite Solar Cells Boosting Their Efficiency", *ACS Appl Energy Mater*, vol. 3, núm. 1, pp. 558–564, ene. 2020, doi: 10.1021/acsaem.9b01784.

[94] A. D. Collord y H. W. Hillhouse, "Germanium Alloyed Kesterite Solar Cells with Low Voltage Deficits", *Chemistry of Materials*, vol. 28, núm. 7, pp. 2067–2073, abr. 2016, doi: 10.1021/acs.chemmater.5b04806.

[95] W. Travis, E. N. K. Glover, H. Bronstein, D. O. Scanlon, y R. G. Palgrave, "On the application of the tolerance factor to inorganic and hybrid halide perovskites: a revised system †", 2016, doi: 10.1039/c5sc04845a.

[96] A. Roy, F. E. Cancino-Gordillo, S. Saha, U. Pal, y S. Das, "Performance of asymmetric supercapacitor fabricated with perovskite-type Sr^{2+}-incorporated $LaMnO_3$ ($La_{0.7}Sr_{0.3}MnO_3$) nanostructures in neutral 1M Na_2SO_4 aqueous electrolyte", *Int J Energy Res*, vol. 45, núm. 9, pp. 14021–14033, jul. 2021, doi: 10.1002/er.6727.

[97] J.-L. Ortiz-Quiñonez, L. García-González, F. E. Cancino-Gordillo, y U. Pal, "Particle dispersion and lattice distortion induced magnetic behavior of $La_{1-x}Sr_xMnO_3$ perovskite nanoparticles grown by salt-assisted solid-state synthesis", *Mater Chem Phys*, vol. 246, p. 122834, may 2020, doi: 10.1016/j.matchemphys.2020.122834.

[98] L. Malavasi, C. Ritter, M. Cristina Mozzati, C. Tealdi, M. Saiful Islam, C. Bruno Azzoni, y G. Flor, "Effects of cation vacancy distribution in doped $LaMnO_{3+\delta}$ perovskites", *J Solid State Chem*, vol. 178, núm. 6, pp. 2042–2049, jun. 2005, doi: 10.1016/j.jssc.2005.04.019.

[99] J. Y. Kim, J. W. Lee, H. S. Jung, H. Shin, y N. G. Park, "High-Efficiency Perovskite Solar Cells", *Chem Rev*, vol. 120, núm. 15, pp. 7867–7918, ago. 2020, doi: 10.1021/ACS.CHEMREV.0C00107/ASSET/IMAGES/MEDIUM/CR0C00107_M019.GIF.

[100] N. G. Park, "Perovskite solar cells: An emerging photovoltaic technology", *Materials Today*, vol. 18, núm. 2. Elsevier B.V., pp. 65–72, el 1 de marzo de 2015. doi: 10.1016/j.mattod.2014.07.007.

[101] R. Singh, S. Sandhu, H. Yadav, y J.-J. Lee, "Stable Triple-Cation (Cs^+–MA^+–FA^+) Perovskite Powder Formation under Ambient Conditions for Hysteresis-Free High-Efficiency Solar Cells", *ACS Appl Mater Interfaces*, vol. 11, núm. 33, pp. 29941–29949, ago. 2019, doi: 10.1021/acsami.9b09121.

[102] M. Oh, S.-I. Jo, B. Parida, A. Singh, K. Ko, J.-W. Kang, y H. Kim, "Electrical, Optical, and Structural Characteristics of $CH_3NH_3PbI_3$ Perovskite Light-Emitting Diodes", *Physica Status Solidi A*, vol. 215, núm. 20, p. 1701014, oct. 2018, doi: 10.1002/pssa.201701014.

[103] Q. Zhou, Z. Bai, W. G. Lu, Y. Wang, B. Zou, y H. Zhong, "In Situ Fabrication of Halide Perovskite Nanocrystal-Embedded Polymer Composite Films with Enhanced Photoluminescence for Display Backlights", *Advanced Materials*, vol. 28, núm. 41, pp. 9163–9168, 2016, doi: 10.1002/adma.201602651.

[104] D. Liu, Q. Li, y K. Wu, "Ethylammonium as an alternative cation for efficient perovskite solar cells from first-principles calculations", *RSC Adv*, vol. 9, núm. 13, pp. 7356–7361, 2019, doi: 10.1039/C9RA00853E.

[105] D. Ma, N. Dai, y Y. Lan, "Solution Route to Single-Crystalline Ethylammonium Lead Halide Microstructures", *ChemistrySelect*, vol. 4, núm. 7, pp. 2174–2180, feb. 2019, doi: 10.1002/slct.201804046.

[106] W. S. Yang, J. H. Noh, N. J. Jeon, Y. C. Kim, S. Ryu, J. Seo, y S. il Seok, "High-performance photovoltaic perovskite layers fabricated through intramolecular exchange", *Science (1979)*, vol. 348, núm. 6240, pp. 1234–1237, jun. 2015, doi: 10.1126/science.aaa9272.

[107] H. Cho, J. S. Kim, C. Wolf, Y. H. Kim, H. J. Yun, S. H. Jeong, A. Sadhanala, V. Venugopalan, J. W. Choi, C. L. Lee, *et al.*, "High-Efficiency Polycrystalline Perovskite Light-Emitting Diodes Based on Mixed Cations", *ACS Nano*, vol. 12, núm. 3, pp. 2883–2892, mar. 2018, doi: 10.1021/acsnano.8b00409.

[108] Y. Ling, Y. Tian, X. Wang, J. C. Wang, J. M. Knox, F. Perez-Orive, Y. Du, L. Tan, K. Hanson, B. Ma, *et al.*, "Enhanced Optical and Electrical Properties of Polymer-Assisted All-Inorganic Perovskites for Light-Emitting Diodes", *Advanced Materials*, vol. 28, núm. 40, pp. 8983–8989, 2016, doi: 10.1002/adma.201602513.

[109] L. Protesescu, S. Yakunin, M. I. Bodnarchuk, F. Krieg, R. Caputo, C. H. Hendon, R. X. Yang, A. Walsh, y M. v. Kovalenko, "Nanocrystals of Cesium Lead Halide Perovskites ($CsPbX_3$, X = Cl, Br, and I): Novel Optoelectronic Materials Showing Bright Emission with Wide Color Gamut", *Nano Lett*, vol. 15, núm. 6, pp. 3692–3696, jun. 2015, doi: 10.1021/nl5048779.

[110] Z. Liang, S. Zhao, Z. Xu, B. Qiao, P. Song, D. Gao, y X. Xu, "Shape-Controlled Synthesis of All-Inorganic $CsPbBr_3$ Perovskite Nanocrystals with Bright Blue Emission", *ACS Appl Mater Interfaces*, vol. 8, núm. 42, pp. 28824–28830, oct. 2016, doi: 10.1021/acsami.6b08528.

[111] N. Marinova, S. Valero, y J. L. Delgado, "Organic and perovskite solar cells: Working principles, materials and interfaces", *J Colloid Interface Sci*, vol. 488, pp. 373–389, feb. 2017, doi: 10.1016/j.jcis.2016.11.021.

[112] A. Kojima, K. Teshima, Y. Shirai, y T. Miyasaka, "Novel Photoelectrochemical Cell with Mesoscopic Electrodes Sensitized by Lead-halide Compounds (5)", *ECS Meeting Abstracts*, vol. MA2007-02, núm. 8, p. 352, sep. 2007, doi: 10.1149/MA2007-02/8/352.

[113] J. H. Im, C. R. Lee, J. W. Lee, S. W. Park, y N. G. Park, "6.5% efficient perovskite quantum-dot-sensitized solar cell", *Nanoscale*, vol. 3, núm. 10, pp. 4088–4093, oct. 2011, doi: 10.1039/C1NR10867K.

[114] H. S. Kim, C. R. Lee, J. H. Im, K. B. Lee, T. Moehl, A. Marchioro, S. J. Moon, R. Humphry-Baker, J. H. Yum, J. E. Moser, *et al.*, "Lead Iodide Perovskite Sensitized All-Solid-State Submicron Thin Film Mesoscopic Solar Cell with Efficiency Exceeding 9%", *Scientific Reports 2012 2:1*, vol. 2, núm. 1, pp. 1–7, ago. 2012, doi: 10.1038/srep00591.

[115] M. Nazeri, M. R. Golobostanfard, H. Kheirabadi, y H. Abdizadeh, "Sulfides as a new class of stable cost-effective materials compared to organic/inorganic hole transport materials for perovskite solar cells", *Ceramics International*, vol. 48, núm. 13. Elsevier Ltd, pp. 17995–18020, el 1 de julio de 2022. doi: 10.1016/j.ceramint.2022.03.163.

[116] Q. Wang, Z. Lin, J. Su, Z. Hu, J. Chang, y Y. Hao, "Recent progress of inorganic hole transport materials for efficient and stable perovskite solar cells", *Nano Select*, vol. 2, núm. 6, pp. 1055–1080, jun. 2021, doi: 10.1002/nano.202000238.

[117] C. Qin, L. Gao, y E. Wang, "Germanium: Inorganic Chemistry", en *Encyclopedia of Inorganic Chemistry*, Chichester, UK: John Wiley & Sons, Ltd, 2006. doi: 10.1002/0470862106.ia079.

[118] M. Pal, N. R. Mathews, F. Paraguay-Delgado, y X. Mathew, "Phase controlled solvothermal synthesis of Cu_2ZnSnS_4, $Cu_2ZnSn(S,Se)_4$ and $Cu_2ZnSnSe_4$ Nanocrystals: The effect of Se and S sources on phase purity", *Mater Chem Phys*, vol. 166, pp. 201–206, sep. 2015, doi: 10.1016/j.matchemphys.2015.10.002.

[119] J. Lu, Y. Xie, F. Xu, y L. Zhu, "Study of the dissolution behavior of selenium and tellurium in different solvents—a novel route to Se, Te tubular bulk single crystals", *J. Mater. Chem.*, vol. 12, núm. 9, pp. 2755–2761, ago. 2002, doi: 10.1039/B204092A.

[120] B. Li, Y. Xie, J. Huang, y Y. Qian, "Synthesis by a Solvothermal Route and Characterization of $CuInSe_2$ Nanowhiskers and Nanoparticles", *Advanced Materials*, vol. 11, núm. 17, pp. 1456–1459, dic. 1999, doi: 10.1002/(SICI)1521-4095(199912)11:17<1456::AID-ADMA1456>3.0.CO;2-3.

[121] Y.-F. Du, W.-H. Zhou, Y.-L. Zhou, P.-W. Li, J.-Q. Fan, J.-J. He, y S.-X. Wu, "Solvothermal synthesis and characterization of quaternary $Cu_2ZnSnSe_4$ particles", *Mater Sci Semicond Process*, vol. 15, núm. 2, pp. 214–217, abr. 2012, doi: 10.1016/j.mssp.2011.09.005.

[122] S. Ito, M. K. Nazeeruddin, P. Liska, P. Comte, R. Charvet, P. Péchy, M. Jirousek, A. Kay, S. M. Zakeeruddin, y M. Grätzel, "Photovoltaic characterization of dye-sensitized solar cells: effect of device masking on conversion efficiency", *Progress in Photovoltaics: Research and Applications*, vol. 14, núm. 7, pp. 589–601, nov. 2006, doi: 10.1002/PIP.683.

[123] "JEOL - Solutions of Innovation". https://www.jeol.com.mx/en-us/

[124] R. F. Egerton, "Physical principles of electron microscopy: An introduction to TEM, SEM, and AEM", *Physical Principles of Electron Microscopy: An Introduction to TEM, SEM, and AEM*, pp. 1–202, 2005, doi: 10.1007/B136495/COVER.

[125] D. B. Williams y C. B. Carter, "Transmission electron microscopy: A textbook for materials science", *Transmission Electron Microscopy: A Textbook for Materials Science*, pp. 1–760, 2009, doi: 10.1007/978-0-387-76501-3/COVER.

[126] E. D. Olsen, "Espectroscopia Raman", en *Métodos ópticos de análisis*, Reverte, Ed. Barcelona, 1990, p. 535.

[127] J. Workman, *The Concise Handbook of Analytical Spectroscopy: Theory, Applications, and Reference Materials: Volume 5: Raman Spectroscopy*. USA.

[128] F. E. Cancino-Gordillo, "Síntesis y caracterización de nanopartículas calcogenuras del sistema Cu-Zn-Sn-Ge", Benemérita Universidad Autónoma de Puebla, 2018.

[129] A. Escobedo Morales, E. Sánchez Mora, y U. Pal, "Use of diffuse reflectance spectroscopy for optical characterization of un-supported nanostructures", *Revista Mexicana de Física S*, vol. 53, núm. 5, pp. 18–22, 2007.

[130] R. Molenaar, J. J. ten Bosch, y J. R. Zijp, "Determination of Kubelka–Munk scattering and absorption coefficients by diffuse illumination", *Appl Opt*, vol. 38, núm. 10, p. 2068, abr. 1999, doi: 10.1364/AO.38.002068.

[131] T. Dittrich, "Basic Characteristics and Characterization of Solar Cells", *Materials Concepts for Solar Cells*, pp. 3–43, mar. 2018, doi: 10.1142/9781786344496_0001.

[132] S. Ravishankar, C. Aranda, P. P. Boix, J. A. Anta, J. Bisquert, y G. Garcia-Belmonte, "Effects of Frequency Dependence of the External Quantum Efficiency of Perovskite Solar Cells", *Journal of Physical Chemistry Letters*, vol. 9, núm. 11, pp. 3099–3104, jun. 2018, doi: 10.1021/ACS.JPCLETT.8B01245/ASSET/IMAGES/LARGE/JZ-2018-01245N_0003.JPEG.

[133] S. S. Hegedus y W. N. Shafarman, "Thin-film solar cells: Device measurements and analysis", *Progress in Photovoltaics: Research and Applications*, vol. 12, núm. 2–3, pp. 155–176, 2004, doi: 10.1002/pip.518.

[134] R. D. Shannon, "Revised effective ionic radii and systematic studies of interatomic distances in halides and chalcogenides", *Acta Crystallographica Section A*, vol. 32, núm. 5, pp. 751–767, sep. 1976, doi: 10.1107/S0567739476001551.

[135] M. Morihama, F. Gao, T. Maeda, y T. Wada, "Crystallographic and optical properties of $Cu_2Zn(Sn_{1-x}Ge_x)Se_4$ solid solution", *Jpn J Appl Phys*, vol. 53, núm. 4S, p. 04ER09, ene. 2014, doi: 10.7567/JJAP.53.04ER09.

[136] J. Chen, W. Li, C. Yan, S. Huang, y X. Hao, "Studies of compositional dependent $Cu_2Zn(Ge_xSn_{1-x})S_4$ thin films prepared by sulfurizing sputtered metallic precursors", *J Alloys Compd*, vol. 621, pp. 154–161, feb. 2015, doi: 10.1016/j.jallcom.2014.09.097.

[137] G. Chen, W. Wang, S. Chen, Z. Whang, Z. Huang, B. Zhang, y X. Kong, "Bandgap engineering of $Cu_2ZnSn_{1-x}Ge_xS(e)_4$ by adjusting Sn-Ge ratios for almost full solar spectrum absorption", *J Alloys Compd*, vol. 718, pp. 236–245, sep. 2017, doi: 10.1016/j.jallcom.2017.05.150.

[138] M. D. Regulacio, S. Y. Tee, S. H. Lim, Z. Zhang, y M.-Y. Han, "Selective formation of ternary Cu–Ge–S nanostructures in solution", *CrystEngComm*, vol. 20, núm. 42, pp. 6803–6810, 2018, doi: 10.1039/C8CE01443D.

[139] I. J. Alverdiyev, Z. S. Aliev, S. M. Bagheri, L. F. Mashadiyeva, Y. A. Yusibov, y M. B. Babanly, "Study of the $2Cu_2S + GeSe_2 \leftrightarrow 2Cu_2Se + GeS_2$ reciprocal system and thermodynamic properties of the $Cu_8GeS_6{-}xSe_x$ solid solutions", *J Alloys Compd*, vol. 691, pp. 255–262, ene. 2017, doi: 10.1016/j.jallcom.2016.08.251.

[140] W. F. Kuhs, R. Nitsche, y K. Scheunemann, "The argyrodites — A new family of tetrahedrally close-packed structures", *Mater Res Bull*, vol. 14, núm. 2, pp. 241–248, feb. 1979, doi: 10.1016/0025-5408(79)90125-9.

[141] M. Onoda, X.-A. Chen, K. Kato, A. Sato, y H. Wada, "Structure refinement of Cu_8GeS_6 using X-ray diffraction data from a multiple-twinned crystal", *Acta Crystallogr B*, vol. 55, núm. 6, pp. 1109–1109, dic. 1999, doi: 10.1107/S0108768199012938.

[142] M. Onoda, H. Wada, A. Sato, y M. Ishii, "Low-temperature forms of superionic conductors, Cu_8GeS_6 and Ag_7TaS_6, and ion conduction path", *J Alloys Compd*, vol. 383, núm. 1–2, pp. 113–117, nov. 2004, doi: 10.1016/j.jallcom.2004.04.018.

[143] M. Ishii, M. Onoda, y K. Shibata, "Structure and vibrational spectra of argyrodite family compounds Cu_8SiX_6 (X=S, Se) and Cu_8GeS_6", *Solid State Ion*, vol. 121, núm. 1–4, pp. 11–18, jun. 1999, doi: 10.1016/S0167-2738(98)00305-1.

[144] D. Brown, *The Chemical Bond in Inorganic Chemistry: The Bond Valence Model*, 1a ed. New York, NY: Oxford University Press, 2002.

[145] B. H. Toby y R. B. von Dreele, "GSAS-II : the genesis of a modern open-source all purpose crystallography software package", *J Appl Crystallogr*, vol. 46, núm. 2, pp. 544–549, abr. 2013, doi: 10.1107/S0021889813003531.

[146] O. V. Parasyuk, L. V. Piskach, Y. E. Romanyuk, I. D. Olekseyuk, V. I. Zaremba, y V. I. Pekhnyo, "Phase relations in the quasi-binary Cu_2GeS_3–ZnS and quasi-ternary Cu_2S–Zn(Cd)S–GeS_2 systems and crystal structure of Cu_2ZnGeS_4", *J Alloys Compd*, vol. 397, núm. 1–2, pp. 85–94, jul. 2005, doi: 10.1016/j.jallcom.2004.12.045.

[147] M. Dimitrievska, A. Fairbrother, X. Fontané, T. Jawhari, V. Izquierdo-Roca, E. Saucedo, y A. Pérez-Rodríguez, "Multiwavelength excitation Raman scattering study of polycrystalline kesterite Cu_2ZnSnS_4 thin films", *Appl Phys Lett*, vol. 104, núm. 2, 2014, doi: 10.1063/1.4861593.

[148] M. Dimitrievska, F. Boero, A. P. Litvinchuk, S. Delsante, G. Borzone, A. Perez-Rodriguez, y V. Izquierdo-Roca, "Structural Polymorphism in Kesterite Cu_2ZnSnS_4: Raman Spectroscopy and First-Principles Calculations Analysis", *Inorg Chem*, vol. 56, núm. 6, pp. 3467–3474, mar. 2017, doi: 10.1021/acs.inorgchem.6b03008.

[149] E. Garcia-Llamas, M. Guc, I. V. Bodnar, X. Fontané, R. Caballero, J. M. Merino, M. León, y V. Izquierdo-Roca, "Multiwavelength excitation Raman scattering of $Cu_2ZnSn_{1-x}Ge_x(S,Se)_4$ single crystals for earth abundant photovoltaic applications", *J Alloys Compd*, vol. 692, pp. 249–256, 2017, doi: 10.1016/j.jallcom.2016.09.035.

[150] E. Garcia-Llamas, J. M. Merino, R. Serna, X. Fontané, I. A. Victorov, A. Pérez-Rodríguez, M. León, I. V. Bodnar, V. Izquierdo-Roca, y R. Caballero, "Wide band-gap tuning $Cu_2ZnSn_{1-x}Ge_xS_4$ single crystals: Optical and vibrational properties", *Solar Energy Materials and Solar Cells*, vol. 158, núm. 4S, pp. 147–153, dic. 2016, doi: 10.1016/j.solmat.2015.12.021.

[151] D. B. Khadka y J. H. Kim, "Band gap engineering of alloyed $Cu_2ZnGe_xSn_{1-x}Q_4$ (Q = S,Se) films for solar cell", *Journal of Physical Chemistry C*, vol. 119, núm. 4, pp. 1706–1713, 2015, doi: 10.1021/jp510877g.

[152] H. J. Shim, U. v. Ghorpade, M. P. Surywanshi, M. Gang, y J. H. Kim, "Studies on the influence of etching solution on the properties of $Cu_2ZnSn(S,Se)_4$ thin film solar cells", *Thin Solid Films*, vol. 670, pp. 1–5, ene. 2019, doi: 10.1016/j.tsf.2018.11.042.

[153] E. Hajdeu-Chicarosh, M. Guc, K. Neldner, G. Gurieva, S. Schorr, E. Arushanov, y K. G. Lisunov, "Mechanisms of conductivity and energy spectrum of near-edge holes in Cu_2ZnSnS_4 powder samples", *J Alloys Compd*, vol. 703, pp. 315–320, may 2017, doi: 10.1016/j.jallcom.2017.01.352.

[154] E. Hajdeu-Chicarosh, "Variable-Range Hopping Conduction in the Kesterite and Wurtzstannite Cu_2ZnGeS_4 Single Crystals", *Surface Engineering and Applied Electrochemistry*, vol. 54, núm. 3, pp. 279–285, may 2018, doi: 10.3103/S1068375518030055.

[155] G. Rey, G. Larramona, S. Bourdais, C. Choné, B. Delatouche, A. Jacob, G. Dennler, y S. Siebentritt, "On the origin of band-tails in kesterite", *Solar Energy Materials and Solar Cells*, vol. 179, pp. 142–151, jun. 2018, doi: 10.1016/j.solmat.2017.11.005.

[156] Y. Fan, G. Wang, R. Wang, B. Zhang, X. Shen, P. Jiang, X. Zhang, H. Gu, X. Lu, y X. Zhou, "Enhanced thermoelectric properties of p-type argyrodites Cu_8GeS_6 through Cu vacancy", *J Alloys Compd*, vol. 822, p. 153665, may 2020, doi: 10.1016/j.jallcom.2020.153665.

[157] L. Q. Xie, L. Chen, Z. A. Nan, H. X. Lin, T. Wang, D. P. Zhan, J. W. Yan, B. W. Mao, y Z. Q. Tian, "Understanding the Cubic Phase Stabilization and Crystallization Kinetics in Mixed Cations and Halides Perovskite Single Crystals", *J Am Chem Soc*, vol. 139, núm. 9, pp. 3320–3323, mar. 2017, doi: 10.1021/jacs.6b12432.

[158] Y. Wang, J. Wu, P. Zhang, D. Liu, T. Zhang, L. Ji, X. Gu, Z. David Chen, y S. Li, "Stitching triple cation perovskite by a mixed anti-solvent process for high performance perovskite solar cells", *Nano Energy*, vol. 39, pp. 616–625, sep. 2017, doi: 10.1016/j.nanoen.2017.07.046.

[159] Z. Ma, D. Huang, Q. Liu, G. Yan, Z. Xiao, D. Chen, J. Zhao, Y. Xiang, C. Peng, H. Li, *et al.*, "Excess PbI_2 evolution for triple-cation based perovskite solar cells with 21.9% efficiency", *Journal of Energy Chemistry*, vol. 66, pp. 152–160, mar. 2022, doi: 10.1016/j.jechem.2021.07.030.

[160] Y. Kumar, E. Regalado-Perez, J. J. Jerónimo-Rendón, y X. Mathew, "Effect of Cs^+ and K^+ incorporation on the charge carrier lifetime, device performance and stability in perovskite solar cells", *Solar Energy Materials and Solar Cells*, vol. 236, p. 111512, mar. 2022, doi: 10.1016/j.solmat.2021.111512.

[161] W. Tress, N. Marinova, T. Moehl, S. M. Zakeeruddin, M. K. Nazeeruddin, y M. Grätzel, "Understanding the rate-dependent J–V hysteresis, slow time component, and aging in $CH_3NH_3PbI_3$ perovskite solar cells: the role of a compensated electric field", *Energy Environ Sci*, vol. 8, núm. 3, pp. 995–1004, mar. 2015, doi: 10.1039/C4EE03664F.

[162] A. Mashreghi, K. Maleki, y M. Moradzadeh, "Two-phase synthesized Cu_2ZnSnS_4 nanoparticles as inorganic hole-transporting material of paintable carbon-based perovskite solar cells", *Solar Energy*, vol. 201, pp. 547–554, may 2020, doi: 10.1016/j.solener.2020.03.036.

[163] Z. Shadrokh, S. Sousani, S. Gholipour, y Y. Abdi, "Enhanced photovoltaic performance and stability of perovskite solar cells by interface engineering with poly(4-vinylpyridine) and Cu_2ZnSnS_4&CNT", *Solar Energy*, vol. 201, pp. 908–915, may 2020, doi: 10.1016/j.solener.2020.03.093.

[164] C.-H. Tien, L.-C. Chen, y K.-L. Lee, "Ultra-thin and high transparent $Cu_2ZnSnSe_4/NiO_x$ double-layered inorganic hole-transporting layer for inverted structure $CH_3NH_3PbI_3$ perovskite solar cells", *J Alloys Compd*, vol. 873, p. 159804, ago. 2021, doi: 10.1016/j.jallcom.2021.159804.

Anexos

Solar Energy 199 (2020) 246–255

Contents lists available at ScienceDirect

Solar Energy

journal homepage: www.elsevier.com/locate/solener

Development of Cu_2ZnSnS_4 films from a non-toxic molecular precursor ink and theoretical investigation of device performance using experimental outcomes

D. Mora-Herrera, R. Silva-González, F.E. Cancino-Gordillo, Mou Pal*

Instituto de Física, BUAP, Av. San Claudio y Blvd. 18 Sur Col., San Manuel, Ciudad Universitaria, C.P. 72570 Puebla, Mexico

ARTICLE INFO

Keywords:
Cu_2ZnSnS_4 films
Molecular precursor ink
Chemical synthesis
Electrical properties
Single-junction solar cell
Numerical simulation

ABSTRACT

In this paper, we reported a facile and cost effective way to deposit Cu_2ZnSnS_4 (CZTS) films using a non-toxic precursor ink and photovoltaic performance of single junction CZTS solar cell by implementing experimentally obtained optical and electrical parameters of our CZTS film in a simulation program known as SCAPS-1D (solar cell capacitance simulator in one dimension). The ink was deposited over glass substrates by drop casting method and the as-deposited films were subjected to thermal annealing at 450 and 500 °C in N_2 atmosphere. X-ray diffraction and Raman scattering analysis revealed the polycrystalline nature of CZTS films with tetragonal kesterite phase. The values of optical band gap (E_g) were found to vary in between 1.26 and 1.41 eV depending on the annealing condition. Hall measurement showed p-type electrical conductivity with good electrical properties, yielding resistivity (ρ) in the range of 18.6–1.9 × 10^2 Ω-cm, carrier concentration (a) = 6.65 × 10^{16}–8.72 × 10^{17} cm^{-3} and mobility (μ) = 10.6–19.4 cm^2/Vs. Numerical simulation of CZTS thin film solar cells with CdS buffer layer was modeled through SCAPS-1D using the experimental data of CZTS films obtained in this work. A maximum efficiency of 14.12% was obtained considering all possible defects and radiative recombination which can be occurred under realistic situation.

1. Introduction

Thin film photovoltaics (PVs) based on earth abundant and nontoxic material can offer low-cost electric energy at terawatt scale without causing environmental risk. Significant progress has been achieved over last two decades and the efficiency has risen up to 23% at laboratory scale and 19% for modules based on $Cu(In.Ga)(S,Se)_2$ (CIGSSe) and CdTe (Green et al., 2019). However, the use of critical raw materials (In, Ga and Te) and heavy metal Cd restricts the production of CIGSSe and CdTe well below the desired TW/year capacity. (Andersson, 2000; Andersson et al., 1998). To further pursue thin film PV technology towards sustainable cleaner energy, the development of ecofriendly and low-cost materials is a challenge to fulfill the requirements of massive PV expansion. Being composed of non-toxic and earth-abundant elements, kesterite Cu_2ZnSnS_4 (CZTS) compounds have received immense interest due to their tunable direct band gap in the range of 1.0–1.5 eV through cation and anion substitution, p-type conductivity and high optical absorption coefficient (Adachi, 2015; Ito, 2015; Katagiri et al., 2001).

Different methods are used for the preparation of CZTS thin films, such as, thermal evaporation (Shi et al., 2012; Sánchez et al., 2016), sputtering (Tanaka et al., 2014), electro-deposition (Scragg et al., 2009), spray pyrolysis (Vigil-Galán et al., 2009; Adelifard and Torkamani, 2015; Diwate et al., 2017), sol-gel (Jiang et al., 2014; Aslan et al., 2016), pulsed layer deposition (Cazzaniga et al., 2017), spin coating of molecular precursor solution (Chen et al., 2016) among others. Evidently, the non-vacuum methods open the possibilities for the low cost fabrication process at large scale. Solution based techniques are becoming popular for their suitability towards cost-effective large area deposition without using vacuum system (Zhang and Jung, 2018). By following hydrazine-based solution method sulfo-selenide $Cu_2ZnSnS_xSe_{4-x}$ solar cells have demonstrated a maximum efficiency of 12.6% (Wang et al., 2014), while slightly lower efficiencies of 8.4% and 9.2% are reported for Se-free CZTS compounds (Shin et al., 2013; Sugimoto et al., 2013). However, the use of hydrazine is not recommended due to its high toxicity and explosive nature. Instead, other harmless solvents such as dimethylsulfoxide (Wang et al., 2015), methoxyethanol (Guchhait et al., 2016), ethylene glycol (Ghediya et al., 2016) and a combination of dimethylsulfoxide and ethanolamine (Wang et al., 2015) are being pursued in order to make a stable

* Corresponding author.
E-mail address: mou@ifuap.buap.mx (M. Pal).

https://doi.org/10.1016/j.solener.2020.01.077
Received 31 October 2019; Received in revised form 22 January 2020; Accepted 27 January 2020

molecular ink. Guchhait et al. reported spin coated CZTS and Ag-doped CZTS using methoxyethanol-based molecular precursor ink and observed an enhancement in device efficiency from 4.88% to 7.24% by Ag doping (Guchhait et al., 2016). Kim et al. fabricated CZTS devices using 2-methoxyethanol hybrid ink which contained chloride salts of Cu and Sn and as Zn-sources they used either solid-state metallic Zn particles or ZnS nanoparticles; their results suggest that the low melting point Zn particles facilitate the formation of dense kesterite layer yielding a device efficiency of 8.17% (Kim et al., 2014a, 2014b). Ghediya et al. reported the electronic transport properties of CZTS film deposited by doctor-blade printing from glycolic molecular (Ghediya et al., 2016). Wang et al. fabricated kesterite CZTS films by spin-coating a DMSO-based precursor ink containing certain amount of ethanolamine (Wang et al., 2015); Lin et al. fabricated good quality CZTSSe absorber layer by inkjet printing with DMSO-based precursor ink followed by reactive annealing (Lin et al., 2015).

On the other hand, there are a number of reports on CZTS device fabrication in substrate and superstrate configurations and the effort to enhance their efficiencies by doping CZTS layer with cation dopant elements such as Na (Yang et al., 2015), Li (Xin et al., 2015) and metalloid like Ge (Giraldo et al., 2018). The dopant elements improve the cell performance mainly in two ways; either by increasing grain recrystallization via the formation of liquid phase (Giraldo et al., 2015) or producing a graded band gap by alloying with CZTS and hence improving the band alignment at absorber/buffer interface (Kim et al., 2014a, 2014b). In spite of several attempts, the efficiency of kesterite-based solar cells lie far below to CIGS and CdTe-based technologies. Therefore, a detailed understanding of physical phenomena involving defect, band offsets, carrier densities at grain boundaries and interfaces is necessary to improve the electrical parameters of the cell.

Computer-based simulation program such as SCAPS-1D has been evolved as an essential tool to design high performance solar cell; it helps to understand the effects of optical and electrical parameters of the materials involved on the cell efficiency and provides feedback to further experimental optimization. There are few reports on numerical studies of CZTS based solar cells using SCAPS-1D simulation software. Adewoyin et al. reported an enhancement in output performance of CZTS thin films solar cells by introducing p-MoS_2 layer at the interface between CZTS and Mo in order to reduce series resistance between them and achieved an efficiency of 18% by systematic optimization of various device parameters (Adewoyin et al., 2017). Simya et al. performed a comparative study on the performance of different kesterite based thin films solar cells by optimizing different parameters including the thickness of absorber layer, back contact work function, different recombination mechanism (Auger and radiative recombination) and the series resistance (Simya et al., 2016). Benzetta et al. considered substrate configuration of ZnO/CdS/CZTS/Mo heterostructure by adding an additional CZTS layer of 50 nm thickness as back surface field layer in between Mo and 2.5 μm CZTS absorber layer and observed an increment in efficiency from 12% to 14% through the reduction of surface recombination velocity (Benzetta et al., 2019).

In the present work we report the fabrication of phase-pure kesterite CZTS films by drop-casting method using DMSO-based molecular precursor ink followed by annealing in inert atmosphere. Thermal treatment has been optimized in terms of annealing temperature, time and heating ramp to produce kesterite films with improved microstructure and electrical properties. Finally, we explored the numerical modeling and simulation of the proposed device structure to test the PV performance of the fabricated CZTS films in an inverted solar cell by implementing our experimental data in SCAPS-1D. The highest simulated efficiency of 14.12% has been achieved with V_{OC} = 0.762 V, J_{SC} = 32.043 mA/cm^2 and FF = 57.809%. The band energy diagram revealed the presence of a cliff-like band alignment at CdS/CZTS interface with conduction band offset of 0.2 eV. The goal of this work is to put forward a combinatorial study merging experimental and theoretical approaches for further improvements in power conversion efficiency of kesterite-based devices.

2. Experimental section

2.1. Ink preparation, film deposition and treatment

In order to make CZTS films, a precursor solution was prepared by adding 1.7 mmol of $CuCl_2{\cdot}2H_2O$ (Aldrich, 99%), 1.0 mmol of Zn $(CH_3COO)_2{\cdot}2H_2O$ (99%, J.T. Baker), 0.9 mmol of $SnCl_4{\cdot}5H_2O$ (Aldrich, 98%) and 5 mmol of thiourea (J.T. Baker, 98%) in 20 mL of dimethyl sulfoxide (DMSO, Aldrich, 99.9%). The mixture was stirred at room temperature for a couple of hours to obtain a clear and slightly yellowish precursor ink.

The microscopic glass substrates (25 × 25 mm) were pre-cleaned, soaked in chromic acid mixture overnight and then thoroughly washed with Alconox detergent solution and deionized water. Finally, the glass substrates were cleaned in an ultrasonic bath using acetone and ethanol followed by drying under nitrogen flow.

To deposit the film, the substrate was placed on a hot-plate set at 150 °C temperature and the ink was directly drop-casted on its surface. The coated substrate was dried at this temperature for 10 min. A smooth and uniform coating was obtained at the end. After several trials we have found that an amount of 400 μL of ink could effectively cover an area of 25 × 25 mm. The films were annealed under nitrogen atmosphere at 450 °C and 500 °C for 30 min and 45 min in a vacuum tubular furnace at a pressure of 5 × 10^2 Torr using a heating ramp of 3–5 °C increment/min; a temporary halt at 350 °C for 15 min was implemented before reaching the final annealing temperature with the intention to achieve a better film densification. A schematic representation of film deposition and the heating ramp used for annealing is shown in Fig. 1.

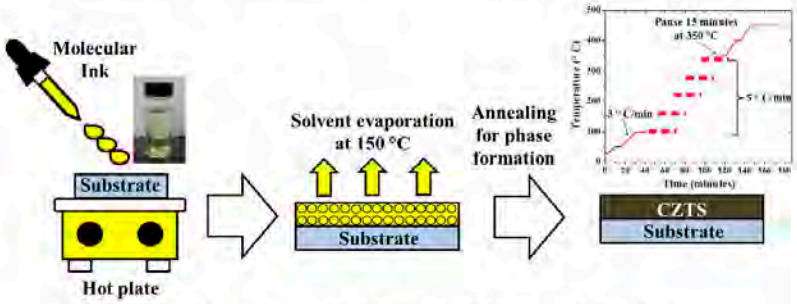

Fig. 1. Schematic diagram of the fabrication of CZTS films using molecular ink.

3. Characterization

The structural, compositional, morphological, optical and electrical properties of the CZTS films were studied using appropriate analytical tools. X-ray diffraction pattern of the films were obtained on an Empyrean-Pan-alytical X-ray Diffractometer operating at 40 kV and 40 mA using CuKα radiation. XRD data were collected in the 2θ range 10-70° with a grazing incidence angle of 1° and a scan rate of 0.02°/sec. The thickness of the annealed films was determined by Bruker Dektak 150 Surface Profilometer. Raman measurements were performed in the backscattering mode using Jobin Yvon LabRAM HR800 equipped with an Olympus BX41 microscope and a charge-coupled device detector. He-Ne laser with a wavelength of 632.8 nm was used as the excitation source. A neutral density filter was used to attenuate the laser intensity and thereby preventing any structural evolution caused by laser heating. An objective lens distance of 50X was employed for Raman measurement. The calibration of the equipment was verified by acquiring Raman spectra of standard silicon wafer. The surface morphology and composition of the films were analyzed using field emission scanning electron microscope (JEOL JSM-7800F) equipped with an Oxford Instrument X-Max energy dispersive X-ray spectrometer attached to the FESEM. To study the light absorption capacity of CZTS films, diffuse reflectance spectra were recorded on a Varian (Agilent) Cary 5000 UV–Vis spectrophotometer with diffuse Reflectance Accessory (DRA-CA-301). The electrical properties of the annealed films were evaluated at room temperature by Hall Effect in an Ecopia HMS-3000 using a magnetic field of 0.5 T. Silver dot contacts were used by painting silver electrodes on the film surface in van der Pauw configuration with a separation of 5 mm.

4. Results and discussion

4.1. CZTS thickness

The thickness of drop casted CZTS films was found to be several micrometers being 7.5 and 7 μm for the films annealed at 450 °C for 30 and 45 min respectively whereas a decrease in film thickness was observed for thermal treatment at 500 °C obtaining 5.8 and 5.5 μm for 30 and 45 min respectively.

4.2. XRD analysis

Fig. 2 shows the XRD patterns of CZTS films heated at 450 and 500 °C for 30 and 45 min in controlled atmosphere. For all the samples, the diffraction peaks located at 2θ = 28.53°, 32.98°, 47.33° and 56.18° correspond to (1 1 2), (2 0 0), (2 2 0) and (3 1 2) planes of kesterite Cu_2ZnSnS_4 (JCPDS# 26-0575) with preferred orientation along (1 1 2) plane. At an annealing temperature of 500 °C, the peaks are narrower compared to 450 °C which could be associated with improved crystallinity and an increase in crystallite size at higher temperature. The crystallite size (D) for the CZTS films is determined using the Scherer equation (1):

$$D = \frac{0.9\lambda}{\beta\cos\theta} \quad (1)$$

where λ is the X-ray wavelength (for CuKα radiation λ = 1.5406 Å), β is the full width half maximum (FWHM) and θ is the diffraction angle. The calculated mean crystallite size is 7.5–8.9 nm for CZTS films annealed at 450 °C for 30 and 45 min and 19–21.4 nm for annealing at 500 °C during 30 and 45 min respectively.

4.3. Raman spectroscopic study

Raman spectroscopy has been recognized as one of the most sensitive tools for studying the structural properties of metal sulfides and metal oxides. Slight differences in the phonon densities of states between the secondary phases can be easily distinguished in this technique. In the case of CZTS, the formation of secondary phases such as tetragonal Cu_2SnS_3 (CTS) and cubic ZnS frequently takes place during the synthesis. Although X-ray diffraction technique is the primary tool for phase identification, in the case of CZTS it is not very effective as tetragonal Cu_2SnS_3 (JCPDS # 89-4714) and cubic ZnS (JCPDS # 5-0566) share very similar XRD patterns to tetragonal CZTS (JCPDS # 26-0575). Hence, a combination of XRD technique along with Raman scattering is necessary to get complete information about the phase purity of CZTS.

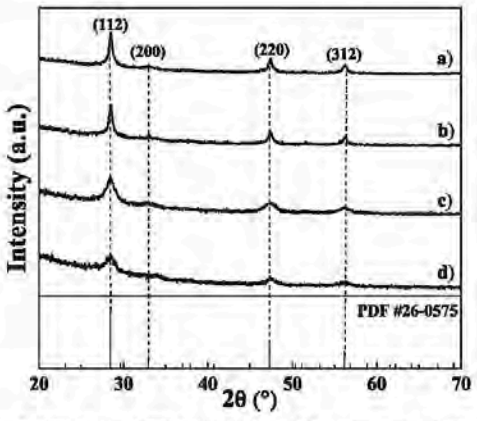

Fig. 2. XRD patterns of CZTS films annealed at different conditions: (a) 500 °C for 45 min; (b) 500 °C for 30 min; (c) 450 °C for 45 min and (d) 450 °C for 30 min.

Fig. 3 shows the Raman spectra of CZTS films annealed at 450 and 500 °C for 30 and 45 min. Insets of Fig. 3a and 3b show the deconvolution of the spectra in 200–500 cm^{-1} region with Lorentzian fitting in order to resolve clearly the shoulder peaks. The formation of kesterite phase was confirmed by the presence of intense peak at 334/337 cm^{-1} and two weak peaks at 289 and 367 cm^{-1} (Aldalbahi et al., 2016). The principal peak at 334 cm^{-1} is attributed to the A1 symmetry of CZTS related to the vibration of S atoms (Kodigala, 2014) while the minor peaks at ~289 and 367 cm^{-1} are associated with LO components of E symmetry mode (Khadka and Kim, 2015). The 289 peak is related to the vibration of Zn and S atoms with some contribution of Cu atoms in CZTS lattice (Garcia-Llamas et al., 2016). The peaks at 668 cm^{-1} (Fig. 3a and b), 672 and 734 cm^{-1} (Fig. 3c and d) are the second harmony of the peaks at 334, 337 and 367 cm^{-1} respectively indicating the good crystalline quality.

Furthermore, it is evident that the principal Raman peak has been shifted from 334 to 337 cm^{-1} with the increase in annealing temperature. This shift is possibly associated with the Cu-content of the films. In the stoichiometric CZTS, this peak is located at 337–338 cm^{-1} while for Cu-poor composition, the peak is found to shift towards lower frequency due to the presence of disordered kesterite phase (Mkawi et al., 2014; Caballero et al., 2014). The observed peak shift is in agreement with the elemental compositions of the samples as revealed by EDS measurements (See Section 4.4). In the case of CZTS film annealed at 500 °C for 45 min, besides the vibrational modes corresponding to kesterite CZTS, a small peak is present at 303 cm^{-1} which can be assigned to cubic Cu_2SnS_3 as reported in the literature (Fig. 3c) (Fernandes et al., 2011). The above results suggest that the single phase kesterite CZTS can effectively be formed by drop-casting of molecular ink.

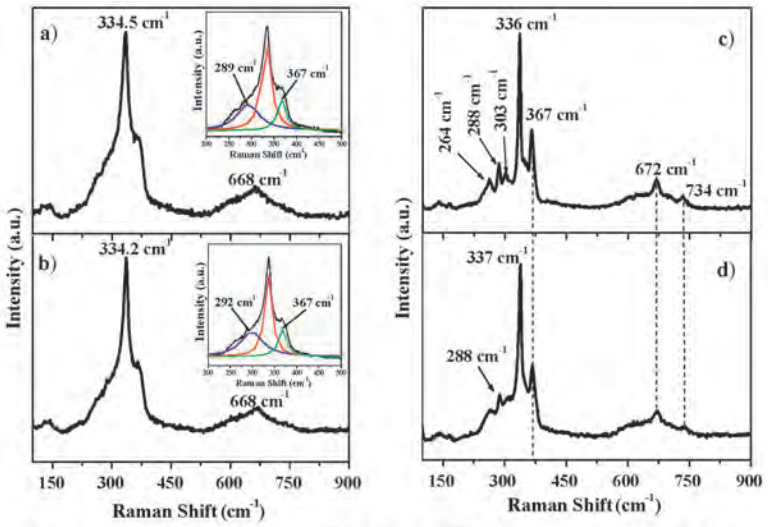

Fig. 3. Raman spectra of thermally treated Cu_2ZnSnS_4 films: (a) 450 °C for 45 min; (b) 450 °C for 30 min; (c) 500 °C for 45 min and (d) 500 °C for 30 min.

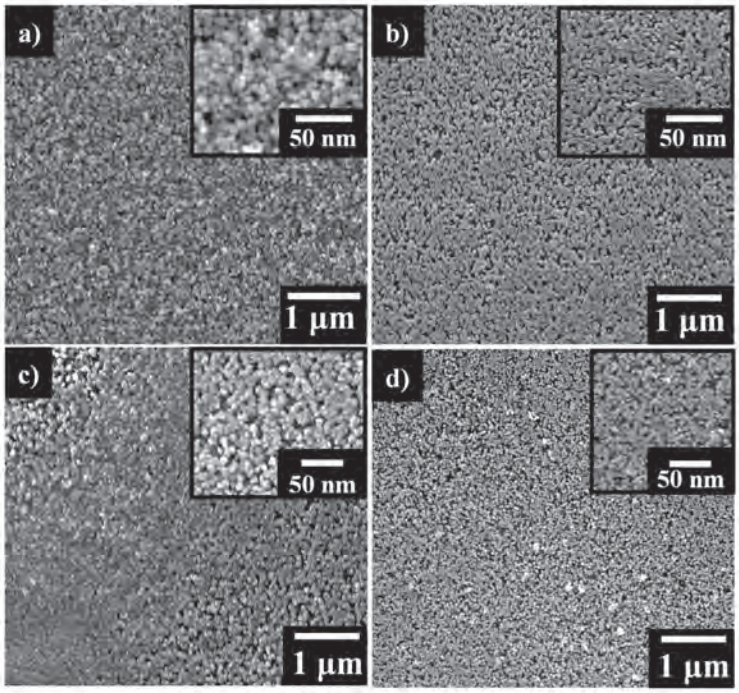

Fig. 4. SEM images of Cu_2ZnSnS_4 films annealed at different conditions: (a) 450 °C for 30 min, (b) 450 °C for 45 min, (c) 500 °C 30 for min and (d) 500 °C for 45 min.

4.4. Morphology and elemental composition

Fig. 4 shows surface scanning electron microscopy (SEM) images of CZTS films annealed at 450 °C and 500 °C for 30 and 45 min. In all cases, the films show granular texture. The surface morphology largely depends on annealing condition. For annealing at 450 °C during 30 min, the surface is composed of small spherical grains and shows uniform, compact and dense texture (Fig. 4a). With the increase in annealing time up to 45 min (Fig. 4b), the small spheres begin to merge with each other showing interconnected network with some voids on the surface. The particle shape changes from spherical to irregular form as can be seen in the inset of Fig. 4b.

The film annealed at 500 °C for 30 min shows dense and homogeneous surface morphology constituted by irregular-shaped particles (Fig. 4c). While, annealing up to 45 min made the surface more porous with tiny spherical grains distributed all over the substrate (Fig. 4d).

The change in surface morphology can be expected to have a significant impact on electrical properties of the films; the densely packed films lead to effective grain boundary passivation resulting in increased electrical conductivity and higher mobility (Rodriguez-Lazcano et al., 2009).

The chemical composition of the CZTS film has great influence on the device performance. One of the common feature for CZTS solar cells with improved device parameters is the non-stoichiometric composition of the CZTS layer; the ideal ratio of Cu:Zn:Sn:S in CZTS is 2:1:1:4, with Cu/(Zn + Sn) = 1, Zn/Sn = 1 and S/(Cu + Zn + Sn) = 1. However, most of the kesterite solar cells with Cu/(Zn + Sn) ratio between 0.75 and 1, and Zn/Sn ratio in the range of 1 to 1.25 showed enhanced performance with efficiencies higher than 8% (Katagiri et al., 2009; Wang, 2011). The difficulty to make Cu-poor and Zn-rich composition is the narrow phase stability in the Cu-deficient region and tendency to form secondary phases which become further complicated by volatile nature of Sn during the synthesis of Cu-poor CZTS (Mendis et al., 2012). In the present work, all the samples exhibit slightly Cu rich as well as Zn rich composition as summarized in Table 1. It is worth to note that the samples annealed at 450 °C showed the ratio of Cu/(Zn + Sn) < 1 and Zn/Sn > 1 while for annealing at 500 °C, this ratio is slightly greater than 1. In all the annealed samples the ratio of S/metal < 1 which is due to the volatile nature of S at higher annealing temperature.

A representative EDS spectra of CZTS film annealed at 450 °C for 45 min is presented in Fig. 5 showing the intense peaks of the constituent elements belonging to Cu2ZnSnS4.

However, we can observe the presence of Si, Na and Ca which may arise from the glass substrate, while the less intense peak corresponding to C may originate from the chemical reagents used in the synthesis.

In order to verify the homogeneous distribution of four elements in the CZTS films, EDS mapping was performed. Fig. 6a and 6b show SEM-EDS elemental mapping in the CZTS films annealed at 450 °C and 500 °C for 45 mins respectively. The EDS analysis suggests that the four constituent elements Cu, Zn, Sn and S are evenly distributed throughout the films.

4.5. Optical properties

The absorption capacity of CZTS thin films was determined from diffuse reflectance spectrum recorded in the wavelength range of 200–1600 nm. Fig. 7 shows Tauc plot of $[F(R_\infty)h\nu]^2$ vs $h\nu$ for different CZTS films. The reflectance data were treated using the Kubelka-Munk formalism to convert them into Kubelka-Munk function or equivalent absorption coefficient, $F(R_\infty)$, with the help of following equation (Murphy, 2007):

$$F(R_\infty) = \frac{(1 - R_\infty)^2}{2R_\infty} = \frac{k}{s} \quad (2)$$

where k is the effective absorption coefficient and s is the effective dispersion coefficient of the sample. It is assumed that the dispersion coefficient is constant in the measured wavelength region and, therefore, is a scale factor. $R_\infty = R_{sample}/R_{reference}$; in the present work we have used teflon as reference. The Kubelka-Munk function is directly proportional to the absorption coefficient α. The optical band gap for direct allowed transition can be estimated from $[F(R_\infty)]^2$ using the following equation:

$$F(R_\infty)^2 = A(h\nu - E_g) \quad (3)$$

where A is a constant, $h\nu$ is the photon energy and the E_g is the band gap.

The band gap was deduced by extrapolating the linear portion of the plot to photon energy axis and found to be 1.37 and 1.41 eV for the films annealed at 450 and 500 °C during 30 min, while 1.26 and 1.32 eV for annealing at 450 and 500 °C during 45 min respectively. The obtained values are in good agreement with earlier reported values for CZTS films (Grenet et al., 2014).

4.6. Electrical properties

To evaluate the electrical properties of CZTS films Hall effect measurements were carried out and the obtained parameters such as resistivity, carrier concentrations and Hall mobility are summarized in the Table 2. All the samples exhibit p-type conductivity as determined from Hall voltage. The resistivity varied from 7.38 to 190 Ω-cm which is found to be highly dependent on Cu content in the samples. As can be seen, resistivity reduced gradually with the increase of Cu concentration. The carrier concentration in the films annealed at 450 °C is in the range of 10^{16}–10^{17} cm^{-3} with relatively low mobility, whereas for the samples annealed at 500 °C, the bulk concentration varies in between 10^{17}–10^{19} cm^{-3} with higher carrier mobility. The values obtained here fall in the range of previously reported values for ink-deposited CZTS films (Ghediya et al., 2016). The dominant p-type acceptor in kesterite CZTS is due to the Cu_{Zn} antisite defect. For Cu-rich stoichiometry, as is the case with our CZTS films annealed at 500 °C, relatively higher concentration of Cu_{Zn} antisite defect produces larger concentration of hole carriers as well as an excess of $2Cu_{Zn} + Sn_{Zn}$ trap electrons (minority carriers) which may limit the solar cell efficiency with Cu-rich composition (Chen et al., 2013). To analyze the performance of our CZTS films in a single heterojunction solar, numerical simulation has been explored using specialized software called SCAPS-1D.

5. Simulation methodology

5.1. Numerical modeling

To perform the numerical simulation, we have used SCAPS 2.7.03.

Table 1
Elemental composition of CZTS films prepared at different annealing conditions.

Sample	Cu (at %)	Zn (at %)	Sn (at %)	S (at %)	Cu/(Zn + Sn)	Zn/Sn	S/metal
450 °C 30 min	28.10	17.98	13.49	40.43	0.89	1.33	0.68
450 °C 45 min	27.35	16.59	13.21	42.85	0.91	1.25	0.74
500 °C 30 min	29.71	13.73	13.41	43.15	1.09	1.02	0.75
500 °C 45 min	28.18	16.14	11.78	43.9	1.00	1.37	0.78

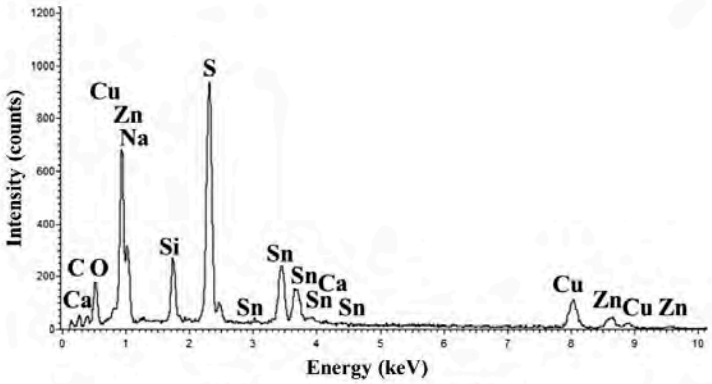

Fig. 5. Representative EDS spectrum of CZTS films.

software developed by the Department of Electronic and Information System at University of Gent, Belgium. SCAPS is a very useful numerical tool to model thin film solar cell and has been designed to simulate electrical characteristics of single heterojunction solar cell with the further possibility to extend for tandem solar cell structures (Gupta and Dixit, 2018). The model is based on solving the basic semiconductor equations (Poisson equation and the electron and hole continuity equations) (Sze and Lee, 2012) using appropriate boundary conditions at the interfaces and contacts; these set of equations result in a system of coupled differential equations which after being resolved provide the most important device parameters such as open circuit voltage (V_{OC}), short circuit current density (J_{SC}), fill factor (FF) and efficiency (η).

5.2. Device structure and simulation approach

We considered single junction solar cell in substrate configuration which is constructed by the following layers: molybdenum (Mo) as back metal contact (due to its good electrical conductivity and high optical reflectivity), CZTS as p-type absorber layer, CdS as n-type buffer layer, ZnO (n-type) as window layer as well as the passivation layer and finally Al doped ZnO (ZnO: Al) as transparent conducting oxide layer (TCO) which actually serves as front contact (Fig. 8).

The proposed model structure was implemented to SCAPS simulation software using the material properties for each layer and certain device parameters such as operating temperature, series resistance (R_s) and shunt resistance (R_{sh}) used in this simulation (Tables 3 and 4). Except for CZTS layer, the material properties of other layers used in

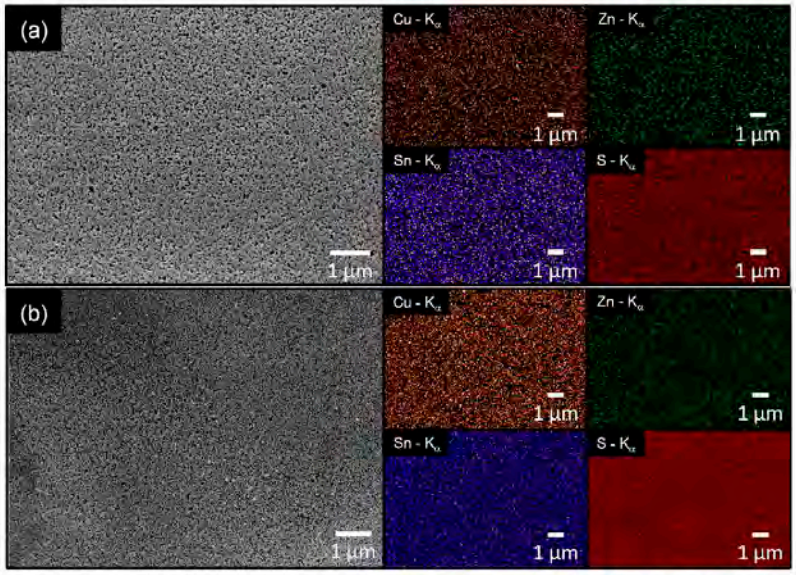

Fig. 6. EDS elemental maps of Cu, Zn, Sn and S along with corresponding microstructure for CZTS films: (a) 450 °C for 45 min and (b) 500 °C for 45 min. All mapping was done with 500 s of acquisition time.

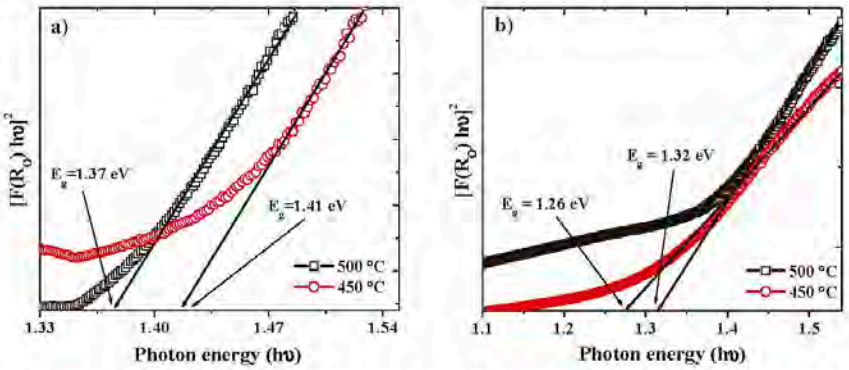

Fig. 7. The plots of $[F(R_\infty)h\upsilon]^2$ vs hυ to estimate the optical band gaps of CZTS thin films annealed at 450 and 500 °C for (a) 30 min and (b) 45 min.

Table 2
Electrical properties of CZTS films obtained from Hall measurements.

Annealing CZTS films	Bulk concentration ($1/cm^3$)	Resistivity (Ω-cm)	Conductivity $(\Omega\text{-cm})^{-1}$	Mobility (cm^2/Vs)
Time 30 min				
450 °C	2.58×10^{17}	6.04×10^{1}	1.71×10^{-2}	1.41
500 °C	1.72×10^{19}	7.88	1.36×10^{-1}	5.28
Time 45 min				
450 °C	6.65×10^{16}	1.9×10^{2}	1.6×10^{-3}	10.6
500 °C	8.72×10^{17}	18.6	5.5×10^{-2}	19.4

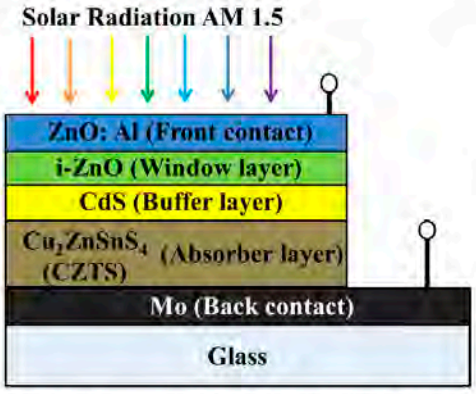

Fig. 8. Schematic representation of Al: ZnO/ZnO/CdS/CZTS/Mo single junction solar cell used to simulate the photovoltaic parameters.

this simulation were taken from theory, literature values and in some cases based on reasonable estimations. In the case of the absorber layer, we used experimentally obtained parameters of our CZTS film such as thickness, band gap, effective density of states in valence and conduction band, Hall mobility and free carrier concentration considering uniform acceptor density. On the other hand, we considered the thickness of CdS, i-ZnO and ZnO: Al as 80 nm, 50 nm and 200 nm respectively. In this simulation, the spectrum was set to the global AM1.5 standard and the operation temperature was maintained at 300 K. In polycrystalline chalcopyrite solar cells, the radiative recombination is believed to be a major contributor in limiting power conversion efficiency, and therefore in the present simulation, we considered the effect of radiative recombination coefficient as 5×10^{-9} cm^3/s and the effect of Auger recombination coefficient for holes and electrons as 1×10^{-29} cm^6/s (Simya et al., 2015). In order to obtain high efficiency solar cells, it is desirable to achieve low series resistance (R_s) and high shunt resistance (R_{sh}). The threshold voltage and the short circuit current are further reduced when series resistance increases, thereby affecting adversely the device efficiency. Even if R_s is assumed to be zero, R_{sh} tends to infinity; so it is not possible to achieve 100% fill factor due to imperfect diode behavior of a solar cell. In this case we consider the series resistance of 4.25 Ω cm^2 and the shunt resistance of 370 Ω cm^2 (Karagiri et al., 2008).

The effective density of states of conduction and valence bands of CZTS was determined using the Eqs. (4) and (5) respectively and the values are shown in Table 3.

$$N_C = 2\left[\frac{2\pi m_e^* kT}{h^2}\right]^{3/2} \quad (4)$$

$$N_V = 2\left[\frac{2\pi m_h^* kT}{h^2}\right]^{3/2} \quad (5)$$

Where m_e^* and m_h^* are the effective mass of electron and hole for p-CZTS, k is the Boltzmanns constant, T is the temperature and h is the Planks constant.

The open circuit voltage (V_{OC}) and the short circuit current density (J_{SC}) are related to carrier concentration in the way that increased carrier concentration reduce the minority carrier life time, implying more recombination and thus, reducing the collection of charge carriers at the contacts. Furthermore, an increased carrier concentration decreases the depletion width towards absorber layer, which reduces the effective separation of photogenerated charge carrier and causes a reduction in the short circuit current density (J_{SC}). The open circuit voltage (V_{OC}) initially increases with the increment in carrier concentration, but later it tends to decrease, because of the compensating nature of donor type defects considered for the system. The carrier concentration in CZTS is considered as N_A because CZTS is an intrinsic semiconductor type-p; therefore, the doping donor concentration N_D is equal to zero. Actually, N_A value is one of the important parameters for any p-n junction device. As carrier concentration increases the semiconductor becomes degenerate which results in the loss of semiconducting properties and an eventual transition to a metallic regime (Mott transition). In addition, higher acceptor concentration (N_A) brings impact on the electric field build-up within the space charge region. A higher electric field reduces the free carrier recombination

Table 3
Basic material parameters used in the simulation. PS: Present study (Gupta et al., 2018)[a]; (Sinya et al., 2015)[b]; (Adachi, 2015)[c].

Material properties	CZTS	CdS	i-ZnO	ZnO: Al (AZO)
Thickness (μm)	5.5–7.5; PS (section 3.1)	0.08	0.05	0.2 [a]
Band Gap [eV]	1.26–1.41; PS	2.42 [a]	3.3 [b]	3.3 [a]
Electron affinity [eV]	4.3 [c]	4.5 [a]	4.4 [b]	4.6 [a]
Dielectric permittivity	6.95 [c]	9 [a]	9 [b]	9 [a]
(Conduction band) effective density of states [cm^{-3}]	1.92×10^{18} (Eq. (4))	1.8×10^{19} [a]	2.2×10^{18} [b]	2.2×10^{18} [a]
(Valence band) Effective density of states [cm^{-3}]	1.504×10^{19} (Eq. (5))	2.4×10^{18} [a]	1.8×10^{19} [b]	1.8×10^{19} [a]
Thermal velocity of electron [cm/s]	1×10^{7} [b]	1×10^{7} [a]	1×10^{7} [b]	1×10^{7} [a]
Thermal velocity of hole [cm/s]	1×10^{7} [b]	1×10^{7} [a]	1×10^{7} [b]	1×10^{7} [a]
Electron mobility [cm^2/Vs]	100 [b]	160 [a]	100 [b]	100 [a]
Hole mobility [cm^2/Vs]	See Table 4	50 [a]	25 [b]	25 [a]
Donor concentration [cm^{-3}]	0	1×10^{17} [a]	1×10^{15}	1×10^{20} [a]
Acceptor concentration [cm^{-3}]	See Table 3; PS	0 [a]	1×10^{15}	0 [a]
Defect type absorber/buffer	Donor/Acceptor	–	–	–
Defect type buffer/Windows	Acceptor	–	–	–
Absorption coefficient	SCAPS	SCAPS	SCAPS	SCAPS

leading to an increase in V_{OC}, which thus reduces the magnitude of the J_{SC}. The limit of carrier acceptor concentration in CZTS is approximately 1.9×10^{18} cm^{-3} which has been calculated by considering the following Mott criterion (Mott, 1968) (6):

$$a_B^*(N_C)^{1/3} \approx 0.2 \tag{6}$$

where, N_C is the critical doping concentration in the semiconductor above which it would behave as a metal, a_B^* is the effective Bohr radius of hydrogen-like donor/acceptor and this value can be estimated by the following Eq. (7):

$$a_B^* = a_B\left(\frac{\epsilon_r}{m_e^*}\right) \tag{7}$$

where, $a_B \approx 0.5$Å is the hydrogen Bohr radius, ϵ_r is the relative permittivity of semiconductor and m_e^* is the effective mass of the electrons, in this case the relative permittivity of CZTS is approximately 6.95 (Adachi, 2015) and the effective mass of the electrons is $m_e^*/m_0 = 0.18$, where m_0 is the rest mass of electron.

Fig. 9 shows the simulated current density vs voltage curves (J-V) of different CZTS solar cells. A maximum efficiency of 14.12% was achieved with CZTS film annealed at 450 °C for 45 min with $V_{OC} = 0.76$ V, $J_{SC} = 32.04$ mA/cm^2 and FF = 57.80 %. While a relatively lower efficiency of 10.37 % was obtained for the solar cell using CZTS film annealed at 450 °C for 30 min. It is worth to mention that solar cell simulation with the CZTS films annealed at 500 °C did not converge in SCAPS which is probably due to the relatively high carrier concentration in these films.

Fig. 9 shows the energy band diagram for the optimum solar cell showing the best performance. The band diagram is taken from the output of SCAPS-1D for analysis purpose. One of the most important aspect of a semiconductor heterojunction is the energy-band alignment which largely influences the transport phenomena across the interface. The misalignment of the conduction bands (ΔE_c) is determined by the electron affinity χ of both materials, known as Anderson affinity rule (Bergelmon, 2006) (8):

$$\Delta E_C = E_C^{CZTS} - E_C^{CdS} = \chi^{CdS} - \chi^{CZTS} \tag{8}$$

As can be observed in Fig. 10, there is a "cliff" at the interface of CdS/CZTS (buffer/absorber) with $\Delta E_c = 0.2$ eV. When exists a "cliff" in the band diagram, the conduction band minimum of the absorber layer locates above the conduction band minimum of the buffer layer which results into high hole concentration at the interface leading to an increased recombination and consequently a drop in V_{OC}. In the case of CZTS films annealed at 500 °C, the convergence failure can be associated with the larger carrier concentration, which further leads to the enhanced recombination at buffer/absorber interface limiting the open circuit voltage of the device.

6. Conclusion

In summary, the kesterite CZTS films were prepared by drop casting method using molecular precursor ink and the performance of the fabricated CZTS in single junction solar cell has been evaluated using SCAPS-1D simulation program. The as-deposited films were subjected to thermal annealing at 450 and 500 °C with a short pause at 350 °C for 15 min. The optimum annealing condition was found to be 450 °C for 45 min after a rigorous inspection of their structural, optical, compositional and electrical properties. Both XRD and Raman scattering confirmed the formation of single phase kesterite with good crystalline quality. The optimized film revealed a dense and compact surface morphology with suitable optical band gap and good electrical parameters for being considered as absorber layer in single heterojunction solar cell. Finally we simulated the device characteristics of CZTS solar cell in substrate configuration by implementing our experimental data of CZTS films. The maximum efficiency obtained was ~14% with open circuit voltage of 0.762 V. The present work provides a combination of theoretical and experimental study for engineering the heterojunctions and gives feedback for experimental optimization in achieving

Table 4
Operating device parameters used in simulation. (Adewoyin et al., 2019)[a].

Cell parameters		
Cell temperature		300 K
Shunt resistance (R_{sh})		370 Ω cm^2
Series resistance (R_s)		4.25 Ω cm^2
Contact	**Right contact (back)**	**Left contact (front)**
Work function	Mo 5 eV [a]	Flat band [a]
Surface recombination velocity of electron	1×10^{7} [a]	1×10^{7} [a]
Surface recombination velocity of hole	1×10^{7} [a]	1×10^{7} [a]

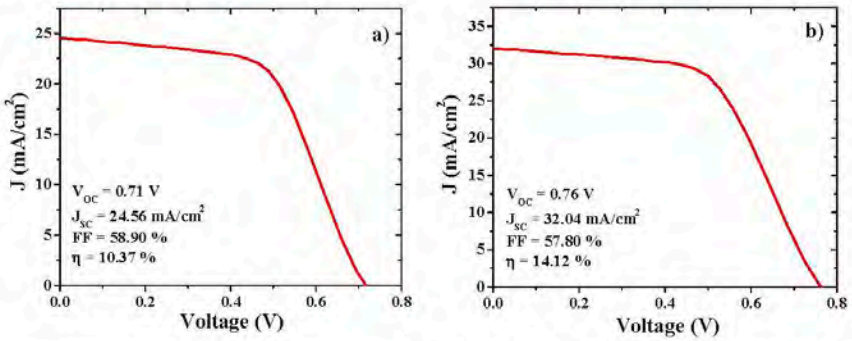

Fig. 9. Current-voltage (J-V) characteristics of single junction solar cell using different CZTS films: (a) 450 °C for 30 min; (b) 450 °C for 45 min. Simulated device parameters are inserted in the graph.

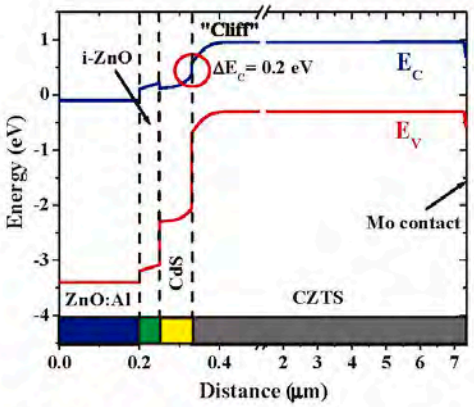

Fig. 10. Band diagram for the Solar Cell with the best performance.

enhanced performance of CZTS-based solar cells.

Declaration of Competing Interest

The authors declare that they have no known competing financial interests or personal relationships that could have appeared to influence the work reported in this paper.

Acknowledgement

D. Mora-Herrera (CVU 862194) and F.E. Cancino-Gordillo (CVU 784149) are thankful to CONACYT for extending doctoral scholarship in Materials Science. Financial helps offered by CONACYT, Mexico (Bilateral Grant #266406) and VIEP-BUAP (Grant # 100468355-BUAP 2019) are acknowledged.

References

Adachi, S., 2015. Earth-Abundant Materials for Solar Cells Cu_2–II–IV–VI_4 Semiconductors, first ed. John Wiley Sons Ltd.

Adelifard, M., Torkamani, R., 2015. Spray deposited Cu_2ZnSnS_4 nanostructured absorber layer: a promising candidate for solar cell applications. J. Mater. Sci.: Mater. Electron. 26 (6), 3700–3706.

Adewoyin, A.D., Olopade, M.A., Chendo, M., 2017. Enhancement of the conversion efficiency of Cu_2ZnSnS_4 thin film solar cell through the optimization of some device parameters. Optik 133, 122–131.

Adewoyin, A.D., Olopade, M.A., Oyebola, O.O., Chendo, M.A., 2019. Development of CZTGS/CZTS tandem thin film solar cell using SCAPS-1D. Optik 176, 132–142.

Aldalbahi, A., Mkawi, E.M., Ibrahim, K., Farrukh, M.A., 2016. Effect of sulfurization time on the properties of copper zinc tin sulfide thin films grown by electrochemical deposition. Sci. Rep. 6, 32431.

Andersson, B.A., Azar, C., Holmberg, J., Karlsson, S., 1998. Material constraints for thin-film solar cells. Energy 23 (5), 407–411.

Andersson, B.A., Azar, C., Holmberg, J., Karlsson, S., 2000. Materials availability for large-scale thin-film photovoltaics. Prog. Photovolt. Res. Appl. 8, 61–76.

Aslan, F., Göktaş, A., Tumbul, A., 2016. Influence of pH on structural, optical and electrical properties of solution processed Cu_2ZnSnS_4 thin film absorbers. Mater. Sci. Semicond. Process. 43, 139–143.

Benzetta, A.E.H., Abderrezek, M., Djeghlal, M.E., 2019. Contribution to improve the performances of Cu_2ZnSnS_4 thin-film solar cell via a back surface field layer. Optik 181, 220–230.

Burgelman, M., 2006. Thin film solar cells fabrication. Characteriz. Appl. 277–324.

Caballero, R., García-Llamas, E., Merino, J.M., León, M., Babichuk, I., Dzhagan, V., Strelchuk, V., Valakh, M., 2014. Non-stoichiometry effect and disorder in Cu_2ZnSnS_4 thin films obtained by flash evaporation: Raman scattering investigation. Acta Mater. 65, 412–417.

Cázzaniga, A., Crovetto, A., Yan, C., Sun, K., Hao, X., Ramis Estelrich, J., Canulescu, S., Stamate, E., Pryds, N., Hansen, O., Schou, J., 2017. Ultra-thin Cu_2ZnSnS_4 solar cell by pulsed laser deposition. Sol. Energy Mater. Sol. Cells 166, 91–99.

Chen, R., Fan, J., Liu, C., Zhang, X., Shen, Y., Mai, Y., 2016. Solution-processed one-dimensional ZnO@CdS heterojunction toward efficient Cu_2ZnSnS_4 solar cell with inverted structure. Sci. Rep. 6, 1–9.

Chen, S., Walsh, A., Gong, X.G., Wei, S.H., 2013. Classification of lattice defects in the kesterite Cu_2ZnSnS_4 and $Cu_2ZnSnSe_4$ earth-abundant solar cell absorbers. Adv. Mater. 25 (11), 1522–1539.

Diwate, K., Mohite, K., Shinde, M., Rondiya, S., Pawbake, A., Date, A., Pathan, H., Jadkar, S., 2017. Synthesis and characterization of chemical spray pyrolysed CZTS thin films for solar cell applications. Energy Procedia 110, 180–187.

Fernandes, P.A., Salomé, P.M.P., Da Cunha, A.F., 2011. Study of polycrystalline Cu_2ZnSnS_4 films by Raman scattering. J. Alloy. Compd. 509 (28), 7600–7606.

García-Llamas, E., Merino, J.M., Serna, R., Fontané, X., Victorov, I.A., Pérez-Rodríguez, A., León, M., Bodnar, I.V., Izquierdo-Roca, V., Caballero, R., 2016. Wide band gap tuning $Cu_2ZnSn_{1-x}Ge_xS_4$ single crystals: optical and vibrational properties. Sol. Energy Mater. Sol. Cells 158, 147–153.

Ghediya, P.R., Chaudari, T.K., Vankhade, D., 2016. Electrical conduction of CZTS films in dark and under light from molecular solution ink. J. Alloy. Compd. 685, 498–506.

Giraldo, S., Neuschitzer, M., Thersleff, T., López-Marino, S., Sánchez, Y., Xie, H., Colina, M., Placidi, M., Pistor, P., Izquierdo-Roca, F., Leifer, K., Pérez-Rodríguez, A., Saucedo, E., 2015. Large efficiency improvement in $Cu_2ZnSnSe_4$ Solar cells by introducing a superficial Ge nanolayer. Adv. Energy Mater. 5 (21), 1–6.

Giraldo, S., Saucedo, E., Neuschitzer, M., Oliva, F., Placidi, M., Alcobé, X., Izquierdo-Roca, V., Kim, S., Tampo, K., Shibata, H., Pérez-Rodríguez, A., Pistor, P., 2018. How small amounts of Ge modify the formation pathways and crystallization of kesterites. Energy Environ. Sci. 11 (3), 582–593.

Green, M.A., Dunlop, E.D., Levi, D.H., Hohl-Ebinger, J., Yoshita, M., Ho-Baillie, A.W.Y., 2019. Solar cell efficiency tables (Version 54). Prog. Photovolt. Res. Appl. 27, 565–575.

Grenet, L., Fillon, R., Altamura, G., Fournier, H., Emieux, F., Faucherand, P., Perraud, S., 2014. Analysis of photovoltaic properties of $Cu_2ZnSn(S, Se)_4$ based solar cells. Sol. Energy Mater. Sol. Cells 126, 135–142.

Guchhait, A., Su, Z., Tay, Y.F., Shukla, S., Li, W., Leow, S.W., Tan, J.M.R., Lie, S., Gunawan, O., Wong, L.H., 2016. Enhancement of open-circuit voltage of solution-processed Cu_2ZnSnS_4 solar cells with 7.2% efficiency by incorporation of silver. ACS Energy Lett. 1, 1256–1261.

Gupta, G.K., Dixit, A., 2018. Theoretical studies of single and tandem $Cu_2ZnSn(S/Se)_4$

junction solar cells for enhanced efficiency. Opt. Mater. 82, 11–20.
Ito, K. Copper, 2015. Zinc Tin sulfide-based thin film solar cells, first ed. John Wiley Sons Ltd.
Jiang, C., Liu, W., Talapin, D.V., 2014. Role of precursor reactivity in crystallization of solution-processed semiconductors: the case of Cu_2ZnSnS_4. Chem. Mater. 26 (13), 4038–4043.
Katagiri, H., Jimbo, K., Yamada, S., Kamimura, T., Maw, W.S., Fukano, T., Ito, T., Motohiro, T., 2008. Detailed balance limit of efficiency of p-n junction solar cells. Appl. Phys. Express 1, 41201.
Katagiri, H., Jimbo, K., Maw, W.S., Oishi, K., Yamazaki, M., Araki, H., Tekeuchi, A., 2009. Development of CZTS-based thin film solar cells. Thin Solid Films 517, 2455–2460.
Katagiri, H., Saitoh, K., Washio, T., Shinohara, H., Kurumadani, T., Miyajima, S., 2001. Development of thin film solar cell based on Cu_2ZnSnS_4 thin films. Sol. Energy Mater. Sol. Cells 65, 141–148.
Khadka, D.B., Kim, J.H., 2015. Band gap engineering of alloyed $Cu_2ZnGe_2Sn_{1-x}Q_4$ (Q = S, Se) films for solar cell. J. Phys. Chem. C 119 (4), 1706–1713.
Kim, I., Kim, K., Oh, Y., Woo, K., Cao, G., Jeong, S., Moon, J., 2014a. Bandgap-graded $Cu_2Zn(Sn_{1-x}Ge_x)S_4$ thin-film solar cells derived from metal chalcogenide complex ligand capped nanocrystals. Chem. Mater. 26 (13), 3957–3965.
Kim, K., Kim, I., Oh, Y., Lee, D., Woo, K., Jeongc, S., Moon, J., 2014b. Influence of precursor type on non-toxic hybrid inks for high-efficiency Cu_2ZnSnS_4 thin-film solar cells. Green Chem. 16, 4323–4332.
Kodigala, S.R., 2014. Thin film solar cells from earth abundant materials growth and characterization of Cu2ZnSn(SSe)4 thin films and their solar cells, pp. 121–137.
Lin, X., Kavalakkatt, J., Ch. Lux-Steiner, M., Ennaoui, A., 2015. Inkjet-printed $Cu_2ZnSn(S, Se)_4$ solar cells. Adv. Sci. 2, 1500028.
Mendis, B.G., Goodman, M.C.J., Major, J.D., Taylor, A.A., Durose, K., Halliday, D.P., 2012. The role of secondary phase precipitation on grain boundary electrical activity in Cu_2ZnSnS_4 (CZTS) photovoltaic absorber layer material. J. Appl. Phys. 112 (12).
Mkawi, E.M., Ibrahim, K., Ali, M.K.M., Farrakh, M.A., Mohamad, A.S., 2014. Dependence of the properties of copper zinc tin sulfide thin films prepared by electrochemical deposition on sulfurization temperature. J Mater Sci: Mater Electron. 25, 857–863.
MOTT, N.F., 1968. Metal-insulator transition. Rev. Mod. Phys. 40 (4), 677–683. https://doi.org/10.1103/RevModPhys.40.677.
Murphy, A.B., 2007. Band-Gap determination from diffuse reflectance measurements of semiconductors films, and application to photoelectrochemical water-splitting. Sol. Energy Mater. Sol. Cells 91, 1326–1337.
Rodríguez-Lazcano, Y., Martínez, H., Calixto-Rodríguez, M., Núñez Rodríguez, A., 2009. Properties of CuS thin films treated in air plasma. Thin Solid Films 517 (21), 5951–5955.
Sánchez, T.G., Mathew, X., Mathews, N.R., 2016. Obtaining phase-pure CZTS thin films by annealing vacuum evaporated CuS/SnS/ZnS stack. J. Cryst. Growth 445, 15–23.
Scragg, J.J., Dale, P.J., Peter, L.M., 2009. Synthesis and characterization of Cu_2ZnSnS_4 absorber layers by an electrodeposition-annealing route. Thin Solid Films 517 (7), 2481–2484.
Shi, C., Shi, G., Chen, Z., Yang, P., Yao, M., 2012. Deposition of Cu_2ZnSnS_4 thin films by vacuum thermal evaporation from single quaternary compound source. Mater. Lett. 73, 89–91.
Shin, B., Gunawan, O., Zhu, Y., Bojarczuk, N.A., Chey, S.J., Guha, S., 2013. Thin film solar cell with 8.4% power conversion efficiency using an earth-abundant Cu_2ZnSnS_4 absorber. Prog. Photovolt: Res. Appl. 21, 72–76.
Simya, O.K., Mahaboobbatcha, A., Balachander, K., 2015. A comparative study on the performance of Kesterite based thin film solar cells using SCAPS simulation program. Superlattices Microstruct. 82, 248–261.
Simya, O.K., Mahaboobbatcha, A., Balachander, K., 2016. Compositional grading of CZTSSe alloy using exponential and uniform grading laws in SCAPS-1D simulation. Superlattices Microstruct. 92, 285–293.
Sugimoto, H., Liao, C., Sakai, N., Kato, T., 2013. In: 39th IEEE Photovoltaic Specialists Conference At: Tampa, Florida, USA, Vols. 3208–3211.
Sze, S.M., Lee, M.K., 2012. Semiconductor devices physics and technology, third ed. John Wiley Sons Ltd.
Tanaka, K., Shinji, T., Uchiki, H., 2014. Photoluminescence from Cu_2ZnSnS_4 thin films with different compositions fabricated by a sputtering-sulfurization method. Sol. Energy Mater. Sol. Cells 126, 143–148.
Vigil-Galán, O., Espíndola-Rodríguez, M., Courel, M., Fontané, X., Sylla, D., Izquierdo-Roca, V., Fairbrother, A., Saucedo, E., Pérez-Rodríguez, A., 2009. Secondary phases dependence on composition ratio in sprayed Cu_2ZnSnS_4 thin films and its impact on the high power conversion efficiency. Sol. Energy Mater. Sol. Cells 117, 246–250.
Wang, H., 2011. Progress in thin film solar cells based on Cu_2ZnSnS_4. Int. J. Photoenergy 11, 1–10.
Wang, W., Winkler, M.T., Gunawan, O., Gokmen, T., Todorov, T.K., Zhu, Y., Mitzi, D.B., 2014. Device characteristics of CZTSSe thin-film solar cells with 12.6% efficiency. Adv. Energy Mater. 4 (7), 1–5.
Wang, X., Sun, S., Zhang, Y.Z., Sun, Y., Liu, J., Wang, H., 2015. Dimethyl sulfoxide-based ink for the fabrication of $Cu_2ZnSn(S, Se)_4$ thin film. Mater. Lett. 138, 265–267.
Xin, H., Vorpahl, S.M., Collord, A.D., Braly, I.L., Uhl, A.R., Krueger, B.W., Gingerbc, D.S., Hillhouse, H.W., 2015. Lithium-doping inverts the nanoscale electric field at the grain boundaries in $Cu_2ZnSn(S, Se)_4$ and increases photovoltaic efficiency. PCCP 17 (37), 23859–23866.
Yang, Y., Kang, X., Huang, L., Wei, S., Pan, D., 2015. Facile and low-cost sodium-doping method for high-efficiency $Cu_2ZnSnSe_4$ thin film solar cells. J. Phys. Chem. C 119 (40), 22797–22802.
Zhang, J., Jung, Y., 2018. Advanced ceramic and metallic coating and thin film materials for energy and environmental applications, pp. 121–175.

Applied Surface Science 571 (2022) 151261

Contents lists available at ScienceDirect

Applied Surface Science

journal homepage: www.elsevier.com/locate/apsusc

Full Length Article

Structure and transport behavior of hydrothermally grown phase pure $Cu_2ZnSn_{1-x}Ge_xS_4$ (x = 0.0, 0.3) nanoparticles

Francisco Enrique Cancino-Gordillo, Julio Villanueva Cab, Umapada Pal*

Instituto de Física, Benemérita Universidad Autónoma de Puebla, Apdo. Postal J 48, Puebla, Pue. 72570, Mexico

ARTICLE INFO

Keywords:
$Cu_2ZnSn_{1-x}Ge_xS_4$ nanoparticles
Kesterite
Band tails
Hydrothermal synthesis
Electrical properties

ABSTRACT

Phase pure Cu_2ZnSnS_4 (CZTS) and $Cu_2ZnSn_{0.7}Ge_{0.3}S_4$ (CZTGS) kesterite nanoparticles of 10–35 nm size range were fabricated through a low-temperature hydrothermal process. Morphology, structure, and structural phase of the nanoparticles were determined utilizing field-emission scanning electron microscopy (FE-SEM), X-ray diffraction (XRD) and Raman spectroscopy. Electrical transport behaviors of the pelletized nanostructures were studied in a physical properties measurement system (PPMS) in the 100–320 K temperature range. Obtained results indicate that both the CZTS and CZTGS nanostructures have p-type conductivity, with high room temperature hole concentration and carrier mobility. Substitution of 30% Sn by Ge enhances the electrical conductivity of CZTS about four times. While the room temperature hole mobility in the kesterite nanostructures reduces to about 60%, the hole concentration increases about one order on Ge incorporation. The limited substitution of Sn atoms by Ge does not affect the position of acceptor levels in the electronic band gap of the kesterite nanostructures. However, it increases the concentration of Cu_{Zn} and Zn_{Cu} antisite defects and affects the transition temperature where the electrical transport of kesterite nanostructures changes from lattice scattering controlled to defect scattering controlled conduction.

1. Introduction

The quaternary chalcogenide Cu_2ZnSnS_4 (CZTS) is an attractive material for utilization in the absorber layers of thin film solar cells, with potential for replacing conventional absorber materials such as CdTe and $CuIn_xGa_{1-x}S_2$ (CIGS). CZTS is an intrinsic p-type semiconductor containing earth-abundant elements of low toxicity with a direct optical band gap energy close to 1.5 eV and high optical absorption coefficient in the visible spectra range ($\sim 10^4$ cm^{-1}) [1–5]. Currently the certified record efficiency of quaternary chalcogenide solar cells fabricated using sulfur (CZTS) and selenium (CZTSe) are 11.1% [6] and 12.6% [7], respectively, which are still much lower than the maximum efficiency of CIGS solar cells which is above 25% [8]. Generally, CZTS kesterite contains several intrinsic defects induced by off-stoichiometric composition (i.e., Cu/(Zn + Sn) < 1.0 and Zn/Sn > 1.0), which significantly influence its electrical and optical behaviors. The defects include Cu, Zn, Sn or S vacancies (V_{Cu}, V_{Zn}, V_{Sn}, or V_s), copper and zinc interstitials (Cu_i and Zn_i), anti-sites (Cu_{Zn}, Zn_{Cu}, Zn_{Sn}, Cu_{Sn}, Sn_{Cu}, Zn_{Sn} and Sn_{Zn}), and several defect complexes, depending on the deviation in cation ratio in the material [9–11]. Typically, CZTS thin films of Cu-poor and Zn-rich (Cu/(Zn + Sn) ≈ 0.8 and Zn/Sn ≈ 1.2) stoichiometry have been utilized in solar cells as these conditions generate V_{Cu} and Zn_{Cu} that increase the carrier concentration and conductivity of the absorber layer. On the other hand, the defects such as V_{Zn}, V_{Sn}, V_s, Sn_{Cu}, Sn_{Zn}, Cu_{Sn}, Zn_{Sn}, Cu_i, and Zn_i are unfavorable for solar cells, as they affect the charge recombination process negatively. Among these defects, Zn_{Cu} and Cu_i form shallow donor levels near the conduction band, while V_{Zn}, V_{Sn}, V_s, Sn_{Cu}, Sn_{Zn}, Cu_{Sn}, Zn_{Sn} and Zn_i form deep-level states in the band gap, acting as trapping or recombination centers. Formation of recombination centers causes a reduction of carrier lifetime, resulting in an increase of dark current (J_0) of solar cells and hence reduces its open circuit voltage (V_{OC}). In fact, one of the limitations of kesterite CZTS in solar cell application is the large deficit in V_{OC} because of several nonideal recombination losses at deep-level states [8,12]. The principal cause of recombination loss in kesterite CZTS is the change in the oxidation state of Sn from +4 to +2 during device operation under illumination. The change in the oxidation state of Sn occurs due to the perturbation of charge balance in crystal lattice during the generation of photoinduced charge carriers. From the solar cell application point of view, the reduction of Sn^{4+} to Sn^{2+} is equivalent to the formation of an

* Corresponding author.
E-mail address: upal@ifuap.buap.mx (U. Pal).

https://doi.org/10.1016/j.apsusc.2021.151261
Received 15 April 2021; Received in revised form 23 August 2021; Accepted 9 September 2021
Available online 17 September 2021
0169-4332/

electron trap inside the band gap. The reduction can occur in two ways; the first is when Sn^{4+} is reduced in its native crystallographic position (Sn_{Sn}) and the second is when Sn^{4+} is reduced in a defect site, such as an antisite. When Sn occupies the Zn site, a Sn_{Zn} antisite defect is formed, which can produce two types of deep levels depending on the oxidation state of Sn. When Sn has an oxidation state 4+, the Sn_{Zn} antisite defect forms a double donor (Sn_{Zn}^{2+}) state inside the band gap, which can trap photogenerated electrons, reducing Sn^{4+} ion to Sn^{2+}. On the other hand, when the Sn atom has oxidation state 2+, the Sn_{Zn} antisite defect forms an isoelectronic center (Sn_{Zn}^{0}) that can trap holes [12]. Therefore, for applying CZTS in solar cell efficiently, it must be grown under the conditions that reduce the possibility of formation of antisite defect centers and the reduction of Sn^{4+} to Sn^{2+}. In this regard, a partial substitution of Sn by an element of the same group with a unique oxidation state such as Ge, is considered as a viable solution to this problem [13–18].

Incorporation of Ge in CZTS causes the formation of $Cu_2ZnSn_{1-x}Ge_xS_4$ (CZTGS) and inhibits the formation of unfavorable defects such as V_{Sn}, Cu_{Sn}, Sn_{Cu}, Zn_{Sn}, Sn_{Zn} due to the unique oxidation state of Ge and its small radius [8,12,19,20]. The tetravalent Ge^{4+} ion cannot exchange electrons with the cations such as Zn^{2+} and Cu^{1+} as occurs in the Sn^{2+} case. Furthermore, the most stable oxidation state of Ge is 4+, so the transformation from Ge^{4+} to Ge^{2+} state hardly occurs. Hages et al. synthesized $Cu_2Zn(Sn_{1-y}Ge_y)(S_xSe_{1-x})_4$ nanocrystals replacing 0% ($Cu_2ZnSnS_{0.2}Se_{3.8}$) and 30% ($Cu_2ZnSn_{0.7}Ge_{0.3}S_{0.2}Se_{3.8}$) of Sn by Ge for utilizing in solar cells [16]. The solar cells fabricated with the former sample revealed 0.41 V open circuit voltage (V_{oc}) with 8.4% internal conversion efficiency, while the cells fabricated with the latter sample revealed 0.46 V open circuit voltage and 9.4% internal conversion efficiency. On the other hand, Giraldo et al. reported a conversion efficiency of 10.1% and 0.453 V open circuit voltage for their solar cells fabricated with sputter deposited $Cu_2ZnSn_{0.8}Ge_{0.2}Se_4$ thin film [17]. Recently, Shinho et al. reported a record ~12.3% of internal conversion efficiency with 0.527 V open circuit voltage for their solar cells fabricated using $Cu_2ZnSn_{0.78}Ge_{0.22}Se_4$ thin films [18]. In all the above mentioned works, the authors reported an enhancement of V_{oc} due to partial substitution of Sn by Ge.

Furthermore, the direct optical band gap energy of CZTS can be tuned by replacing Sn with Ge. On substitution of Sn by Ge, the optical band gap of $Cu_2ZnSn_{1-x}Ge_xS_4$ can be tuned from 1.5 to 2.2 eV in quasi-linear way with the increase of x value [19–23]. However, high concentration of Ge in $Cu_2ZnSn_{1-x}Ge_xS_4$ ($x \geq 0.25$) can generate its nanostructures or thin films with tetragonal (kesterite) and orthorhombic mixed phase [20]. Segregation of secondary phases such as ZnS and Cu_xS can also occur for $x \geq 0.8$ [13]. Moreover, substitution of Sn by Ge in high concentration induces deep-level defects due to the formation of Sn vacancies (V_{Sn}) [15,24]. Therefore, a limited substitution Sn by Ge ($x \leq 0.5$) is recommended for fabricating $Cu_2ZnSn_{1-x}Ge_xS_4$ nanostructures and thin films in pure kesterite phase with reduced defect contents [15].

Several researchers have tried to fabricate Cu_2ZnSnS_4 [25–29] and $Cu_2ZnSn_{1-x}Ge_xS_4$ [19,20,22,30] nanostructures with special attention on the control of stoichiometry, shape, size, and structural phase, encountering difficulties in preserving the kesterite phase for higher x values. Apart from synthesizing these nanostructures with controlled structure and composition, controlling electrical transport behavior is very important for their application in photovoltaic devices. While the room temperature electrical properties of $Cu_2ZnSn_{1-x}Ge_xS_4$ thin films prepared by physical deposition methods such as sputtering and thermal evaporation have been reported in the literature [31–34], only a few works have been published on the electrical behaviors of $Cu_2ZnSn_{1-x}Ge_xS_4$ nanocrystals [20,22,35]. Moreover, the works reported on the electrical properties of $Cu_2ZnSn_{1-x}Ge_xS_4$ nanostructures and nanostructured thin films correspond to their room temperature behaviors. As the pursuance of the development $Cu_2ZnSn_{1-x}Ge_xS_4$ nanostructures is basically meant for applying them in solar cells, which often operate in a variable temperature range depending on the geographical location and season change of the locations of application, it is important to know the electrical transport behavior of these nanostructures beyond room temperature. In fact, a study on the electrical transport behavior of $Cu_2ZnSn_{1-x}Ge_xS_4$ nanostructures at different temperatures is important not only in the context of their photovoltaic applications, but also to understand how the defect structures control carrier transport in them.

Here we present the electrical transport properties of $Cu_2ZnSn_{1-x}Ge_xS_4$ (x = 0.0 & 0.3) nanoparticles in the 100–320 K temperature range. The nanoparticles were grown by a low temperature hydrothermal process using germanium tetrachloride as a Ge precursor. The structure, crystallinity, and structural phases of the nanoparticles were analyzed by X-ray diffraction (XRD) and Raman spectroscopy. Morphology and elemental composition of nanoparticles were analyzed by scanning electron microscopy (SEM) and X-ray energy dispersive spectroscopy (EDS), respectively. Effect of Ge incorporation on the defect structure and transport behaviors of the CZTS nanocrystals are discussed. Incorporation of Ge is seen to cause an early transition from lattice scattering controlled conduction to hopping conduction due to an enhancement of Cu_{Zn} and Zn_{Cu} antisite defects concentration.

2. Experimental

2.1. Reactive & solvents

Zinc acetate dihydrate ($Zn(CH_3COO)_2{\cdot}2H_2O$, J.T. Baker, 99%), copper acetate ($Cu(CH_3COO)_2{\cdot}H_2O$, Sigma Aldrich, ≥98%), tin chloride pentahydrate ($SnCl_4{\cdot}5H_2O$, Sigma-Aldrich, 98%), germanium tetrachloride ($GeCl_4$, Sigma-Aldrich, 99.9999%), ethylenediamine ($C_2H_8N_2$, Sigma-Aldrich, ≥98%), sublimed sulfur powder (S, Fermont, 99.95%), and acetone (C_3H_6O, J.T. Baker, ≥99.5%) were acquired from the market. Deionized water from a Millipore system ($\rho > 10^{18}$ Ohm cm) was used for the synthesis of the fabricated nanostructures. All reagents were utilized as received, without further purification.

2.2. Fabrication of nanoparticles

A low-temperature hydrothermal process was adopted for the synthesis of Cu_2ZnSnS_4 (CZTS) and $Cu_2ZnSn_{0.7}Ge_{0.3}S_4$ (CZTGS) nanoparticles, following the method reported in the literature [22]. Due to the highly reactive nature of $GeCl_4$ towards atmospheric humidity, a $GeCl_4$–acetone mixture of 1:31 M ratio was prepared in a glove box under Ar atmosphere and magnetic stirring (6 h) to utilize as germanium precursor. A typical synthesis process included the dissolution of copper acetate (4 mmol), zinc acetate (2 mmol), germanium precursor ($GeCl_4$–acetone mixture) and tin chloride pentahydrate ($GeCl_4$ + $SnCl_4$ = 2.2 mmol) in 10 mL of deionized water under magnetic stirring. Separately, a sulfur solution was prepared by dissolving the sublimed sulfur powder (12 mmol) in 10 mL of ethylenediamine under magnetic stirring. The two solutions were mixed and transferred to a 30 mL Teflon container. The Teflon container was capped and placed inside a stainless steel autoclave. The sealed autoclave was placed inside a Lindberg Blue gravity furnace and heated to 200 °C (at 3 °C/min). After 24 h of heating, the reactor was cooled down to room temperature. The generated solid product was separated and washed repeatedly with acetone under centrifugation (7000 rpm, 10 min). Finally, the product was dried at 60 °C for 8 h and used for further characterizations.

2.3. Characterization

X-ray diffraction (XRD) patterns of the powder samples were recorded in a Bruker D8 Discover diffractometer using CuKα radiation (λ = 1.5406 Å). The spectra were recorded at 0.02°/step with a scan rate of 2°/step in the 2θ range 10–80°. The samples were inspected in a JEOL JSM-7800F field-emission scanning electron microscope (FE-SEM) coupled with X-Max (Oxford Instruments) spectrometer for energy dispersive spectroscopic (EDS) analysis. For the SEM-EDS analysis, the

samples were prepared by placing a drop of ethanol dispersed nanostructures over silicon substrate and drying at room temperature. After that, the silicon substrates covered with the nanoparticle samples were attached with the sample holder for SEM and EDS analysis. Morphology and crystallinity of the nanostructures were analyzed by recording their low- and high-resolution transmission electron microscopic (TEM and HR-TEM) images in a JEOL 2100F microscope operating at 200 keV. For TEM analysis, the samples were dispersed over carbon-coated copper grids by drop-casting the colloidal suspension of the nanoparticles (in ethanol). A Horiba Lab Ram HR spectrometer equipped with 633 nm He-Ne laser and a thermoelectrically cooled charge-coupled device (CCD) detector was used for recording the Raman spectra of the samples. Room temperature diffuse reflectance spectra (DRS) of the samples were recorded in a Cary-5000 spectrophotometer (Varian) with diffuse reflectance accessory (integrating sphere DRA-CA-30I) attachment. To study the electrical properties of the powder samples, solid pellets of 10 mm diameter and about 0.5 mm thick were fabricated by cold pressing the powders in a pellet press die (Specac) under 3 ton pressure for 15 min. Au contacts (~1.1 mm diameter and ~50 nm thick dots) were deposited over the pellets by r.f. sputtering of an Au target. A DynaCool-9 (Quantum Design) physical property measurement system (PPMS) was utilized to measure the electrical conductivity and Hall voltage of the samples in 100–320 K temperature range, in four-point probe configuration.

3. Results and discussion

Typical SEM images of the synthesized CZTS and CZTGS nanostructures are presented in Fig. 1a, b. Formation of nanometer size quasi-spherical particles in both samples can be perceived in the micrographs. Typical EDS spectra of the samples are presented in Fig. 1c. While the EDS spectrum of the CZTS sample revealed Cu, Zn, Sn, S and C signals, the CZTGS samples revealed Cu, Zn, Sn, Ge and S signals along with adventitious C. The emission band appeared around 1.7 KeV in both the samples corresponds to the silicon substrates used to support the samples for SEM-EDS analysis. EDS estimated elemental composition of the CZTS and CZTGS nanostructures are presented in Table 1. As can be noticed, both the samples grown with Cu-poor and Zn-rich ($Cu/(Zn + Sn + Ge) \leq 1$ and $Zn/(Sn + Ge) \geq 1$) stoichiometry, which is ideal for their application in the absorber layers of solar cells [8]. The EDS estimated $Ge/(Sn + Ge)$ ratios (Table 1) in the samples matched perfectly to the corresponding nominal mol fractions of the precursors in the reaction mixtures, which indicates that almost all the Ge atoms were incorporated into the kesterite lattice by substituting Sn atoms.

TEM and high-resolution TEM (HR-TEM) analyses were performed on the samples to monitor their crystallinity and structural phase (Fig. 2). The TEM images of CZTS and CZTGS samples also revealed the formation of dispersed, quasi-spherical nanoparticles in the samples (Fig. 2a, d). Size distribution histograms of the nanoparticles prepared using corresponding TEM micrographs revealed 9.6 ± 2.3 nm and 10.7 ± 3.4 nm average particle sizes for the CZTS and CZTGS samples, respectively. Nanoparticles of both the samples revealed their good

Table 1
EDS estimated elemental composition and cation mole fractions in the kesterite nanoparticles.

Sample	Cu (at %)	Zn (at %)	Sn (at %)	Ge (at %)	S (at %)	Cu/(Zn + Sn + Ge)	Zn/(Sn + Ge)	Ge/(Sn + Ge)
CZTS	26.06	14.10	12.31	-	47.54	0.98	1.15	0.0
CZTGS	27.39	16.34	7.72	3.85	44.71	0.98	1.41	0.33

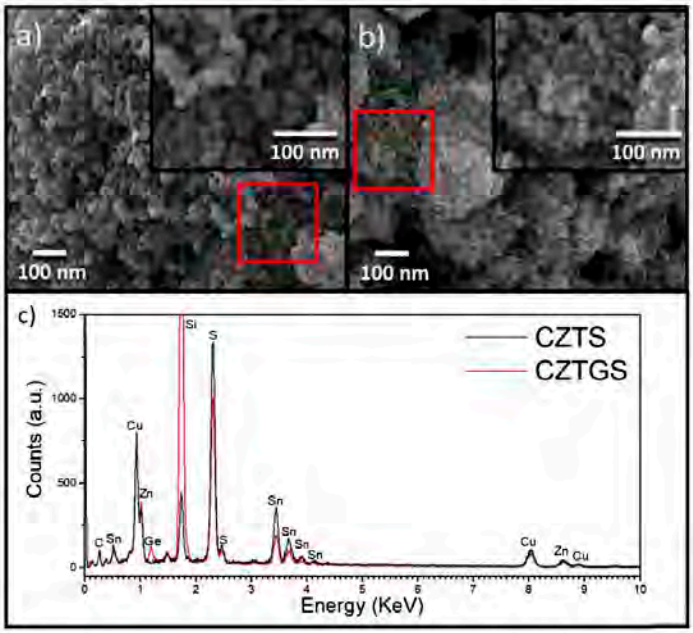

Fig. 1. Typical SEM images of (a) CZTS and (b) CZTGS nanostructures. Magnified images of selected sections (red square) are shown in the insets. Typical EDS spectra of the samples are presented in (c).

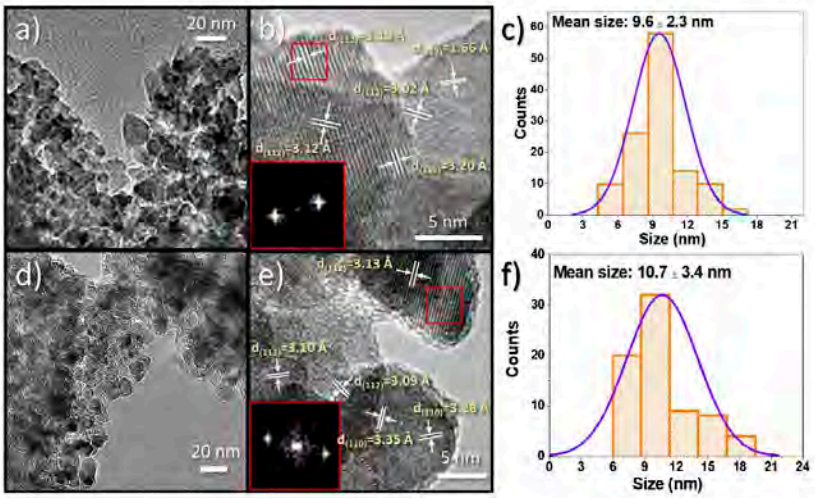

Fig. 2. Typical low- and high-resolution TEM micrographs and corresponding size distribution histograms of (a-c) CZTS and (d-f) CZTGS nanoparticles. The insets in the HR-TEM micrographs are the FFT patterns of selected areas (red square zones) of the samples.

crystallinity, with well-resolved atomic planes in their HR-TEM micrographs (Fig. 2b, e) and well-defined diffraction spots in their fast Fourier transform (FFT) patterns (inserts of Fig. 2b, e).

Room temperatures XRD patterns of the samples are presented in Fig. 3. XRD pattern of both the samples revealed well-resolved diffraction peaks around 28.74, 33.28, 47.78, 56.62, 69.21, and 76.53° Bragg angles, which correspond to the (112), (200), (220), (312), (400) and (136) lattice planes, respectively, of CZTS in tetragonal kesterite phase (PDF # 04-017-3032). Although both the CZTS and CZTGS samples revealed the same diffraction bands (i.e., the diffraction bands of the same Miller indices), their peak positions in the latter sample are slightly shifted towards higher angles in comparison to their positions in the former sample. Such a higher angle shift of the diffraction peaks for the CZTGS sample is expected as the unit cell volume of the kesterite lattice shrinks due to the substitution of Sn atoms of higher ionic radius (ionic radius of Sn^{4+} is 0.69 Å) [36] by the Ge atoms of smaller ionic radius (ionic radius of Ge^{4+} is 0.39 Å) [20–23].

Several structural parameters of the CZTS and CZTGS nanoparticles were extracted by Rietveld refinement of their XRD patterns using GSAS-II software (version 4379) [37]. The Rietveld analysis used pseudo-Voight function, the kesterite structure with space group $I\bar{4}$ (PDF # 04-017-3032), and Chebyshev polynomial-based background construction to obtain the lattice parameters and grain size. The quality of refinement and reliability of the extracted parameters were validated by measuring the goodness of fitting (GoF), which is the ratio of the weighted profile R-factor (R_{wp}) and expected R-factor (R_{exp}), where R is

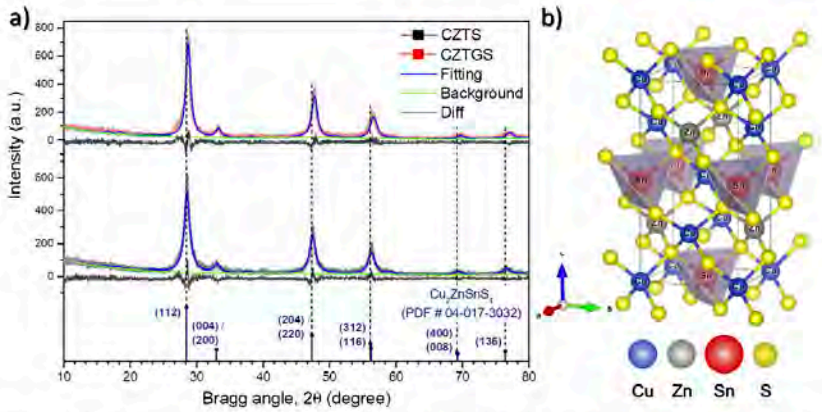

Fig. 3. (a) Rietveld analysis output profiles of CZTS and CZTGS nanoparticles fabricated by hydrothermal process and (b) schematic presentation of the kesterite lattice, highlighting the tetrahedral sites occupied by Sn cations. The blue, gray, red and yellow spheres correspond to Cu, Zn, Sn, and S atoms in the kesterite lattice, respectively.

the square root of the quantity minimized [38]. The GoF and R_{wp} values of the fitted patterns for the CZTS and CZTGS samples are 1.15 with 15.0% and 1.21 with 15.66%, respectively. As we can see, the GoF values for the samples are not exactly 1.0 (the ideal value), which probably due to high noise signal of the experimental diffraction patterns. Moreover, the materials (CZTS and CZTGS nanostructures) have a relatively complex atomic structure (Fig. 3b) for which the conventional XRD analysis cannot provide sufficient information about the positions and occupation fraction of the atoms in the kesterite structure, which we discussed latter [39]. While a high noise signal in the experimental XRD pattern introduces uncertainties in Rietveld refinement, and hence in the estimated values of lattice parameters, it also increases the GoF value [38]. The experimental and refined XRD data of the samples are plotted in Fig. 3 and the extracted structural parameters such as lattice constants, grain size, microstrain and mass density are presented in Table 2. As can be noted, the average grain size of the CZTGS nanocrystals (11.0 nm) is a bit larger than the average grain size of the CZTS nanocrystals (9.0 nm), although both the samples were synthesized under similar experimental conditions. The nucleation and growth rates of kesterite nanocrystals depend on the nature of used solvent and the precursors [40]. As the metal ions such as Zn^{2+} and Ge^{4+} form stronger bonds with Cl^- ions in comparison with the CH_3COO^- ions, utilization of metal acetate precursors induces faster nucleation and growth of the kesterite particles than when their chloride precursors are utilized. In the present case, we utilized zinc acetate and copper acetate as zinc and copper precursors, respectively. On the other hand, tin chloride and germanium chloride were utilized as tin and germanium precursor, respectively. In the present case, we utilized a mixture of $GeCl_4$ and acetone as germanium precursor. The Lewis acid $GeCl_4$ mixed with acetone forms a stable organometallic species with relatively weak Ge^{4+} - oxygen bond [41]. On the other hand, ethylenediamine was utilized in the reaction mixture (to dissolve sulfur powder). Therefore, the $GeCl_4$-acetone complex coordinates with the ethylenediamine to form a new complex with six-coordinated Ge ion [41]. This new complex possesses low thermal stability, and consequently during hydrothermal process, the Ge^{4+} ions incorporate in the kesterite lattice in faster rate, inducing a larger grain growth in the CZTGS nanostructures.

All the peaks revealed in the XRD patterns of the samples correspond to the kesterite phase, indicating their high structural purity. The quaternary CZTS and CZTGS can acquire two crystal structures, kesterite (space group $I\bar{4}$) and stannite (space group $I\bar{4}2m$), depending on the distribution of Cu and Zn cations in their lattice. However, if the Zn and Cu ions are randomly distributed in the lattice, a disordered kesterite structure can be formed with both the kesterite and stannite phases [39,42,43]. Due to the small difference in atomic scattering form factors (f) of Cu^+ and Zn^{2+} cations (the cations have the same number of electrons and f is proportional to the atomic number) it is impossible to distinguish these phases (kesterite and stannite) in their XRD patterns, which might be another reason for the high GoF values of the Rietveld fittings of the samples [39]. Also, the nonstoichiometric conditions such as Cu-poor and Zn-rich, can lead to the coexistence of disordered kesterite, along with the formation of binary or ternary sulfides such as ZnS, $Cu_{2-x}S$ or Cu_2SnS_3 in the samples [44–47]. As all these compounds posse similar crystal structures and hence produce almost identical diffraction patterns, conventional XRD analysis alone cannot ensure the phase purity of the CZTS and CZTGS nanostructures. Therefore, to investigate further the phase purity of the synthesized nanostructures along with structural disorder, we performed their Raman spectroscopy at room temperature.

Table 2
Structural parameters of CZTS and CZTGS nanoparticles extracted from Rietveld analysis of their XRD patterns.

Structural parameter	CZTS	CZTGS	Cu_2ZnSnS_4 (PDF#04-017-3032)
a (Å)	5.43	5.41	5.43220
c (Å)	10.81	10.72	10.8431
Unit cell volume (Å^3)	318.2	314.3	319.98
Grain size (nm)	9	11	–
Microstrain (10^{-5})	539.0	679.3	–
Density (g/cm^3)	4.58	4.48	4.56

Room temperature Raman spectra of the kesterite nanostructures are presented in Fig. 4a. Raman spectra of both the samples revealed an intense dispersion band around 330 cm^{-1}. However, the dispersion band is considerably wide and contains multiple humps at lower and higher energy sides. To analyze the contribution of other dispersion modes in the 330 cm^{-1} signal, the Raman bands of both samples were computer-deconvoluted using Lorentzian curve fitting analysis (Fig. 4a). We can see that the principal Raman dispersion band of the CZTS sample contains three components, peaked around 280, 330, and 357 cm^{-1}. According to the literature, the principal Raman dispersion bands of stoichiometric Cu_2ZnSnS_4 single crystals, the so-called A vibrational modes are located at 287 and 337 cm^{-1} [48–50]; and for non-stoichiometric, e.g., Cu-poor and Zn-rich Cu_2ZnSnS_4, these A modes shift towards lower wavenumbers [51]. The component bands revealed around 280 and 330 cm^{-1} we assigned to the rotation and stretching vibrations of Sn-S bonds (A modes) in the SnS_4 tetrahedron of CZTS, respectively [48–50]. The movements of anions in rotation and stretching vibration modes are presented schematically in Fig. 4b. The component band located at 357 cm^{-1} corresponds to the displacement of cations along the c axis direction, commonly known as B vibrational mode of CZTS [48–50]. On the other hand, substitution of Sn by Ge in the kesterite lattice (CZTGS) modifies the force constants of the Ge-S and Sn-S bonds because of mass and size differences of the Sn^{4+} (m = 118.7 amu, r = 0.69 Å) and Ge^{4+} (m = 72.6 amu, r = 0.39 Å) ions. Consequently, the dispersion bands are slightly shifted towards higher wavenumbers (blue-shift) [26–28,52,53]. As can be noticed in the Raman spectrum of the CZTGS nanostructures presented in Fig. 4, the component bands are shifted towards higher wavenumbers, clearly indicating the substitution of Sn by Ge in the kesterite lattice. To inspect the phase and composition homogeneity in the synthesized nanostructures, we recorded multiple Raman spectra of each sample at different zones (not presented), finding no significant change in the position and shape of the principal dispersion band (around 330 cm^{-1}). Raman spectroscopy analysis of the samples indicates that the CZTS and CZTGS nanostructures synthesized by our low-temperature hydrothermal process are of high purity, well-crystalline, and free from detectable binary or ternary sulfide (secondary phase).

According to theoretical reports [54–57], in Cu_2ZnSnS_4, the Cu_{Zn} antisite, ($Cu_{Zn} + Zn_{Cu}$), ($2Cu_{Zn} + Sn_{Zn}$) and ($V_{Cu} + Zn_{Cu}$) defect complexes have the low formation energy (0.2, 0.4, 0.55 and 0.6 eV, respectively). When the Cu/(Zn + Sn) and Zn/Sn ratios in the Cu_2ZnSnS_4 is close to one (i.e., Cu/(Zn + Sn) ≈ 1 and Zn/Sn ≈ 1), intrinsic defects with low formation energy such as Cu_{Zn} antisite, ($Cu_{Zn} + Zn_{Cu}$), and ($2Cu_{Zn} + Sn_{Zn}$) are formed. The concentration of these defects decreases when the stoichiometry of CZTS becomes Cu-poor, Zn-rich, and Sn-poor [54–57].

CZTS nanostructures of Cu-poor and Zn-rich stoichiometry (close to Cu/(Zn + Sn) = 0.8 and Zn/Sn = 1.2) are frequently utilized in photovoltaic devices due to the lower contents of Cu_{Zn} antisite and ($2Cu_{Zn} + Sn_{Zn}$) defect complex in them, which favors the formation of ($V_{Cu} + Zn_{Cu}$) defect complex. In the present study, the sample without germanium (i.e., Cu_2ZnSnS_4) has a Cu-poor and Zn-rich stoichiometry with Cu/(Zn + Sn) = 0.98 and Zn/Sn = 1.15. However, as the Cu deficiency in the sample only marginal (not very high), neutral ($Cu_{Zn} + Zn_{Cu}$) and ($2Cu_{Zn} + Sn_{Zn}$) defect complexes are formed and the content of ($V_{Cu} + Zn_{Cu}$) defect complex is low. On the other hand, although the sample with germanium ($Cu_2ZnSn_{0.7}Ge_{0.3}S_4$) is also Cu-poor and Zn-rich, it has a higher Zn content (Table 1) than in the Ge-free sample (CZTS), and hence an increase in Zn_{Cu} antisite concentration is expected. Therefore, a reduction of ($2Cu_{Zn} + Sn_{Zn}$) concentration and an increment of ($V_{Cu} + Zn_{Cu}$) defect complex concentration are expected in the sample. The

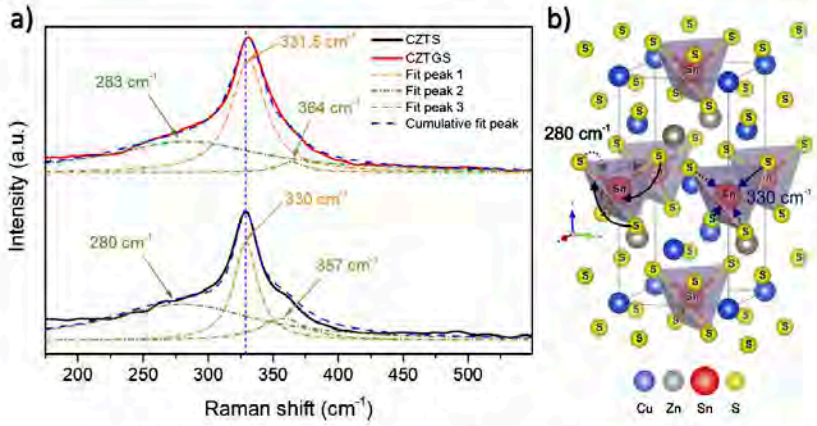

Fig. 4. (a) Room temperature Raman spectra of the CZTS and CZTGS nanoparticles and their Lorentzian deconvolutions, (b) schematic presentation of the rotation (around c-axis) and stretching vibration (around Sn) of Sn-S bonds in SnS_4 tetrahedra in Cu_2ZnSnS_4 lattice.

Cu_{Zn} antisite and V_{Cu} induces the p-type conductivity of Cu_2ZnSnS_4 kesterite. Meanwhile, the Zn_{Cu} antisite forms a shallow level near the conduction band that repels the holes and helps to collect the minority charge carrier in photovoltaic device [11]. However, the concentration of Cu_{Zn} and Zn_{Cu} antisite defects determines the degree of disorder in the kesterite structure [9–11]. The full width at half maximum (FHWM) of the principal A mode of CZTS (appeared around 330 cm^{-1} in our sample) has been associated to the existence of structural inhomogeneities within the disordered cation sublattice in the kesterite structure due to the formation of Cu_{Zn} and Zn_{Cu} antisites [51]. The FWHM of the A mode near 330 cm^{-1} (Fig. 4) increased due to incorporation of Ge in the CZTS nanostructures. The FWHM of the dispersion band for the CZTS and CZTGS nanostructures were 22 cm^{-1} and 41 cm^{-1}, respectively, indicating that the CZTGS nanostructures have higher structural disorder than in the CZTS nanostructures.

As the optical properties of CZTS and CZTGS nanoparticles are important parameters for their application as solar cell absorber material, we recorded their diffuse reflectance spectra in 300–1500 nm

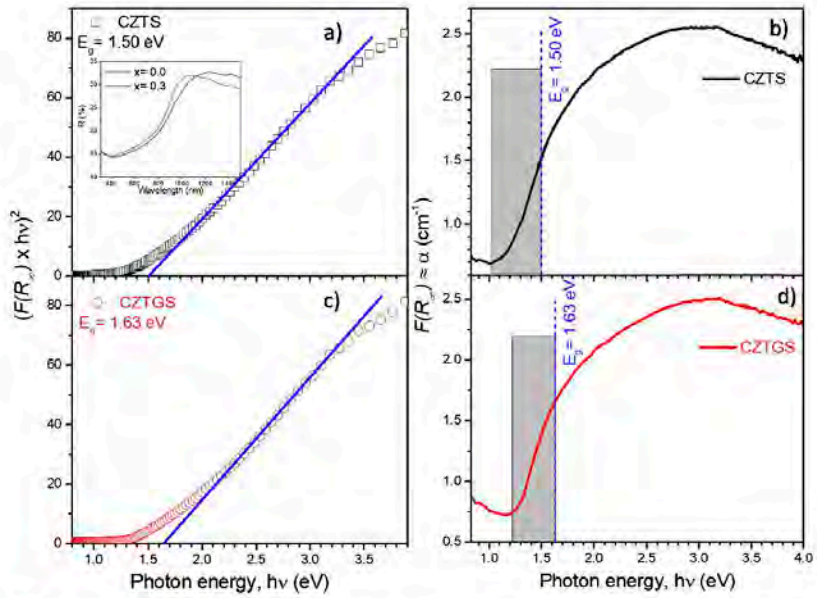

Fig. 5. The K-M plots used to estimate the optical band gap energies of (a) CZTS and (c) CZTGS nanoparticles. DRS spectra of the samples are presented in the inset of (a). K-M coefficient plots of the samples presented in (b, d) demonstrate their band tail regions (gray colored regions).

wavelength range (insert of Fig. 5a). The reflectance of both the samples decreased sharply at wavelengths below 950 nm, indicating their strong absorbance in the visible spectral range. The Kubelka Munk (K-M) formalism (Eq. (1)) was used to estimate the optical band gap of the nanoparticles [58,59]:

$$F(R_\infty) = \frac{(1-R_\infty)^2}{2R_\infty} = \frac{K}{S} \quad (1)$$

where K and S are the absorption and scattering coefficient of the sample, and R_∞ is the reflectance at infinite thickness of the sample. Fig. 5(a, c) shows the K-M plots for the samples with linear extrapolation to determine their band gap energy values. The optical band gap energy values for the CZTS and CZTGS nanostructures were estimated to be 1.50 and 1.63 eV, respectively, indicating an enhancement in band gap energy due to the substitution of Sn by Ge. The estimated band gap energy values of the samples are in good agreement with their values reported in the literature [19,20,22]. According to the literature, the kesterite Cu_2ZnSnS_4 presents band tail (absorption tail) owing to its structural disorder and high defect concentration [60,61]. Thus, the diffuse reflectance spectra of the samples were utilized to estimate their tentative Urbach energies using K-M formalism. The K-M absorption coefficient K becomes equal to 2α (α is the linear absorption coefficient of the material) when the material scatters in perfectly diffuse manner. Therefore, the K-M coefficient $F(R_\infty)$ is proportional to the absorbance of the material and its $F(R_\infty)$ plot is analogous to the absorbance spectrum. As can be seen in the $F(R_\infty)$ plots presented in Fig. 5(b,d), the band tail regions (gray zone) of both the samples remain close to their optical band gap edges. In band tail region, the spectral dependence of the absorption coefficient can be approximated with Urbach's empirical rule, which is given by the equation [62]:

$$\alpha = \alpha_0 e^{\left(\frac{h\nu}{E_u}\right)} \quad (2)$$

where α_0 is a constant and E_u is the energy of the band tail or Urbach energy. To estimate the Urbach energy values, we performed the $\ln(F(R_\infty))$ vs. photon energy plots for the samples (Fig. 6) and interpolated the linear regions (band tail region). Urbach energy values were estimated from the slopes of the linear fits.

Estimated Urbach energy values for the CZTS and CZTGS nanoparticles were 469 and 390 meV, respectively. It should be noted that the Urbach energy value we estimated for the CZTS nanostructures is considerably higher than its values reported (30–125 meV) in the literature [60,61,62]. The difference between the reported and estimated Urbach energy values for the samples probably lies in our approximation, where we considered the scattering coefficient S a constant, i.e., independent of excitation wavelength and there exists no boundary reflection (when the average grain size is larger than the wavelength) [58,59]. However, as we can see in Fig. 6, the Urbach energy value for the CZTS nanostructures decreased on substituting Sn by Ge. The principal origin of band tails in the kesterite Cu_2ZnSnS_4 is the $[2Cu_{Zn} + Sn_{Zn}]$ defect complex [60]. Therefore, the obtained results clearly indicate that substitution of Sn by Ge affects the formation of Sn_{Zn} antisite defects, causing a decrease of $[2Cu_{Zn} + Sn_{Zn}]$ defect concentration and reduction of Urbach energy.

The Sn_{Zn} antisite defects are formed in CZTS (the sample without germanium) as the Sn^{4+} ions can occupy the Zn sites due to the similar ionic radii of Sn^{4+} (0.55 Å) and Zn^{2+} (0.6 Å) ions. On the other hand, Ge^{4+} ions hardly occupy Zn sites, due to the smaller size of Ge^{4+} ions (0.39 Å) in comparison to the size of Zn^{2+} ions. Therefore, the concentrations of Sn_{Zn} and $(Cu_{Zn} + Sn_{Zn})$ defect complex are much lower in the sample containing germanium.

To understand the electrical conduction behavior of the fabricated kesterite nanostructures (CZTS and CZTGS), electrical resistivity (ρ), carrier concentration (p), and carrier mobility (μ) of the pelletized samples were measured in 100–320 K temperature interval. A typical pellet sample mounted over the ETO (electrical transport option) puck of

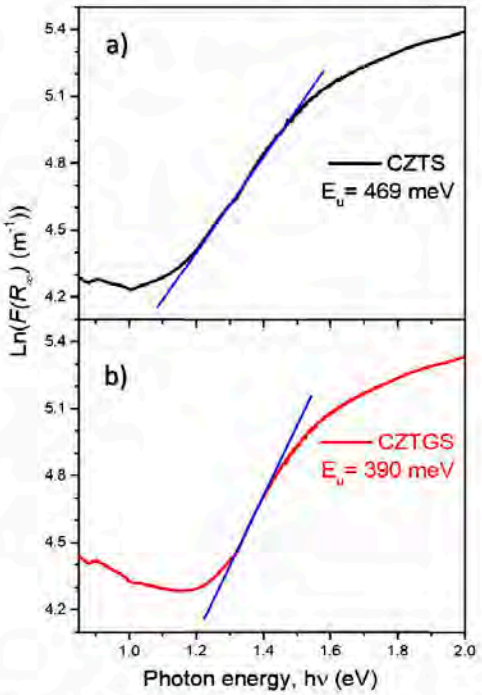

Fig. 6. Plots of $\ln(F(R_\infty))$ vs hν used to estimate the Urbach energy of (a) CZTS and (b) CZTGS nanoparticles.

the PPMS with electrical contacts is shown in Fig. 7a. A current was flown between the I_1^+ to I_1^- terminals and the voltage drop across V_1^+ and V_1^- terminals was measured to determinate the resistance of the sample. To calculate the resistivity of the sample, we use the four-probe method considering the sample geometry: [64]

$$\rho = \frac{\pi}{\ln(2)} GR \quad (3)$$

where G is a correction factor ($G = (0.998\pi t)/\ln(2)$) equal to 3.483 and 3.664 mm for the CZTS and CZTGS sample, respectively; and R is the resistance of the sample. Fig. 7b shows the temperature variation of resistivity of the samples in 100–320 K range. As can be seen, the resistivity of CZTS decreased due to incorporation of Ge in the kesterite lattice. Room temperature (300 K) resistivity of the CZTS nanoparticles decreased from 415.48 Ωcm to 99.27 Ωcm on substituting 30% of Sn by Ge (Table 3). The estimated resistivities of the kesterite nanostructures are in good agreement with their values reported in the literature [3,20,35]. The Hall voltage was measured by flowing 0.1 mA current across the I_2^+ to I_2^- terminals and applying 5.0 T magnetic field perpendicular to the sample surface. Both the samples revealed positive Hall voltage, indicating their p-type conductivity. Hole concentrations in the samples were estimated using Eq. (4), where t is the thickness of the pellet (0.77 mm and 0.81 mm for CZTS and CZTGS samples, respectively).

$$p = \frac{BI}{V_H t q} \quad (4)$$

The variations of hole concentration in the samples with temperature

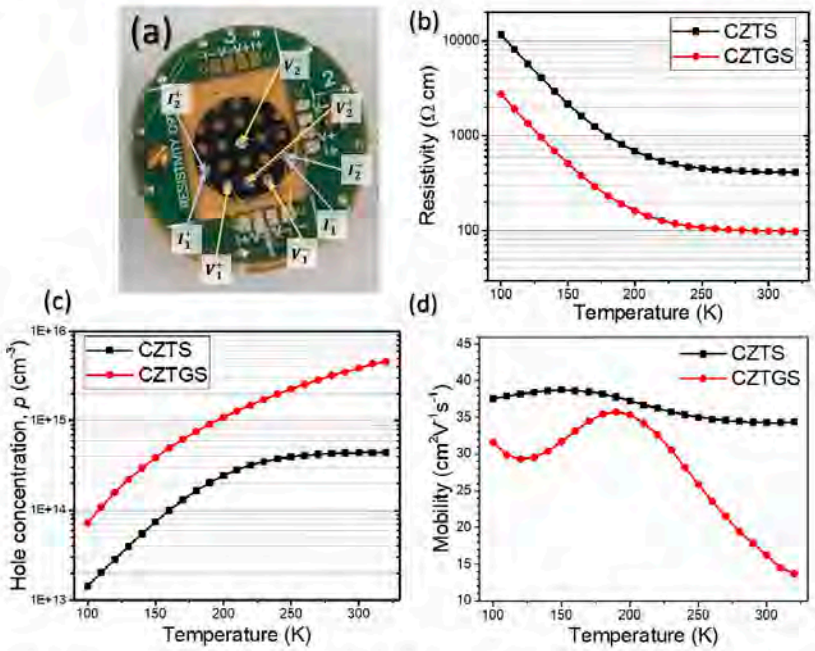

Fig. 7. (a) Photograph showing a typical sample mounting over PPMS puck with electrical contacts; and temperature variations of (b) resistivity, (c) hole concentration, (d) and carrier mobility in the CZTS and CZTGS nanostructures.

Table 3
Estimated electrical transport parameters of CZTS and CZTGS nanoparticles at 300 (room temperature) and 100 K.

Parameters	CZTS		CZTGS	
	100 K	300 K	100 K	300 K
resistivity (Ω cm)	11556.30	415.48	2732.66	99.27
hole concentration (cm^{-3})	1.43×10^{13}	4.38×10^{14}	7.22×10^{13}	3.88×10^{15}
hole mobility ($cm^2V^{-1}s^{-1}$)	37.54	34.25	31.62	16.21

are presented in Fig. 7c. As can be seen in this figure, the hole concentration at room temperature in CZTGS ($\sim 10^{15}$ cm^{-3}) is higher than CZTS by almost an order of magnitude ($\sim 10^{14}$ cm^{-3}). The room temperature hole concentrations (Table 3) estimated from Hall voltage are 4.38×10^{14} cm^{-3} and 3.87×10^{15} cm^{-3} for the CZTS and CZTGS nanostructures, respectively, which are in good agreement with their literature reported values [3,20,65]. From the estimated resistivity and hole concentration, we determined the carrier mobility (μ) in the samples using Eq. (5):

$$\mu = \frac{1}{\rho p q} \tag{5}$$

where ρ is the resistivity, p is the hole concentration, and q is the electronic charge. Temperature variations of hole mobility in the CZTS and CZTGS nanostructures are presented in Fig. 7d.

The observed increase in hole concentration and decrease in resistivity of CZTS nanostructures due to Ge incorporation are closely associated with the change in defect concentration in their electronic band gap [20]. As has been discussed earlier, the presence of Cu_{Zn} antisite and V_{Cu} defects in the kesterite lattice is responsible for its p-type conductivity. The EDS results presented in Table 1 indicate that on replacing 30% Sn atoms by Ge, while the Cu/(Zn + Sn + Ge) fraction remained fixed at 0.98, the Zn/(Sn + Ge) fraction in the CZTS lattice increased from 1.15 to 1.41. This clearly indicates an increase in Zn fraction in the kesterite lattice, which increases the concentration of (V_{Cu} + Zn_{Cu}) defect complex in the sample. As we can see in Fig. 7, at room temperature, the hole concentration in the CZTGS nanoparticles increased along with a reduction of charge carrier mobility. While the increase of carrier concentration in the sample is due to an increase of V_{Cu} concentration, the decrease of hole mobility is due to the increase of Zn_{Cu} concentration in the sample.

In fact, a substantial increase in the FWHM of the principal A mode (331.5 cm^{-1}) in the Raman spectrum of the CZTGS sample supports this assumption. On the other hand, due to incorporation of Ge, the concentration of Sn_{Zn} antisites decreased, as has been confirmed by the decrease in Urbach energy of the CZTGS sample. According to the previous reports, the Cu_{Zn} antisite and V_{Cu} defects form an acceptor level (at 63 to 132 meV over the valence band) and contribute to the p-type conductivity in Cu_2ZnSnS_4 kesterite [9,65–67]. We estimated the activation energy (E_a) of this acceptor level (associated with Cu_{Zn} and V_{Cu} defects) using the logarithm of the Arrhenius equation [67]:

$$\sigma(T) = \sigma_0 e^{-\left(\frac{E_a}{k_B T}\right)} \quad (6)$$

where $\sigma(T)$ is the conductivity of the sample at a particular temperature T, k_B is the, Boltzmann constant, σ_0 is the conductivity of the sample at absolute zero, and E_a is the activation energy. Fig. 8 shows the $\ln(\sigma)$ vs 1000/T plots for the CZTS and CZTGS nanoparticles in the 100–320 K temperature range. From the slopes of the linear interpolations of $\ln(\sigma)$, we estimated the activation energies of Cu_{Zn} antisites and V_{Cu} in CZTS and CZTGS nanostructures as 56.0 and 55.9 meV, respectively, which are close to their reported values [9,65–67]. While the results obtained from Raman analysis indicate an increase in concentration of Cu_{Zn} and Zn_{Cu} antisite defects in the CZTGS nanostructures, almost no change in position (or activation energy) of this acceptor level in the two samples (CZTS and CZTGS) clearly indicates the presence of these defects in both the sample, preserving their p-type electrical conductivity. Moreover, the increase in $(V_{Cu} + Zn_{Cu})$ antisite defect complex concentration in the CZTGS nanostructures increases their carrier (hole) concentration. As can be seen in Fig. 7c, incorporation of Ge in the kesterite lattice does not affect its usual semiconducting behavior throughout the measured temperature range.

Room temperature hole mobility in the CZTS nanostructures was estimated to be about 34.25 $cm^2V^{-1}S^{-1}$ (Table 3), which is considerably higher than the hole mobility values reported for CZTS nanoparticles (~25.4 $cm^2V^{-1}S^{-1}$) prepared by solvothermal process [20] and polycrystalline thin films (8.9–19.4 $cm^2V^{-1}S^{-1}$) prepared by physical and chemical deposition processes [3,4,68]. However, the hole mobility of the nanostructures decreased from 34.25 to 16.21 $cm^2V^{-1}S^{-1}$ (Table 3) on incorporating Ge (30% Sn substitution by Ge). As can be noticed in Fig. 7, the trend of variation of resistivity, hole concentration and mobility of charge carriers in the samples remain same even above the room temperature (up to 320 K).

In a semiconductor, the mobility and carrier concentration are temperature dependent. Moreover, the mobility of charge carriers in a semiconductor is controlled mainly by two processes: i) lattice scattering and ii) defect scattering [69]. As can be seen in Fig. 7d, the hole mobility of the CZTS nanostructures increased gradually with the decrease of temperature in the 320–150 K range, indicating a usual lattice scattering limited conduction in the semiconducting nanocrystals [69]. However, below 150 K, the hole mobility decreased slowly on decreasing the sample temperature, indicating a defect induced hopping conduction in this temperature range [70,71]. On the other hand, in the case of CZTGS nanocrystals, the hole mobility revealed a normal lattice scattering controlled transport behavior (i.e., increase of mobility with the decrease of temperature) above 200 K (200–320 K). However, at lower temperatures (<200 K), the mobility decreased gradually, indicating that defect scattering plays important role in this temperature region [70,71]. The temperatures of mobility maxima (150 K for CZTS and 200 K for CZTGS) can be considered as the onset temperatures, where the transition from lattice scattering controlled transport to hopping transport (through impurity scattering) occurs in the kesterite nanostructures. According to previous reports, the Cu_2ZnSnS_4 polycrystalline thin films [72,73], powder [66], and single crystals [65,71] present Mott variable range hopping conduction in 30–230 K temperature range. In fact, the temperature of transition from lattice scattering controlled conduction to hopping conduction in CZTS has been seen to occur in the order: powder (100–230 K) > polycrystalline thin film (70–170 K) > single crystal (<100 K), which clearly indicates the contribution of defect structure on this parameter. Therefore, incorporation of Ge in the kesterite lattice apparently induces an early transition (from lattice scattering controlled conduction to hopping conduction), caused by the increment of Cu_{Zn} and Zn_{Cu} antisite defects concentration due to Ge incorporation.

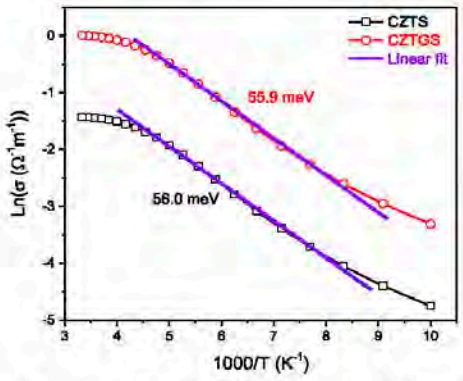

Fig. 8. Temperature dependence of the logarithm conductivity of CZTS and CZTGS nanoparticles to determine the activation energy.

The results presented in this article demonstrate that on incorporating a limited amount of Ge, it is possible to enhance the electrical conductivity of CZTS nanocrystal about four times, without sacrificing their carrier mobility considerably. Such a limited incorporation of Ge (x = 0.3) into CZTS lattice also avoids the formation of undesired phases (e.g., ZnS, Cu_xS, Cu_2SnS_3) which normally impose restrictions for the utilization of CZTGS nanostructures in photovoltaic devices [9,15,20]. Temperature dependent electrical transport behaviors of the kesterite nanostructures indicate that at room temperature, the hole transport in these p-type semiconductor nanocrystals is controlled by lattice scattering. Whereas, at low temperature the hole transport is controlled by defect scattering. The transition from predominant lattice scattering to predominant defect scattering controlled carrier transport occurs at a certain temperature, depending on the defect concentration in the kesterite nanostructures. While this transition occurs around 150 K in the CZTS nanocrystals, it shifts to about 200 K for CZTGS nanocrystals, probably due to the enhanced concentration of Cu_{Zn} and Zn_{Cu} antisites.

4. Conclusions

In summary, we could successfully synthesize phase pure, quasi-spherical $Cu_2ZnSn_{1-x}Ge_xS_4$ (x = 0.0 and 0.3) nanoparticles of 10–35 nm size range through a low-temperature hydrothermal process. The kesterite nanoparticles posse good crystallinity and free from any undesired secondary phase. Incorporation of Ge in the kesterite lattice induces the formation of $(V_{Cu} + Zn_{Cu})$ antisite complex and reduces the concentration of Sn_{Zn} antisite defects. Formation of Cu vacancies (V_{Cu}) in the kesterite lattice enhances hole concentration in the nanostructures, causing about one order increase of their electrical conductivity. However, the incorporation of Ge at Sn sites of the kesterite lattice does not affect the position of the acceptor level associated with Cu_{Zn} antisites and Cu vacancies (V_{Cu}) in their band structure. Temperature dependent electrical characterization revealed that depending on temperature, carrier transport in the kesterite nanocrystals is controlled either by lattice scattering or defect scattering. Cu_{Zn} and Zn_{Cu} antisite defects induce a transition from lattice scattering controlled conduction to hopping conduction. The results presented in this work indicate the CZTGS nanoparticles synthesized by substituting 30% Sn by Ge atoms in CZTS nanoparticles very attractive absorber layer material in photovoltaic devices.

CRediT authorship contribution statement

Umapada Pal: Conceptualization, Planning, Fund raising, Supervision, Writing and Reviewing. **Francisco Enrique Cancino-Gordillo:** Execution of experiments, Manuscript preparation. **Julio Villanueva Cab:** Writing and Reviewing.

Declaration of Competing Interest

The authors declare that they have no known competing financial interests or personal relationships that could have appeared to influence the work reported in this paper.

Acknowledgements

This work was supported by CONACyT (Grant # CB 2017-2018/A1-S-26720), Mexico. FECG acknowledges CONACyT, Mexico, for the doctoral fellowship (CVU # 784149).

References

[1] Y. Cao, M.S. Denny, J.V. Caspar, W.E. Farneth, Q. Guo, A.S. Ionkin, L.K. Johnson, M. Lu, I. Malajovich, D. Radu, H.D. Rosenfeld, K.R. Choudhury, W. Wu, High-Efficiency Solution-Processed $Cu_2ZnSn(S, Se)_4$ Thin-Film Solar Cells Prepared from Binary and Ternary Nanoparticles, J. Am. Chem. Soc. 134 (2012) 15644–15647, https://doi.org/10.1021/ja3057985.

[2] S.-Y. Wei, Y.-C. Liao, C.-H. Hou, C.-H. Cai, W.-C. Huang, M.-C. Huang, C.-H. Lai, Achieving high efficiency $Cu_2ZnSn(S, Se)_4$ solar cells by non-toxic aqueous ink: Defect analysis and electrical modeling, Nano Energy 26 (2016) 74–82, https://doi.org/10.1016/j.nanoen.2016.04.059.

[3] D. Mora-Herrera, R. Silva-González, F.E. Cancino-Gordillo, M. Pal, Development of Cu_2ZnSnS_4 films from a non-toxic molecular precursor ink and theoretical investigation of device performance using experimental outcomes, Sol. Energy 199 (2020) 246–255, https://doi.org/10.1016/j.solener.2020.01.077.

[4] Y. P. Lin, T. E. Hsieh, Y.-C. Chen, K.-P. Huang, Characteristics of $Cu_2ZnSn(S_xSe_{1-x})_4$ thin-film solar cells prepared by sputtering deposition using single quaternary Cu_2ZnSnS_4 target followed by selenization/sulfurization treatment, Sol. Energy Mater. Sol. Cell. 162 (2017) 55–61, https://doi.org/10.1016/j.solmat.2016.12.042.

[5] I.G. Orletskyi, M.M. Solovan, V.V. Brus, P. Pinna, G. Cicero, P.D. Maryanchuk, E. V. Maistruk, M.I. Ilashchuk, T.I. Boichuk, E. Tresso, Structural, optical and electrical properties of Cu_2ZnSnS_4 films prepared from a non-toxic DMSO-based sol-gel and synthesized in low vacuum, J. Phys. Chem. Solids 100 (2017) 154–160, https://doi.org/10.1016/j.jpcs.2016.09.015.

[6] C. Yan, J. Huang, K. Sun, S. Johnston, Y. Zhang, H. Sun, A. Pu, M. He, F. Liu, K. Eder, L. Yang, J.M. Cairney, N.J. Ekins-Daukes, Z. Hameiri, J.A. Stride, S. Chen, M.A. Green, X. Hao, Cu_2ZnSnS_4 solar cells with over 10% power conversion efficiency enabled by heterojunction heat treatment, Nat. Energy. 3 (2018) 764–772, https://doi.org/10.1038/s41560-018-0206-0.

[7] W. Wang, M.T. Winkler, O. Gunawan, T. Gokmen, T.K. Todorov, Y. Zhu, D.B. Mitzi, Device Characteristics of CZTSSe Thin-Film Solar Cells with 12.6% Efficiency, Adv. Energy Mater. 4 (2014) 1301465, https://doi.org/10.1002/aenm.201301465.

[8] K. Pal, P. Singh, A. Bhaduri, K.B. Thapa, Current challenges and future prospects for a highly efficient (20%) kesterite CZTS solar cell: A review, Sol. Energy Mater. Sol. Cell. 196 (2019) 138–156, https://doi.org/10.1016/j.solmat.2019.03.001.

[9] S. Schorr, G. Gurieva, M. Guc, M. Dimitrievska, A. Pérez-Rodríguez, V. Izquierdo-Roca, C.S. Schnohr, J. Kim, W. Jo, J.M. Merino, Point defects, compositional fluctuations, and secondary phases in non-stoichiometric kesterites, J. Phys. Energy 2 (2019) 012002, https://doi.org/10.1088/2515-7655/ab4a25.

[10] M. Grossberg, J. Krustok, C.J. Hages, D.M. Bishop, O. Gunawan, R. Scheer, S. M. Lyam, H. Hempel, S. Levcenco, T. Unold, The electrical and optical properties of kesterites, J. Phys. Energy 1 (2019) 044002, https://doi.org/10.1088/2515-7655/ab29a0.

[11] M. Kumar, A. Dubey, N. Adhikari, S. Venkatesan, Q. Qiao, Strategic review of secondary phases, defects and defect-complexes in kesterite CZTS–Se solar cells, Energy Environ. Sci. 8 (2015) 3134–3159, https://doi.org/10.1039/C5EE01615D.

[12] K. Biswas, S. Lany, A. Zunger, The electronic consequences of multivalent elements in inorganic solar absorbers: Multivalency of Sn in Cu_2ZnSnS_4, Appl. Phys. Lett. 96 (2010) 201902, https://doi.org/10.1063/1.3427435.

[13] X. Lv, C. Zhu, H. Hao, R. Liu, Y. Wang, J. Wang, Improving the performance of low-cost water-based solution-synthesised $Cu_2ZnSn_{1-x}Ge_x(S, Se)_4$ absorber thin films by germanium doping, Ceram. Int. 46 (2020) 25638–25645, https://doi.org/10.1016/j.ceramint.2020.07.039.

[14] S. Kim, K.M. Kim, H. Tampo, H. Shibata, K. Matsubara, S. Niki, Ge-incorporated $Cu_2ZnSnSe_4$ thin-film solar cells with efficiency greater than 10%, Sol. Energy Mater. Sol. Cell. 144 (2016) 488–492, https://doi.org/10.1016/j.solmat.2015.09.039.

[15] M. Neuschitzer, M.E. Rodriguez, M. Guc, J.A. Marquez, S. Giraldo, I. Forbes, A. Perez-Rodriguez, E. Saucedo, Revealing the beneficial effects of Ge doping on $Cu_2ZnSnSe_4$ thin film solar cells, J. Mater. Chem. A 6 (2018) 11759–11772, https://doi.org/10.1039/C8TA02851G.

[16] C.J. Hages, S. Levcenco, C.K. Miskin, J.H. Alsmeier, D. Abou-Ras, R.G. Wilks, M. Bär, T. Unold, R. Agrawal, Improved performance of Ge-alloyed CZTGeSSe thin-film solar cells through control of elemental losses, Prog. Photovoltaics Res. Appl. 23 (2015) 376–384, https://doi.org/10.1002/pip.2442.

[17] S. Giraldo, M. Neuschitzer, T. Thersleff, S. López-Marino, Y. Sánchez, H. Xie, M. Colina, M. Placidi, P. Pistor, V. Izquierdo-Roca, K. Leifer, A. Pérez-Rodríguez, E. Saucedo, Large Efficiency Improvement in $Cu_2ZnSnSe_4$ Solar Cells by Introducing a Superficial Ge Nanolayer, Adv. Energy Mater. 5 (2015) 1501070, https://doi.org/10.1002/aenm.201501070.

[18] S. Kim, K.M. Kim, H. Tampo, H. Shibata, S. Niki, Improvement of voltage deficit of Ge-incorporated kesterite solar cell with 12.3% conversion efficiency, Appl. Phys. Express 9 (2016) 102301, https://doi.org/10.7567/APEX.9.102301.

[19] Y. Li, W. Ling, Q. Han, W. Shi, Colloidal $Cu_2Zn(Sn_{1-x}Ge_x)S_4$ nanocrystals: electrical properties and comparison between their wurtzite and kesterite structures, RSC Adv. 4 (2014) 55016–55022, https://doi.org/10.1039/C4RA10780H.

[20] D. Mora-Herrera, M. Pal, F. Paraguay-Delgado, Facile solvothermal synthesis of $Cu_2ZnSn_{1-x}Ge_xS_4$ nanocrystals: Effect of Ge content on optical and electrical properties, Mater. Chem. Phys. 257 (2021) 123764, https://doi.org/10.1016/j.matchemphys.2020.123764.

[21] E. Garcia-Llamas, J.M. Merino, R. Serna, X. Fontané, I.A. Victorov, A. Pérez-Rodríguez, M. León, I.V. Bodnar, V. Izquierdo-Roca, R. Caballero, Wide band-gap tuning $Cu_2ZnSn_{1-x}Ge_xS_4$ single crystals: Optical and vibrational properties, Sol. Energy Mater. Sol. Cell. 158 (2016) 147–153, https://doi.org/10.1016/j.solmat.2015.12.021.

[22] X. Peng, S. Zhang, Y. Xiang, Solvothermal synthesis of $Cu_2Zn(Sn_{1-x}Ge_x)S_4$ and $Cu_2(Sn_{1-x}Ge_x)S_3$ nanoparticles with tunable band gap energies, J. Alloys Compd. 640 (2015) 75–81, https://doi.org/10.1016/j.jallcom.2015.03.248.

[23] D.B. Khadka, J.H. Kim, Band gap engineering of alloyed $Cu_2ZnGe_xSn_{1-x}Q_4$ (Q = S, Se) films for solar cell, J. Phys. Chem. C 119 (2015) 1706–1713, https://doi.org/10.1021/jp510877g.

[24] M. Neuschitzer, J. Marquez, S. Giraldo, M. Dimitrievska, M. Placidi, I. Forbes, V. Izquierdo-Roca, A. Pérez-Rodríguez, E. Saucedo, V_{oc} Boosting and Grain Growth Enhancing Ge-Doping Strategy for $Cu_2ZnSnSe_4$ Photovoltaic Absorbers, J. Phys. Chem. C 120 (2016) 9661–9670, https://doi.org/10.1021/acs.jpcc.6b02115.

[25] W. Xie, X. Jiang, C. Zou, D. Li, J. Zhang, J. Quan, L. Shao, Synthesis of highly dispersed Cu_2ZnSnS_4 nanoparticles by solvothermal method for photovoltaic application, Physica E 45 (2012) 16–20, https://doi.org/10.1016/j.physe.2012.05.022.

[26] W.-H. Zhou, Y.-L. Zhou, J. Feng, J.-W. Zhang, S.-X. Wu, X.-C. Guo, X. Cao, Solvothermal synthesis of flower-like Cu_2ZnSnS_4 nanostructures and their application as anode materials for lithium-ion batteries, Chem. Phys. Lett. 546 (2012) 115–119, https://doi.org/10.1016/j.cplett.2012.07.060.

[27] M. Zhou, Y. Gong, J. Xu, G. Fang, Q. Xu, J. Dong, Colloidal CZTS nanoparticles and films: Preparation and characterization, J. Alloys Compd. 574 (2013) 272–277, https://doi.org/10.1016/j.jallcom.2013.05.143.

[28] A.G. Kannan, T.E. Manjulavalli, J. Chandrasekaran, Influence of Solvent on the Properties of CZTS Nanoparticles, Procedia Eng. 141 (2016) 15–22, https://doi.org/10.1016/j.proeng.2015.08.1112.

[29] A. Méndez-López, A. Morales-Acevedo, Y.J. Acosta-Silva, M. Ortega-López, Synthesis and Characterization of Colloidal CZTS Nanocrystals by a Hot-Injection Method, J. Nanomaterials 2016 (2016) 1–7, https://doi.org/10.1155/2016/7486094.

[30] J. Li, X. Gao, L. Han, X. Yang, H. Liu, L-cystine-assisted synthesis of Cu_2ZnGeS_4 nanocrystal powder via solvothermal process, Mater. Lett. 163 (2016) 111–114, https://doi.org/10.1016/j.matlet.2015.10.065.

[31] R. Caballero, J.M. Cano-Torres, E. Garcia-Llamas, X. Fontané, A. Pérez-Rodríguez, D. Greiner, C.A. Kaufmann, J.M. Merino, I. Victorov, G. Baraldi, M. Valakh, I. Bodnar, V. Izquierdo-Roca, M. León, Towards the growth of $Cu_2ZnSn_{1-x}Ge_xS_4$ thin films by a single-stage process: Effect of substrate temperature and composition, Sol. Energy Mater. Sol. Cell. 139 (2015) 1–9, https://doi.org/10.1016/j.solmat.2015.03.004.

[32] J.R. González-Castillo, F.A. Pulgarín-Agudelo, E. Rodríguez-González, O. Vigil-Galán, M. Courel-Piedrahita, J.A. Andrade-Arvizu, Influence of Ge content on $Cu_2Zn(SnGe)Se_4$ physical properties deposited by sequential thermal evaporation technique, Mater. Sci. Semicond. Process. 83 (2018) 96–101, https://doi.org/10.1016/j.mssp.2018.04.024.

[33] M. Courel, T.G. Sanchez, N.R. Mathews, X. Mathew, Cu_2ZnGeS_4 thin films deposited by thermal evaporation: the impact of Ge concentration on physical properties, J. Phys. D 51 (2018) 095107, https://doi.org/10.1088/1361-6463/aaa7db.

[34] M. Grossberg, K. Timmo, T. Raadik, E. Kärber, V. Mikli, J. Krustok, Study of structural and optoelectronic properties of $Cu_2Zn(Sn_{1-x}Ge_x)Se_4$ ($x = 0$ to 1) alloy compounds, Thin Solid Films 582 (2015) 176–179, https://doi.org/10.1016/j.tsf.2014.10.055.

[35] M. Singh, T.R. Rana, J.H. Kim, Fabrication of band gap tuned $Cu_2Zn(Sn_{1-x}Ge_x)(S, Se)_4$ absorber thin film using nanocrystal-based ink in non-toxic solvent, J. Alloys Compd. 675 (2016) 370–376, https://doi.org/10.1016/j.jallcom.2016.03.158.

[36] R.D. Shannon, Revised effective ionic radii and systematic studies of interatomic distances in halides and chalcogenides, Acta Crystallogr. Sect. A. 32 (1976) 751–767, https://doi.org/10.1107/S0567739476001551.

[37] B.H. Toby, R.B. Von Dreele, GSAS-II : the genesis of a modern open-source all purpose crystallography software package, J. Appl. Crystallogr. 46 (2013) 544–549, https://doi.org/10.1107/S0021889813003531.

[38] B.H. Toby, R factors in Rietveld analysis: How good is good enough? Powder Diffr. 21 (2006) 67–70, https://doi.org/10.1154/1.2179804.

[39] S. Schorr, The crystal structure of kesterite type compounds: A neutron and X-ray diffraction study, Sol. Energy Mater. Sol. Cell. 95 (2011) 1482–1488, https://doi.org/10.1016/j.solmat.2011.01.002.

[40] C.-M. Fan, M.D. Regulacio, C. Ye, S.H. Lim, S.K. Lua, Q.-H. Xu, Z. Dong, A.-W. Xu, M.-Y. Han, Colloidal nanocrystals of orthorhombic Cu_2ZnGeS_4: phase-controlled synthesis, formation mechanism and photocatalytic behavior, Nanoscale. 7 (2015) 3247–3253, https://doi.org/10.1039/C4NR07012G.

[41] C. Qin, L. Gao, E. Wang, Germanium: Inorganic Chemistry, in: Encycl. Inorg. Chem., John Wiley & Sons, Ltd, Chichester, UK, 2006, https://doi.org/10.1002/0470862106.ia070.

[42] M. Dimitrievska, F. Boero, A.P. Litvinchuk, S. Delsante, G. Borzone, A. Perez-Rodriguez, V. Izquierdo-Roca, Structural Polymorphism in "Kesterite" Cu_2ZnSnS_4: Raman Spectroscopy and First-Principles Calculations Analysis, Inorg. Chem. 56 (2017) 3467–3474, https://doi.org/10.1021/acs.inorgchem.6b03008.

[43] N. Kattan, B. Hou, D.J. Fermín, D. Cherns, Crystal structure and defects visualization of Cu_2ZnSnS_4 nanoparticles employing transmission electron microscopy and electron diffraction, Appl. Mater. Today 1 (2015) 52–59, https://doi.org/10.1016/j.apmt.2015.08.004.

[44] W.-S. Liu, S.-Y. Chen, C.-S. Huang, M.-Y. Lee, H.-C. Kuo, Investigation of Zn/Sn ratio for improving the material quality of CZTS thin films with the reduction of $Cu_{2-x}S$ secondary phase, J. Alloys Compd. 853 (2021) 157237, https://doi.org/10.1016/j.jallcom.2020.157237.

[45] X. Li, H. Cao, Y. Dong, F. Yue, Y. Chen, P. Xiang, L. Sun, P. Yang, J. Chu, Investigation of Cu_2ZnSnS_4 thin films with controllable Cu composition and its influence on photovoltaic properties for solar cells, J. Alloys Compd. 694 (2017) 833–840, https://doi.org/10.1016/j.jallcom.2016.10.024.

[46] J. Just, C.M. Sutter-Fella, D. Lützenkirchen-Hecht, R. Frahm, S. Schorr, T. Unold, Secondary phases and their influence on the composition of the kesterite phase in CZTS and CZTSe thin films, Phys. Chem. Chem. Phys. 18 (2016) 15988–15994, https://doi.org/10.1039/C6CP00178E.

[47] M. Dimitrievska, A. Fairbrother, E. Saucedo, A. Pérez-Rodríguez, V. Izquierdo-Roca, Influence of compositionally induced defects on the vibrational properties of device grade $Cu_2ZnSnSe_4$ absorbers for kesterite based solar cells, Appl. Phys. Lett. 106 (2015) 073903, https://doi.org/10.1063/1.4913262.

[48] M. Guc, S. Levcenko, I.V. Bodnar, V. Izquierdo-Roca, X. Fontane, L.V. Volkova, E. Arushanov, A. Pérez-Rodríguez, Polarized Raman scattering study of kesterite type Cu_2ZnSnS_4 single crystals, Sci. Rep. 6 (2016) 19414, https://doi.org/10.1038/srep19414.

[49] M. Dimitrievska, A. Fairbrother, X. Fontané, T. Jawhari, V. Izquierdo-Roca, E. Saucedo, A. Pérez-Rodríguez, Multiwavelength excitation Raman scattering study of polycrystalline kesterite Cu_2ZnSnS_4 thin films, Appl. Phys. Lett. 104 (2014), https://doi.org/10.1063/1.4861593.

[50] D. Dumcenco, Y.-S.-S. Huang, The vibrational properties study of kesterite Cu_2ZnSnS_4 single crystals by using polarization dependent Raman spectroscopy, Opt. Mater. 35 (2013) 419–425, https://doi.org/10.1016/j.optmat.2012.09.031.

[51] M.Y. Valakh, O.F. Kolomys, S.S. Ponomaryov, V.O. Yukhymchuk, I.S. Babichuk, V. Izquierdo-Roca, E. Saucedo, A. Perez-Rodriguez, J.R. Morante, S. Schorr, I. V. Bodnar, Raman scattering and disorder effect in Cu_2ZnSnS_4, Phys. Stat. Sol. - Rapid Res. Lett. 7 (2013) 258–261, https://doi.org/10.1002/pssr.201307073.

[52] E. Garcia-Llamas, M. Guc, I.V. Bodnar, X. Fontané, R. Caballero, J.M. Merino, M. León, V. Izquierdo-Roca, Multiwavelength excitation Raman scattering of $Cu_2ZnSn_{1-x}Ge_xS(S, Se)_4$ single crystals for earth abundant photovoltaic applications, J. Alloys Compd. 692 (2017) 249–256, https://doi.org/10.1016/j.jallcom.2016.09.035.

[53] J.M. Cano-Torres, R. Caballero, I. Victorov, M. León, E. Garcia-Llamas, V. O. Yukhymchuk, A.M. Yaremko, Y.O. Havryliuk, I. Bodnar, J.M. Merino, Raman characterization and modelling of $Cu_2ZnSn_{1-x}Ge_xS_4$ single crystals grown using chemical vapor transport, Opt. Mater. 66 (2017) 671–677, https://doi.org/10.1016/j.optmat.2017.03.016.

[54] S. Chen, L.-W. Wang, A. Walsh, X.G. Gong, S.-H. Wei, Abundance of $Cu_{Zn} + Sn_{Zn}$ and $2Cu_{Zn} + Sn_{Zn}$ defect clusters in kesterite solar cells, Appl. Phys. Lett. 101 (2012) 223901, https://doi.org/10.1063/1.4768215.

[55] D. Han, Y.Y. Sun, J. Bang, Y.Y. Zhang, H.B. Sun, X. Bin Li, S.B. Zhang, Deep electron traps and origin of p-type conductivity in the earth-abundant solar-cell material Cu_2ZnSnS_4, Phys. Rev. B - Condens. Matter Mater. Phys. 87 (2013), https://doi.org/10.1103/PhysRevB.87.155206.

[56] S. Chen, A. Walsh, X.-G. Gong, S.-H. Wei, Classification of Lattice Defects in the Kesterite Cu_2ZnSnS_4 and $Cu_2ZnSnSe_4$ Earth-Abundant Solar Cell Absorbers, Adv. Mater. 25 (2013) 1522–1539, https://doi.org/10.1002/adma.201203146.

[57] H. Nishihara, T. Maeda, A. Shigemi, T. Wada, First-principles study of defect formation in the photovoltaic semiconductors Cu_2GeS_3 and Cu_2ZnGeS_4 for comparison with Cu_2SnS_3, Cu_2ZnSnS_4 and $CuInSe_2$, Jpn. J. Appl. Phys. 56 (2017) 04CS08, https://doi.org/10.7567/JJAP.56.04CS08.

[58] A. Escobedo Morales, E. Sánchez Mora, U. Pal, Use of diffuse reflectance spectroscopy for optical characterization of un-supported nanostructures, Rev. Mex. Fis. S 53 (2007) 18–22.

[59] R. Molenaar, J.J. ten Bosch, J.R. Zijp, Determination of Kubelka-Munk scattering and absorption coefficients by diffuse illumination, Appl. Opt. 38 (1999) 2068, https://doi.org/10.1364/AO.38.002068.

[60] G. Rey, G. Larramona, S. Bourdais, C. Choné, B. Delatouche, A. Jacob, G. Dennler, S. Siebentritt, On the origin of band-tails in kesterite, Sol. Energy Mater. Sol. Cell. 179 (2018) 142–151, https://doi.org/10.1016/j.solmat.2017.11.005.

[61] J.K. Larsen, J.J.S. Scragg, N. Ross, C. Platzer-Björkman, Band Tails and Cu–Zn Disorder in Cu_2ZnSnS_4 Solar Cells, ACS Appl. Energy Mater. 3 (2020) 7520–7526, https://doi.org/10.1021/acsaem.0c00926.

[62] I. Studenyak, M. Kranjec, M. Kurik, Urbach Rule in Solid State Physics, Int. J. Opt. Appl. 4 (2014) 76–83, https://doi.org/10.5923/j.optics.20140403.02.

[63] M. Valentini, C. Malerba, F. Menchini, D. Tedeschi, A. Polimeni, M. Capizzi, A. Mittiga, Effect of the order-disorder transition on the optical properties of Cu_2ZnSnS_4, Appl. Phys. Lett. 108 (2016) 211909, https://doi.org/10.1063/1.4952973.

[64] I. Miccoli, F. Edler, H. Pfnür, C. Tegenkamp, The 100th anniversary of the four-point probe technique: the role of probe geometries in isotropic and anisotropic systems, J. Phys.: Condens. Matter 27 (2015) 223201, https://doi.org/10.1088/0953-8984/27/22/223201.

[65] A. Nagaoka, H. Miyake, T. Taniyama, K. Kakimoto, K. Yoshino, Correlation between intrinsic defects and electrical properties in the high-quality Cu_2ZnSnS_4 single crystal, Appl. Phys. Lett. 103 (2013) 112107, https://doi.org/10.1063/1.4821279.

[66] E. Hajdeu-Chicarosh, M. Guc, K. Neldner, G. Gurieva, S. Schorr, E. Arushanov, K. G. Lisunov, Mechanisms of conductivity and energy spectrum of near-edge holes in Cu_2ZnSnS_4 powder samples, J. Alloys Compd. 703 (2017) 315–320, https://doi.org/10.1016/j.jallcom.2017.01.352.

[67] N. Muhunthan, O.P. Singh, V.N. Singh, K.N. Sood, Rashmi, Electric field-effect-assisted persistent photoconductivity in CZTS, Adv. Mater. Lett. 6 (2015) 290–293, https://doi.org/10.5185/amlett.2015.5704.

[68] X. Wu, W. Liu, S. Cheng, Y. Lai, H. Jia, Photoelectric properties of Cu_2ZnSnS_4 thin films deposited by thermal evaporation, J. Semicond. 33 (2012) 022002, https://doi.org/10.1088/1674-4926/33/2/022002.

[69] S. Kasap, C. Koughia, H.E. Ruda, Electrical Conduction in Metals and Semiconductors, in: S. Kasap, P. Capper (Eds.), Springer Handbook of Electronic and Photonic Materials. Springer Handbooks, Springer, Cham, 2017, https://doi.org/10.1007/978-3-319-48933-9_2.

[70] S. Schuler, S. Siebentritt, S. Nishiwaki, N. Rega, J. Beckmann, S. Brehme, M.C. Lux-Steiner, Self-compensation of intrinsic defects in the ternary semiconductor $CuGaSe_2$, Phys. Rev. B 69 (2004) 045210, https://doi.org/10.1103/PhysRevB.69.045210.

[71] A. Nagaoka, H. Miyake, T. Taniyama, K. Kakimoto, Y. Nose, M.A. Scarpulla, K. Yoshino, Effects of sodium on electrical properties in Cu_2ZnSnS_4 single crystal, Appl. Phys. Lett. 104 (2014) 152101, https://doi.org/10.1063/1.4871208.

[72] V. Kosyak, M.A. Karmarkar, M.A. Scarpulla, Temperature dependent conductivity of polycrystalline Cu_2ZnSnS_4 thin films, Appl. Phys. Lett. 100 (2012) 263903, https://doi.org/10.1063/1.4731875.

[73] M. Zubair Ansari, N. Khare, Thermally activated band conduction and variable range hopping conduction in Cu_2ZnSnS_4 thin films, J. Appl. Phys. 117 (2015) 025706, https://doi.org/10.1063/1.4905673.

Applied Surface Science 617 (2023) 156617

Contents lists available at ScienceDirect

Applied Surface Science

journal homepage: www.elsevier.com/locate/apsusc

Full Length Article

Removal of secondary phases and its effect on the transport behavior of $Cu_2ZnSn_{1-x}Ge_xS_4$ kesterite nanoparticles

Francisco Enrique Cancino-Gordillo, José-Luis Ortiz-Quiñonez, Mou Pal, Rutilo Silva González, Umapada Pal*

Instituto de Física, Benemérita Universidad Autónoma de Puebla, Apdo. Postal J-48, Puebla, Pue. 72570, Mexico

ARTICLE INFO

Keywords:
CZTGS nanoparticles
Chemical treatment
Kesterite
Phase separation
Transport behavior

ABSTRACT

Hole-transporting materials are very important for achieving high efficiency in perovskite solar cells. Thin films made of $Cu_2ZnSn_{1-x}Ge_xS_4$ have attracted the attention of researchers due to their potential as hole-transporting layers. However, defects and impurities define their effectiveness in solar cells. In this work, we present a facile wet chemical approach to remove the ZnS and Cu_6GeS_6 impurities from small (~11 nm) $Cu_2ZnSn_{1-x}Ge_xS_4$ (x 0.0 to 0.7) nanoparticles synthesized by a hydrothermal process. The wet chemical process converted the nanostructures Cu-rich Zn-poor from their initial Zn-rich Cu-poor stoichiometry. Moreover, the bandgap energies of the nanostructures were reduced by about 0.1 eV after chemical treatment due to change the oxidation state of Cu from Cu^{1+} to Cu^{2+}. The kesterite films prepared by spin coating of chemically treated nanoparticle inks revealed enhanced electrical conductivity and hole concentration in comparison to the films prepared using untreated nanoparticle inks. While the highest hole concentration of about $0.52x10^{18}$ cm^{-3} was obtained for the films made of $Cu_2ZnSn_{1-x}Ge_xS_4$ nanoparticles with the highest x value (x 0.7), the highest hole mobility (18.9 $cm^2V^{-1}s^{-1}$) was achieved for x 0.3. The effects of secondary phase elimination on carrier concentration and mobility variation have been discussed.

1. Introduction

Quaternary chalcogenide Cu_2ZnSnS_4 (CZTS) is one of the most attractive materials for absorber layers of thin film-based photovoltaic devices, with the potential of replacing conventional absorber materials such as CdTe and $CuIn_xGa_{1-x}S_2$ (CIGS), which contain toxic, scarce or costly elements like Cd and In. Apart from its non-toxic constituents, CZTS exhibits a high optical absorption coefficient (~10^4 cm^{-1}) in the visible spectra range, intrinsic p-type conductivity, and direct bandgap energy close to 1.5 eV [1,2], which are some essential features of a material to be used in the absorber layers of photovoltaic devices. In fact, by utilizing kesterite absorber layers containing sulfur (CZTS) and selenium (CZTSe), the power conversion efficiency of solar cells could be achieved up to 11.8% [3] and 12.6 % [4], respectively. However, those values are considerably lower in comparison to the power conversion efficiency (>20%) of the solar cells fabricated using CIGS [2,5]. One of the principal reasons for lower conversion efficiency or large open-circuit voltage (V_{oc}) deficit of CZTS-based solar cells is the presence of electronic defects in off-stoichiometric (i.e., Cu/(Zn + Sn) < 1 and Zn/Sn > 1) CZTS, affecting its electrical and optical properties [6].

On the other hand, due to p-type conduction and moderate resistivity, recently CZTS thin films have been utilized as hole-transporting layers (HTLs) in perovskite solar cells (PSC), replacing conventional hole transporting layers such as PEDOT:PSS and spiro-OMETAD, which suffer from high cost, poor environmental and current-voltage (I-V) stabilities [7,8]. For utilization as absorber layer, the CZTS films should have a high absorption coefficient, high environmental stability, low cost, low defect content, and a direct bandgap in the range of 1.4–1.5 eV, which overlaps with the bandgap value (~1.35 eV) of the ideal semiconductor for single-junction solar cells [9,10]. Meanwhile, for utilization as HTL, apart from p-type conductivity, the CZTS films should have low resistivity, high hole mobility, and low electronic defect contents [11]. Wu et al. utilized CZTS film made of corresponding nanoparticle ink, as HTL in an n-i-p configured perovskite ($CH_3NH_3PbI_3$) solar cell and compared the performance of the device with the performance of a PSC fabricated with spiro-OMeTAD-based HTL [12], demonstrating the HTL made of CZTS nanoparticles can transport holes as effectively as commonly used HTLs such as spiro-OMeTAD. They observed a decrease in fill factor (*FF*)

* Corresponding author.
E-mail address: upal@ifuap.buap.mx (U. Pal).

https://doi.org/10.1016/j.apsusc.2023.156617
Received 14 December 2022; Received in revised form 22 January 2023; Accepted 27 January 2023
Available online 2 February 2023
0169-4332/

from 65% using spiro-OMeTAD to 58.7% using CZTS for the PSC fabricated with CZTS nanoparticle based HTL and associated to an increase in series resistance (R_s) of the device. On the other hand, a higher J_{sc} in the cell fabricated with CZTS nanoparticle ink was associated to the improved light absorption of the perovskite solar cell in the 400–850 nm spectral range and improved interfacial contact between the perovskite layer and Au electrode, which reduces the charge carrier (electron-hole) recombination. On the other hand, Yuan et al. utilized CZTS quantum dots for HTL in n-i-p configured perovskite ($CH_3NH_3PbI_3$) solar cells [13]. The CZTS quantum dots were synthesized using a hot injection method, and their bandgap was tuned by replacing sulfur with selenium. Substitution of S with Se reduced the resistivity of the kesterite HTL substantially (112.3 Ω•cm to 4.56 Ω•cm). The PSC fabricated with CZTSe as HTL exhibited a lower V_{oc} (0.808 V) than the PSC fabricated with CZTS (0.945 V), which was attributed to the reduction of bandgap energy from 1.64 eV (for CZTS) to 1.14 eV (for CZTSe). The reduction of bandgap energy in CZTSe is associated with an up-shift of its valence band edge, which induces higher recombination of charge carrier at the perovskite/HTL interface [13]. Therefore, for applying CZTS in PSCs, it must be grown under such conditions that reduce its resistivity, conserve the high light absorption capacity, and increase the bandgap to get a favorable alignment with the valence band of the perovskite layer.

As has been mentioned earlier, the compositional stoichiometry of CZTS affects its electrical and optical properties due to the formation of point defects such as Cu_{Zn}, Sn_{Zn}, V_{Cu}, and defect complexes [1,2,14]. One of the principal defects present in CZTS kesterite is the Sn_{Zn} antisite. Due to low formation energy, the Sn_{Zn} antisites produce ($2Cu_{Zn} + Sn_{Zn}$) defect complex, which acts as a deep-level recombination center for electron-hole pairs or causes strong electron trapping [15–17]. Moreover, as Sn is a multivalent element, its oxidation state can interchange between Sn^{4+} and Sn^{2+} spontaneously due to the perturbation of charge balance in crystal lattice during the generation of photoinduced charge carriers. The reduction of Sn (Sn^{4+} to Sn^{2+}) can occur either in its native crystallographic position (Sn_{Sn}) or when Sn^{4+} is in an antisite defect. In both the cases, it can generate defect states in the bandgap which act as traps for electrons and holes [18]. Therefore, for applying CZTS in solar cells, it must be grown under specific conditions that reduce the concentration of Sn_{Zn} antisite defects and inhibits $Sn^{4+} \leftrightarrow Sn^{2+}$ transition.

The Cu_{Sn}, Cu_{Zn} and Sn_{Zn} antisite defects are easily formed in stoichiometric composition due to their low formation energies. One of the convenient ways to reduce the concentration of antisite defects in CZTS is by performing its synthesis under Cu-poor and Zn-rich condition (i.e., $Cu/(Zn + Sn) \approx 0.8$ and $Zn/Sn \approx 1.2$). This condition reduces the concentration of the antisite defects, enhancing the PCE of the fabricated solar cells [15–17]. However, according to the phase diagram of CZTS, the single kesterite phase is difficult to achieve due to the narrow composition region where the pure CZTS kesterite phase can be formed [19,20]. Consequently, several secondary phases (e.g., ZnS, $Cu_{2-x}S$ and Cu_2SnS_3) are formed during the growth of CZTS and its post-growth processing [14,20–23]. One of the principal secondary phases formed during CZTS growth is ZnS [20,23], which is a high-resistive semiconductor with wide bandgap energy (3.84 eV). Presence of the ZnS phase reduces the active area for generating electron-hole pairs and current collection, along with an increase in series resistance of the device [14,20]. Thus, it is necessary to search for the ways to reduce the antisite defects, especially the defects associated with the unusual occupation of Sn atoms in the kesterite lattice and get rid of the secondary phases. In this regard, a partial substitution of Cu, Zn and Sn cations in kesterite lattice with other cations such as Ag^+ [24–26], Cd^{2+} [27,28] and Ge^{4+} [29–33], respectively, has been explored. For example, the partial substitution of Cu^+ by Ag^+ in the kesterite lattice was seen to diminish the concentration of antisite defects such as Cu_{Zn} and Zn_{Cu} and related defect complexes (i.e., $V_{Cu} + Zn_{Cu}$, $Cu_{Zn} + Sn_{Zn}$, and $2Cu_{Zn} + Sn_{Zn}$). In addition, formation of Ag_{Zn}, ($Ag_{Zn} + Zn_{Ag}$) and ($2Ag_{Sn} + Sn_{Zn}$) antisite defects in the Ag-substituted kesterite is not expected because the Ag ions have unique +1 valence state and their ionic radius (1.14 Å) is substantially larger than the ionic radii of Cu^{+1} (0.74 Å) and Zn^{2+} (0.74 Å) ions [34]. On the other hand, when the Cd^{2+} (0.92 Å) substitutes the Zn^{2+} cation to form the $Cu_2Cd_xZn_{1-x}SnS_4$, the formation energy of Cu_{Cd} and Cd_{Cu} antisite defects in the kesterite is expected to be high due to the significant difference in the ionic radii and valance state of the two atoms [34].

A partial substitution of Sn by Ge has been seen to improve the V_{oc} of solar cells fabricated using CZTS as an absorber material [29–33]. Incorporation of Ge atoms substituting Sn in CZTS causes the formation of $Cu_2ZnSn_{1-x}Ge_xS_4$ (CZTGS) and reduces the possibility of formation of undesired defects such as Sn_{Zn}. The concentration of Sn_{Zn} antisite defects decreases in CZTGS, as the energy of formation of such defects increases due to the tetravalent Ge^{4+} ion, which cannot exchange crystallographic sites with the cations such as Zn^{2+} and Cu^+, as occurs in the Sn case [35,36]. However, obtaining CZTGS with single kesterite phase is difficult as a high concentration of Ge ($x \geq 0.25$) in CZTGS can generate tetragonal (kesterite) and orthorhombic mixed phase [37], segregation of secondary phases such as ZnS and Cu_xS ($x \geq 0.8$) [38], or generate deep-level defects due to the formation of Sn vacancies (V_{Sn}) [36,39]. Moreover, the power conversion efficiency of the solar cells fabricated using CZTGS absorber layers containing larger Ge mol fractions of Ge ($x > 0.25$) is seen to reduce from 11 % (for $x \approx 0.25$) to 1 % (for $x \approx 0.75$) [40]. Therefore, while eliminating secondary phases in CZTGS is an essential task for applying it in solar cell, a systematic study of the impact of defects and secondary phases on the transport behaviors of CZTGS is very important for utilizing CZTGS nanostructures in the hole transporting layers of PSCs. Some specific chemical treatment processes have been applied by the researchers for the selective removal of secondary phases from CZTS and CZTSe films. For example, Buffière et al. utilized KCN treatment (carried out for 120 s at 20 °C using 5 wt% KCN aqueous solution in 0.5 wt% KOH) for removing $Cu_{2-x}Se$, Se^0, Cu_xSnSe_y, $SnSe_2$ and SnO_2 secondary phases from the surface of CZTSe thin films [41]. On the other hand, Fairbrother et al. utilized dilute HCl solution (10 % v/v at 75 °C for 300 s) for etching out ZnS phase from CZTS thin films [42]. Mousel et al. used HCl and Br_2-MeOH solutions to remove ZnSe and Cu_2SnSe_3, respectively, from CZTSe film surface [43]. Nevertheless, while the formation of secondary phases in CZTGS nanostructures and thin films has been reported by several research groups [29,32,33,37,38], utilization of chemical treatment for etching out secondary phases from CZTGS films or nanostructures has not been explored so far.

In this article, we present a chemical treatment process for eliminating secondary phases from the CZTGS (from $x = 0.0$ to 0.7) nanoparticles synthesized by hydrothermal process. The effect of the wet-chemical treatment on the elimination of secondary phases and its impact on the structural and optical properties of the nanostructures have been studied. Electrical properties of the films fabricated using those secondary phase-eliminated nanoparticles were evaluated by measuring their resistivity and Hall coefficient. We demonstrate that removal of secondary phases such as Cu_8GeS_6 and ZnS improves the electrical transport behaviors of CZTGS films, without affecting their microstructural and optical behaviors significantly.

2. Experimental

2.1. Reactive & solvents

Copper acetate hydrate ($Cu(CH_3COO)_2{\cdot}H_2O$, ≥98%), tin chloride pentahydrate ($SnCl_4{\cdot}5H_2O$, 98%), germanium tetrachloride ($GeCl_4$, 99.9999%), ethylenediamine ($C_2H_8N_2$, ≥98%), hexanethiol ($C_6H_{14}S$, 95%), and acetone (C_3H_6O, ≥99.5%) were purchased from Sigma-Aldrich, Mexico. Zinc acetate dihydrate ($Zn(CH_3COO)_2{\cdot}2H_2O$, 99%), potassium hydroxide pellets (KOH), and sublimed sulfur powder (S, 99.95%) were acquired from J.T. Baker and Fermont, respectively. Hydrochloric acid (HCl) was purchased from CTR scientific, Mexico. All

the reagents were utilized as received, without further purification. Deionized (DI) water from a Millipore system ($\rho > 10^{18}$ Ω·cm) was used for the synthesis of the nanostructures.

2.2. Fabrication of $Cu_2ZnSn_{1-x}Ge_xS_4$ nanoparticles

The hydrothermal process used for the synthesis of $Cu_2ZnSn_{1-x}Ge_xS_4$ (CZTGS) nanoparticles was adopted from previous works [44,45]. The synthesis process included the preparation of two solutions: (i) a solution with all the cation precursors in 10 mL of DI water, and (ii) a solution of sublimed sulfur in 10 mL of ethylenediamine. In a typical synthesis process, the contents of copper acetate, zinc acetate, and sulfur were fixed at 4 mmol, 2 mmol, and 12 mmol, respectively. As the $GeCl_4$ precursor is highly reactive to humidity, a $GeCl_4$-acetone mixture of 1:31 M ratio was prepared in a glove box under Ar atmosphere and magnetic stirring (6 h), to utilize as a germanium precursor. For preparing the nanostructures with different Ge contents, the $GeCl_4$-acetone mixture precursor and $SnCl_4$ precursor in the reaction mixtures were adjusted to make the nominal Ge mol fractions in the reaction mixture x = Ge/(Sn + Ge) = 0.0, 0.15, 0.30, 0.40, 0.60 and 0.70. The two homogenous solutions were mixed and transferred to a 30 ml. Teflon container. The Teflon container was capped and placed inside a stainless-steel autoclave. The sealed autoclave was placed inside a Lindberg Blue gravity furnace and heated to 200 °C (at 3 °C/min). After 24 h of heating, the reactor was naturally cooled down to room temperature. The generated solid product was separated and washed several times with acetone under centrifugation (7000 rpm, 10 min). Finally, the product was dried at 60 °C for 8 h. Several samples were prepared by changing the molar concentrations of Ge and Sn precursors in the reaction solution, maintaining all the other conditions same.

2.3. Elimination of secondary phases by chemical treatment

To remove the byproducts (secondary phases), the freshly prepared CZTGS samples were washed in a 35 mL glass vial, adapting following procedure. First about 700 mg of the sample was mixed with 90 mL of dilute (10 vol% in DI water) HCl. From the 90 mL mixture, 30 mL was taken into the glass vial, covered with its hermetic screw cap, and heated at 80 °C for 45 min under magnetic stirring. Then, the solid was recovered by centrifugation. The same procedure was followed for the remaining 60 mL of the HCl solution. The recovered material was immersed in 30 mL of aqueous KOH (1 M) solution and shaken for 5 min. Finally, the solid was washed with DI water several times, dried under vacuum, and stored under Ar atmosphere. The chemical treatment process was repeated for two times for the $Cu_2ZnSn_{0.3}Ge_{0.7}S_4$ (x = 0.70) sample.

2.4. Deposition of $Cu_2ZnSn_{1-x}Ge_xS_4$ films

For preparing the films of the as-prepared and chemically processed CZTGS nanoparticles, the nanoparticle inks were prepared by dispersing about 150 mg of each of the samples in 0.9 mL of hexanethiol under magnetic stirring for 16 h. The CZTGS nanoparticle inks were spin coated over well cleaned corning glass substrates (1.5 × 1.5 cm^2). About 25 μL of the prepared ink was dropped over the glass substrate spinning at 2000 rpm for 30 s. After deposition, the films were heated at 95 °C for 10 min. The deposition process was repeated for another time to obtain the films of about 2 μm thickness.

2.5. Characterization

X-ray diffraction (XRD) patterns of the as prepared and chemically treated CZTGS nanoparticles were recorded in a Panalytical – Empyrean diffractometer using CuKα$_1$ radiation ($\lambda = 1.5406$ Å) at room temperature. The spectra were recorded at 0.02°/step in the 2θ range of 20–85°. Elemental composition of the samples was estimated by energy dispersive X-ray spectroscopy (EDS) in a JEOL JSM-7800F scanning electron microscope (SEM) with X-Max spectrometer (Oxford Instruments) attached, operating at 15 KeV. Crystalline and vibrational properties of the nanoparticles were studied further by microRaman spectroscopy using a Horiba Lab Ram HR spectrometer equipped with a 633 nm He-Ne laser and a thermoelectrically cooled charge-coupled device (CCD) detector. For analyzing the morphology and fine-structure, the low- and high-resolution transmission electron microscopic images (TEM and HR-TEM) of the nanostructures were recorded in a JEOL 2100F microscope operating at 200 keV. For TEM and HR-TEM analysis, the samples were dispersed over carbon-coated copper grids by drop casting their colloidal suspension in ethanol. UV–Vis diffuse reflectance spectra of the samples were recorded in a Cary 5000 spectrophotometer with diffuse reflectance accessory attachment (integrating sphere DRA-CA-30I). Electrical properties of the CZTGS films were evaluated at room temperature by measuring the Hall effect in an Ecopia HMS-3000 system under an applied magnetic field of 0.5 T and sample current of 0.1 mA. For electrical characterizations, silver dot contacts were fabricated on the surface of the films in van der Pauw configuration with a separation of 5.0 mm between them. The electrical measurements were performed over 5 films of each of the samples to obtain the average value of each of the parameters. The thickness of the prepared CZTGS films was estimated in a Bruker Dektak 150 Surface Profilometer.

3. Results and discussion

EDS estimated elemental compositions of the as-synthesized CZTGS nanoparticles are listed in Table 1. As can be noticed, all the samples grew with Cu-poor and Zn-rich stoichiometry (Cu/(Zn + Sn + Ge) ≤ 1 and Zn/(Sn + Ge) ≥ 1), and the Ge mol fractions (Ge/(Sn + Ge) ratios) in them are close to the corresponding nominal mol fractions in the reaction mixtures. While such a Cu-poor and Zn-rich stoichiometry of the nanostructures is ideal for their application in photovoltaic devices, formation of secondary phases such as ZnS, $Cu_{2-x}S$ and Cu_2SnS_3 is expected to occur in them [21,46,47]. To investigate whether the Cu-based secondary phases such as $Cu_{2-x}S$ and Cu_2SnS_3 are formed in the samples, they were analyzed by XRD. The room temperature XRD patterns of the nanoparticles synthesized with different nominal Ge mol fractions are shown in Fig. 1a. XRD patterns of all the samples revealed well-resolved diffraction peaks around 28.70, 33.23, 47.65, 56.41, 69.52, and 76.77° Bragg angles, which correspond to the (112), (200), (220), (312), (400) and (136) lattice planes of CZTS in tetragonal kesterite phase (PDF # 04-017-3032), respectively. As can be seen in Fig. 1a, the positions of main XRD peaks such as (112), (220) and (312) of the nanostructures gradually shifted to higher diffraction angles. Such a higher angle shift of the diffraction peaks for the samples containing Ge is probably due to the substitution of Sn atoms of higher ionic radius (Sn^{4+} = 0.69 Å) [48] by the Ge atoms of smaller ionic radius (Ge^{4+} = 0.39 Å). The shift of diffraction peaks towards higher angles in comparison to their positions in the Ge-free (i.e., x = 0.0) sample also indicates the incorporation of Ge in crystallite lattice was successful [49–51]. However, for the samples with x = 0.6 and 0.7, there appeared several diffraction peaks associated to Cu_8GeS_6 ternary phase (PDF # 04-010-4016); intensity of which increased gradually with the increase of x value (x ≥ 0.6). In none of the samples we could detect other Cu-based impurity/secondary phases such as $Cu_{2-x}S$ or Cu_2SnS_3 from the XRD patterns.

The incorporation of Ge^{4+} ions in CuS (covellite) and $Cu_{1.81}S$ (roxbyite) phases has been seen to generate Cu_2GeS_3 and Cu_8GeS_6, respectively [52]. As we obtained Cu_8GeS_6 byproduct, it is highly probable that $Cu_{1.81}S$ intermediate was formed at the beginning of the reaction during the hydrothermal treatment utilized for the synthesis of the CZTGS nanostructures. It should be noted that the oxidation states of Cu ions in CuS and $Cu_{1.81}S$ are +2 and +1, respectively. Although the oxidation state of copper in $Cu(CH_3COO)_2·H_2O$ used as copper precursor

Table 1
EDS estimated elemental composition and cation mole fractions in the $Cu_2ZnSn_{1-x}Ge_xS_4$ nanoparticles before washing with HCl solution.

Sample (x-value)	Cu (at%)	Zn (at%)	Sn (at%)	Ge (at%)	S (at%)	Cu/(Zn + Sn + Ge)	Zn/(Sn + Ge)	Ge/(Sn + Ge)
0.0	26.06	14.10	12.31	–	47.54	0.99 ± 0.02	1.15 ± 0.13	0.0
0.15	26.15	13.45	10.54	1.60	48.27	1.02 ± 0.03	1.11 ± 0.05	0.13 ± 0.02
0.30	27.39	16.34	7.72	3.85	44.71	0.98 ± 0.05	1.41 ± 0.09	0.33 ± 0.03
0.40	26.44	13.68	7.54	4.62	47.72	1.02 ± 0.02	1.13 ± 0.06	0.38 ± 0.01
0.60	27.10	15.64	5.23	6.42	45.61	0.99 ± 0.07	1.34 ± 0.06	0.55 ± 0.04
0.70	27.14	16.93	3.79	8.97	43.17	0.91 ± 0.05	1.33 ± 0.06	0.70 ± 0.01

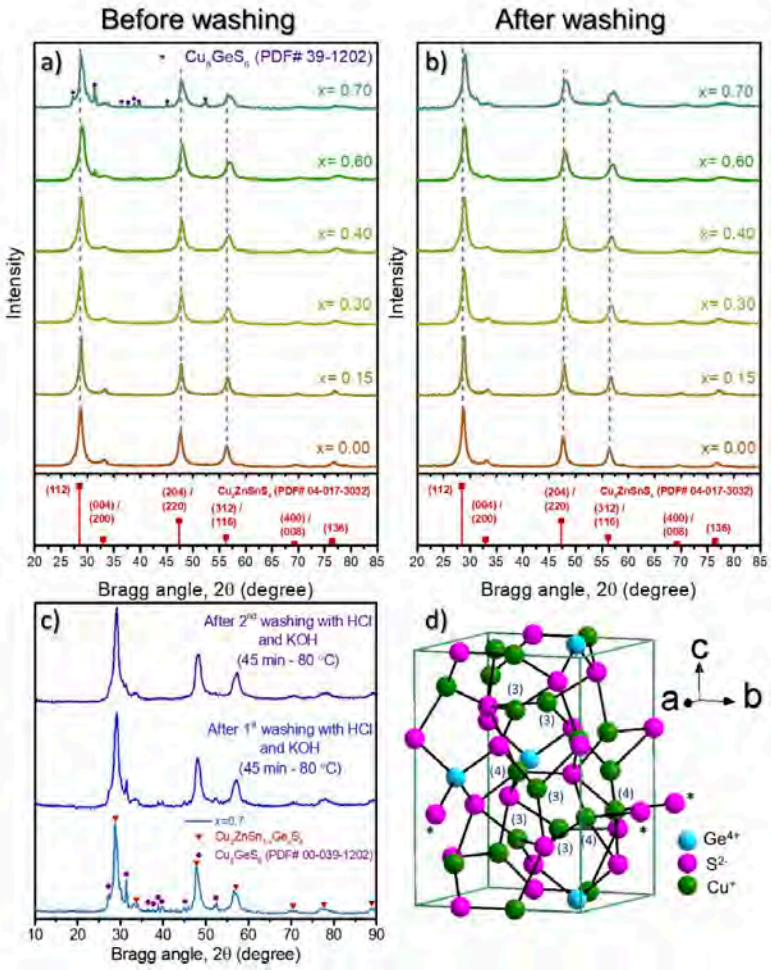

Fig. 1. XRD patterns of the $Cu_2ZnSn_{1-x}Ge_xS_4$ nanoparticles with different nominal Ge fractions (a) before and (b) after washing them with HCl solution (10%). (c) XRD patterns of the $Cu_2ZnSn_{1-x}Ge_xS_4$ nanoparticles prepared with nominal x 0.7, before and after 1st and 2nd washing with HCl solution. (d) Schematic presentation of Cu_8GeS_6 structure highlighting that copper ions have coordination number either of three or four, as indicated by the numbers in parenthesis in the scheme. The atoms marked with the asterisk symbols are the ones outside the unit cell.

in the present work was +2, it reduced to +1 by ethylenediamine [53], which facilitated the formation of $Cu_{1.81}S$ intermediate, and finally produce Cu_8GeS_6 phase on reacting with the Ge-precursor. Once the Cu_8GeS_6 phase is formed, it cannot be decomposed even performing the hydrothermal treatment at higher temperature due to its high thermal stability (melting point = 1250 K) [54]. Moreover, the Cu_8GeS_6 phase is reported to be formed around 100 °C, during hydrothermal process [52].

To remove the secondary Cu_8GeS_6 phase, we performed HCl treatment on the $Cu_2ZnSn_{1-x}Ge_xS_4$ samples as described in the previous section. As can be seen in Fig. 1b, the byproduct Cu_8GeS_6 could be

removed successfully through the used wet-chemical treatment. On HCl treatment, the intensity of the diffraction peaks associated with Cu_8GeS_6 phase reduced progressively in the samples prepared with the highest Ge content, without altering the relative intensity of diffraction peaks corresponding to $Cu_2ZnSn_{1-x}Ge_xS_4$ in kesterite phase (Fig. 1(b-c)). While the position of the principal diffraction peaks shifted only marginally towards higher Bragg angles, their full-width at half maximum (FWHM) reduced very slightly after HC treatment. The results indicate the used HCl treatments has no significant effect on the crystallinity or grain size of the nanoparticles. The Cu_8GeS_6 phase has argyrodite-type structure and most of the compounds with such a structure are superionic conductors due to hopping of Cu^+ ions across the lattice [55–57]. The distance between the neighboring Cu^+ ions in Cu_8GeS_6 is <2.9 Å. Some Cu^+ cations in Cu_8GeS_6 remain bonded to three S^2 anions and some remain bonded with four S^2 anions (see Fig. 1d). Therefore, the Cu–S bond distances in Cu_8GeS_6 vary in-between 2.219 and 2.590 Å [57,58]. On the contrary, in the kesterite CZTGS lattice, all the Cu^+ cations remain bonded with four S^2 anions in regular tetrahedral configuration (Fig. 2c) and the Cu–S bond distance varies in-between 2.26 and 2.29 Å [49]. The longer Cu–S bond distance in Cu_8GeS_6 compared with its distance in CZTGS phase makes the Cu_8GeS_6 phase less stable, which facilitates its etching by diluted HCl [59].

To monitor the effect of Ge incorporation on the lattice structure of the nanostructures, lattice parameters (a = b, c), unit cell volume and grain size were estimated by Rietveld refinement of the XRD patterns of the samples after their chemical treatment, using GSAS-II software (version 4379) [60]. Rietveld refinement outputs of the XRD patterns of the samples are presented in Fig. 2a. For Rietveld refinement, we utilized the EDS estimated composition of the samples, pseudo-Voigt function, the kesterite structure with space group $I\bar{4}$ (PDF# 04-017-3032), and Chebyshev polynomial-based background construction. EDS estimated elemental composition and cation mol fraction in the samples after washing with HCl solution are presented in Table 2. From the EDS estimated compositions of the as-prepared nanostructures, we can observe a gradual increase of Ge content in them with the increase of nominal mol fraction of Ge precursor in the reaction mixture. However, as the Ge/(Ge + Sn) ratio is also dependent on the fraction of Sn substitution by Ge, it is possible that not all the Ge atoms present in the reaction mixture were incorporated into the CZTGS lattice. Those non-participating Ge atoms can produce the ternary Cu_8GeS_6 phase by reacting with the Cu and S precursors in the reaction medium. Fig. 2b presents the Rietveld refinement extracted structural parameters of the samples after their chemical treatment. As can be observed (Fig. 2b), the values of both the lattice parameters and the unit cell volume decreased almost linearly with the increase of Ge content in the samples. Such linear variations of lattice parameters with x value indicate they follow the Vegard's law [61]:

$$\xi(x) = x\xi_{CZGS} + (1-x)\xi_{CZTS} - \delta x(1-x) \quad (1)$$

where $\xi(x)$ is the lattice parameter (a or c) of CZTGS, ξ_{CZTS} is the lattice parameter (a or c) of CZTS, ξ_{CZGS} is the lattice parameter of Cu_2ZnGeS_4 (CZGS), δ is the deviation parameter for the lattice constant, and x is the Ge mol fraction in CZTGS. For using in Eq. (1), we considered the lattice parameters of CZTS extracted from the Rietveld analysis of the XRD pattern of the sample without Ge (x = 0.0) and the lattice parameters of CZGS reported in the literature [61]. The best fits to the variations of lattice constant a and c were obtained for the deviation parameter $\delta = 0.01$ and $\delta = 0.1$ Å, respectively.

To study the effect of chemical treatment on the size, morphology and crystallinity of the nanostructures, if any, we performed their SEM, TEM and HR-TEM analyses before and after washing with HCl solution. Fig. 3 shows the typical SEM images of the CZTGS nanoparticles with different nominal Ge mol fractions before and after washing with HCl solution. Formation of quasi-spherical particles of nanometer sizes can be observed in the micrographs. As can be observed in Fig. 3, the nanoparticles of all the samples retained their quasi-spherical shape even after washing with HCl solution.

Size distribution histograms performed by measuring the dimensions of individual particles in the HCl-treated samples revealed an average particle size of 12.2 ± 3.6 nm for the sample prepared with 15% of Ge (Fig. 4b). On increasing the amount of Ge in the samples, average size of the nanoparticles reduced marginally (to 11.3 ± 2.5 nm for x = 0.7 sample). Well-resolved atomic planes in the HR-TEM images (Fig. 4(c, f, i and l)) of the HCl-treated nanoparticles indicate their good crystallinity. Intense spots in the fast Fourier transform (FFT) patterns of the selected areas (marked by red squares) of the HR-TEM images clearly indicate the good crystallinity of the nanoparticles. As can be observed in the HR-TEM images presented in the Fig. 4, interplanar distance of the principal lattice (1 1 2) plane of the CZTGS kesterite nanostructures decreases from 3.2 to 2.9 Å with the increase of Ge content. The reduction of average particle size and interplanar distance can be associated to the reduction of the unit cell volume in the crystal lattice on the

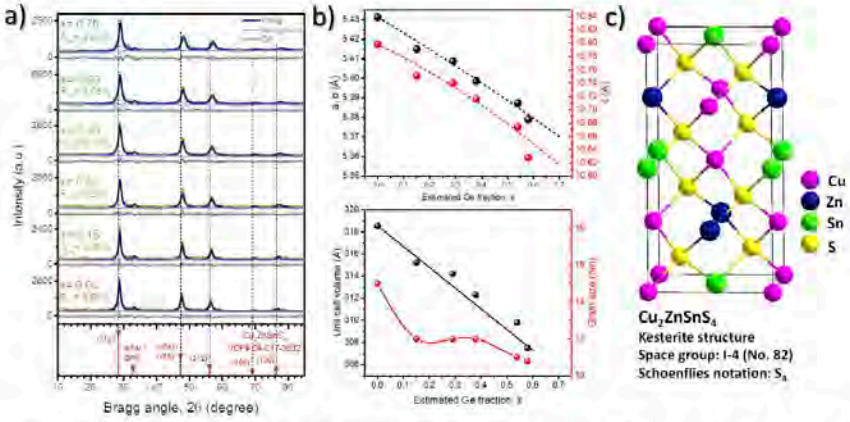

Fig. 2. (a) Rietveld analysis output profiles of the $Cu_2ZnSn_{1-x}Ge_xS_4$ nanoparticles for different Ge fractions (x) after washing them with HCl (10%). (b) Structural parameters extracted from Rietveld analysis of XRD patterns of the nanoparticles after washing. (c) Schematic presentation of the kesterite structure.

Table 2
EDS estimated elemental composition and cation mol fractions in the $Cu_2ZnSn_{1-x}Ge_xS_4$ nanoparticles after washing with HCl solution.

Sample (x-value)	Cu (at%)	Zn (at%)	Sn (at%)	Ge (at%)	S (at%)	Cu/(Zn + Sn + Ge)	Zn/(Sn + Ge)	Ge/(Sn + Ge)
0.0	28.92	10.67	10.62	-	49.79	1.36 ± 0.03	1.02 ± 0.22	0.00
0.15	27.07	10.32	9.38	1.64	51.60	1.27 ± 0.05	0.95 ± 0.20	0.15 ± 0.02
0.30	28.95	10.97	7.55	3.14	49.39	1.34 ± 0.03	1.03 ± 0.05	0.29 ± 0.02
0.40	29.09	10.28	6.86	4.26	49.52	1.36 ± 0.16	0.92 ± 0.02	0.38 ± 0.06
0.60	28.14	12.45	5.08	6.09	48.24	1.20 ± 0.13	1.12 ± 0.18	0.54 ± 0.05
0.70	29.81	9.38	4.48	6.31	50.02	1.48 ± 0.03	0.87 ± 0.04	0.58 ± 0.03

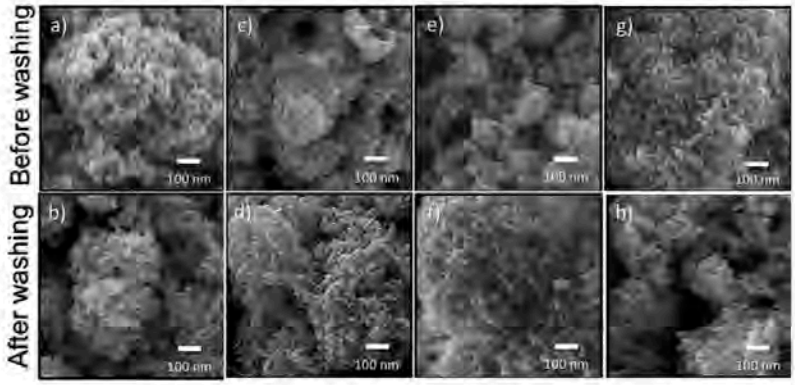

Fig. 3. Typical SEM images of the $Cu_2ZnSn_{1-x}Ge_xS_4$ nanoparticles with different nominal Ge fractions: (a,b) x 0.0, (c,d) 0.30, (e,f) 0.60, and (g,h) 0.70, before (upper case) and after (lower case) washing them with HCl (10%).

incorporation of Ge, as observed in the structural parameters extracted from Rietveld analysis of XRD patterns of the nanoparticles (Fig. 2**b**).

As the phase purity and the crystallinity of the nanostructures can be confirmed from their Raman spectra, we performed Raman spectroscopy of the as-prepared and HCl-treated CZTGS nanoparticles at room temperature taking adequate precautions by selecting appropriate objective lenses and filters (neutral density filters) to avoid their oxidation or burning. Room temperature Raman spectra of the CZTGS nanoparticles before and after washing with HCl solution are presented in Fig. 5**(a, b)**, respectively. The Raman spectra of as-prepared and HCl-treated samples revealed an intense dispersion band around 330 cm^{-1}. However, the dispersion band is wide and asymmetric, contains humps at both the sides (lower and higher wavenumber sides) around its maximum. To analyze the features of Raman spectra, the principal Raman band of each of the samples was carefully deconvoluted using Lorentzian curve fitting analysis (Fig. 5**(a, b)**).

We can see that the principal dispersion band of all the samples (before and after HCl washing) contains three component peaks around 280, 330 and 350 cm^{-1}. According to the literature, the principal dispersion bands of stoichiometric CZTS, the so-called A vibrational modes, are located at 287 and 337 cm^{-1}, which correspond to the rotational and stretching vibration of Sn-S bonds in the SnS_4 tetrahedron of CZTS, respectively. Meanwhile, the component band located around 350 cm^{-1} corresponds to the displacement of cations along the c-axis (called as B vibrational mode) [62,63]. However, the A vibrational modes can shift towards lower wavenumbers due to non-stoichiometric composition [64]. In Table 2, we can observe a change in the Zn/(Sn + Ge) and Cu/(Zn + Sn + Ge) ratios for HCl-treated samples in comparison to their values in as-prepared (untreated) samples. The observed change in cation ratios for the HCl-treated samples is probably due to a reduction in Zn content in them (as observed from EDS analysis). The Zn fraction not incorporated into the $Cu_2ZnSn_{1-x}Ge_xS_4$ lattice reacts with sulfur, generating ZnS secondary phase. However, we could not detect any peak in the XRD patterns of the as-grown nanoparticles associated to the ZnS phase. In fact, the ZnS phase is difficult to be detected in the XRD patterns of the samples as its crystal structure (cubic, $a = 5.41$ Å) is similar to kesterite structure (tetragonal, $a = 5.43$ Å and $c = 10.84$ Å) [20], which produces diffraction peaks at the similar Bragg angles as that of crystalline CZTS. Although Raman spectroscopy with He-Cd laser excitation ($\lambda = 325$ nm) has been utilized to detect the traces of ZnS phase in CZTS films by Fairbrother et al. [42], we could not detect any signal associated to ZnS in our as-prepared nanostructures, probably due to the utilization of He-Ne laser ($\lambda = 633$ nm) for excitation, the energy of which is far below the band gap energy of ZnS ($E_g = 3.6$ eV).

The vibrational modes of the kesterite structure are expected to be sensitive to Ge, incorporated in its lattice. Substitution of Sn by Ge in the kesterite (CZTS) lattice replaces some of the Sn-S bonds by Ge-S bonds, modifying the effective force constant of the cation-anion bonds due to the mass and size differences of the Sn^{4+} and Ge^{4+} ions. Consequently, the positions of Raman dispersion bands are slightly shifted towards higher wavenumber (blue shift) [28,51,65]. The displacement of the principal component band around of 330 cm^{-1} as the function of EDS estimated Ge fraction in the as-prepared and HCl-treated nanostructures are presented in Fig. 5c. As can be noticed, the principal component band in both the as-prepared and HCl-treated samples shifted towards higher wavenumbers with Ge mol fraction, clearly indicating the substitution of Sn by Ge in the kesterite lattice. Moreover, we can observe an offset between the positions of the principal component band of the as-prepared and HCl-treated samples. As revealed from EDS analysis (Table 2), after HCl-treatment, the CZTGS nanoparticles are Cu-rich and Zn-poor ($Cu/(Zn + Sn + Ge) \geq 1$ and $Zn/(Sn + Ge) \leq 1$), which is the ideal stoichiometry for their application in photovoltaic devices [32]. The small change (≤ 3 cm^{-1}) in the position of the principal Raman band of the HCl-treated samples is probably attributed to the change in the composition of the nanostructures from Cu-poor to Cu-rich, as has been reported by Valakh et al. [64].

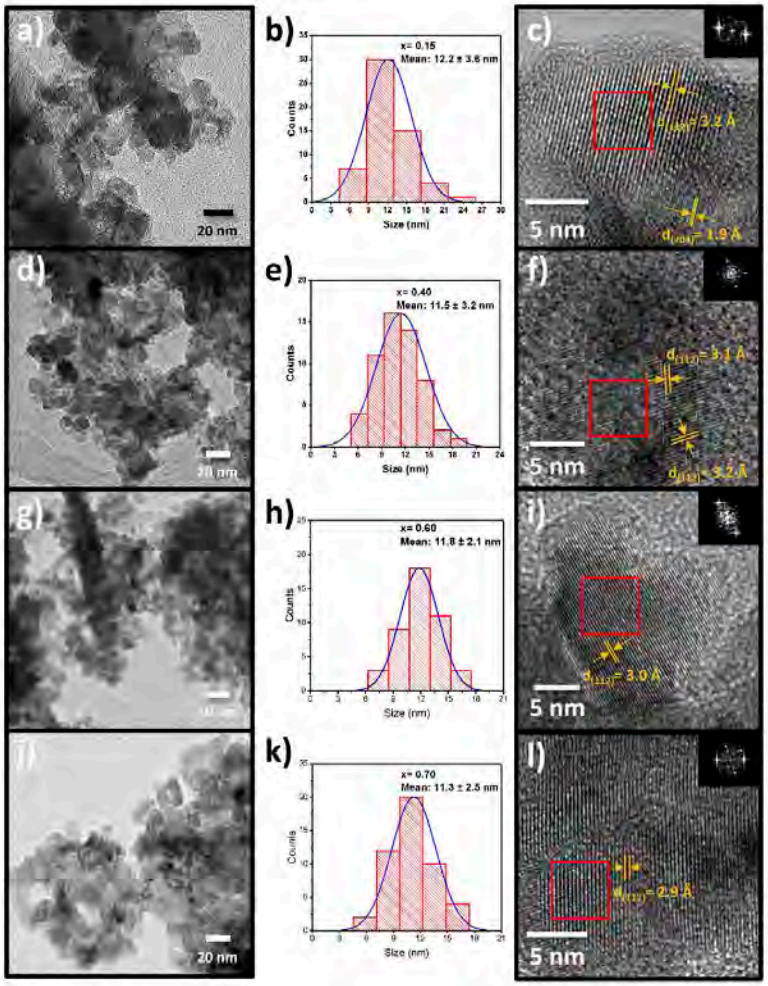

Fig. 4. Typical low- and high-resolution TEM micrographs and corresponding size distribution histograms of the $Cu_2ZnSn_{1-x}Ge_xS_4$ nanoparticles with different nominal Ge fractions: (a-c) x 0.15, (d-f) x 0.40, (g-i) x 0.60, and (j-l) x 0.70, after washing with HCl solution. Insets in the HR-TEM micrographs correspond to the FFT patterns of the selected areas (red square zones) in each HR-TEM image. (For interpretation of the references to colour in this figure legend, the reader is referred to the web version of this article.)

On the other hand, the full width at half maximum (FWHM) of Raman bands is associated with defect-induced disorder in the kesterite structure (owing to the formation of Cu_{Zn} or Zn_{Cu} antisite defects). The value of FWMH increases with the increase of Cu_{Zn} or Zn_{Cu} antisite defect concentration [64]. As we can see in Fig. 5**d**, in general, the value of FWHM of the principal Raman band increases with the increase of Ge content in the kesterite lattice. The nanoparticles treated with HCl in this work have Cu-rich and Zn-poor stoichiometry, in which the Cu ions in excess can occupy the Zn sites and produce Cu_{Zn} antisite defects. There occurs also a lattice disorder in the kesterite structure due to the random occupation of Cu and Zn atoms, increasing the concentration of Cu_{Zn} or Zn_{Cu} antisite defects. The disorder in the kesterite lattice also increases due to the substitution of Sn by Ge as observed by several research groups [37,45]. Therefore, the observed increase of FWHM value (Fig. 5**d**) in the CZTGS nanoparticles prepared in this investigation is probably associated to an increment of disorder in the crystal structure owing to an increase of Cu_{Zn} antisite defect concentration and the incorporation of Ge at Sn sites of the kesterite lattice. The results obtained from the EDS and Raman spectroscopy analysis of the nanostructures (Table 2 and Fig. 5**c**, respectively) indicate that under the used synthesis conditions, there exists a maximum limit for the incorporation of Ge in the CZTGS nanoparticles. Incorporation of Ge precursor in the reaction mixture beyond that limit causes the formation of Cu_8GeS_6 secondary phase.

For determining the bandgap energy of the as-prepared and HCl-treated CZTGS nanoparticles, we recorded their diffuse reflectance spectra in 300–920 nm wavelength range (Fig. 6**(a, b)**). The diffuse reflectance spectra were converted to equivalent absorption spectra using the Kubelka-Munk (K-M) formalism [66]. Fig. 6**(c, d)** show the K-M plots for the as-prepared and HCl-treated nanoparticles, with linear extrapolations to determine their bandgap energy values. The optical bandgap energy values increased from 1.55 to 1.81 eV and 1.42 to 1.70

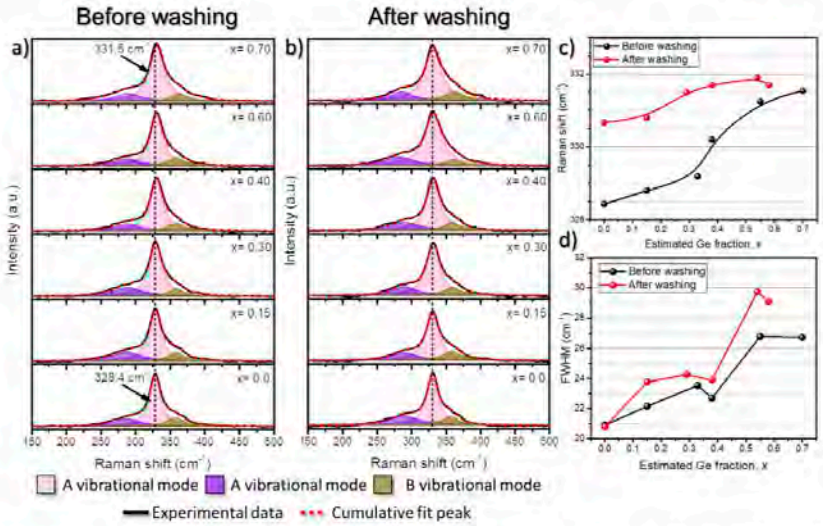

Fig. 5. Room temperature Raman spectra and their deconvolutions for the $Cu_2ZnSn_{1-x}Ge_xS_4$ nanoparticles prepared with different nominal x values: (a) before and (b) after washing with HCl (10%). (c) Variation of peak position and (d) FWHM of the principal component band (around 330 cm^{-1}) with the increase of true (EDS estimated) Ge mol fraction.

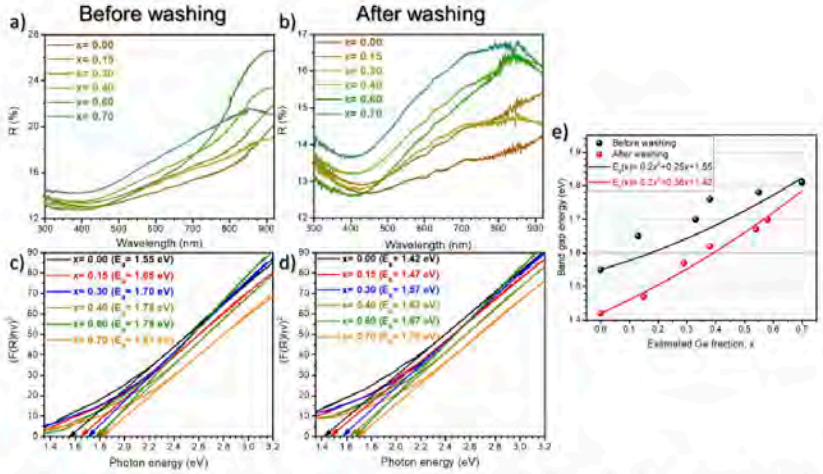

Fig. 6. Diffuse reflectance spectra and Kubelka-Munk plots used to estimate the bandgap energy values of $Cu_2ZnSn_{1-x}Ge_xS_4$ nanoparticles (a,c) before and (b,d) after washing with HCl solution. (e) Variation of bandgap energy with real (EDS estimated) Ge fraction in the nanoparticles. The solid black and red lines correspond to the ideal bandgap energy values according to the Vegard's law. (For interpretation of the references to colour in this figure legend, the reader is referred to the web version of this article.)

eV with the increase of Ge fraction in the samples before and after their HCl treatment, respectively, clearly indicating an increase in bandgap energy due to the substitution of Sn by Ge. The observed increase in the bandgap energy value with increased Ge mol fraction (x) in the kesterite nanoparticles is in good agreement with the results reported by several research groups [38,51,67,68]. The difference in bandgap energy values of a sample containing a certain Ge mol fraction before and after its HCl treatment corresponds to the elimination of impurity phases from it. HCl solution has the capacity of breaking Zn–S bonds in materials of zinc blende structure such as ZnS [42,69]. So, there is a good possibility that HCl attacks $Cu_2ZnSn_{1-x}Ge_xS_4$ kesterite, which has a double zinc blend structure, removing selectively some of the Zn^{2+} ions from the surface of the nanoparticles. To maintain the electroneutrality of the kesterite lattice, equivalent numbers of S^{2-} anions should also be removed from it

or the valence state of its Cu ions should be changed from 1+ to 2+. The removal of Zn^{2+} ions from the surface of kesterite nanoparticles is in accordance with the increment in Cu atomic percentage and reduction of Zn atomic percentage as shown in Table 2. The reduction of the bandgap energy for the HCl-treated samples can be explained in terms of the positions of the valence band maximum (VBM) and conduction band minimum (CBM). In CZTS, the VBM is composed of antibonding Cu-3d and S-3p orbitals, and the CBM is composed of antibonding combinations of Sn-5s and S-3p orbitals [17]. Selective elimination of the Zn^{2+} ions from the surface of CZTGS nanoparticles due on HCl treatment probably promotes the formation of acceptor levels close to the VBM owing to change the oxidation state of Cu from Cu^{1+} to Cu^{2+} [16,70–72], reducing their effective bandgap energy.

The empirical relationship between the bandgap energy value and Ge/(Ge + Sn) ratio in the kesterite can be expressed by the Vegard's relation (Eq. (2)) with a correction term, known as bowing parameter (associated to the curvature of the bandgap energies):

$$E_g^{CZTGS}(x) = xE_g^{CZGS} + (1-x)E_g^{CZTS} - bx(1-x) \quad (2)$$

where E_x^{CZTS} and E_x^{CZGS} are the bandgap energies of CZTS and CZGS respectively, x is the Ge mol fraction in CZTGS and b is the bowing parameter which describes the degree of nonlinearity. The experimentally obtained data for both the untreated and HCl treated samples were found to be best fitted for a bowing constant equal to 0.2 eV, as has also been reported by Mora-Herrera et al. and Chen et al. [37,51]. The small bowing constant implies that the bandgap energy of CZTGS nanostructures increase almost linearly with the increase of Ge mol fraction (x). For calculating bandgap energies of the $Cu_2ZnSn_{1-x}Ge_xS_4$ nanostructures we utilized the experimentally determined bandgap energy values of the CZTS nanoparticles before and after HCl treatment (1.55 and 1.42 eV) and the literature reported bandgap energy value of pure CZGS (2.0 eV) [38,51]. The solid black and red colored curves in Fig. 6e show the calculated bandgap energy variations for the CZTGS nanoparticles with different x values before and after their HCl treatment. As can be noticed, the experimentally determined bandgap energy values of the chemically treated samples are very close to their empirical values. However, the experimentally determined bandgap energy values of the as-prepared (untreated) samples deviated significantly from their empirical ones due to the presence of secondary phases Cu_8GeS_6 and ZnS.

As the transport properties of the kesterite semiconductors, such as their electrical resistivity (ρ), carrier concentration (p), and carrier mobility (μ), are important parameters which define their application in optoelectronic devices such as PSCs, we performed room temperature conductivity and Hall measurements on the spin-coated films of the as-prepared and chemically treated nanoparticles. Average thickness of the as-prepared and chemically treated films utilized for electrical characterizations were 2.34 ± 0.44 and 2.21 ± 0.66 μm, respectively. The arrangement of the silver contacts over CZTGS films utilized to measure the resistivity and Hall effect is present in Fig. 7a.

As can be seen in Fig. 7b, electrical conductivity of the kesterite films prepared with as-prepared nanoparticles did not vary substantially with the increase of nominal mol fraction of Ge. However, the films prepared with chemically treated nanoparticles revealed significant increase in conductivity, for all the Ge fraction values (Fig. 7b). All the samples revealed positive Hall voltage, indicating their p-type electrical conductivity at room temperature. In fact, CZTS is intrinsically a p-type semiconductor due to the presence of Cu_{Zn} antisite and Cu-vacancy defects [16,70–72]. As can be seen in Fig. 7c, all the films prepared with untreated nanoparticles revealed high carrier concentration, which

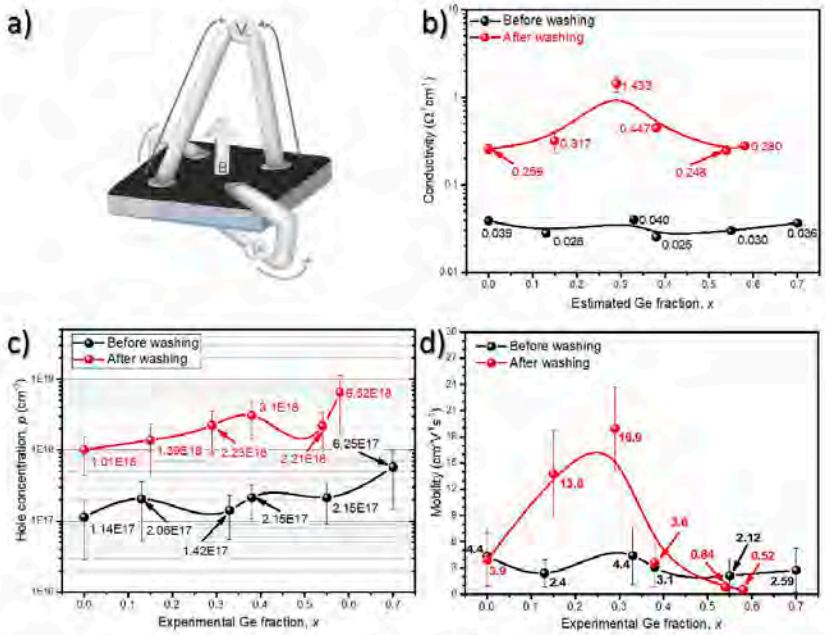

Fig. 7. (a) Schematic representation of the arrangement of the silver dot contacts over the CZTGS films used to measure resistivity and Hall voltage (V_H). The arrow B shows the direction of applied magnetic field. Variations of (b) electrical conductivity (σ), (c) carrier concentration (p) and (d) carrier mobility (μ), in the $Cu_2ZnSn_{1-x}Ge_xS_4$ films prepared with as-prepared and HCl-treated.

increased from $1.14x10^{17}$ to $6.25x10^{17}$ cm^{-3} with the increase of Ge mol fraction (x) from 0.0 to 0.7. Such an increase in hole concentration in the films can be associated to an increase in Cu_{Zn} antisite defects in the nanostructures with the increase of Ge mol fraction. In fact, the increase of Cu_{Zn} antisite defects with increased x value was also noticed in the Raman spectra of the samples (Fig. 5). The Cu_{Zn} antisite defects form an acceptor level in the bandgap of kesterite close to its valence band and contribute to the concentration of the charge carriers in the kesterite [16,70–72]. Therefore, the observed increase in carrier concentration of the CZTGS films with increased Ge mol fraction is probably due to higher concentration of Cu_{Zn} antisite defects in them. Besides, we can observe a substantial increase in carrier concentration by about one order of magnitude (from $\sim10^{17}$ to $\sim10^{18}$ cm^{-3}) for the films prepared with HCl-treated kesterite nanoparticles. This increase is due to higher concentration of Cu_{Zn} antisite defects in the films prepared with HCl-treated kesterite nanoparticles. The increment in Cu_{Zn} antisite defects is in accordance with the results observed in the diffuse reflectance spectroscopy of the samples.

Electrical conductivity of the films fabricated using as-prepared nanoparticles remained almost unchanged with the increase of Ge content. However, the conductivity increased noticeably after washing the nanoparticles with HCl, probably due to the removal of secondary phases from them. It should be recalled that we could not detect the presence of secondary phases such as $Cu_{2-x}S$ or Cu_2SnS_3 in the XRD or Raman spectra either of the as-prepared or HCl-treated samples. Therefore, the observed change in conductivity must be associated to ZnS in the nanostructures, which was eliminated by HCl treatment. On the other hand, the mobility of the charge carrier in the films prepared using as-prepared nanoparticles did not vary significantly with the variation of nominal Ge fraction (Fig. 7d). The observed non-variant nature of carrier mobility in the samples probably due to the presence of ZnS phase, which is an insulator material. Therefore, we expected an increase in carrier mobility for the films prepared using HCl-treated nanostructures. However, as can be observed in Fig. 7d, the HCl treatment enhanced the carrier mobility only up to $x \sim 0.3$. For higher Ge content ($x \geq 0.4$) kesterite films, the mobility decreased from 3.6 to 0.52 $cm^2V^{-1}s^{-1}$. The observed reduction in carrier mobility for higher Ge content films prepared with HCl-treated nanoparticles is probably due to the removal of Cu_8GeS_6 phase, which has been reported as a p-type semiconductor with high hole mobility (~16 $cm^2V^{-1}s^{-1}$) [73]. The Cu_8GeS_6 formed in the samples has a large particle size, as evidenced by the narrow diffraction peak at around $2\theta = 43.73°$ in the XRD spectra of the CZTGS films of higher Ge content (Fig. 1a), which enhances the carrier mobility. Removal or etching out of those bigger Cu_8GeS_6 grains from the samples causes a reduction in the hole mobility for the films prepared with HCl-treated CZTGS nanoparticles. On the other hand, the reduction of hole mobility for higher x-value ($x > 0.3$) samples can also be due to their very high carrier concentration, which induces carrier scattering (hole-lattice) in the sample, even at room temperature.

4. Conclusions

In summary, we demonstrated the fabrication of quasi-spherical $Cu_2ZnSn_{1-x}Ge_xS_4$ nanoparticles of about 11 nm average size with predominant kesterite phase through a low-temperature hydrothermal process. Incorporation of Ge in the kesterite nanostructures induces the formation of secondary phases such as ZnS and Cu_8GeS_6, depending on the mole fraction of Ge used to prepare them. The secondary phases formed in the nanoparticles could be completely removed by treating them with dilute (10%) HCl solution at 80 °C. The HCl treatment does not affect the kesterite structure, neither it affects the size and morphology of the nanoparticles. Incorporation of Ge enhances the concentration of Cu_{Zn} antisite defect in the kesterite lattice, enhances the hole concentration in the kesterite nanoparticles. Transport behaviors of the CZTGS films prepared using HCl-treated kesterite nanoparticles indicate that they are promising candidates for utilization as HTLs. The results presented in this study are useful for developing CZTGS based photovoltaic devices with high photoconversion efficiency.

CRediT authorship contribution statement

Francisco Enrique Cancino-Gordillo: Methodology, Formal analysis, Investigation, Visualization, Writing - original draft, Writing - review & editing. **José-Luis Ortiz-Quiñonez:** Investigation, Writing-review & editing, Validation, Formal analysis. **Mou Pal:** Writing-review & editing, Validation. **Rutilo Silva González:** Formal analysis, Validation, Visualization. **Umapada Pal:** Conceptualization, Methodology, Supervision, Funding acquisition, Project administration, Resources, Writing - original draft, Writing - review & editing.

Declaration of Competing Interest

The authors declare that they have no known competing financial interests or personal relationships that could have appeared to influence the work reported in this paper.

Data availability

Data will be made available on request.

Acknowledgments

This work was supported by CONACyT (Grant # CB A1-S-26720), Mexico. FECG acknowledges CONACyT, Mexico, for the doctoral fellowship (CVU # 784149).

References

[1] M. Grossberg, J. Krustok, C.J. Hages, D.M. Bishop, O. Gunawan, R. Scheer, S. M. Lyam, H. Hempel, S. Leveenco, T. Unold, The electrical and optical properties of kesterites, J. Phys. Energy. 1 (2019) 044002, https://doi.org/10.1088/2515-7655/ab29a0.

[2] K. Pal, P. Singh, A. Bhaduri, K.B. Thapa, Current challenges and future prospects for a highly efficient (20%) kesterite CZTS solar cell: A review, Sol. Energy Mater. Sol. Cells 196 (2019) 138–156, https://doi.org/10.1016/j.solmat.2019.03.003.

[3] C. Yan, J. Huang, K. Sun, S. Johnston, Y. Zhang, H. Sun, A. Pu, M. He, F. Liu, K. Eder, L. Yang, J.M. Cairney, N.J. Ekins-Daukes, Z. Hameiri, J.A. Stride, S. Chen, M.A. Green, X. Hao, Cu_2ZnSnS_4 solar cells with over 10% power conversion efficiency enabled by heterojunction heat treatment, Nat. Energy 3 (2018) 764–772, https://doi.org/10.1038/s41560-018-0206-0.

[4] W. Wang, M.T. Winkler, O. Gunawan, T. Gokmen, T.K. Todorov, Y. Zhu, D.B. Mitzi, Device Characteristics of CZTSSe Thin-Film Solar Cells with 12.6% Efficiency, Adv. Energy Mater. 4 (2014) 1301465, https://doi.org/10.1002/aenm.201301465.

[5] M.A. Green, E.D. Dunlop, J. Hohl-Ebinger, M. Yoshita, N. Kopidakis, X. Hao, Solar cell efficiency tables (Version 58), Prog. Photovoltaics Res. Appl. 29 (2021) 657–667, https://doi.org/10.1002/pip.3444.

[6] M.H. Sharif, T. Enkhbat, E. Enkhbayar, J. Kim, Control of Defect States of Kesterite Solar Cells to Achieve More Than 11% Power Conversion Efficiency, ACS Appl. Energy Mater. 3 (2020) 8500–8508, https://doi.org/10.1021/acsaem.0c01141.

[7] P. Liu, W. Wang, S. Liu, H. Yang, Z. Shao, Fundamental Understanding of Photocurrent Hysteresis in Perovskite Solar Cells, Adv. Energy Mater. 9 (2019) 1803017, https://doi.org/10.1002/aenm.201803017.

[8] A.M. Elseman, S. Sajid, A.E. Shalan, S.A. Mohamed, M.M. Rashad, Recent progress concerning inorganic hole transport layers for efficient perovskite solar cells, Appl. Phys. A Mater. Sci. Process. 125 (2019), https://doi.org/10.1007/s00339-019-2766-7.

[9] I.M. Peters, T. Buonassisi, Energy Yield Limits for Single-Junction Solar Cells, Joule 2 (2018) 1160–1170, https://doi.org/10.1016/j.joule.2018.03.009.

[10] M.M.S. Sanad, A.M. Elseman, M.M. Elsenety, M.M. Rashad, B.A. Elsayed, Facile synthesis of sulfide-based chalcogenide as hole-transporting materials for cost-effective efficient perovskite solar cells, J. Mater. Sci. Mater. Electron. 30 (2019) 6868–6875, https://doi.org/10.1007/s10854-019-01001-6.

[11] U. Syafiq, N. Ataollahi, P. Scardi, Progress in CZTS as hole transport layer in perovskite solar cell, Sol. Energy. 196 (2020) 399–408, https://doi.org/10.1016/j.solener.2019.12.016.

[12] Q. Wu, C. Xue, Y. Li, P. Zhou, W. Liu, J. Zhu, S. Dai, C. Zhu, S. Yang, Kesterite Cu_2ZnSnS_4 as a Low-Cost Inorganic Hole-Transporting Material for High-Efficiency Perovskite Solar Cells, ACS Appl. Mater. Interfaces 7 (2015) 28466–28473, https://doi.org/10.1021/acsami.5b09572.

[13] M. Yuan, X. Zhang, J. Kong, W. Zhou, Z. Zhou, Q. Tian, Y. Meng, S. Wu, D. Kou, Controlling the Band Gap to Improve Open-Circuit Voltage in Metal Chalcogenide

based Perovskite Solar Cells, Electrochim. Acta 215 (2016) 374–379, https://doi.org/10.1016/j.electacta.2016.08.130.
[14] M. Kumar, A. Dubey, N. Adhikari, S. Venkatesan, Q. Qiao, Strategic review of secondary phases, defects and defect-complexes in kesterite CZTS–Se solar cells, Energy Environ. Sci. 8 (2015) 3134–3159, https://doi.org/10.1039/C5EE01265G.
[15] S. Chen, L.-W. Wang, A. Walsh, X.G. Gong, S.-H. Wei, Abundance of $Cu_{Zn} + Sn_{Zn}$ and $2Cu_{Zn} + Sn_{Zn}$ defect clusters in kesterite solar cells, Appl. Phys. Lett. 101 (2012), 223901, https://doi.org/10.1063/1.4768215.
[16] D. Han, Y.Y. Sun, J. Bang, Y.Y. Zhang, H.-B. Sun, X.-B. Li, S.B. Zhang, Deep electron traps and origin of p-type conductivity in the earth-abundant solar-cell material Cu_2ZnSnS_4, Phys. Rev. B 87 (2013), 155206, https://doi.org/10.1103/PhysRevB.87.155206.
[17] S. Chen, A. Walsh, X.-G. Gong, S.-H. Wei, Classification of Lattice Defects in the Kesterite Cu_2ZnSnS_4 and $Cu_2ZnSnSe_4$ Earth-Abundant Solar Cell Absorbers, Adv. Mater. 25 (2013) 1522–1539, https://doi.org/10.1002/adma.201203146.
[18] K. Biswas, S. Lany, A. Zunger, The electronic consequences of multivalent elements in inorganic solar absorbers: Multivalency of Sn in Cu_2ZnSnS_4, Appl. Phys. Lett. 96 (2010), 201902, https://doi.org/10.1063/1.3427433.
[19] H. Du, F. Yan, M. Young, B. To, C.-S. Jiang, P. Dippo, D. Kuciauskas, Z. Chi, E. A. Lund, C. Hancock, W.M. Hlaing OO, M.A. Scarpulla, G. Teeter, Investigation of conbinatorial coevaporated thin film Cu_2ZnSnS_4. I. Temperature effect, crystalline phases, morphology, and photoluminescence, J. Appl. Phys. 115 (2014), 173502, https://doi.org/10.1063/1.4871664.
[20] G. Altamura, J. Vidal, Impact of Minor Phases on the Performances of CZTSSe Thin-Film Solar Cells, Chem. Mater. 28 (2016) 3540–3563, https://doi.org/10.1021/acs.chemmater.6b00069.
[21] W.-S. Liu, S.-Y. Chen, C.-S. Huang, M.-Y. Lee, H.-C. Kuo, Investigation of Zn/Sn ratio for improving the material quality of CZTS thin films with the reduction of $Cu_{2-x}S$ secondary phase, J. Alloys Compd. 853 (2021), 157237, https://doi.org/10.1016/j.jallcom.2020.157237.
[22] J. Xu, J. Yang, S. Jiang, S. Shang, Secondary phases and disorder degree investigation of Cu_2ZnSnS_4 films, Ceram. Int. 47 (2021) 4135–4142, https://doi.org/10.1016/j.ceramint.2020.09.290.
[23] I.S. Babichuk, M.O. Semenenko, S. Golovynskyi, R. Caballero, O.I. Datsenko, I. V. Babichuk, J. Li, G. Xu, R. Qiu, C. Huang, R. Hu, I. Golovynska, V. Garnus, B. Li, J. Qu, M. Leon, Control of secondary phases and disorder degree in Cu_2ZnSnS_4 films by sulfurization at varied subatmospheric pressures, Sol. Energy Mater. Sol. Cells. 200 (2019), 109915, https://doi.org/10.1016/j.solmat.2019.109915.
[24] M.G. Gang, V.C. Karade, M.P. Suryawanshi, H. Yoo, M. He, X. Hao, I.J. Lee, B. H. Lee, S.W. Shin, J.H. Kim, A Facile Process for Partial Ag Substitution in Kesterite $Cu_2ZnSn(S, Se)_4$ Solar Cells Enabling a Device Efficiency of over 12%, ACS Appl. Mater. Interfaces 13 (2021) 3959–3968, https://doi.org/10.1021/acsami.0c19373.
[25] C. Ma, H. Guo, K. Zhang, N. Yuan, J. Ding, Fabrication of p-type Kesterite Ag_2ZnSnS_4 thin films with a high hole mobility, Mater. Lett. 186 (2017) 390–393, https://doi.org/10.1016/j.matlet.2016.10.013.
[26] H. Guo, C. Ma, K. Zhang, X. Jia, Y. Li, N. Yuan, J. Ding, The fabrication of Cd-free Cu_2ZnSnS_4-Ag_2ZnSnS_4 heterojunction photovoltaic devices, Sol. Energy Mater. Sol. Cells 178 (2018) 146–153, https://doi.org/10.1016/j.solmat.2018.01.022.
[27] S. Hadke, S. Levcenko, G. Sai Gautam, C.J. Hages, J.A. Márquez, V. Izquierdo-Roca, E.A. Carter, T. Unold, L.H. Wong, Suppressed Deep Traps and Bandgap Fluctuations in Cu_2CdSnS_4 Solar Cells with ≈8% Efficiency, Adv. Energy Mater. 9 (2019) 1902509, https://doi.org/10.1002/aenm.201902509.
[28] M. Cao, L. Li, W.Z. Fan, X.Y. Liu, Y. Sun, Y. Shen, Quaternary Cu_2CdSnS_4 nanoparticles synthesized by a simple solvothermal method, Chem. Phys. Lett. 534 (2012) 34–37, https://doi.org/10.1016/j.cplett.2012.03.016.
[29] C.J. Hages, S. Levcenco, C.K. Miskin, J.H. Alsmeier, D. Abou-Ras, R.G. Wilks, M. Bär, T. Unold, R. Agrawal, Improved performance of Ge-alloyed CZTGeSSe thin-film solar cells through control of elemental losses, Prog. Photovoltaics Res. Appl. 23 (2015) 376–384, https://doi.org/10.1002/pip.2442.
[30] S. Giraldo, M. Neuschitzer, T. Thersleff, S. López-Marino, Y. Sánchez, H. Xie, M. Colina, M. Placidi, P. Pistor, V. Izquierdo-Roca, K. Leifer, A. Pérez-Rodríguez, E. Saucedo, Large Efficiency Improvement in $Cu_2ZnSnSe_4$ Solar Cells by Introducing a Superficial Ge Nanolayer, Adv. Energy Mater. 5 (2015) 1501070, https://doi.org/10.1002/aenm.201501070.
[31] S. Kim, K.M. Kim, H. Tampo, H. Shibata, S. Niki, Improvement of voltage deficit of Ge-incorporated kesterite solar cell with 12.3% conversion efficiency, Appl. Phys. Express. 9 (2016), 102301, https://doi.org/10.7567/APEX.9.102301.
[32] K.-S. Lim, S.-M. Yu, S. Seo, H. Shin, T.-S. Oh, J.-B. Yoo, Incorporation of Ge in Cu_2ZnSnS_4 thin film in a Zn-poor composition range, Mater. Sci. Semicond. Process. 89 (2019) 194–200, https://doi.org/10.1016/j.mssp.2018.09.030.
[33] L. Choubrac, M. Bär, X. Kozina, R. Félix, R.G. Wilks, G. Brammertz, S. Levcenko, L. Arzel, N. Barreau, S. Harel, M. Meuris, B. Vermang, Sn Substitution by Ge: Strategies to Overcome the Open-Circuit Voltage Deficit of Kesterite Solar Cells, ACS Appl. Energy Mater. 3 (2020) 5830–5839, https://doi.org/10.1021/acsaem.0c00763.
[34] J. Li, D. Wang, X. Li, Y. Zeng, Y. Zhang, Cation Substitution in Earth-Abundant Kesterite Photovoltaic Materials, Adv. Sci. 5 (2018), https://doi.org/10.1002/advs.201700744.
[35] M. Rütze, S. Schönherr, P. Schöppe, W. Wisniewski, S. Giraldo, G. Gurieva, A. Johannes, C.T. Plass, K. Ritter, G. Martínez-Criado, S. Schorr, E. Saucedo, C. Ronning, C.S. Schnohr, On the Germanium Incorporation in $Cu_2ZnSnSe_4$ Kesterite Solar Cells Boosting Their Efficiency, ACS Appl. Energy Mater. 3 (2020) 558–564, https://doi.org/10.1021/acsaem.9b01784.
[36] M. Neuschitzer, M.E. Rodriguez, M. Guc, J.A. Marquez, S. Giraldo, I. Forbes, A. Perez-Rodriguez, E. Saucedo, Revealing the beneficial effects of Ge doping on $Cu_2ZnSnSe_4$ thin film solar cells, J. Mater. Chem. A 6 (2018) 11759–11772, https://doi.org/10.1039/C8TA02551C.
[37] D. Mora-Herrera, M. Pal, F. Paraguay-Delgado, Facile solvothermal synthesis of $Cu_2ZnSn_{1-x}Ge_xS_4$ nanocrystals: Effect of Ge content on optical and electrical properties, Mater. Chem. Phys. 257 (2021), 123764, https://doi.org/10.1016/j.matchemphys.2020.123764.
[38] X. Lv, C. Zhu, H. Hao, R. Liu, Y. Wang, J. Wang, Improving the performance of low-cost water-based solution-synthesised $Cu_2ZnSn_{1-x}Ge_x(S, Se)_4$ absorber thin films by germanium doping, Ceram. Int. 46 (2020) 25638–25645, https://doi.org/10.1016/j.ceramint.2020.07.039.
[39] M. Neuschitzer, J. Marquez, S. Giraldo, M. Dimitrievska, M. Placidi, I. Forbes, V. Izquierdo-Roca, A. Pérez-Rodríguez, E. Saucedo, V_{oc} Boosting and Grain Growth Enhancing Ge-Doping Strategy for $Cu_2ZnSnSe_4$ Photovoltaic Absorbers, J. Phys. Chem. C 120 (2016) 9661–9670, https://doi.org/10.1021/acs.jpcc.6b02215.
[40] A.D. Collord, H.W. Hillhouse, Germanium Alloyed Kesterite Solar Cells with Low Voltage Deficits, Chem. Mater. 28 (2016) 2067–2073, https://doi.org/10.1021/acs.chemmater.5b04806.
[41] M. Buffière, G. Brammertz, S. Sahayaraj, M. Batuk, S. Khelifi, D. Mangin, A. A. El Mel, L. Arzel, J. Hadermann, M. Meuris, J. Poortmans, KCN Chemical Etch for Interface Engineering in $Cu_2ZnSnSe_4$ Solar Cells, ACS Appl. Mater. Interfaces 7 (2015) 14690–14698, https://doi.org/10.1021/acsami.5b02122.
[42] A. Fairbrother, E. García-Hemme, V. Izquierdo-Roca, X. Fontané, F.A. Pulgarín-Agudelo, O. Vigil-Galán, A. Pérez-Rodríguez, E. Saucedo, Development of a Selective Chemical Etch To Improve the Conversion Efficiency of Zn-Rich Cu_2ZnSnS_4 Solar Cells, J. Am. Chem. Soc. 134 (2012) 8018–8021, https://doi.org/10.1021/ja3012373c.
[43] M. Mousel, A. Redinger, R. Djemour, M. Arasimowicz, N. Valle, P. Dale, S. Siebentritt, HCl and Br_2-MeOH etching of $Cu_2ZnSnSe_4$ polycrystalline absorbers, Thin Solid Films 535 (2013) 83–87, https://doi.org/10.1016/j.tsf.2012.12.095.
[44] X. Peng, S. Zhang, Y. Xiang, Solvothermal synthesis of $Cu_2Zn(Sn_{1-x}Ge_x)S_4$ and $Cu_2(Sn_{1-x}Ge_x)S_3$ nanoparticles with tunable band gap energies, J. Alloys Compd. 640 (2015) 75–81, https://doi.org/10.1016/j.jallcom.2015.03.248.
[45] F.E. Cancino-Gordillo, J.V. Cab, U. Pal, Structure and transport behavior of hydrothermally grown phase pure $Cu_2ZnSn_{1-x}Ge_xS_4$ (x = 0.0, 0.3) nanoparticles, Appl. Surf. Sci. 571 (2022), 151261, https://doi.org/10.1016/j.apsusc.2021.151261.
[46] A. Fairbrother, X. Fontané, V. Izquierdo-Roca, M. Espindola-Rodríguez, S. López-Marino, M. Placidi, L. Calvo-Barrio, A. Pérez-Rodríguez, E. Saucedo, On the formation mechanisms of Zn-rich Cu_2ZnSnS_4 films prepared by sulfurization of metallic stacks, Sol. Energy Mater. Sol. Cells 112 (2013) 97–105, https://doi.org/10.1016/j.solmat.2013.01.015.
[47] A. Fairbrother, X. Fontané, V. Izquierdo-Roca, M. Placidi, D. Sylla, M. Espindola-Rodriguez, S. López-Mariño, F.A. Pulgarín, O. Vigil-Galán, A. Pérez-Rodríguez, E. Saucedo, Secondary phase formation in Zn-rich $Cu_2ZnSnSe_4$ based solar cells annealed in low pressure and temperature conditions, Prog. Photovoltaics Res. Appl. 22 (2014) 479–487, https://doi.org/10.1002/pip.2473.
[48] R.D. Shannon, Revised effective ionic radii and systematic studies of interatomic distances in halides and chalcogenides, Acta Crystallogr. Sect. A 32 (1976) 751–767, https://doi.org/10.1107/S0567739476001551.
[49] M. Motihama, F. Gao, T. Maeda, T. Wada, Crystallographic and optical properties of $Cu_2Zn(Sn_{1-x}Ge_x)Se_4$ solid solution, Jpn. J. Appl. Phys. 53 (2014) 04ER09, https://doi.org/10.7567/JJAP.53.04ER09.
[50] J. Chen, W. Li, C. Yan, S. Huang, X. Hao, Studies of compositional dependent $Cu_2Zn(Ge_xSn_{1-x})S_4$ thin films prepared by sulfurizing sputtered metallic precursors, J. Alloys Compd. 621 (2015) 154–161, https://doi.org/10.1016/j.jallcom.2014.09.097.
[51] G. Chen, W. Wang, S. Chen, Z. Whang, Z. Huang, B. Zhang, X. Kong, Bandgap engineering of $Cu_2ZnSn_{1-x}Ge_xS(e)_4$ by adjusting Sn-Ge ratios for almost full solar spectrum absorption, J. Alloys Compd. 718 (2017) 236–245, https://doi.org/10.1016/j.jallcom.2017.05.150.
[52] M.D. Regulacio, S.Y. Tee, S.H. Lim, Z. Zhang, M.-Y. Han, Selective formation of ternary Cu–Ge–S nanostructures in solution, CrystEngComm. 20 (2018) 6803–6810, https://doi.org/10.1039/C8CE01443D.
[53] B. Li, Y. Xie, J. Huang, Y. Qian, Synthesis by a Solvothermal Route and Characterization of $CuInSe_2$ Nanowhiskers and Nanoparticles, Adv. Mater. 11 (1999) 1456–1459, https://doi.org/10.1002/(SICI)1521-4095(199912)11:17<1456::AID-ADMA1456>3.0.CO;2-3.
[54] L.I. Alverdiyev, Z.S. Aliev, S.M. Bagheri, L.F. Mashadiyeva, Y.A. Yusibov, M. B. Babanly, Study of the $2Cu_2S + GeSe_2 \leftrightarrow 2Cu_2Se + GeS_2$ reciprocal system and thermodynamic properties of the $Cu_8GeS_{6-x}Se_x$ solid solutions, J. Alloys Compd. 691 (2017) 255–262, https://doi.org/10.1016/j.jallcom.2016.08.251.
[55] M. Onoda, H. Wada, A. Sato, M. Ishii, Low-temperature forms of superionic conductors, Cu_8GeS_6 and Ag_7TaS_6, and ion conduction path, J. Alloys Compd. 383 (2004) 113–117, https://doi.org/10.1016/j.jallcom.2004.04.018.
[56] W.F. Kuhs, R. Nitsche, K. Scheunemann, The argyrodites — A new family of tetrahedrally close-packed structures, Mater. Res. Bull. 14 (1979) 241–248, https://doi.org/10.1016/0025-5408(79)90125-9.
[57] M. Onoda, X.-A. Chen, K. Kato, A. Sato, H. Wada, Structure refinement of Cu_8GeS_6 using X-ray diffraction data from a multiple-twinned crystal, Acta Crystallogr. Sect. B Struct. Sci. 55 (1999) 1109–1109. 10.1107/S0108768199012938.
[58] M. Ishii, M. Onoda, K. Shibata, Structure and vibrational spectra of argyrodite family compounds Cu_8SiX_6 (X=S, Se) and Cu_8GeS_6, Solid State Ionics. 121 (1999) 11–18, https://doi.org/10.1016/S0167-2738(98)00305-1.
[59] D. Brown, The Chemical Bond in Inorganic Chemistry: The Bond Valence Model, 1st ed., Oxford University Press, New York, NY, 2002.

[60] B.H. Toby, R.B. Von Dreele, GSAS-II : the genesis of a modern open source all purpose crystallography software package, J. Appl. Crystallogr. 46 (2013) 544–549, https://doi.org/10.1107/S0021889813003531.
[61] O.V. Parasyuk, L.V. Piskach, Y.E. Romanyuk, I.D. Olekseyuk, V.I. Zaremba, V. I. Pekhnyo, Phase relations in the quasi-binary Cu_2GeS_3–ZnS and quasi-ternary Cu_2S–Zn(Cd)S–GeS_2 systems and crystal structure of Cu_2ZnGeS_4, J. Alloys Compd. 397 (2005) 85–94, https://doi.org/10.1016/j.jallcom.2004.12.045.
[62] M. Dimitrievska, A. Fairbrother, X. Fontané, T. Jawhari, V. Izquierdo-Roca, E. Saucedo, A. Pérez-Rodríguez, Multiwavelength excitation Raman scattering study of polycrystalline kesterite Cu_2ZnSnS_4 thin films, Appl. Phys. Lett. 104 (2014), https://doi.org/10.1063/1.4861593.
[63] M. Dimitrievska, F. Boero, A.P. Litvinchuk, S. Delsante, G. Borzone, A. Perez-Rodriguez, V. Izquierdo-Roca, Structural Polymorphism in Kesterite Cu_2ZnSnS_4: Raman Spectroscopy and First-Principles Calculations Analysis, Inorg. Chem. 56 (2017) 3467–3474, https://doi.org/10.1021/acs.inorgchem.6b03006.
[64] M.Y. Valakh, O.F. Kolomys, S.S. Ponomaryov, V.O. Yukhymchuk, I.S. Babichuk, V. Izquierdo-Roca, E. Saucedo, A. Perez-Rodriguez, J.R. Morante, S. Schorr, I. V. Bodnar, Raman scattering and disorder effect in Cu_2ZnSnS_4, Phys. Status Solidi Rapid Res. Lett. 7 (2013) 258–261, https://doi.org/10.1002/pssr.201307073.
[65] E. Garcia-Llamas, M. Guc, I.V. Bodnar, X. Fontané, R. Caballero, J.M. Merino, M. León, V. Izquierdo-Roca, Multiwavelength excitation Raman scattering of $Cu_2ZnSn_{1-x}Ge_x(S, Se)_4$ single crystals for earth abundant photovoltaic applications, J. Alloys Compd. 692 (2017) 249–256, https://doi.org/10.1016/j.jallcom.2016.09.035.
[66] A. Escobedo Morales, E. Sánchez Mora, U. Pal, Use of diffuse reflectance spectroscopy for optical characterization of un-supported nanostructures, Rev. Mex. Física S. 53 (2007) 18–22.
[67] E. Garcia-Llamas, J.M. Merino, R. Serna, X. Fontané, I.A. Victorov, A. Pérez-Rodríguez, M. León, I.V. Bodnar, V. Izquierdo-Roca, R. Caballero, Wide band-gap tuning $Cu_2ZnSn_{1-x}Ge_xS_4$ single crystals: Optical and vibrational properties, Sol. Energy Mater. Sol. Cells 158 (2016) 147–153, https://doi.org/10.1016/j.solmat.2015.12.021.
[68] D.B. Khadka, J.H. Kim, Band gap engineering of alloyed $Cu_2ZnGe_xSn_{1-x}Q_4$ (Q = S, Se) films for solar cell, J. Phys. Chem. C 119 (2015) 1706–1713, https://doi.org/10.1021/jp510877g.
[69] H.J. Shim, U.V. Ghorpade, M.P. Suryawanshi, M. Gang, J.H. Kim, Studies on the influence of etching solution on the properties of $Cu_2ZnSn(S, Se)_4$ thin film solar cells, Thin Solid Films 670 (2019) 1–5, https://doi.org/10.1016/j.tsf.2018.11.042.
[70] G. Rey, G. Larramona, S. Bourdais, C. Choné, B. Delatouche, A. Jacob, G. Dennler, S. Siebentritt, On the origin of band-tails in kesterite, Sol. Energy Mater. Sol. Cells 179 (2018) 142–151, https://doi.org/10.1016/j.solmat.2017.11.005.
[71] E. Hajdeu-Chicarosh, Variable-Range Hopping Conduction in the Kesterite and Wurtzstannite Cu_2ZnGeS_4 Single Crystals, Surf. Eng. Appl. Electrochem. 54 (2018) 279–285, https://doi.org/10.3103/S1068375518030055.
[72] E. Hajdeu-Chicarosh, M. Guc, K. Neldner, G. Gurieva, S. Schorr, E. Arushanov, K. G. Lisunov, Mechanisms of conductivity and energy spectrum of near-edge holes in Cu_2ZnSnS_4 powder samples, J. Alloys Compd. 703 (2017) 315–320, https://doi.org/10.1016/j.jallcom.2017.01.352.
[73] Y. Fan, G. Wang, R. Wang, B. Zhang, X. Shen, P. Jiang, X. Zhang, H. Gu, X. Lu, X. Zhou, Enhanced thermoelectric properties of p-type argyrodites Cu_8GeS_6 through Cu vacancy, J. Alloys Compd. 822 (2020), 153665, https://doi.org/10.1016/j.jallcom.2020.153665.

Materials Chemistry and Physics 246 (2020) 122834

Contents lists available at ScienceDirect

Materials Chemistry and Physics

journal homepage: www.elsevier.com/locate/matchemphys

Particle dispersion and lattice distortion induced magnetic behavior of $La_{1-x}Sr_xMnO_3$ perovskite nanoparticles grown by salt-assisted solid-state synthesis

Jose-Luis Ortiz-Quiñonez, Lorena García-González, Francisco Enrique Cancino-Gordillo, Umapada Pal [*,1]

Instituto de Física, Benemérita Universidad Autónoma de Puebla, Apdo. Postal J-48, Puebla Pue, 72570, Mexico

HIGHLIGHTS

- $La_{1-x}Sr_xMnO_3$ perovskite nanoparticles of 90–255 nm av. Size range were fabricated by ball-milling.
- Presence of Na^+ ion at surface promotes the dispersion of $LaMnO_{3+\delta}$ nanoparticles.
- Particle dispersion modifies the T_{RT} of $La_{1-x}Sr_xMnO_3$ nanostructures.
- Substitution of La^{3+} by Sr^{2+} in $La_{1-x}Sr_xMnO_3$ increases their T_{Curie} and M_s.
- Jahn-Teller distortion and La^{3+} vacancy induced Mn^{3+} oxidation affect their magnetic behavior.

GRAPHICAL ABSTRACT

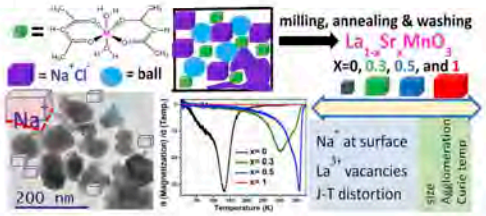

ARTICLE INFO

Keywords:
$La_{0.7}Sr_{0.3}MnO_3$ particles
Mechanosynthesis
Perovskite structure
Lanthanum manganites
Magnetic properties

ABSTRACT

$La_{1-x}Sr_xMnO_3$ perovskites are of enormous current interest due to their superior magnetoresistance and application as cathode material for solid oxide fuel cells. However, practical applications of these perovskites critically depend on size, composition, and concentration of La^{3+} vacancies at their surfaces. Here we present the fabrication of size controlled (90–255 nm average size), highly crystalline $La_{1-x}Sr_xMnO_3$ (x = 0, 0.3, 0.5, and 1) nanoparticles, simply by ball-milling of metal acetylacetonate precursors in NaCl and subsequent air-annealing. The size of the nanoparticles increased in the order $LaMnO_{3+\delta} < La_{0.7}Sr_{0.3}MnO_3 \approx La_{0.5}Sr_{0.5}MnO_3 < SrMnO_3$. While $LaMnO_{3+\delta}$ particles remain well dispersed, a fraction of particles containing Sr remains partially interconnected after air-annealing (900 °C). A change in site symmetry of the Mn^{3+}-O_6 octahedron promoted by the Jahn-Teller distortion of $LaMnO_{3+\delta}$ lattice was detected. Substitution of La^{3+} ions by Sr^{2+} increases the ferromagnetic interaction in $La_{1-x}Sr_xMnO_3$ (x = 0, 0.3, 0.5) nanostructures, increasing their Curie temperature and magnetization (M_s) progressively. Effect of particle dispersion due to Sr^{2+} incorporation on the lattice and magnetic behavior of the nanostructures is discussed considering the Jahn-Teller distortion and La^{3+} vacancy induced Mn^{3+} ion oxidation (to Mn^{4+}) in the lattice.

* Corresponding author.
E-mail address: upal@ifuap.buap.mx (U. Pal).
[1] Presently at: The Korea Centre for Artificia Photosyntheis and Department of Chemistry, Sogang University, Seoul, Republic of Korea.

https://doi.org/10.1016/j.matchemphys.2020.122834
Received 27 September 2019; Received in revised form 19 January 2020; Accepted 18 February 2020
Available online 19 February 2020
0254-0584/

1. Introduction

$La_{1-x}Sr_xMnO_3$ is an interesting perovskite material, which manifests colossal magnetoresistance (CMR) induced by the "double-exchange" mechanism, and low field magnetoresistance (LFMR) properties [1–6]. The LFMR behavior of $La_{1-x}Sr_xMnO_3$ was seen to be further enhanced in its metal oxide composites such as $La_{1-x}Sr_xMnO_3$:CuO, CeO_2, Mn_3O_4, NiO, and MgO [5]. While $La_{1-x}Sr_xMnO_3$ nanoparticles have been utilized as catalysts for CO oxidation [7,8], NO oxidation and reduction [9], electrochemical oxygen reduction [10–12], and photocatalytic water oxidation [13], single crystalline $La_{0.5}Sr_{0.5}MnO_3$ particles of micrometric dimension have been utilized as effective cathode material in solid oxide fuel cells (SOFCs) [12]. On the other hand, $La_{1-x}Sr_xMnO_3$ nanostructures have been tested effective in hyperthermia applications for tumor therapy [14–16]. The catalytic and magnetic applications of $La_{1-x}Sr_xMnO_3$ nanoparticles are seen to depend strongly on the ratio of lanthanum and strontium ions in their lattice structure, especially at their surfaces [13,17–21].

$La_{1-x}Sr_xMnO_3$ has a distorted ABO_3-type perovskite structure for x = 0.0, 0.3 and 1.0. On the other hand, it is cubic for x = 0.5 [22]. While for x = 0.23–0.6 it manifests ferromagnetic behavior at room temperature, for the x values lower than 0.23, it behaves as insulator with paramagnetic ordering [23]. In perovskite lattice, the A cations remain in dodecahedral coordination, and the B cations stay in octahedral coordination with oxygen anions (Fig. 1). A few specific compositions of the perovskite such as $La_{0.7}Sr_{0.3}MnO_3$ and $La_{0.5}Sr_{0.5}MnO_3$ have been utilized for optoelectronic applications [24]. Mn^{4+}/Mn^{3+} ratio in them was seen to play a critical role in their magnetic and electrical properties. In fact, the Mn^{4+}/Mn^{3+} ratio determines the charge carrier concentration, and hence the viability of optoelectronic applications of these manganites [25]. On the other hand, the observed colossal magnetoresistance (CMR) in $La_{1-x}Sr_xMnO_3$ thin films is governed by the displacement of Mn^{3+} cations out of the center of the Mn^{3+}-O_6 polyhedron due to Jann-Teller effect. It should be recalled that the number of unpaired electrons in the 3d orbitals of Mn^{3+} and Mn^{4+} cations are 4 and 3, respectively. Therefore, controlling Mn^{4+}/Mn^{3+} ratio at the surface of these manganites is a key factor, which determines their technological applications.

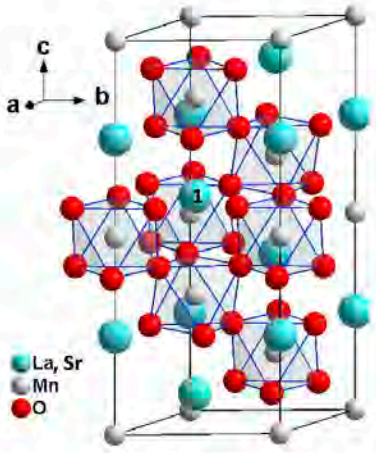

Fig. 1. Schematic representation of the lattice structure of $La_{0.7}Sr_{0.3}MnO_3$ perovskite (hexagonal unit cell). Data for the atomic positions were taken from Ref. [1]. The La/Sr cation labeled by 1 allows seeing the nearest oxygen atoms in the neighboring gray octahedra. Note that all the neighboring octahedra share only one oxygen atom.

Nanostructures such as nanoparticles and nanorods of $La_{1-x}Sr_xMnO_3$ have been synthesized earlier using solid-state such as mechanochemical synthesis [26], and chemical methods such as sol-gel [27], hydro- and solvothermal [10,11,28], etc. However, in most of the cases, the obtained nanostructures are of non-homogeneous size with poor dispersion [15,17,25,29–36]. A considerable improvement in size dispersion has been accomplished by using a molten salt such as KNO_3 [37], $NaNO_3$ and KNO_3 mixture as solvent and/or the addition of organic capping agents [32]. On the other hand, strongly ionic salts such as NaCl and KCl have been utilized as dispersing medium in the mechanochemical synthesis of metal-organic framework (MOF) nanostructures [38] and nanodiamonds [39]. The use of these solid ionic solvents has been seen effective for controlling both the morphology and porosity of the nanostructures, along with improving their dispersion. For example, the presence of NaCl during high temperature (900 °C) sintering of ceria (CeO_2) nanoparticles was seen to avoid their aggregation [40].

Use of a strongly ionic salt such as NaCl in the synthesis of manganite nanostructures involving high temperature thermal annealing for inducing crystallinity has several other advantages besides acting as a dispersion medium: (i) Due to the high thermal stability of NaCl (melting point ~ 800.7 °C), it avoids the aggregation of the formed nanoparticles; (ii) Above 800 °C NaCl is a molten salt, which can work as an ionic liquid solvent, facilitating high-temperature diffusion of La^{3+}, Sr^{2+}, $Mn^{3+,4+}$ and O^{2-} ions, avoiding the formation of point defects in $La_{1-x}Sr_xMnO_3$ nanoparticles due to nonuniform cation distribution; (iii) As the Shannon ionic radius of the Na^+ ion (1.18 Å) is close to the ionic radii of Sr^{2+} (1.26 Å) and La^{3+} (1.16 Å) [41], a partial substitution of La^{3+} and Sr^{2+} cations at the surface of the $La_{1-x}Sr_xMnO_3$ particles might occur, which can modify the concentration of oxygen vacancies at their surfaces, modifying their reactivity/catalytic activity; and (iv) Since $La_{1-x}Sr_xMnO_3$ particles can oxidize CO and NO molecules [7,8,42], Cl^- ions from the molten NaCl might also be oxidized at the surface of $La_{1-x}Sr_xMnO_3$ at high temperature. In other words, $La_{1-x}Sr_xMnO_3$ particles can oxidize the Cl^- ions to Cl_2(g), avoiding the formation of undesired chloride-based impurities.

In this article, we present the fabrication of well-dispersed $La_{1-x}Sr_xMnO_3$ nanoparticles containing different mol fractions of La and Sr by ball-milling, utilizing NaCl as dispersing medium and metal acetylacetonate complexes as precursors. Effects of NaCl use on particle size, particle aggregation, structural distortion, and magnetic behavior of the perovskite nanostructures have been studied extensively. X-ray diffraction (XRD), scanning electron microscopy (SEM), and transmission electron microscopy (TEM) were utilized for structural and morphological characterization of the nanostructures. MicroRaman and X-ray photoelectron spectroscopy (XPS) were utilized for determining the structural phase and chemical bonding of elements in the nanoparticles. Vibrating sample magnetometry (VSM) was performed to study the magnetic behavior of the perovskite nanostructures.

2. Experimental

2.1. Materials

Manganese nitrate tetrahydrate ($Mn(NO_3)_2 \bullet 4H_2O$, >97.0%), lantharum nitrate hexahydrate ($La(NO_3)_3 \bullet 6H_2O$, 99.99%), strontium nitrate ($Sr(NO_3)_2$, 99+%) and acetylacetone ($C_5H_8O_2$, >99.5%) were purchased from Sigma-Aldrich, Mexico. Sodium hydroxide (NaOH, 98.15%) was purchased from J.T. Baker, Mexico. Sodium chloride (NaCl, >99%) was purchased from Omnichem, Mexico. Deionized (DI) water from a Millipore system (ρ > 18.2 M Ω•cm) was utilized for washing the fabricated nanostructures.

2.2. Synthesis of metal acetylacetonates

Metal acetylacetonate complexes (Mn (acac)$_2$, La (acac)$_3$ and Sr (acac)$_2$) were synthesized through co-precipitation, as reported by Nforna et al., [31]. For the synthesis of Mn (acac)$_2$, first, a solution of sodium acetylacetonate was prepared as precipitating agent by dropwise addition of stoichiometric amount (15 mL) of acetylacetone to a NaOH solution (5.82 g of NaOH in 60 mL of water) at 50 °C under magnetic stirring for 20 min. A precursor solution of Mn was prepared by dissolving 48.49 mmol of $Mn(NO_3)_2 \bullet 4H_2O$ in 50 mL of DI water under magnetic stirring. After that, the hot solution of sodium acetylacetonate was slowly added to the precursor solution of Mn and kept at this temperature for 30 min under magnetic stirring. The product of the reaction was a pale yellow precipitate of manganese acetylacetonate, (Mn (acac)$_2$). The precipitate was cooled down to room temperature, filtered by suction in a Büchner funnel, washed four times with DI water, and vacuum dried for 12 h. This process was repeated for La $(NO_3)_3 \bullet 6H_2O$ and $Sr(NO_3)_2$ to obtain a white precipitate of lanthanum acetylacetonate and a white-pearl precipitate of strontium acetylacetonate.

2.3. Synthesis of $La_{1-x}Sr_xMnO_3$ nanoparticles

$La_{1-x}Sr_xMnO_3$ nanoparticles were prepared by thermal decomposition of metal acetylacetonates of Mn, La and Sr in presence of sodium chloride under high energy ball milling. The nominal x values utilized for the synthesis of $La_{1-x}Sr_xMnO_3$ were 0.0, 0.3, 0.5 and 1.0. In a typical synthesis, for example, in the case of $La_{0.7}Sr_{0.3}MnO_3$, 0.5783 g of Mn (acac)$_2$, 0.6863 g of La (acac)$_3$, and 0.1823 g of Sr (acac)$_2$ were mixed with 7.234 g of NaCl. The w/w ratio {Mn (acac)$_2$ + La (acac)$_3$ + Sr (acac)$_2$}/NaCl was 1:5. The metal acetylacetonates and sodium chloride mixture was then placed inside a 100 mL agate milling jar filled with 32 agate gridding balls (10 mm diameter). Then the jar was set up in a planetary ball mill (PQ-N2 Gear Drive 4) station, and the milling was performed for 24 h at 200 rpm. The obtained fine powder was then transferred to an alumina crucible and air-annealed inside a Carbolite tubular furnace at 750 °C for 6 h, heating the sample at 5 °C/min rate. After cooling down to room temperature, the product was washed in 1.0 L of DI water to remove NaCl used as dispersing material. After washing, the product was separated by decantation. The obtained precipitate was re-dispersed in 500 mL of DI water, ultrasonicated for 2 min, and recovered by centrifugation. This step was repeated for 4 times. Finally, the obtained product was dried at 70 °C for 5 h. To induce crystallization, the obtained powder sample was subjected to another thermal annealing carried out at 900 °C for 5 h in air, with a heating rate of 5 °C/min. A similar procedure was followed for the synthesis of $La_{1-x}Sr_xMnO_3$ with x = 0.0, 0.5 and 1.0.

2.4. Characterization of $La_{1-x}Sr_xMnO_3$ nanoparticles

To analyze the crystallinity and phase structure, powder XRD patterns of the samples were recorded in a Bruker D8 diffractometer, utilizing CuKα (λ = 1.5406 Å) radiation. The spectra were recorded at 0.02°/step with a scan rate of 0.2 s/step in the 2θ range of 20 – 80°. For morphology and composition analysis, a small amount of each of the powder samples was dispersed in ethanol and deposited over clean Si wafer. The samples were inspected in a JEOL JSM 7800 F field-emission scanning electron microscope (FE-SEM) coupled with an Oxford Instrument X-Max energy dispersive spectrometer (EDS). Vibrational characteristics of nanostructures were analyzed by Raman spectroscopy at room temperature. A Horiba LabRamHR system equipped with a 633 nm He–Ne laser and a thermoelectrically cooled charge-coupled device (CCD) detector was utilized for recording the Raman spectra of the samples. MicroRaman spectra of the samples were acquired using appropriate objective lenses and filters (neutral density filters) to avoid their laser-induced (due to the high intensity of the exciting laser beam) burning. The nanostructures were analyzed further by recording their low- and high-resolution transmission electron microscopy (TEM) images in a JEOL 2100 F transmission electron microscope, operating at 200 kV accelerating voltage. The samples for TEM analysis were prepared by drop-casting their colloidal suspension (in ethanol) over carbon-coated copper grids. For the analysis of composition and chemical states of constituting elements, X-ray photoelectrons spectra (XPS) of the samples were recorded in a Thermo Scientific spectrometer with Al Kα (1486.6 eV) radiation source. Deconvolution of the core-level emission bands was performed using Pseudo-Voight2 functions with 70% Gaussian and 30% Lorentzian components, after subtracting Shirley type backgrounds. Magnetic properties of the nanostructures were studied by recording their magnetization (M – H) curves and magnetization under zero-field cooling (ZFC) and applied field cooling (FC) curves in a DynaCool physical property measurement system (PPMS, DynaCool, Quantum Design).

3. Results and discussion

3.1. X ray diffraction

Room temperature XRD patterns of the fabricated $La_{1-x}Sr_xMnO_3$ nanoparticles are presented in Fig. 2. Rietveld refinement of the XRD patterns of the $La_{1-x}Sr_xMnO_3$ samples and corresponding cell parameters are included in Fig. S1 (Supporting Information). All the samples revealed well-resolved diffraction peaks of single phase. Position and relative intensity of the diffraction peaks of the $LaMnO_{3+\delta}$ (x = 0.0) and $La_{0.7}Sr_{0.3}MnO_3$ (x = 0.3) samples correspond well to their rhombohedral perovskite phase of space group $R\bar{3}c$ (PDF # 04-012-5560 and 00-056-0616, respectively). The structure with space group $R\bar{3}c$ was derived from the simple-cubic perovskite ($Pm\bar{3}m$) lattice by rotation of adjacent MnO_6 octahedra in opposite direction around the $[111]_c$ (cubic) axis [43].

Stoichiometric (with no oxygen excess, i.e. δ = 0.0), and low oxygen excess (δ ≤ 0.07) $LaMnO_{3+\delta}$ perovskites have orthorhombic unit cells of *Pbnm* space group. However, for δ ≥ 0.09, they contain rhombohedral unit cells (space group $R\bar{3}c$) [44,45]. The unit cell volumes for δ = 0.9, 0.10, 0.11, 0.12, 0.13, and 0.14 are reported to be of 118.9, 118.25, 117.63, 117.92, 117.44, 117.18 Å^3, respectively [44]. The volume of the rhombohedral unit cell for $LaMnO_{3+\delta}$ obtained in the present work is 116.78 Å^3 (lattice parameters a = 5.462 Å and α = 60.59°), which is slightly lower than the value determined by Töpfer and Goodenough

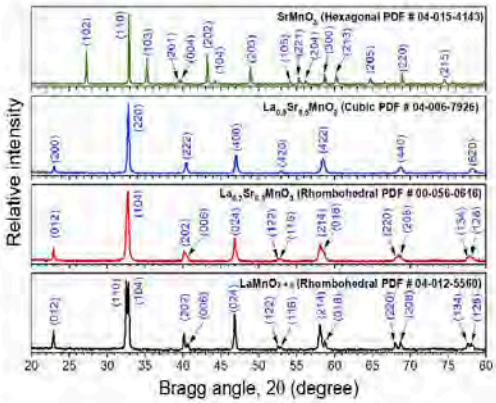

Fig. 2. Room temperature XRD patterns of the $La_{1-x}Sr_xMnO_3$ samples annealed at 900 °C.

(cell volume = 117.18 Å^3, a = 5.469 Å, α = 60.58°) for $LaMnO_{3+\delta}$ with δ = 0.14. The oxygen excess (δ) in $LaMnO_{3+\delta}$ has been demonstrated in previous studies using neutron diffraction by other authors [45–49]. The lower unit cell volume (and also the d values) estimated for the $LaMnO_{3+\delta}$ nanostructures fabricated in this work is probably due to the formation of metal ion vacancies in them. The formation of one La^{3+} vacancy in the perovskite lattice induces the transformation of three Mn^{3+} ions into Mn^{4+} cations to maintain its charge neutrality. As the ionic radius of Mn^{4+} ion is smaller than the ionic radius of Mn^{3+}, the observed change in unit cell volume of the perovskite unit cell is probably also caused by the oxidation of Mn^{3+} cations.

On the other hand, the positions of the diffraction peaks revealed for the $La_{0.5}Sr_{0.5}MnO_3$ (x = 0.5) sample are in good agreement with its pseudo-cubic perovskite structure, with space group $Fm\bar{3}m$ (PDF # 04-006-7926). Finally, the diffraction pattern of the $SrMnO_3$ sample matches well with its four-layered hexagonal phase (PDF # 04-015-4143; space group $P6_3/mmc$), which is the most stable phase of $SrMnO_3$ below 1308 K [50]. To explain the change in the type of unit cell with increase in x value, the Goldschmidt tolerance factor (τ) for the $La_{1-x}Sr_xMnO_3$ perovskites was estimated. The τ value is important because it determines whether the structure of the perovskite is rhombohedral ($0.8 < \tau < 0.89$), cubic ($0.89 < \tau < 1.0$), or hexagonal ($1.0 < \tau < 1.13$) [51]. The τ values estimated for the perovskite nanostructures correspond to x values 0.0, 0.3, 0.5 and 1.0 were 0.844, 0.878, 0.934, and 0.982, respectively (see Tables S1 and S2, Supporting information). Appearance of well-resolved diffraction bands of high intensity in all the samples indicate their good crystallinity after annealing at 900 °C for 5 h. To highlight the effect of high temperature annealing on the crystallinity of the perovskite nanostructures, we present a typical XRD pattern of the $La_{0.7}Sr_{0.3}MnO_3$ sample annealed at 750 °C in Fig. S2 (supporting information). As can be seen, while the rhombohedral phase of the perovskite was formed even at this temperature, the intensity (or the signal-to-noise ratio) of the diffraction bands is considerably low, indicating their partial crystallization at this lower annealing temperature.

3.2. Scanning electron microscopy (SEM)

Typical SEM images of the $La_{1-x}Sr_xMnO_3$ samples are presented in Fig. 3. Formation of quasi-spherical particles in 30 to a few hundred nanometer size range is very clear in the micrographs. The particles appear partially fused and interconnected. As can be observed in the size distribution histograms presented as insets, the size of the particles in

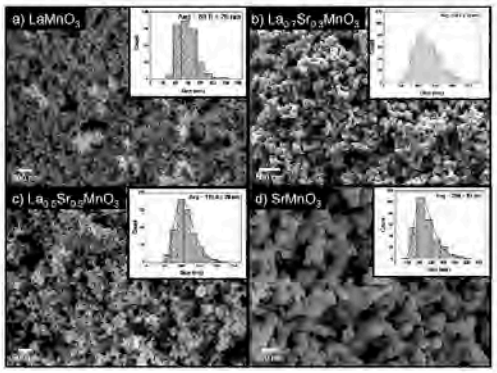

Fig. 3. Typical SEM images of $La_{1-x}Sr_xMnO_3$ samples prepared with nominal x values of (a) 0.0, (b) 0.3 (c) 0.5 and (d) 1.0. Corresponding particle size distribution histograms with their log-normal fits are presented as insets.

lanthanum containing samples remained in between 30 and 225 nm, while the size of the particles in $SrMnO_3$ sample varies in between 100 and 550 nm. The average size of the particles increased from 89.6 ± 26 to 128.8 ± 39 nm with the increase of Sr mole fraction from x = 0.0 to x = 0.5. In fact, the estimated average size of the $SrMnO_3$ (x = 1.0) particles is considerably larger (255 ± 87 nm) than in other samples. The average crystallite size in the manganites containing Sr mole fractions x = 0.0, 0.3, and 0.5 estimated from the Rietveld refinement of their XRD spectra were 111, 110, and 124 nm, respectively, which are in accordance with the particle size values estimated from their SEM images. The narrowest diffraction peaks for the $SrMnO_3$ sample agree very well with the largest particle size (255 ± 87 nm) found in its SEM images. The results indicate the particle size in the perovskite nanostructures is controlled by the Sr mole fraction in them.

Typical EDS spectra for the $La_{1-x}Sr_xMnO_3$ samples are shown in Fig. S3 (supporting information). The EDS estimated elemental composition of the $La_{1-x}Sr_xMnO_3$ samples presented in Table 1 demonstrates a gradual increase of Sr content in the nanostructures with the increase of its nominal content in the reaction mixture. As can be observed in Table 1, all samples revealed their oxygen excess. Also, a subtle atomic percentage of Na could be detected in all the samples. The amount of Na in $LaMnO_{3+\delta}$ sample is about five times larger than in the other three samples. However, presence of chlorine was not detected in the nanostructures, which confirms the absence of NaCl in the samples. EDS estimated Sr/(Sr + La) ratios in the samples remained very close to their nominal values, indicating adequate incorporation of Sr in the particle lattice. Although the (La + Sr)/Mn ratio in all the samples should be 1.0, it was seen to be a bit higher for $LaMnO_{3+\delta}$ (1.11), which decreased progressively (Table 1) with the increase of Sr content in the samples.

3.3. Transmission electron microscopy (TEM)

Typical TEM images of the $La_{1-x}Sr_xMnO_3$ samples are shown in Fig. 4. As can be noticed from Figs. 4a and S4 (supporting information), the majority of the $LaMnO_{3+\delta}$ particles remain dispersed without fusing after high-temperature thermal annealing. Similarly (Figs. 4c and 5b), most of the $La_{0.5}Sr_{0.5}MnO_3$ nanoparticles remained dispersed after the thermal treatment. The average particle sizes determined from the TEM images (considering more than 80 particles of each sample) of the samples are 52 ± 17 and 88 ± 29 nm (Fig. S6, supporting information) for the $LaMnO_{3+\delta}$ and $La_{0.5}Sr_{0.5}MnO_3$ samples, respectively.

On the other hand, the HRTEM images of the $LaMnO_{3+\delta}$ particles revealed their high crystallinity (see the red square in Fig. 5). Presence of La vacancy sites in the crystal lattice of the particles can be noticed (marked by yellow arrows) in the HRTEM image enclosed by the blue square in Fig. 5. Interplanar distances (d) determined for this defective particle are 3.82, 3.18 and 2.19 Å, which correspond well both to the (012), (103), and (006) planes of $LaMnO_{3+\delta}$ and (211), (122) and (411) planes of Mn_2O_3. Therefore, this particle could either correspond to $LaMnO_{3+\delta}$ with several vacancies induced by the partial substitution of La^{3+} with Na^+ cations, or an impurity of Mn_2O_3 phase. $LaMnO_3$ with cation vacancies is usually referred to as $LaMnO_{3\pm\delta}$. In this regard, Zakhvalinskiĭ et al. prepared $LaMnO_{3+\delta}$ (δ = 0.065, 0.100, 0.112, 0.125, 0.133, 0.140, and 0.154) particles and claimed the presence of cation

Table 1
EDS estimated elemental composition of the $La_{1-x}Sr_xMnO_3$ particles.

Sample	Na (at %)	Mn (at%)	Sr (at %)	La (at %)	O (at %)	Sr/(Sr + La)	(La + Sr)/Mn
$LaMnO_3$	1.79	14.44	–	16.00	67.75	0.00	1.11
$La_{0.7}Sr_{0.3}MnO_3$	0.41	16.24	4.90	13.22	65.24	0.27	1.12
$La_{0.5}Sr_{0.5}MnO_3$	0.14	17.63	7.80	10.29	64.15	0.43	1.03
$SrMnO_3$	0.13	17.66	18.06	–	64.15	1.00	1.02

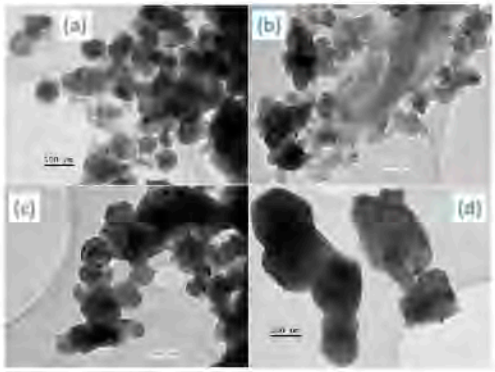

Fig. 4. Typical TEM images of $La_{1-x}Sr_xMnO_3$ samples prepared with nominal x values of (a) 0.0, (b) 0.3 (c) 0.5 and (d) 1.0.

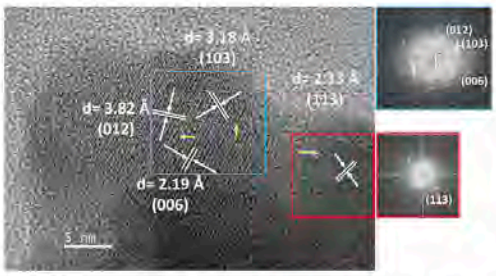

Fig. 5. A typical high resolution TEM (HRTEM) image of the $LaMnO_{3+\delta}$ particles. Interplanar distances (*d*) and corresponding lattice planes are shown. Cation vacancies in the lattice are shown by yellow arrows. The spot patterns correspond to the fast Fourier transform (FFT) of the two zones highlighted with blue and red squares in the image. (For interpretation of the references to color in this figure legend, the reader is referred to the Web version of this article.)

vacancies in the samples [26]. While rhombohedral $LaMnO_{3+\delta}$ particles with $\delta = 0.12–0.15$ [52], 0.13–0.18 [44], and 0.15–0.26 [53] have been fabricated by several other research groups, they either did not consider or could not detect the formation of cation vacancy in the perovskite lattice through HRTEM imaging [17,54–56]. Although the formation of cation vacancy in $LaMnO_{3+}\delta$ and $(La, M)MnO_{3+}\delta$ (where M = Na, Ca) and its effect on the magnetic behavior of the perovskites have been discussed by Horyn et al. [57], and Malavasi et al. [46], they did not provide any direct evidence such as HRTEM images of the perovskites demonstrating the formation of cation vacancies in their lattice. While the incorporation of Na^+ ions in the fabricated nanostructures is very clear from their EDS analysis (Table 1), the formation of Na^+ ion doping-induced La^{3+} vacancies in $LaMnO_{3+\delta}$ lattice is also clear in the HRTEM image of the sample presented in Fig. 5.

However, due to large particle size (>100 nm) of the $La_{1-x}Sr_xMnO_3$ perovskites with x = 0.3, 0.5 and 1.0, it was not possible to acquire their HRTEM images (difficult for the electron beam to pass through these large particles).

3.4. Raman spectroscopy

As the lattice distortion and possible presence of impurities in solid samples can be detected from their Raman spectra, we performed Raman spectroscopy of the fabricated particles at room temperature (Fig. 6). The Raman spectrum of $LaMnO_{3+\delta}$ revealed the presence of two broad bands located at 512 and 640 cm^{-1} (Fig. 6), corresponding to out-of-phase O–Mn–O bending vibration and in-phase stretching vibration of Mn–O in the MnO_6 octahedron, respectively [58]. Appearance of broad Raman bands for the $LaMnO_{3+\delta}$ nanoparticles confirms the lattice distortion discussed in the XRD section. These results agree well with the reported Raman features of $LaMnO_{3+\delta}$ obtained using crossed polarization of the incident and scattered beams [43]. Also, the intensity of these bands depends on the degree of the Jahn-Teller distortion in Mn^{3+}-O_6 octahedra. As the Sr content in $La_{1-x}Sr_xMnO_3$ (x = 0, 0.3, and 0.5) increases, the extent of Jahn-Teller distortion decreases, diminishing the intensity of these Raman bands [43,59]. Moreover, due to defect-induced lattice perturbation, the bands become broader [58].

To explain the differences in the degree of the Jahn-Teller distortion in the perovskites, we should consider that the electron configurations of Mn^{3+} and Mn^{4+} cations in $La_{1-x}Sr_xMnO_3$ are high-spin d^4 and high-spin d^3, respectively. While the energy of 3d electrons in Mn^{3+} cations can be decreased through Jahn-Teller effect by forming a geometrically distorted octahedron, it does not occur for Mn^{4+} cations. The ground state of Mn^{3+} cation in the Mn^{3+}-O_6 octahedron is electronically degenerated, and an extension or compression of Mn^{3+}-O^{2-} bond pair along the z axis breaks the degeneracy of these states. In other words, the presence of Mn^{3+} cations decreases the site symmetry form O_h to D_{4h}, and the Mn^{3+}-O^{2-} bond distances along the z axis become larger than the ones in the xy plane. The driving force for this change in site symmetry is the decrease in the global energy of the solid.

On the other hand, group theory analysis predicts eight Raman active phonons for the perovskites with hexagonal symmetry [60], such as $SrMnO_3$. The Raman spectrum of $SrMnO_3$ (x = 1.0) sample presented in Fig. 6 shows 3 bands, peaked around 342, 431 and 642 cm^{-1}, which have been ascribed to one phonon processes related to Mn displacements inside the Mn^{4+}-O_6 octahedral tilting (E_{1g}), octahedral asymmetric

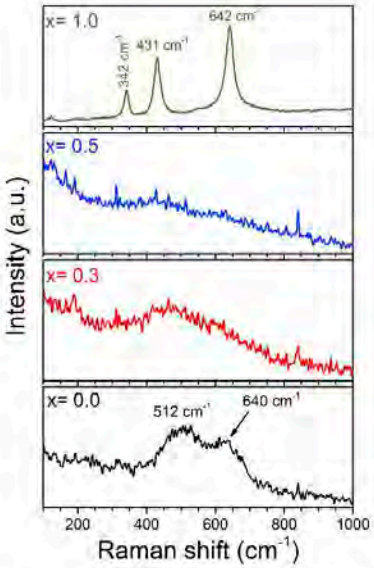

Fig. 6. Raman spectra of $La_{1-x}Sr_xMnO_3$ samples prepared with different nominal x values.

stretching (E_{2g}), and symmetric stretching (A_{1g}), respectively [60]. It must be noticed that the Raman spectrum of the $SrMnO_3$ nanoparticles strongly differs from the Raman spectra of rest of the samples (x = 0.0, 0.3 and 0.5), since $SrMnO_3$ (x = 1.0) belongs to different space group, and its structure is Mn^{4+} centered, which does not produce Jahn-Teller-distorted octahedral [43,59]. From XRD analysis, it is clear that incorporation of Sr in $La_{1-x}Sr_xMnO_3$ nanoparticles generates nanostructures with different unit cells (rhombohedral, cubic and hexagonal) due to the rotation of adjacent MnO_6 octahedra in opposite direction around the [111] axis. This difference in the type of unit cell (and hence of local symmetry) is further supported by the high variation in the number and width of the Raman peaks observed for each sample.

3.5. X-ray photoelectron spectroscopy (XPS)

XPS survey spectra of the $La_{1-x}Sr_xMnO_3$ perovskites are presented in Fig. 7. As expected, we could detect only the emissions corresponding to La, Sr, Mn and O elements in the samples, along with the signal of adventitious carbon. In addition, traces of Na associated to remaining of NaCl were detected in all the samples. Orbitals associated to the main emission peaks in the XPS spectra are indicated in Fig. 7. Auger lines located at 494, 900, 973, and 1226 eV correspond to Na ($KL_{23}L_{23}$), Mn ($L_3M_{23}M_{45}$), O ($KL_{23}L_{23}$), and C (KVV) elements (see blue arrows in Fig. 7), respectively [61]. However, no emission associated with chlorine was observed in the samples, which should appear around 199 and 201 eV binding energies for the Cl $2p_{3/2}$ and Cl $2p_{1/2}$ orbitals, respectively. Elimination of chlorine ions from the samples occurred due to the significant change in the standard reduction potential (E°) of the Cl_2/Cl couple at high annealing temperature, 900 °C (see Supporting Information).

Normalized high-resolution XPS spectra for selected orbital are depicted in Fig. 8. Binding energies (BEs) of the La $3d_{3/2}$ and La $3d_{5/2}$ orbitals in $La_{1-x}Sr_xMnO_3$ perovskites were estimated to be 850.29 and 833.54 eV, respectively (Fig. 8a). The La $3d_{5/2}$ orbital revealed a satellite peak located at 837.56 eV. No detectable shift in the position of these peaks was observed due to progressive substitution of La ions by Sr ions. However, for $LaMnO_3$ (x = 0), the band correspond to La $3d_{5/2}$ orbital (appeared in-between 833.67 and 836.01 eV) is more intense than its intensity in the remaining manganites. This difference might be due to the presence of La–OH bonds at the surface of $LaMnO_{3+\delta}$. Since the Sr^{2+} ($pKa = 13.3$), La^{3+} ($pKa = 8.5$) and $Mn^{3+,4+}$ ($pKa < 5$) ions are classified as very weakly acidic, weakly acidic, and moderately acidic cations, respectively [62], formation of -La-OH species can occur at the surface of $LaMnO_3$ by H_2O hydrolysis.

High-resolution XPS spectra of Mn $2p_{3/2}$ and Mn $2p_{1/2}$ orbitals in the $La_{1-x}Sr_xMnO_3$ perovskites are presented in Fig. 8b. The binding energy position of the Mn $2p_{3/2}$ orbital at 640.92 eV in $LaMnO_{3+\delta}$ indicates the Mn cations in the sample remain both in 3+ and 4+ oxidation states (the 4+ oxidation state preserves the charge electroneutrality around La^{3+} vacancies and Na^+ substitutions). However, on substitution of La^{3+} cations by Sr^{2+} cations, the peak position of the Mn $2p_{1/2}$ emission gradually shifted to higher binding energies. A right (low energy) shoulder around 640.44 eV appeared for the $La_{0.7}Sr_{0.3}MnO_3$ and $La_{0.5}Sr_{0.5}MnO_3$ samples due to the presence of Mn^{3+} cations, in addition to the Mn^{4+} cations. For the $SrMnO_3$ sample, in which the oxidation state of all the Mn cations is 4+, the Mn $2p_{3/2}$ peak is centered at higher BE, i.e. at 641.67 eV.

It should be noted that while the FWHM (full width at high maximum) of the Mn $2p_{3/2}$ emission from the lanthanum (La) containing perovskites is about 3.47 eV, it is only about 2.3 eV for the $SrMnO_3$ perovskite. Such a drastic difference in the FWHM value of Mn $2p_{3/2}$ orbitals between the La containing and La free perovskites is the result of: (i) presence of both Mn^{3+} and Mn^{4+} cations in the same phase, and (ii) Jahn-Teller effect (i.e. the two Mn–O bonds along the z axis are longer than the four Mn–O bonds in the xy plane). Overlapping of orbitals is weaker in longer Mn–O bonds than in shorter Mn–O bonds,

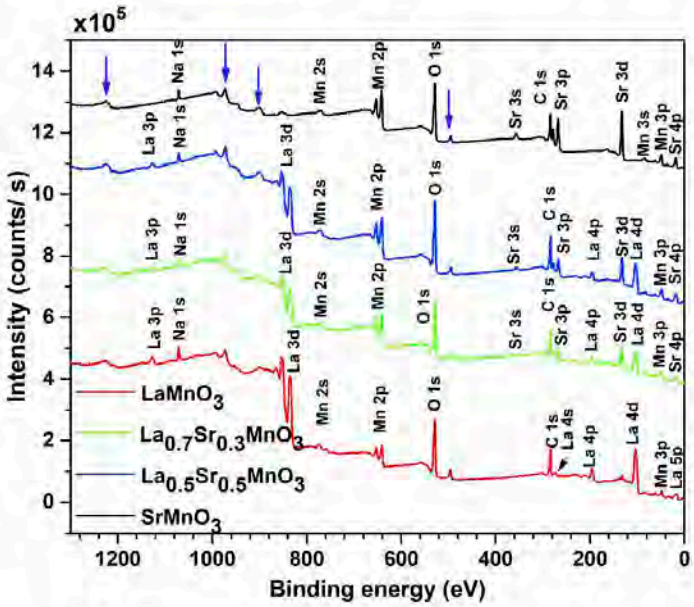

Fig. 7. XPS survey spectra of $La_{1-x}Sr_xMnO_3$ perovskites with x = 0, 0.3, 0.5, and 1.0.

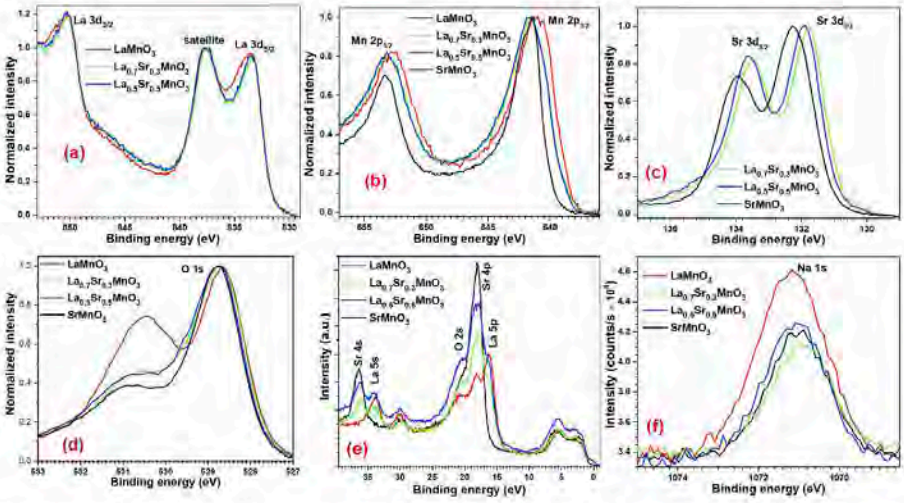

Fig. 8. High-resolution of XPS spectra of $La_{1-x}Sr_xMnO_3$ perovskites with x 0.0, 0.3 0.5, and 1.0. (a) La $3d_{5/2}$ and La $3d_{5/2}$, (b) Mn $3p_{1/2}$ and Mn $3p_{3/2}$, (c) Sr $3d_{3/2}$ and Sr $3d_{5/2}$. (d) O 1s, (e) O 2s, Sr 4p, La 5p; and (f) Na 1s.

affecting the BE of Mn $2p_{3/2}$ orbital. As a result, the Mn $2p_{3/2}$ emission band is broader in $LaMnO_3$, $La_{0.7}Sr_{0.3}MnO_3$, and $La_{0.5}Sr_{0.5}MnO_3$ than in $SrMnO_3$ (see Fig. 8b). As has been discussed in section 3.4, there is no Jahn-Teller effect in the $SrMnO_3$ phase. Since the Jahn-Teller effect plays a key role in the colossal magnetoresistance exhibited by $La_{0.7}Sr_{0.3}MnO_3$ below a certain critical temperature [63], it is worth to highlight the differences in the FWHM of the Mn $2p_{3/2}$ emission bands in their XPS spectra of the perovskites (Fig. 8b).

There exists another contribution to the observed difference in the FWHM values. The La^{3+} cations in $LaMnO_{3+\delta}$ are coordinated by 12 O^{2-} anions with varied La–O bond distances (i.e. 2.418, 2.46, 2.579, 2.65, 2.72, 3.156, 3.189, 3.35 Å) [64]. Consequently, the electron density around the oxygen anions in the La–O bonds are different; which also affects the BE of the Mn $2p_{3/2}$ orbital in the perovskites. On the contrary, in $SrMnO_3$ the twelve Sr–O bond distances are very similar (2.73, 2.73, 2.76 and 2.85 Å) [65]. Likewise, the Mn–O bond distances in $SrMnO_3$ are very close (1.87 and 1.89 Å) [65], and therefore the BEs of the Mn $2p_{3/2}$ emission bands are similar, making its XPS emission sharper.

Fig. 8c shows the core-level XPS spectra of Sr $3d_{3/2}$ and Sr $3d_{5/2}$ orbitals for the $La_{1-x}Sr_xMnO_3$ perovskites. The Sr $3d_{5/2}$ (Sr $3d_{3/2}$) peaks for the $La_{0.7}Sr_{0.3}MnO_3$, $La_{0.5}Sr_{0.5}MnO_3$, and $SrMnO_3$ perovskites are centered at 131.76 (133.49), 131.92 (133.60), and 132.25 (133.91) eV, respectively. As can be observed, the BE of electrons in the Sr $3d_{5/2}$ and Sr $3d_{3/2}$ orbitals shift gradually towards lower energy with the incorporation of La. It should be noted further that while in $SrMnO_3$ there are Sr–O–Mn^{4+} moieties, in $La_{0.5}Sr_{0.5}MnO_3$ and $La_{0.7}Sr_{0.3}MnO_3$, there are both Sr–O–Mn^{3+} and Sr–O–Mn^{4+} moieties. As the Mn^{4+} cation has a larger electron-withdrawing capacity from Sr atoms than the Mn^{3+} cations, the BEs of the Sr $3d_{5/2}$ and Sr $3d_{3/2}$ orbitals shift gradually towards higher energy with the increase of Sr content.

The O1s orbital emissions from $LaMnO_{3+\delta}$ and $SrMnO_3$ are centered at 528.68 and 528.77 eV, respectively (Fig. 8d). This difference makes sense since the reported BE for the O 1s orbital for the La_2O_3 and SrO are 528.8 and 530.3 eV, respectively [66]. Deconvolution of the O 1s emission bands is depicted in Fig. S7 (supporting information). The areas of the fitted component bands (fit peaks) are included in Table S3 (supporting information). In the spectrum of $LaMnO_{3+\delta}$ there is a second peak centered at 530.47 eV (with a shoulder at 529.87 eV), which is associated to surface hydroxyl groups, such as –LaOOH or –Mn-OH bonded to the surface of this manganite (see the fit peaks in green color in Fig. S7). The intensity ratios of the components associated to the M – OH and M-O-M (M = Sr^{2+}, La^{3+}, and $Mn^{3+,4+}$) bonds for the $LaMnO_3$, $La_{0.7}Sr_{0.3}MnO_3$, $La_{0.7}Sr_{0.3}MnO_3$, and $SrMnO_3$ were estimated to be 0.87, 0.40, 0.33, and 0.37, respectively. Zhi et al. [12], used powder $La_{0.5}Sr_{0.5}MnO_3$ samples and microtubes in electrochemical oxygen reduction at operating temperatures between 700 and 900 °C, obtaining M-OH/(M-O-M) ratios of 0.97 for the powder and 1.32 for microtubes [12]. Therefore, the presence of O 1s peak at 530.5 eV in the core-level XPS spectra of our $La_{1-x}Sr_xMnO_3$ samples indicates the occurrence of reduction-oxidation reactions at the surface of the manganites.

Presence of –OH groups at the surface of $La_{1-x}Sr_xMnO_3$ perovskite samples exposed to water agrees with the observations made by Stoerzinger et al. for their humidity exposed $La_{1-x}Sr_xMnO_3$ samples [11]. In fact, generation of M – OH groups at the surface of $La_{0.6}Sr_{0.4}MnO_3$ thin films has been demonstrated by Li et al. by treating them in oxidizing mixture ($5H_2O$, 1 NH_4OH, $1H_2O_2$) [67]. Furthermore, the formation of LaOOH bonds at the surface of $LaCoO_3$ causing a splitting of the O 1s band has also been observed by Natile et al. [68], and Stoerzinger et al., [69]. An emission band around 532 eV attributed to physisorbed H_2O molecule was detected in all the samples (see the red component in Fig. S7).

As can be seen in Fig. 8e, the Sr 4p, O 2s, and La 5p orbitals overlap due to closeness of binding energies. This finding is interesting because atomic orbitals of same (or closer) binding energies (and proper symmetry) usually form strong chemical bonds, and consequently, increase the thermal stability of the oxides. Reported theoretical calculations of the density of states (DOS) for the $La_{0.7}Sr_{0.3}MnO_3$ perovskite indicate that the DOS for the Sr 4p and La 5p orbitals are located at −15.0 and −16.0 eV, respectively [70]. However, the XPS spectra presented in Fig. 8e indicate the DOS for the Sr 4p and La 5p orbitals are located at −18.09 and −16.31 eV, respectively.

As can be noticed in Fig. 8f, and the surface elemental compositions of $La_{1-x}Sr_xMnO_3$ samples presented in Table 2, all the samples contain Na^+ cations, with the highest atomic percentage in $LaMnO_{3+\delta}$ sample. The higher XPS estimated atom % of Na (Table 2) in the samples in comparison to their EDS estimated values (Table 1), clearly indicates the

Table 2
XPS estimated elemental composition at the surface of $La_{1-x}Sr_xMnO_3$ nanoparticles.

Sample	Na (at%)	Mn (at%)	Sr (at%)	La (at%)	O (at%)
$LaMnO_3$	12.13	15.59	–	8.05	64.23
$La_{0.7}Sr_{0.3}MnO_3$	5.26	17.62	18.64	3.14	55.33
$La_{0.5}Sr_{0.5}MnO_3$	5.14	16.67	22.26	3.13	52.78
$SrMnO_3$	4.82	17.88	30.62	–	46.69

Na^+ cations are incorporated mainly at the surface of the manganites, bonding with surface oxygen atoms.

3.6. Magnetic properties

Since the magnetic moment per unit mass (emu/g) is a tool to find structural changes in magnetic materials, we recorded the magnetization vs applied magnetic field (M – H) curves of the synthesized $La_{1-x}Sr_xMnO_3$ nanostructures (Fig. 9). As can be noticed in Fig. 9, non-stoichiometric lanthanum manganite ($LaMnO_{3+\delta}$) nanoparticles exhibit paramagnetic behavior at 300 K. However, at lower temperatures they adopt a ferromagnetic (FM) phase with saturation magnetization (M_s) of 59.54 emu/g at 1.8 K (Fig. 9b). La^{3+} vacancies present in the $LaMnO_{3+\delta}$ nanoparticles transform some of the Mn^{3+} ions into Mn^{4+} cations to maintain the charge neutrality of the $LaMnO_{3+\delta}$ lattice (Fig. 10). According to the double-exchange mechanism proposed by Zener [71], the Mn^{3+}-O-Mn^{4+} moieties in $LaMnO_{3+\delta}$ adopt FM order below the Curie temperature (T_C), while the Mn^{3+}-O-Mn^{3+} moieties adopt an antiferromagnetic (AFM) order. Interestingly, the *Ms* value (59.54 emu/g at 1.8 K) we detected for the $LaMnO_{3+\delta}$ nanoparticles is very similar to the value found in nanofiber composed of 20 nm $LaMnO_{3+\delta}$ grains (65.0 emu/g) [72], larger than that of 18 nm (45.0 emu/g) and 35 nm (~42.0 emu/g) $LaMnO_{3+\delta}$ nanoparticles [73,74], but smaller than 55 nm $LaMnO_{3+\delta}$ nanoparticles (75.0 emu/g) [74].

Presence of stoichiometric $LaMnO_3$ in the sample fabricated in this study was rule out as stoichiometric $LaMnO_3$ adopts an orthorhombic lattice structure (instead of rhombohedral observed in the present study) and presents AFM ordering [45,75]. For the sake of reference, reported M_s value for $LaMnO_3$ single-crystal is 12.5 emu/g in the easy direction of magnetization at 2 K at 5 T applied magnetic field [76].

On the other hand, $La_{0.7}Sr_{0.3}MnO_3$ perovskites revealed a mixed superparamagnetic (SP) - paramagnetic behavior at 300 K with M_s value of about 26 emu/g (Fig. 9b). At 1.8 K, the value of M_s increased up to 56.90 emu/g. This value at 1.8 K is similar to the value reported for $La_{0.7}Sr_{0.3}MnO_3$ nanoparticles [16,22,37], but about 30 and 23 emu/g lower than that of microspheres [77], and small nanoparticles with well-connected grain boundaries (i.e. particles containing fused grains) [1], respectively. The *Ms* value at 1.8 K estimated for the $La_{0.7}Sr_{0.3}MnO_3$ nanoparticles fabricated in the present work is in good accordance with their well-dispersed (not fused, see Fig. 3b) characteristic.

The $La_{0.5}Sr_{0.5}MnO_3$ nanostructures revealed their SP ordering at 300 K with a M_s value about 29.59 emu/g. However, at 200 K, they exhibited a FM ordering, with M_s and H_c values of 41.87 emu/g and 31.0 Oe, respectively (Fig. 9a and b & S8). A comparison of the M_s values of the $La_{1-x}Sr_xMnO_3$ nanostructures displayed at different temperatures (Fig. 9b) indicates that the fabricated $La_{0.5}Sr_{0.5}MnO_3$ nanostructures are best suited for utilization in room-temperature magnetic hyperthermia.

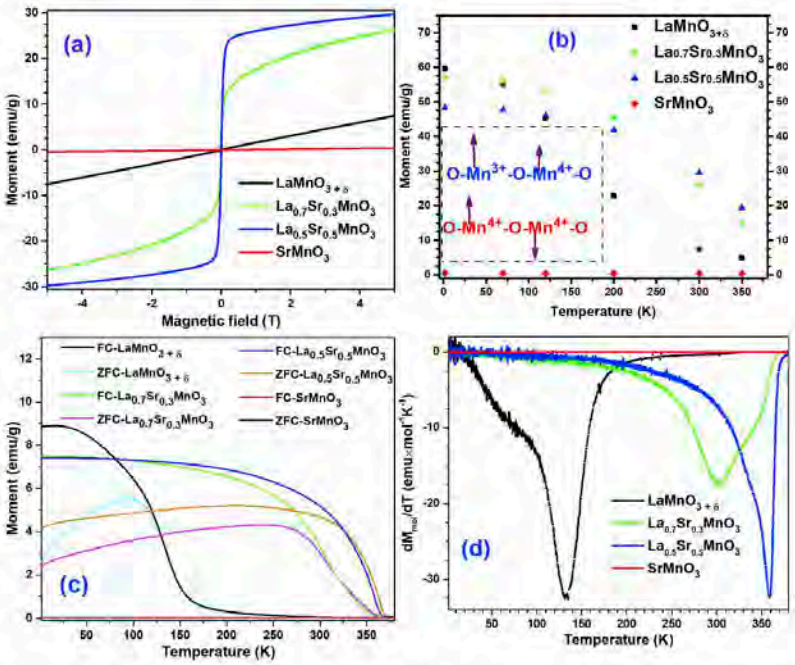

Fig. 9. Magnetic behaviors of the $La_{1-x}Sr_xMnO_3$ perovskites: (a) Magnetization (M) vs applied magnetic field (H) curves recorded at 300 K; (b) Saturation magnetization (M_s) measured at 5 T at different temperatures; inset shows the relative magnitude and alignment of the atomic magnetic moments in Mn^{3+} and Mn^{4+} cations; (c) Zero field cooling (ZFC) and field cooling (FC) curves measured at 100 Oe; (d) Temperature variation of the first derivative of molar magnetization (M_{mol}) for the $La_{1-x}Sr_xMnO_3$ perovskites with different x values.

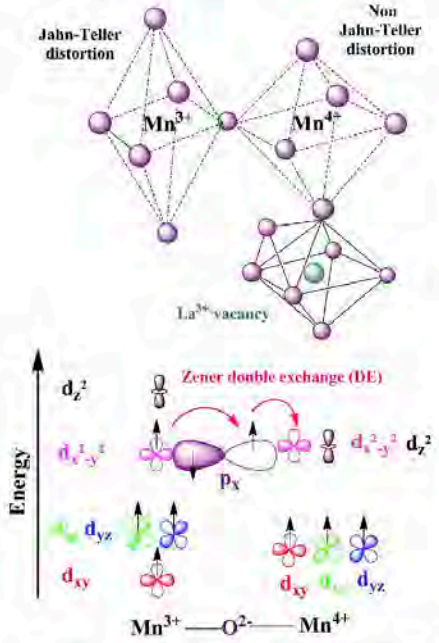

Fig. 10. (Top) Schematic representation of the geometric distortion of $Mn^{3+}O_6$ octahedron in $LaMnO_{3+\delta}$ perovskite lattice due to Jahn-Teller (J-T) effect. J-T distortion does not occur in Mn^{4+}-O_6 octahedron. The green sphere inside the polyhedron represents a La^{3+} vacancy. The La^{3+} vacancy transforms some neighboring Mn^{3+} cations into Mn^{4+} cations. (Bottom) Schematics of the relative energy positions of the 3d orbitals in Mn^{3+} and Mn^{4+} cations (five orbitals for each cation) present in the $La_{1-x}Sr_xMnO_3$ (x = 0, 0.3 and 0.5) perovskites; orbital in purple color represents the $2p_x$ orbital of the O^{2-} anion in Mn^{3+}-O-Mn^{4+} moiety. Black arrows in each orbital indicate the spin of the electrons. Note that the spin alignment corresponds to a ferromagnetic material (provided that the temperature is below its Curie temperature). Pink arrows show the double electron exchange (DE) responsible for the magnetoresistance under an external magnetic field.

Finally, the $SrMnO_3$ nanostructures exhibited an antiferromagnetic (AFM) behavior at all the temperatures (Fig. 9a & b), as expected for a solid composed of Mn^{4+}-O-Mn^{4+} moieties, in which there is no possibility of occurring the double exchange (DE) interaction phenomenon.

The zero-field cooling (ZFC) and field cooling (FC) curves (2 K/min) for the $La_{1-x}Sr_xMnO_3$ perovskites recorded applying 100 Oe magnetic field are shown in Fig. 9c. A paramagnetic to ferromagnetic transition around 130 K can be clearly observed for the $LaMnO_{3+\delta}$ nanostructures, which explains the large increase in magnetic moment (Fig. 9b) below this temperature. Irreversibility temperature (T_{irr}, the point at which the ZFC and FC curves bifurcate) for the $LaMnO_{3+\delta}$ sample (around 130 K) is close to its reported Curie temperature (T_c= 135 K) [78]. T_{irr} for the $LaMnO_{3+\delta}$, $La_{0.7}Sr_{0.3}MnO_3$, and $La_{0.7}Sr_{0.3}MnO_3$ phases are 125, 318, and 325 K, respectively (Fig. 9c). As can be seen in Table 3, the T_{irr} for $LaMnO_{3+\delta}$ nanoparticles fabricated in the present work is considerably lower than the values reported in the literature. The lower T_{irr} value of the nanoparticles might be associated to their non-aggregated (particles are not fused) arrangement. However, estimated T_{irr} values for the $La_{0.7}Sr_{0.3}MnO_3$ nanoparticles fabricated in the present study are close to the values reported for dispersed nanoparticles (see Table 3). Notably, the FC and ZFC curves of the sample cross at the T_{irr}, instead of merging.

Table 3
Irreversibility temperature (T_{irr}) for the $LaMnO_{3+\delta}$ and $La_{0.7}Sr_{0.3}MnO_3$ nanoparticles in comparison to their values reported in the literature. The ZFC and FC curves were recorded under 100 Oe applied magnetic field.

Phase	Particle size (nm)	Aggregation behavior	T_{irr} (K)	Reference
$LaMnO_{3+\delta}$	52	Highly dispersed nanoparticles	125	**Present work**
$LaMnO_{3+\delta}$	18	(a)	220	[75]
$LaMnO_{3+\delta}$	–	(a)	230	[84]
$LaMnO_{3+\delta}$	20	Fused grains forming nanofibers.	240	[72]
$LaMnO_{3-\delta}$	40	Fused nanoparticles.	255	[74]
$La_{0.7}Sr_{0.3}MnO_3$	25	(a)	275 (b)	[37]
$La_{0.7}Sr_{0.3}MnO_3$	50	Highly fused nanoparticles.	300 (c)	[85]
$La_{0.7}Sr_{0.3}MnO_3$	20	Highly fused nanoparticles.	300	[1]
$La_{0.7}Sr_{0.3}MnO_3$	25	Dispersed nanoparticles functionalized with betaine hydrochloride	325	[15]
$La_{0.7}Sr_{0.3}MnO_3$	129	Dispersed nanoparticles	290 (d)	**Present work**
$La_{0.7}Sr_{0.3}MnO_3$	129	Dispersed nanoparticles	318	**Present work**
$La_{0.7}Sr_{0.3}MnO_3$	129	Dispersed nanoparticles	336 (e)	**Present work**
$La_{0.5}Sr_{0.5}MnO_3$	–	(a)	300	[84]
$La_{0.5}Sr_{0.5}MnO_3$	88	Dispersed nanoparticles	325	**Present work**

(a) TEM images were not included in the reference. ZFC and FC curves were measured at (b) 200 Oe, (c) 10 Oe, (d) 200 Oe and (e) 50 Oe.

Such a crossing/inversion between the ZFC and FC curves has been observed in $Tb(Co_{0.94}Fe_{0.06})_2$ [79], $CoFe_2O_4$ [80], $La_{0.275}Pr_{0.35}Ca_{0.375}MnO_3$ [81], $NiFe_2O_4$ [82], and graphene oxide/$NiFe_2O_4$ composite [83]. Such anomaly in magnetic behavior of the nanostructures has been attributed to their large magnetostriction [80,81], presence of a frustrated spin system [83], or a spin-glass-like surface disorder [82].

Broadening of the Mn $3p_{3/2}$ XPS peaks (Fig. 8b) and high saturation magnetization (Fig. 9b) in the $La_{1-x}Sr_xMnO_3$ perovskite (x = 0, 0.3 and 0.5) can be obtained only if both the Mn^{3+} and M^{4+} ions are present in the perovskite. Therefore, the use of XPS and vibrating sample magnetometry (VSM) techniques in combination is important, as they help to confirm the presence of Mn cations in mixed valence states in the perovskites. Besides, for $LaMnO_{3+\delta}$, both the high M-OH/M-O-M (M = Sr^{2+}, La^{3+}, and $Mn^{3+,4+}$) ratio found through XPS analysis and the low T_{irr} value determined from the FC/ZFC curves support the claim that the $LaMnO_{3+\delta}$ nanoparticles have small size and are not aggregated.

The temperature of the transition from paramagnetic to ferromagnetic, T_c, could be estimated from the maximum of the first derivative of molar magnetization (M_{mol}) with respect to temperature (Fig. 9d). The T_c values obtained for the $La_{1-x}Sr_xMnO_3$ nanoparticles with x = 0, 0.3 and 0.5 were 133, 303, and 358 K, respectively. Such a gradual increase in T_c value with the increase of strontium mole fraction in the perovskites can be understood considering its dependence on the interionic spin interaction of nearest-neighbors. The interaction between localized spins of the neighboring ions are treated by a perturbation theory in which the spin-dependent resonance integrals for parallel coupling of spins are:

$$t_{ij} \approx \varepsilon_\sigma \lambda_\sigma^2 \cos\varphi \cos\left(\frac{\theta_{ij}}{2}\right) \quad (1)$$

where ε_σ is the stabilization energy of the band formed by the $Mn^{3+,4+}$ d^{22}_{x-y} and O $2p_x$ orbitals (see Fig. 10), λ_σ is the overlap integral between atomic orbitals, $(180° - \varphi)$ is the angle in the Mn–O–Mn bond, and θ_{ij} is the angle between the spins on neighboring Mn cations [46,86]. In other words, t_{ij} is a measure of the strength of the ferromagnetic Mn^{3+}-O-Mn^{4+} interactions in perovskites.

The higher T_c observed (Fig. 9d) for the $La_{0.5}Sr_{0.5}MnO_3$ sample can be attributed to the higher ferromagnetic interaction, caused by the following two factors: (i) Since the reported Mn–O–Mn angle in $La_{0.5}Sr_{0.5}MnO_3$ is 180° but only 164° in $La_{0.7}Sr_{0.3}MnO_3$ [84], $cos\varphi$ in eq. (1) is 1 for $La_{0.5}Sr_{0.5}MnO_3$ and 0.96 for $La_{0.7}Sr_{0.3}MnO_3$. (ii) The radius of Mn^{4+} cation is smaller than the radius Mn^{3+} cation, and also the $La_{0.5}Sr_{0.5}MnO_3$ has higher Mn^{4+} content than $La_{0.7}Sr_{0.3}MnO_3$. The smaller size of Mn^{4+} generates a greater overlapping of orbitals (λ_0) of the Mn^{4+} and oxygen ions, increasing the value of t_{ij} in eq. (1). The results presented in this article clearly demonstrate that the size and aggregation determine the T_{irr} and M_S value of $LaMnO_{3+\delta}$ nanoparticles. While the use of common salt in solid-state mechano-synthesis of $La_{1-x}Sr_xMnO_3$ nanoparticles helps to increase their dispersion, substitution of La^{3+} ions by Sr^{2+} ions induces changes in the Mn–O–Mn angle and Mn^{3+}/Mn^{4+} ratio, which affect the magnetic behavior (M_s, T_{irr}, and T_c values) of the perovskite nanoparticles.

4. Conclusions

Quasi-spherical $La_{1-x}Sr_xMnO_3$ (x = 0, 0.3, 0.5, and 1) nanoparticles of 90–255 nm average sizes could be synthesized through solvent-free ball milling process utilizing NaCl as a dispersing medium, and subsequent thermal annealing. While the Cl ions of the used NaCl (as dispersing agent) escape during high temperature (900 °C) air-annealing, the Na^+ ions remain at the surface of the perovskite particles preventing their aggregation. The poor dispersion of $SrMnO_3$ particles is due to lower concentration of Na^+ ions at their surface. Substitution of La^{3+} ions by Sr^{2+} causes a gradual increase in the average size of $La_{1-x}Sr_xMnO_3$ nanoparticles. It also progressively increases the ferromagnetic interaction in $La_{1x}Sr_xMnO_3$ (x = 0, 0.3, 0.5) nanostructures, increasing their Curie temperature gradually. Incorporation of Sr not only reduces the Jahn-Teller distortion in $LaMnO_{3+\delta}$ lattice (up to x = 0.5), but also decreases the concentration of La^{3+} vacancies. Creation of La^{3+} vacancies in $LaMnO_{3+\delta}$ lattice generates Mn^{4+} ions (through oxidation of Mn^{3+} ions) to preserve the charge neutrality of the lattice, enhancing the magnetization (M_S) of the nanostructures through inter-ionic spin interaction. While the presence of Na^+ ions at the surface of $La_{1-x}Sr_xMnO_3$ nanoparticles helps to keep them disaggregated during high-temperature thermal annealing, it causes a reduction of irreversibility temperature (T_{irr}) and saturation magnetization (M_s) values of the nanostructure.

Declaration of competing interest

The authors declare that they have no known competing financial interests or personal relationships that could have appeared to influence the work reported in this paper.

Acknowledgements

FECG and JLOQ thank CONACyT, Mexico for extending doctoral (CVU # 784149) and postdoctoral (CONACyT-SENER) fellowships, respectively. Financial helps offered by VIEP-BUAP (Grant # 100236944-BUAP 2019) and CONACYT, Mexico (Grants # INFR-2014-02-23053, INFR-2011-1-163153, and A1-S-26720) are acknowledged.

Appendix A. Supplementary data

Supplementary data to this article can be found online at https://doi.org/10.1016/j.matchemphys.2020.122834.

References

[1] A. Sadhu, S. Bhattacharyya, Enhanced low-field magnetoresistance in $La_{0.7}Sr_{0.29}MnO_3$ nanoparticles synthesized by the nonaqueous sol gel route, Chem. Mater. 26 (2014) 1702–1710, https://doi.org/10.1021/cm4041665.

[2] T. Walter, K. Dörr, K. Müller, B. Holzapfel, D. Eckert, M. Wolf, D. Schlafer, L. Schultz, R. Grotzsched, Low-field magnetoresistance of $La_{0.7}Sr_{0.3}MnO_3$ thin films with gradually changed texture, Appl. Phys. Lett. 74 (1999) 2218–2220, https://doi.org/10.1063/1.123806.

[3] Y. Tokura, A. Urushibara, Y. Moritomo, T. Arima, A. Asamitsu, G. Kido, N. Furukawa, Giant magnetotransport phenomena in filling-controlled kondo lattice system: $La_{1-x}Sr_xMnO_3$, J. Phys. Soc. Japan. 63 (1994) 3931–3935.

[4] Z.X. Cheng, H.F. Zhen, A.H. Li, X.L. Wang, H. Kimura, CMR $La_{0.7}Ca_{0.3}MnO_3$ and $La_{0.7}Sr_{0.3}MnO_3$ thin film fabricated by sol – gel method, J. Cryst. Growth 275 (2005) 2415–2419, https://doi.org/10.1016/j.jcrysgro.2004.11.351.

[5] M. Pan, H. Wang, S. Misra, B. Zhang, Z. Qi, X. Sun, J. Huang, H. Wang, Microstructure, magnetic, and magnetoresistance properties of $La_{0.7}Sr_{0.3}MnO_3$: CuO nanocomposite thin films, ACS Appl. Mater. Interfaces 10 (2018) 5779–5784, https://doi.org/10.1021/acsami.7b17396.

[6] T.D. Thanh, P.T. Phong, D.H. Manh, N. V Khien, L. V Hong, T.L. Phan, S.C. Yu, Low-field magnetoresistance in $La_{0.7}Sr_{0.3}MnO_3$/$BaTiO_3$ composites, J. Mater. Sci. Mater. s Electron. 24 (2013) 1389–1394, https://doi.org/10.1007/s10854-012-0943-y.

[7] K. Huang, X. Chu, W. Feng, C. Zhou, W. Si, X. Wu, L. Yuan, S. Feng, Catalytic behavior of electrospinning synthesized $La_{0.75}Sr_{0.25}MnO_3$ nanofibers in the oxidation of CO and CH_4, Chem. Eng. J. 244 (2014) 27–32, https://doi.org/10.1016/j.cej.2014.01.056.

[8] F. Teng, W. Han, S. Liang, B. Gaugeu, R. Zong, Y. Zhu, Catalytic behavior of hydrothermally synthesized $La_{0.5}Sr_{0.5}MnO_3$ single-crystal cubes in the oxidation of CO and CH_4, J. Catal. 250 (2007) 1–11, https://doi.org/10.1016/j.jcat.2007.05.007.

[9] X. Wu, L. Xu, D. Weng, The NO selective reduction on the $La_{1-x}Sr_xMnO_3$ catalysts, Catal. Today 90 (2004) 199–206, https://doi.org/10.1016/j.cattod.2004.04.027.

[10] K. Huang, L. Yuan, Yilan Jiang, J. Zhang, Z. Geng, L. Luo, S. Feng, Hydrothermal shape controllable synthesis of $La_{0.5}Sr_{0.5}MnO_3$ crystals and facet effect on electron transfer of oxygen reduction, Inorg. Chem. Front. 5 (2018) 732–738, https://doi.org/10.1039/c7qi00687j.

[11] K.A. Stoerzinger, W.T. Hong, X.R. Wang, R.R. Rao, S. Bengaluru Subramanyam, C. Li, Ariando, T. Venkatesan, Q. Liu, E.J. Crumlin, K.K. Varanasi, Y. Shao-Horn, Decreasing the hydroxylation affinity of $La_{1-x}Sr_xMnO_3$ perovskites to promote oxygen reduction electrocatalysis, Chem. Mater. 29 (2017) 9990–9997, https://doi.org/10.1021/acs.chemmater.7b03199.

[12] M. Zhi, G. Zhou, Z. Hong, J. Wang, R. Gemmen, K. Gerdes, A. Manivannan, D. Ma, N. Wu, Single crystalline $La_{0.5}Sr_{0.5}MnO_3$ microcubes as cathode of solid oxide fuel cell, Energy Environ. Sci. 4 (2011) 139–144, https://doi.org/10.1039/c0ee00300j.

[13] C. Zhou, K. Huang, L. Yuan, W. Feng, X. Chu, Z. Geng, X. Wu, L. Wang, S. Feng, Green catalyst: magnetic $La_{0.7}Sr_{0.3}MnO_3$ hollow microspheres, New J. Chem. 39 (2015) 2413–2416, https://doi.org/10.1039/c4nj01955c.

[14] N.D. Thorat, K.P. Shinde, S.H. Pawar, K.C. Barick, C.A. Betty, R.S. Ningthoujam, Polyvinyl alcohol: an efficient fuel for synthesis of superparamagnetic LSMO nanoparticles for biomedical application, Dalton Trans. 41 (2012) 3060–3071, https://doi.org/10.1039/c2dt11035a.

[15] N.D. Thorat, R.M. Patil, V.M. Khot, A.B. Salunkhe, A.I. Prasad, K.C. Barick, R. S. Ningthoujam, S.H. Pawar, Highly water-dispersible surface-functionalized LSMO nanoparticles for magnetic fluid hyperthermia application, New J. Chem. 37 (2013) 2733–2742, https://doi.org/10.1039/c3nj00607a.

[16] P.T. Phong, D.H. Manh, L.H. Nguyen, D.K. Tung, H.X. Phuc, I.J. Lee, Studies of superspin glass state and AC-losses in $La_{0.7}Sr_{0.3}MnO_3$ nanoparticles obtained by high-energy ball milling, J. Magn. Magn Mater. 368 (2014) 240–245, https://doi.org/10.1016/j.jmmm.2014.05.025.

[17] P. Tiwari, C. Rath, Evolution of structure and magnetic properties of stoichiometry and oxygen rich $LaMnO_3$ nanoparticles, J. Magn. Magn Mater. 441 (2017) 635–641, https://doi.org/10.1016/j.jmmm.2017.06.020.

[18] A. Maignan, C. Martin, B. Vertruyen, D. Flahaut, S. H, Magnetic and electronic ground states of B-site-substituted $LaMnO_3$: from antiferromagnetism to ferromagnetism, J. Magn. Magn Mater. 280 (2004) 75–83, https://doi.org/10.1016/j.jmmm.2004.02.023.

[19] K.P. Shinde, S.S. Pawar, S.H. Pawar, Influence of annealing temperature on morphological and magnetic properties of $La_{0.9}Sr_{0.1}MnO_3$, Appl. Surf. Sci. 257 (2011) 9996–9999, https://doi.org/10.1016/j.apsusc.2011.06.126.

[20] K.P. Shinde, S.S. Pawar, P.M. Shirage, S.H. Pawar, Studies on morphological and magnetic properties of $La_{1-x}Sr_xMnO_3$, Appl. Surf. Sci. 258 (2012) 7417–7420, https://doi.org/10.1016/j.apsusc.2012.04.052.

[21] K. Huang, X. Chu, L. Yuan, W. Feng, X. Wu, X. Wang, S. Feng, Engineering the surface of perovskite $La_{0.5}Sr_{0.5}MnO_3$ for catalytic activity of CO oxidation, Chem. Commun. 50 (2014) 9200–9203, https://doi.org/10.1039/C4CC00023D.

[22] Y. Tian, D. Chen, X. Jiao, $La_{1-x}Sr_xMnO_3$ (x = 0, 0.3, 0.5, 0.7) nanoparticles nearly freestanding in water: preparation and magnetic properties, Chem. Mater. 18 (2006) 6088–6090, https://doi.org/10.1021/cm062234o.

[23] M.C. Martin, G. Shirane, Magnetism and structural distortion in the $La_{0.7}Sr_{0.3}MnO_3$ metallic ferromagnet, Phys. Rev. B 53 (1996) 285–290, https://doi.org/10.1103/PhysRevB.53.14285.

[24] Z.G. Sheng, M. Nakamura, W. Koshibae, T. Makino, Y. Tokura, M. Kawasaki, Magneto-tunable photocurrent in manganite-based heterojunctions, Nat. Commun. 5 (2014) 1–7, https://doi.org/10.1038/ncomms5584.

[25] Y. Zhou, X. Zhu, S. Li, Effect of heat treatment condition on magnetic, electrical transport and magnetoresistance properties of $La_{0.67}Sr_{0.33}MnO_3$ manganite coatings, Ceram. Int. 44 (2018) 15010–15018, https://doi.org/10.1016/j.ceramint.2018.05.120.

[26] V.S. Zakhvalinski, R. Laiho, K.G. Lisunov, E. Lähderanta, P.A. Petrenko, Y. P. Stepanov, J. Salminen, V.N. Stamov, Preparation and magnetic properties of

$LaMnO_{3+\delta}$, Phys. Solid State 48 (2006) 2300–2309, https://doi.org/10.1134/S1063783406120109.

[27] K. Navin, R. Kurchania, The effect of particle size on structural, magnetic and transport properties of $La_{0.7}Sr_{0.3}MnO_3$ nanoparticles, Ceram. Int. 44 (2018) 4973–4980, https://doi.org/10.1016/j.ceramint.2017.12.091.

[28] R. Huang, L. Yuan, Y. Jiang, J. Zhang, Z. Geng, L. Luo, S. Feng, Hydrothermal shape controllable synthesis of $La_{0.8}Sr_{0.8}MnO_3$ crystals and facet effect on electron transfer of oxygen reduction, Inorg. Chem. Front. 5 (2018) 732–738, https://doi.org/10.1039/c7qi00687j.

[29] Y.H. Huang, Z.G. Xu, C.H. Yan, Z.M. Wang, T. Zhu, C.S. Liao, S. Gao, G.X. Xu, Soft chemical synthesis and transport properties of $La_{0.7}Sr_{0.3}MnO_3$ granular perovskites, Solid State Commun. 114 (2000) 43–47, https://doi.org/10.1016/S0038-1098(99)00575-X.

[30] X. Wu, L. Xu, B. Yang, D. Weng, Surface characterization and catalytic performance of $La_{0.7}Sr_{0.3}MnO_{3+\delta}$ coating deposited by plasma spraying, Surf. Coating. Technol. 184 (2004) 40–46, https://doi.org/10.1016/j.surfcoat.2003.10.052.

[31] E.A. Nforna, Structure and magnetic properties of lanthanum strontium ferrites nanopowders synthesized by thermal decomposition of mixed metal acetyl acetonates, Int. J. Eng. Res. Technol. 4 (2015) 907–914.

[32] M. Popa, L. Van Horg, M. Kakihana, Particle morphology characterization and magnetic properties of $LaMnO_{3+\delta}$ perovskites, Physica B 327 (2003) 237–240.

[33] T. Ahmad, I.H. Lone, M. Ubaidullah, K. Coolhan, Low-temperature synthesis, structural and magnetic properties of sol-gel-dopant $LaMnO_{3+\delta}$ nanoparticles from a metal-organic polymeric precursor, Mater. Res. Bull. 48 (2013) 4723–4728, https://doi.org/10.1016/j.materresbull.2013.08.007.

[34] R.S. Guo, Q.T. Wei, H.L. Li, F.H. Wang, Synthesis and properties of $La_{0.7}Sr_{0.3}MnO_3$ cathode by gel combustion, Mater. Lett. 60 (2006) 261–265, https://doi.org/10.1016/j.matlet.2005.08.027.

[35] V. Ravi, S.D. Kulkarni, V. Samuel, S.N. Kale, J. Mona, R. Rajgopal, A. Daundkar, P. S. Lahoti, R.S. Joshee, Synthesis of $La_{0.7}Sr_{0.3}MnO_3$ at 800 °C using citrate gel method, Ceram. Int. 33 (2007) 1129–1132, https://doi.org/10.1016/j.ceramint.2006.02.008.

[36] A.B. Antipov, A.N. Grigoriev, S.V. Zayats, V.V. Ivanov, A.R. Kaul, Low-field magnetoresistance of $La_{0.7}Sr_{0.3}MnO_3$ nanoceramics processed by different precursor approaches and powder compaction techniques, Mendeleev Commun. 14 (2004) 148–150, https://doi.org/10.1070/mc2004v014n04abeh001959.

[37] F. Luo, Y.H. Huang, C.H. Yan, S. Jiang, X.H. Li, Z.M. Wang, C.S. Liao, Molten alkali metal nitrate flux to well-crystallized and homogeneous $La_{0.7}Sr_{0.3}MnO_3$ nanocrystallites, J. Magn. Magn Mater. 260 (2003) 173–180, https://doi.org/10.1016/S0304-8853(02)01317-3.

[38] J. Yang, X. Feng, G. Lu, Y. Li, C. Mao, Z. Wen, W. Yuan, NaCl as a solid solvent to assist the mechanochemical synthesis and post-synthesis of hierarchical porous MOFs with high I_2 vapour uptake, Dalton Trans. 47 (2018) 5065–5071, https://doi.org/10.1039/c8dt00339d.

[39] A. Pentecost, S. Gour, V. Mochalin, I. Knoke, Y. Gogotsi, Deaggregation of nanodiamond powders using salt- and sugar-assisted milling, ACS Appl. Mater. Interfaces 2 (2010) 3289–3294, https://doi.org/10.1021/am100720n.

[40] Y. Xiu, W. Fan, X. Zhen, Z. Ying, C. Ming, Synthesis of CeO_2 nanoparticles by mechanochemical processing and the inhibiting action of NaCl on particle agglomeration, Mater. Lett. 59 (2005) 48–52, https://doi.org/10.1016/j.matlet.2004.05.089.

[41] R.D. Shannon, Revised effective ionic radii and systematic studies of interatomic distances in halides and chalcogenides, Acta Crystallogr. A 32 (1976) 751–767.

[42] F. Lin, J. Shao, H. Tang, Y. Li, Z. Wang, G. Chen, D. Yuan, K. Cen, Enhancement of NO oxidation activity and SO_2 resistance over $LaMnO_{3+\delta}$ perovskites catalysts with metal substitution and acid treatment, Appl. Surf. Sci. 479 (2019) 234–246, https://doi.org/10.1016/j.apsusc.2019.02.104.

[43] M. V Abrashev, A.P. Litvinchuk, M.N. Iliev, R.L. Meng, V.N. Popov, V.G. Ivanov, R. A. Chakalov, C. Thomsen, Comparative study of optical phonons in the rhombohedrally distorted perovskites $LaAlO_3$ and $LaMnO_3$, Phys. Rev. B 59 (1999) 4146–4153, https://doi.org/10.1103/PhysRevB.59.4146.

[44] J. Töpfer, J.B. Goodenough, $LaMnO_{3+\delta}$ revisited, J. Solid State Chem. 130 (1997) 117–128.

[45] C. Ritter, M.R. Ibarra, J.M. De Teresa, P.A. Algarabel, C. Marquina, J. Blasco, J. García, S. Oseroff, S. W. Cheong, Influence of oxygen content on the structural, magnetotransport, and magnetic properties of $LaMnO_{3+\delta}$, Phys. Rev. B 56 (1997) 8902–8911.

[46] L. Malavasi, C. Ritter, M. Cristina, C. Tealdi, M.S. Islam, C. Bruno, G. Flor, Effects of cation vacancy distribution in doped $LaMnO_{3+\delta}$ perovskites, J. Solid State Chem. 178 (2005) 2042–2049, https://doi.org/10.1016/j.jssc.2005.04.019.

[47] J.A. Alonso, Non-stoichiometry and properties of mixed-valence manganites, Phil. Trans. Roy. Soc. Lond. 356 (1998) 1617–1634, https://doi.org/10.1098/rsta.1998.0238.

[48] Q. Huang, J.W. Lynn, Structure and magnetic order in undoped lanthanum manganite, Phys. Rev. B 55 (1997) 14987–14999.

[49] L. Malavasi, Role of defect chemistry in the properties of perovskite manganites, J. Mater. Chem. 18 (2008) 3295–3308, https://doi.org/10.1039/b800099a.

[50] H. Taguchi, A. Shimizu, M. Nagao, H. Kido, Synthesis and characterization of four-layered hexagonal $(Sr_{1-x}Ba_x)MnO_3$ ($0.0<x<0.5$), J. Ceram. Soc. Japan. 115 (2007) 77–80, https://doi.org/10.2109/jcersj.115.77.

[51] Ulrich Muller, Inorganic Structural Chemistry, second ed., John Wiley & Sons, Chichester, UK, 2006.

[52] R. Laiho, K.G. Lisunov, E. LaLahderanta, P.A. Petrenko, J. Salminen, V.N. Stamov, Y.P. Stepanov, V.S. Zakhvalinskii, Low-field magnetic properties of $LaMnO_{3+\delta}$, J. Phys. Chem. Solid. 64 (2003) 2313–2319, https://doi.org/10.1016/S0022-3697(03)00266-X.

[53] J.A. Alonso, M.J. Martínez-Lope, M.T. Casais, A. Muñoz, Magnetic structures of $LaMnO_{3+\delta}$ perovskites (δ=0.11, 0.15, 0.26), Solid State Commun. 102 (1997) 7–12.

[54] S. Das, P. Roychoudhury, S. De, A. Roy, S. Chatterjee, K. De, Magnetic and electrical transport of the cation-deficient $LaMnO_3$: common origin for both Sr-doping and sel f-doping effects, Phys. B Condens. Matter 544 (2018) 17–22, https://doi.org/10.1016/j.physb.2018.05.004.

[55] M. Iqbal, M.N. Khan, A.A. Khan, Structural, magnetic, magnetocaloric and critical behavior studies in the vicinity of the paramagnetic to ferromagnetic phase transition temperature in $LaMnO_{3+\delta}$ compound, J. Magn. Magn Mater. 465 (2018) 670–677, https://doi.org/10.1016/j.jmmm.2018.06.026.

[56] G. Papastaikoudis, E. Syskakis, Unusual magnetic properties of $LaMnO_{3+\delta}$, J. Magn. Magn Mater. 276 (2004) 444–445, https://doi.org/10.1016/j.jmmm.2003.11.152.

[57] R. Horyn, A.J. Zaleski, E. Bukowska, A. Sikora, On magnetic properties of $LaMnO_{3\pm\delta}$ phase within its domain, J. Alloys Compd. 383 (2004) 80–84, https://doi.org/10.1016/j.jallcom.2004.04.012.

[58] M.N. Iliev, M.V. Abrashev, Raman phonons and Raman Jahn-Teller bands in perovskite-like manganites, J. Raman Spectrosc. 32 (2001) 805–811, https://doi.org/10.1002/jrs.770.

[59] V.B. Podobedov, A. Weber, D.B. Romero, J.P. Rice, H.D. Drew, Raman scattering in $La_{1-x}Sr_xMnO_3$ single crystals ($x = 0, 0.1, 0.2, 0.3$), Solid State Commun. 105 (1998) 589–593, https://doi.org/10.1016/S0038-1098(97)10185-5.

[60] A. Sacchetti, M. Baldini, P. Postorino, C. Martin, A. Maignan, Raman spectroscopy on cubic and hexagonal $SrMnO_3$, J. Raman Spectrosc. 37 (2006) 591–596, https://doi.org/10.1002/jrs.1484.

[61] J.F. Moulder, W.F. Stickle, P.E. Sobol, B.D. Kenneth, Handbook of X-Ray Photoelectron Spectroscopy, first ed., Perkin-Elmer Corporation, Eden Prairie, 1992.

[62] G. Wulfsberg, Inorganic Chemistry, first ed., Science, University Books, Sausalito, 2000.

[63] A.J. Millis, B.I. Shraiman, R. Mueller, Dynamic Jahn-Teller effect and colossal magnetoresistance in $La_{1-x}Sr_xMnO_3$, Phys. Rev. Lett. 77 (1996) 175–178.

[64] P. Norby, I.G.K. Andersen, E.K. Andersen, The crystal structure of lanthanum manganate (III), $LaMnO_3$, at room temperature and at 1273 K under H_2, J. Solid State Chem. 119 (1995) 191–196.

[65] K. Kuroda, H. Ishizawa, N. Mizutani, M. Kato, The crystal structure of alfa-$SrMnO_3$, J. Solid State Chem. 38 (1981) 297–299.

[66] D.A. Pawlak, M. Ito, M. Oku, K. Shimamura, T. Fukuda, Interpretation of XPS O (1s) in mixed oxides peoved on mixed perovskite crystals, J. Phys. Chem. B 106 (2002) 504–507.

[67] F. Li, Y. Zhan, T. Lee, X. Liu, A. Chikamatsu, T. Guo, H. Lin, J.C.A. Huang, M. Fuhlman, Modified surface electronic and magnetic properties of $La_{0.8}Sr_{0.2}MnO_3$ thin films for spintronics applications, J. Phys. Chem. C 115 (2011) 16947–16953.

[68] M.M. Natile, A. Galenda, A. Glisenti, M. Maria, A. Galenda, A. Glisenti, From La_2O_3 to $LaCoO_3$: XPS analysis, Surf. Sci. Spectra 15 (2008) 1–13, https://doi.org/10.1116/11.20061006.

[69] K.A. Stoerzinger, W.T. Hong, E.J. Crumlin, H. Bluhm, M.D. Biegalski, Water reactivity on the $LaCoO_3$ (001) surface: an ambient pressure, J. Phys. Chem. C 118 (2014) 19733–19741, https://doi.org/10.1021/jp502970v.

[70] F. Geng, H. Zhang, Electronic structure of the perovskite oxides $La_{1-x}Sr_xMnO_3$, Phys. Lett. 351 (2006) 314–318.

[71] C. Zener, Interaction between the d-Shells in the Transition Metals. I) Ferromagnetic compounds of manganese with perovskite structure, Phys. Rev. 81 (1951) 403–405.

[72] X. Zhou, J. Xue, D. Zhou, Z. Wang, Y. Bai, X. Wu, X. Liu, J. Meng, Mn valence, magnetic, and electrical properties of $LaMnO_{3+\delta}$ nanofibers by electrospinning, ACS Appl. Mater. Interfaces 2 (2010) 2689–2693, https://doi.org/10.1021/am1004738.

[73] V. Markovich, G. Jung, I. Fita, D. Mogilyansky, X. Wu, A. Wisniewski, R. Puzniak, N. Froumin, L. Titelman, L. Vradman, M. Herskowitz, G. Gorodetsky, Magnetotransport in granular $LaMnO_{3+\delta}$ manganite with nano-sized particles, J. Phys. D Appl. Phys. 41 (2008), 185001, https://doi.org/10.1088/0022-3727/41/18/185001.

[74] P.S. Tola, H.S. Kim, D.H. Kim, T.L. Phan, J.S. Rhyee, W.H. Shon, D.S. Yang, D. H. Manh, B.W. Lee, Tunable magnetic properties and magnetocaloric effect of off-stoichiometric $LaMnO_3$ nanoparticles, J. Phys. Chem. Solid. 111 (2017) 219–228, https://doi.org/10.1016/j.jpcs.2017.07.022.

[75] J.S. Z, J.B. Goodenough, Unusual evolution of the magnetic interactions versus structural distortions in $RMnO_3$ perovskites, Phys. Rev. Lett. 96 (2006) 247202.

[76] Y.M. Mukovskii, Anisotropy of magnetic properties in $LaMnO_3$ single crystals, J. Magn. Magn Mater. 272–276 (2004) 98–99, https://doi.org/10.1016/j.jmmm.2003.11.042.

[77] C. Zhou, K. Huang, L. Yuan, W. Feng, X. Chu, Z. Geng, X. Wu, L. Wang, S. Feng, Green catalyst: magnetic $La_{0.7}Sr_{0.3}MnO_3$ hollow microspheres, New J. Chem. 39 (2015) 2413–2416, https://doi.org/10.1039/c4nj01955e.

[78] A. Biswas, S. Chandra, M. Phan, H. Srikanth, Magnetocaloric properties of nanocrystalline $LaMnO_3$: enhancement of refrigerant capacity and relative cooling power, J. Alloys Compd. 545 (2012) 157–161, https://doi.org/10.1016/j.jallcom.2012.08.001.

[79] Y. Wang, T. Ma, C. Wu, M. Yan, C. Zhang, X. Chen, G. Sun, S. Yang, Yu Wang, T. Chang, C. Zhou, X. Liao, X. Zheng, Correlation between magnetostriction and magnetic structure in pseudobinary compounds $Tb(Co_{1-x}Fe_x)_2$, AIP Adv. (2017), 075311, https://doi.org/10.1063/1.4991734.

[80] U. Salazar-kuri, J.O. Estevez, N.R. Silva-gonzález, U. Pal, Large magnetostriction in chemically fabricated $CoFe_2O_4$ nanoparticles and its temperature dependence,

J. Magn. Magn Mater. 460 (2018) 141–145, https://doi.org/10.1016/j.jmmm.2018.03.074.
[81] B.C. Zhao, Y.Q. Ma, W.H. Song, Y.P. Sun, Magnetization steps in the phase separated manganite $La_{0.275}Pr_{0.35}Ca_{0.375}MnO_3$, Phys. Lett. 354 (2006) 472–476, https://doi.org/10.1016/j.physleta.2006.01.088, 354.
[82] G.N. Chinnasamy, A. Narayanasamy, N. Ponpandian, K. Chattopadhyay, K. Shinoda, B. Jeyadevan, K. Tohji, K. Nakatsuka, T. Furubayashi, I. Nakatani, Mixed spinel structure in nanocrystalline $NiFe_2O_4$, Phys. Rev. B 63 (2001) 184108, https://doi.org/10.1103/PhysRevB.63.184108.
[83] P. Kollu, S. Prathapani, E.K. Varaprasadarao, C. Santosh, S. Mallick, N. Grace, D. Bahadur, Anomalous magnetic behavior in nanocomposite materials of reduced graphene oxide-Ni/$NiFe_2O_4$, Appl. Phys. Lett. 105 (2014), 052412, https://doi.org/10.1063/1.4892476.
[84] R. Mahendiran, S.K. Tiwary, A.K. Raychaudhuri, T. V Ramakrishnan, Structure, electron-transport properties, and giant magnetoresistance of hole-doped $LaMnO_3$ systems, Phys. Rev. B 53 (1996) 3348–3358.
[85] D.H. Manh, P.T. Phong, P.H. Nam, D.K. Tung, H.N. Phuc, I. Lee, Structural and magnetic study of $La_{0.7}Sr_{0.3}MnO_3$ nanoparticles and AC magnetic heating characteristics for hyperthermia applications, Physica B 444 (2014) 94–102.
[86] J.B. Goodenough, Localized to itinerant electronic transition in perovskite oxides, in: Structure and Bonding, first ed., Springer, Berlin, 2001.

Received: 22 January 2021 | Revised: 22 March 2021 | Accepted: 22 March 2021

DOI: 10.1002/er.6727

SHORT COMMUNICATION

INTERNATIONAL JOURNAL OF ENERGY RESEARCH WILEY

Performance of asymmetric supercapacitor fabricated with perovskite-type Sr^{2+}-incorporated $LaMnO_3$ ($La_{0.7}Sr_{0.3}MnO_3$) nanostructures in neutral 1M Na_2SO_4 aqueous electrolyte

Atanu Roy[1] | **Francisco Enrique Cancino-Gordillo**[2] | **Samik Saha**[1,3] | **Umapada Pal**[2] | **Sachindranath Das**[1]

[1]Department of Instrumentation Science, Jadavpur University, Kolkata, India

[2]Instituto de Física, Benemérita Universidad Autónoma de Puebla, Puebla, Mexico

[3]Department of Physics, Jadavpur University, Kolkata, India

Correspondence
Sachindranath Das, Department of Instrumentation Science, Jadavpur University, Kolkata 700032, India.
Email: sachindas15@gmail.com; sachindran.das@jadavpuruniversity.in

Umapada Pal, Instituto de Física, Benemérita Universidad Autónoma de Puebla, Apdo. Postal J-48, Puebla 72570, Mexico.
Email: upal@ifuap.buap.mx

Funding information
Consejo Nacional de Ciencia y Tecnología, Grant/Award Number: CB-A1-S-26720; Council of Scientific and Industrial Research, India, Grant/Award Number: 09/096(0898)/2017-EMR-I; RUSA 2.0, Jadavpur University, Grant/Award Number: R-11/281/19; Science and Engineering Research Board, Grant/Award Number: CRG/2019/001575

Summary

Strontium (Sr) incorporated $LaMnO_3$ ($La_{0.7}Sr_{0.3}MnO_3$) nanoparticles have been synthesized by ball-milling-assisted solid-state reaction to study their performance as electrode material for energy storage applications. The $La_{0.7}Sr_{0.3}MnO_3$ nanoparticles exhibit superior electrochemical performance in neutral aqueous electrolyte (1 M Na_2SO_4) in comparison to $LaMnO_3$ and $SrMnO_3$ nanoparticles. This neutral electrolyte provides relatively higher ionic conductivity and viscosity compared to the ionic liquids and a wider potential window compared to the alkaline electrolytes. Electrochemical study of the electrodes prepared using $La_{0.7}Sr_{0.3}MnO_3$ nanoparticles reveals pseudocapacitive behaviors with fast reversible Faradaic charge storage, which plays a key role in charge storage. The composite materials exhibit highest specific capacitance of 393.5 F g^{-1} at a scan rate of 2 mV s^{-1}. Asymmetric supercapacitors fabricated using $La_{0.7}Sr_{0.3}MnO_3$ nanoparticle and activated carbon operates over a wide potential window of 1.8 V, and it reveals high specific capacitance (197 F g^{-1}) as well as high capacitive retention (87%) even after 4000 charge–discharge cycles.

KEYWORDS

nanostructured electrode, neutral electrolyte, perovskite, pseudocapacitance, supercapacitor

1 | INTRODUCTION

Energy is the foremost concern of the present day society because of the exponential rise in global energy demand and rapid depletion of fossil fuel reserve. In order to mitigate the energy crisis as well as pollution issues associated with fossil fuel burning, continuous innovation in the energy sector is essential. Current processes involved in energy generation, delivery, and storage need tremendous upgradation to meet the global challenge for the generation of clean and inexpensive energy. Solar radiation, ocean tide, wind, and biofuels have been envisioned as some of the most attractive renewable energy resources which can provide clean energy at a reasonable cost. However, due to the intermittent nature of these renewable energy sources, not only the generation but

also the storage of generated energy needs substantial attention. In fact, several energy storage devices such as supercapacitors, batteries, and fuel cells of enhanced performance have been developed in the past two decades, although they remained insufficient to fulfill the global energy demand.

A supercapacitor or electrochemical capacitor or ultracapacitor is a class of energy storage device, which received a tremendous attention in recent time because of its rapid charge–discharge rates, high power density, and relatively large cycle life compared to Li-ion battery.[1,2] Supercapacitors are broadly categorized into two classes depending upon their charge storage mechanism: (a) electric double-layer capacitors (EDLCs) and (b) pseudocapacitors. In EDLCs, a double layer is formed at the electrode/electrolyte interface. Mainly, carbonaceous materials and their derivatives belong to this category.[5-6] On the other hand, a pseudocapacitor stores charge via rapid faradaic reaction within the electrode material. Transition metal oxides (eg, RuO_2, MnO_2, NiO, Co_2O_3, etc.) and conducting polymers (eg, Polyaniline, poly-pyrrole, etc.) follow this mechanism.[7-14]

Among the metal oxides, ABO_3-type perovskite materials have gained ample research interest because of their excellent electronic structure, outstanding thermal stability, and exceptional ionic conductivity. Because of high electron-ion double conductivities and structural stability at elevated temperatures, metal oxide perovskite materials are the automatic choice as electrode materials in solid oxide fuel cells.[15-17] High ionic and electronic conductivity enable them to be efficient electrode materials for supercapacitors. ABO_3-type perovskites also possess the ability of rapid faradaic redox reaction at their surface, which enables them to be potential candidates for supercapacitor electrodes.[18,19] Moreover, ABO_3-type perovskites with lanthanide or alkaline-earth elements as A and transition metals as B atom have intrinsic oxygen vacancies, which enable them to act as electrode material for supercapacitors via faradic redox reaction. Pseudocapacitive charge storage mechanism involves mainly three processes: (a) adsorption of electrolyte ions to form a monolayer over metal or metal oxide surface, known as underpotential deposition, (b) fast reversible redox reaction at the electrode surface, and (c) fast intercalation/deintercalation of electrolyte ions into bulk electrode.[20] $LaMnO_{3+\delta}$ is a popular metal oxide of perovskite structure, which can form with substoichiometric as well as superstoichiometric oxygen content, that is, . $-0.25 \leq \delta \geq 0.25$.[21-23] Moreover, it is well-known that a partial replacement of A site in $LaMnO_3$ with Sr^{2+} or Ca^{2+} (lower valance cation) generates holes in B site. To maintain the charge neutrality, Mn^{3+} ions of $LaMnO_3$ lattice oxidize to form Mn^{4+} ions. This oxidization enhances the electrical conductivity as well as ion diffusion rate, which in turn enhances the overall electrochemical performance of the material. $LaMnO_3$ is the most commonly used perovskite electrode material for supercapacitors. It has been observed that substituting at A site (position of La) as well as B sites (position of Mn) with suitable element enhances the electrochemical performance of $LaMnO_3$. As has been reported by Wang et al, the specific capacitance of $LaMnO_3$ increases from 187 to 198 F g^{-1} on Sr doping. At the same time, the cyclic stability of the supercapacitors made of $LaMnO_3$ increases from 40% to 80% after 1000 cycles.[24] Cao et al have also seen an enhancement of specific capacitance of $LaMnO_3$-based supercapacitors from 100 to 464.5 F g^{-1} by incorporating Sr and Cu at A and B sites, respectively.[16] However, both the above mentioned works as well as most of the previously reported works have utilized either toxic nonaqueous electrolyte or aqueous alkaline electrolytes (NaOH or KOH) of high concentrations. Replacement of these electrolytes with neutral and commonly available aqueous electrolytes such as Na_2SO_4 solution will improve the potential window as the hydrogen or oxygen evolution potential will shift toward higher potential due to the low concentration of H^+ and OH^- ions in the solution.[25] Neutral aqueous electrolytes are less corrosive compared to high concentration acidic or basic electrolytes, providing relatively long life for the supercapacitors.[26] Aqueous Na_2SO_4 electrolyte provides high power and wide operational temperature over nonaqueous electrolytes and wide potential window over KOH electrolyte.[27-30] Moreover, the Na_2SO_4 electrolyte provides better ionic conductivity and low viscosity compared to the ionic liquid electrolytes.[30] The natural abundance and low cost of Na_2SO_4 may act as an advantagious feature for the commercialization of the supercapacitor.

In the present work, we synthesized $La_{0.7}Sr_{0.3}MnO_3$ nanoparticles along with $LaMnO_3$ and $SrMnO_3$ via ball-milling and analyzed their structural and electrochemical properties in an aqueous 1 M Na_2SO_4 electrolyte. The potential of the nanoparticles as supercapacitor electrode material has been studied by fabricating asymmetric supercapacitors (ASC), which provided a wide potential window with high specific capacitance and capacitive retention.

2 | EXPERIMENTAL SECTION

2.1 | Chemicals

Precursors and reactants such as manganese nitrate tetrahydrate ($Mn[NO_3]_2{\cdot}4H_2O$, >97.0%), lanthanum nitrate hexahydrate ($La[NO_3]_3{\cdot}6H_2O$, 99.99%), strontium nitrate ($Sr[NO_3]_2$, 99 + %), and acetylacetone ($C_5H_8O_2$,

>99.5%) were acquired from Sigma-Aldrich, Mexico. Sodium hydroxide (NaOH, 98.15%) and sodium chloride (NaCl, >99%) were purchased from J.T. Baker, and Omnicom, Mexico, respectively. Deionized (DI) water from a Millipore system (ρ >18.2 M Ω cm) was utilized for washing (samples and glasswares) purpose.

2.2 | Synthesis

Metal acetylacetonate complexes ($Mn(acac)_2$, $La(acac)_3$ and $Sr(acac)_2$) were initially synthesized through co-precipitation method.[31] For the synthesis of $Mn(acac)_2$, sodium acetylacetonate solution (solution 1), which was used as a precipitating agent, was prepared by drop-wise addition of 15 mL acetylacetone to 60 mL NaOH solution (8.7 mM) at 50°C under magnetic stirring. A precursor solution (solution 2) of Mn was then prepared separately by dissolving 48.49 mM of manganese nitrate tetrahydrate in 50 mL of DI water. After that, the hot sodium acetylacetonate solution (solution 1) was slowly added to the Mn precursor solution (solution 2) and kept at 50°C for 30 minutes under magnetic stirring. After cooling, the pale-yellow precipitate of manganese acetylacetonate ($Mn(acac)_2$) was separated by vacuum filtering in a Büchner funnel, washed four times with DI water, and vacuum dried for 12 hours. The same procedure was followed to synthesize the $La(acac)_3$ and $Sr(acac)_2$ precursors. Colors of the latter two precursors were white and pearl-white, respectively.

$La_{1-x}Sr_xMnO_3$ nanoparticles were then prepared by ball-milling-assisted solid-state reaction of the metal acetylacetonate precursors in presence of sodium chloride, which acted as a dispersing agent. For the synthesis of $La_{0.7}Sr_{0.3}MnO_3$, 0.5783 g of $Mn(acac)_2$, 0.6863 g of $La(acac)_3$, and 0.1823 g of $Sr(acac)_2$ were mixed with 7.234 g of NaCl. Then, the mixture was placed inside a 100 mL agate milling jar filled with 32 agate grinding balls (10 mm diameter) and placed in a planetary ball-milling (PQ-N2 Gear Drive 4) station. The milling was performed at 200 rpm for 24 hours. The obtained fine powder was then transferred to an alumina crucible and air-annealed inside a tubular (Carbolite) furnace at 700°C (increased at 5°C/min rate) for 8 hours. To remove NaCl, the obtained product was washed repeatedly with warm (70°C) DI water. Finally, the sample was collected by centrifugation and dried at 70°C for 5 hours. To induce crystallization in the formed nanostructures, the powder sample was further air-annealed at 850°C (at 5°C/min heating rate) for 12 hours. The same procedure was followed for the fabrication of $SrMnO_3$ and $LaMnO_3$ nanostructures.

2.3 | Characterization

To analyze the crystallinity and phase structure of the synthesized nanostructures, powder X-ray diffraction (XRD) was performed using a Bruker D8 diffractometer, utilizing CuKα (λ = 1.5406 Å) radiation. The spectra were recorded at 0.02°/step with a scan rate of 0.2 second/step in 20 to 80° span. Chemical composition and morphology of the nanostructures were analyzed in a JEOL JSM-7800F field-emission scanning electron microscope (FE-SEM) attached with an Oxford analytical system.

2.4 | Electrode fabrication

To fabricate electrodes, a gel was first prepared by mixing the sample material ($La_{1-x}Sr_xMnO_3$, $SrMnO_3$, and $LaMnO_3$), activated carbon, and polyvinylidene fluoride (PVDF) (mass ratio 85:10:5) in *N*-methyl-2-pyrrolidine (NMP) under ultrasonic agitation. The working electrodes were then prepared by drop-casting the active material gel on Teflon-coated carbon rods and then dried overnight at 60°C under vacuum.

2.5 | Device fabrication

The ASCs were fabricated by coating the aforesaid gel on one side of a stainless steel current collector (3 cm × 4 cm) which served as a positive electrode and a gel of activated carbon on one side of another stainless steel current collector which served as a negative electrode. These two electrodes were assembled along with a separator (Whatman filter paper, pore diameter 25 μm). The filter paper was soaked with 1 M Na_2SO_4 electrolyte solution. The masses of the active materials were selected by charge balancing theory ($Q_+ = Q_-$). According to this theory, the mass ratio of two electrodes should be:

$$\frac{m_+}{m_-} = \frac{C_- \times \Delta V_-}{C_+ \times \Delta V_+} \quad (1)$$

where, m, C, and ΔV refers to the masses, specific capacitance (F g^{-1}), and the potential window (V) of respective electrode materials.[32,33]

2.6 | Electrochemical measurements

A conventional three-electrode set up was utilized to study the electrochemical performance of the electrode materials with Ag/AgCl (saturated KCl) and Pt plate (1 cm × 1 cm) as the reference electrode and counter

electrode, respectively, and 1 M Na_2SO_4 aqueous solution as the electrolyte. An electrochemical analyzer (CS313, CorrTest, China) was used to measure the cyclic voltammetry (CV), galvanostatic charge–discharge (GCD), and electrochemical impedance spectroscopy (EIS). The values of specific capacitance were calculated from CV curves using Equation (2):

$$C_s = \frac{1}{2mv(V_f - V_i)} \int_{V_i}^{V_f} I(V)dV \quad (2)$$

where C_s is the capacitance per unit mass ($F\,g^{-1}$), $\int_{V_i}^{V_f} I(V)dV$ refers total area enclosed by the CV curve, m refers to the mass of the active electrode (g), v is the potential scan rate ($V\,s^{-1}$), and $(V_f - V_i)$ is the working window (V).[33-35] GCD curves were also used to compute the same, using the Equation (3):

$$C_s = \frac{I}{m \times \frac{dV}{dt}} \quad (3)$$

where I/m refers to the discharge current density ($A\,g^{-1}$) and $\frac{dV}{dt}$ refers to the average slope of the discharge curve.

All three electrochemical measurements, that is, CV, GCD, and EIS were also performed on the fabricated ASC devices. Specific energy and specific power of the devices were estimated from the GCD data. Energy density (E) ($Wh\,kg^{-1}$) and power density (P) ($W\,kg^{-1}$) of the ASC devices were obtained using the equations:

$$E = \frac{1}{2}\left[\frac{C_s(V_f - V_i)^2}{3.6}\right] \quad (4)$$

and

$$P = \frac{3600 \times E}{\Delta t} \quad (5)$$

where Δt is the discharge time.[36]

3 | RESULTS AND DISCUSSION

X-ray diffraction (XRD) patterns of the nanoparticles were recorded to study their structure, phase, and phase purity (Figure 1). As can be noticed in Figure 1A, diffraction peaks of the as-prepared $SrMnO_3$ and $LaMnO_3$ nanoparticles correspond fully to their hexagonal (JCPDF #04-015-4143) and rhombohedral (JCPDF #04-012-5560) phase, respectively. No peak associated with impurity or undesired phase was observed. All the diffraction peaks of the $La_{0.7}Sr_{0.3}MnO_3$ sample also corresponded to its rhombohedral (JCPDF #00-056-0616) phase. XRD study confirms that all the three compounds have ABO_3-type perovskite structures. With the incorporation of Sr^{2+} in $LaMnO_3$, the intensity of the diffraction peaks decreased, probably due to the partial replacement of La^{3+} ions of

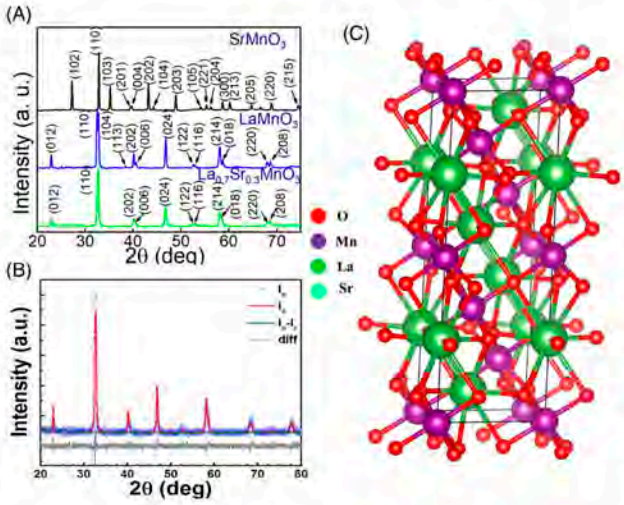

FIGURE 1 A, The XRD curves of $SrMnO_3$, $LaMnO_3$, and $La_{0.7}Sr_{0.3}MnO_3$; B, typical Rietveld analysis output profiles of $La_{0.7}Sr_{0.3}MnO_3$ nanostructures; and C, schematic atomic model of $La_{0.7}Sr_{0.3}MnO_3$ [Colour figure can be viewed at wileyonlinelibrary.com]

A-sites by Sr^{2+} ions. Microstructural properties of the $La_{0.7}Sr_{0.3}MnO_3$ nanostructures were further investigated through Rietveld refinement, using GSAS-II (version 4379) data analysis software.[37] The experimental and refined XRD data of $La_{0.7}Sr_{0.3}MnO_3$ are shown in Figure 1B. Rietveld refinement also confirms the rhombohedral structure of $La_{0.7}Sr_{0.3}MnO_3$ with R-3c:H space group symmetry and lattice parameters $a = b = 5.51$ Å and $c = 13.37$ Å. Marquardt least-square technique was used to minimize the difference between experimental and refined diffraction pattern. Microstrain and lattice parameters of the crystallites were calculated using the Pseudo-Voigt (PV) function. The quality of refinement and reliability of the extracted parameters were guaranteed by measuring the goodness of fitting (GoF), which is the ratio of weighted residual error (R_{wp}) and expected error (R_{ex}). The goodness of fitting (GoF) value was 1.06, which is close to unity and implies a good fitting of the data. The refined output was used to construct the unit cell, using VESTA software package, as shown in Figure 1C. Typical FE-SEM micrographs of the $LaMnO_3$, $SrMnO_3$, and $La_{0.7}Sr_{0.3}MnO_3$ nanoparticles are presented in Figure 2A-C. As can be seen, the $SrMnO_3$ sample consists of quasi-spherical particles of 110 to 500 nm (ca. 256 ± 87 nm) sizes, and the $LaMnO_3$ sample contains agglomerated quasi-spherical particles of 35 to 180 nm sizes (ca. 89.6 ± 26 nm). Incorporation of Sr^{2+} ions in $LaMnO_3$ through partial substitution of La^{3+} ions at A-sites causes an increment of particle size as observed in the sample $La_{0.7}Sr_{0.3}MnO_3$ (ca. particle size 128.7 ± 39 nm). Incorporation of Sr^{2+} ions causes a reduction in the dispersion of $LaMnO_3$ particles, causing the formation of an interconnected network due to their partial fusion during high-temperature annealing. Such

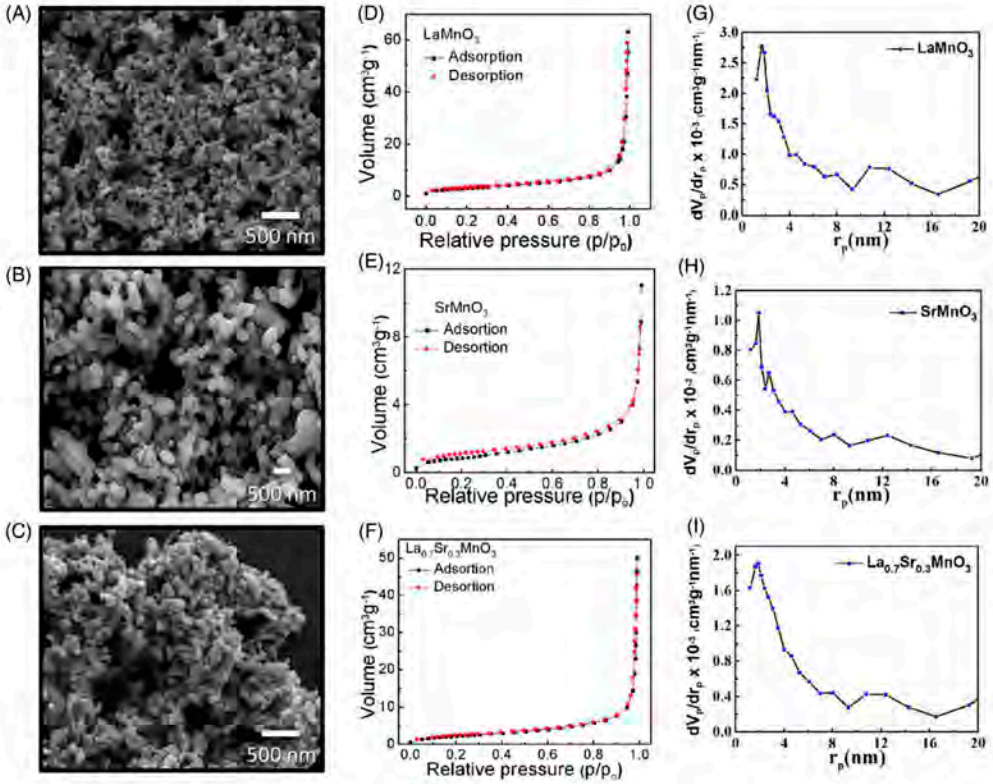

FIGURE 2 FE-SEM images (left column) A-C, N_2 adsorption–desorption isotherms (middle column) D-F, and pore size distributions (right column) G-I, in the synthesized $LaMnO_3$, $La_{0.7}Sr_{0.3}MnO_3$, and $SrMnO_3$ nanostructures [Colour figure can be viewed at wileyonlinelibrary.com]

interconnected nanostructures are useful for energy storage applications since they provide a larger accessible interlinked surface to the electrolyte ions.[38]

Nitrogen adsorption–desorption isotherms of the $LaMnO_3$, $SrMnO_3$, and $La_{0.7}Sr_{0.3}MnO_3$ samples recorded at 77 K are shown in Figure 2D-F. All the isotherms revealed type III characteristics, with H1-type hysteresis loop. These type III materials are found to have relatively week adsorption–desorption interaction with nitrogen and are not very common. The H1 loops indicate well-defined cylindrical pore channels in the nanostructures which are useful for electrolyte ion transport.[39,40] Brunauer-Emmett-Teller (BET) analysis was used to estimate the specific surface area of the three materials. The specific surface area of $SrMnO_3$, $LaMnO_3$, and $La_{0.7}Sr_{0.3}MnO_3$ samples were 7.8, 10.7, and 7.9 $m^2\ g^{-1}$, respectively. BJH pore size distribution graphs of the nanostructures are presented in Figure 2G-I. Estimated average pore diameters in the $LaMnO_3$, $SrMnO_3$, and $La_{0.7}Sr_{0.3}MnO_3$ samples were 20.1, 32.9, and 37.8 nm, respectively. Even though the BET surface area of the $La_{0.7}Sr_{0.3}MnO_3$ nanoparticles is relatively low, larger pores in them probably allow a large number of electrolyte ions to interact with the electrochemically active sites, resulting in a rapid redox reaction. In our previous manuscript, we have already demonstrated the TEM, EDS, XPS, and Raman spectroscopy results.[41] EDS of $La_{0.7}Sr_{0.3}MnO_3$ shows the atomic % of La, Sr, Mn, O, and Na are 13.22%, 4.90%, 16.24%, 65.24%, and 0.41%, respectively. The existence of Na is also observed from the XPS measurement as well. The survey scan of the XPS spectra reveals that there is no trace of chlorine as there is no peaks at 199 and 201 eV binding energies which are designated for Cl $2p_{3/2}$ and Cl $2p_{1/3}$, respectively. All the chlorine ions are removed because of the annealing at 900°C. Thus, we can conclude that there is no role of Cl^- ions in the electrochemical process. High-resolution XPS study of $La_{0.7}Sr_{0.3}MnO_3$ shows the presence of La $3d_{5/2}$ and $3d_{3/2}$ at binding energies (BE) 850.29 and 833.54 eV, respectively. High-resolution XPS study of Mn 2p confirms the presence of both Mn^{3+} and Mn^{4+} states. However, these peaks shift toward higher BEs upon the substitution of Ls^{3+} ions by Sr^{2+} ions. Existence of multiple cationic states of Mn is useful for the rapid redox reaction.

The CV study of the electrodes made of $SrMnO_3$, $LaMnO_3$, and $La_{0.7}Sr_{0.3}MnO_3$ nanoparticles was performed in 1 M Na_2SO_4 aqueous electrolyte within a potential window −0.2 to 1.0 V (vs Ag/AgCl) at different scan rates ranging from 2 to 100 mV s^{-1}. Figure 3A presents a comparison of CV data of $SrMnO_3$, $LaMnO_3$, and $La_{0.7}Sr_{0.3}MnO_3$ nanostructures at a fixed scan rate of 10 mV s^{-1}. Areas under these CV curves are directly proportional to the charge storage capacity of the materials. As can be noticed, the area under the CV curve of $La_{0.7}Sr_{0.3}MnO_3$ is larger than the same of other two samples for the same scan rate, which directly implies that $La_{0.7}Sr_{0.3}MnO_3$ possesses better charge storage capacity among the three samples. The CV curves of $La_{0.7}Sr_{0.3}MnO_3$ recorded at different scan rates are shown in Figure 3B (CV curves of other materials are presented as Figure S1A, B in supplementary information). As can be noticed in Figure 3A, the shape of the CV curve corresponds to $SrMnO_3$ is almost rectangular. But, the CV curve of $LaMnO_3$ shows a deviation from the rectangular shape which indicates the pseudocapacitive mechanism dominates in charge storage. The highest specific capacitance obtained for $La_{0.7}Sr_{0.3}MnO_3$ is 393.5 F g^{-1}, which is higher than the specific capacitance corresponds to $SrMnO_3$ (54.2 F g^{-1}) and $LaMnO_3$ electrodes (268.8 F g^{-1}). The variations of specific capacitance with scan rate for all three materials are presented in Figure 3C. At lower scan rates, the electrolyte ions get sufficient time to interact with the electrochemically

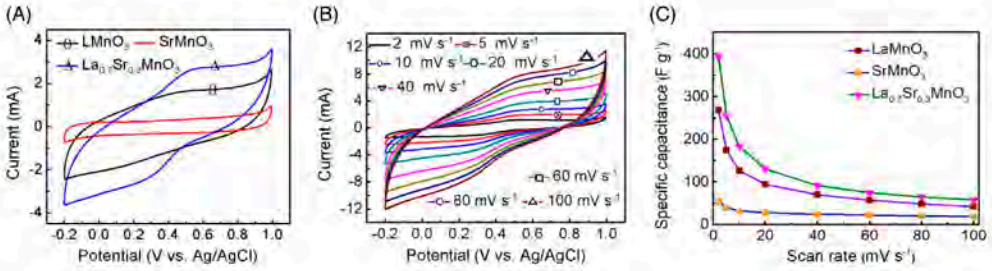

FIGURE 3 A, CV curve of $LaMnO_3$, $SrMnO_3$, and $La_{0.7}Sr_{0.3}MnO_3$ electrode at fixed scan rate 10 mV s^{-1}. B, CV curves at all scan rates for $La_{0.7}Sr_{0.3}MnO_3$ electrode. C, Specific capacitance vs scan rates for all three samples [Colour figure can be viewed at wileyonlinelibrary.com]

active sites, resulting in greater specific capacitance. At higher scan rates, the electrolyte ions get lesser interaction time which effectively decreases the specific capacitance. In the CV curves of $La_{0.7}Sr_{0.3}MnO_3$, there is a redox peak around 0.55 V (vs Ag/AgCl), which corresponds to the transition $Mn^{3+} \leftrightarrow Mn^{4+}$.[16] The charge imbalance developed in $LaMnO_3$ lattice due to the substitution of La^{3+} ions by Sr^{2+} ions is compensated either by oxidizing the Mn^{3+} ions to Mn^{4+} or by introducing oxygen vacancies. In both alkaline and neutral electrolytes, intercalation of ions with active sites plays the main role in charge storage. The redox reaction occurs in the present case can be expressed as[19]:

$$La_{0.7}Sr_{0.3}\left[Mn^{3+}_{2\delta}/Mn^{4+}_{2\delta}\right]O_{3-\delta} + 2\delta e^- + \delta H_2O \leftrightarrow La_{0.7}Sr_{0.3}\left[Mn^{3+}_{2\delta}/Mn^{4+}_{(1-2\delta)}\right]O_{3-\delta} + 2\delta OH^- \quad (6)$$

Therefore, more oxygen vacancies are formed in the lattice, there would be more room for OH^- ions to fill. This results in greater charge storage. Thus, it is confirmed that the pseudocapacitive mechanism plays the main role in charge storage. The charging and discharging curves are symmetric to each other, which reflect excellent redox reversibility and outstanding supercapacitive behavior of $La_{0.7}Sr_{0.3}MnO_3$ electrode. The underlying charge storage mechanisms of $La_{0.7}Sr_{0.3}MnO_3$ can be estimated using the power law. According to this law, the anodic peak current (I_p) increases with scan rates (v). This law can be expressed as $I_p = av^b$, where, both a and b are adjustable parameters, and the role of b is important to determine the storage mechanism.[38,42,43] $b = 0.5$ implies that the storage mechanism is controlled via faradic redox reaction, whereas $b = 1$ indicates that the charge storage occurs via

Double-layer formation. The slope of log I_p vs log v plot (Figure 4A) corresponds to the value of b. For $La_{0.7}Sr_{0.3}MnO_3$, the value of b is 0.48, which indicates the charge storage in the sample is dominated by the redox process. This result indicates that the peak current varies linearly with the square roots of scan rate in agreement with the graph obtained from the experimental data (Figure 4B). Thus, the faradaic redox process plays dominating role in charge storage. The charge storage mechanisms can be quantitatively evaluated by the method suggested by Dunn.[43] According to this method, the current at any particular potential is the sum of the contribution from the capacitive part ($\propto v$) as well as the contribution of the faradic reaction ($\propto v^{1/2}$). This can be expressed by Equation (7).

$$i(V) = k_1 v + k_2 v^{1/2} \quad (7)$$

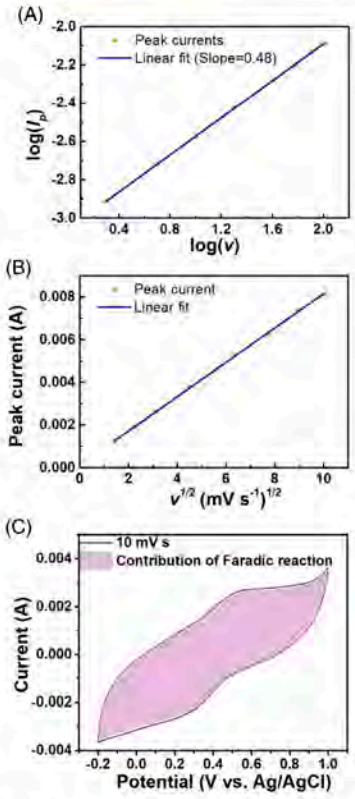

FIGURE 4 A, Plots for power law method; B, variation of peak current with the square root of scan rates; and C, CV curve of $La_{0.7}Sr_{0.3}MnO_3$ at a scan rate of 10 mV s^{-1} showing the redox contribution due to Dunn [Colour figure can be viewed at wileyonlinelibrary.com]

The CV curve of $La_{0.7}Sr_{0.3}MnO_3$ reveals that 97.5% of the total capacity is controlled by faradaic charge storage process (Figure 4C). This means that the charge storage of $La_{0.7}Sr_{0.3}MnO_3$ composite is fully controlled by the faradaic redox process rather than capacitive process.

The charge storage behavior of $La_{0.7}Sr_{0.3}MnO_3$ electrode can be further understood following the method introduced by Trasatti.[44] According to Trasatti, the total specific capacitance (C_{total}) is the sum of the specific capacitances of the inner part (C_{in}) and the outer part (C_{out}) of the electrode, that is, $C_{total} = C_{in} + C_{out}$.[44-46] The inner part comes from the bulk of the material which is

due to the redox reactions. On the other hand, C_{out} arises from the capacitive process. The total specific capacitance, that is, C_{total} can be obtained if we allow adequate time to interact the electrolyte ions with the electrode, which can be estimated from the C_{sp} vs $v^{1/2}$ curve upto $v \rightarrow 0$ (Figure 5A). The estimated C_{total} was 473.4 F g^{-1}, which is the highest possible specific capacitance $La_{0.7}Sr_{0.3}MnO_3$ can attain. Subsequently, C_{out} could be estimated by extrapolating the C_{sp} vs $v^{-1/2}$ curve upto $v^{-1/2} \rightarrow 0$, that is, the scan rate tends to very high value (Figure 5B). For the extrapolation of the curves, we used the low scan rate (2–20 mVs^{-1}) data only, since at higher scan rates, these curves deviate from linear behavior. The deviation arises from the ohmic drop and irreversible redox process. For $La_{0.7}Sr_{0.3}MnO_3$, the highest possible surface contribution to the specific capacitance was estimated to be approximately 11.7 F g^{-1}, while the rest, that is, 461.7 F g^{-1} is due to the redox controlled process. This study also agrees with the Dunn method which reveals that the redox process is the key player for charge storage.

Electrochemical performance of $La_{0.7}Sr_{0.3}MnO_3$ could be further investigated by performing GCD at different current densities between 1 and 10 A g^{-1}, within the same potential range (−0.2-1 V) in 1 M Na_2SO_4 electrolyte. Figure 6A presents the comparative GCD plots of all three samples at a particular current density of 1 A g^{-1}. As can be noticed, for a particular current density, the $La_{0.7}Sr_{0.3}MnO_3$ electrode takes longer time for charging and discharging, which ensures a higher charge capacity of the electrode. On the other hand, the discharge curves of $LaMnO_3$ and $La_{0.7}Sr_{0.3}MnO_3$ are deviated from linearity, indicating the contribution of redox-dominated storage process in these electrodes. This observation is also in full agreement with that obtained from CV data. The GCD plots of $La_{0.7}Sr_{0.3}MnO_3$ at different current densities are shown in Figure 6B. The highest specific capacitance offered by $La_{0.7}Sr_{0.3}MnO_3$ was 409.4 F g^{-1} at the lowest current density (1 A g^{-1}), which decreases for higher current densities. The material exhibits high rate capability due to its excellent charge reversibility. On the other hand, the highest specific capacitance values offered by $LaMnO_3$ and $SrMnO_3$ at the lowest current density (1 A g^{-1}) were 256.6 and 45.7 F g^{-1}, respectively (GCD plots of these two materials are shown in Figure S2A, B of the supplementary information).

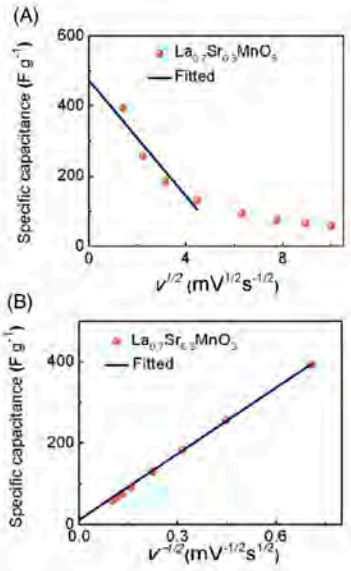

FIGURE 5 A, Plot of specific capacitance vs $v^{1/2}$ and B, variation of specific capacitance vs $v^{-1/2}$ for $La_{0.7}Sr_{0.3}MnO_3$ [Colour figure can be viewed at wileyonlinelibrary.com]

Performances of the electrode materials have also been investigated by EIS, which is a nondestructive process, providing important kinetic information about the electrode materials. The data have been recorded in the 0.01 Hz-100 kHz frequency range, applying a small perturbation voltage of 10 mV. The EIS results of the samples are presented in Figure 6C in the form of Nyquist plots. In the high-frequency region, a small semi-circular loop appeared at the beginning of the curve (inset of Figure 6C). This semi-circular loop arises due to small series resistance (R_s) and a parallel combination of charge transfer resistance (R_{ct}) and constant phase element (CPE). From the EIS curves, it is clear that the $La_{0.7}Sr_{0.3}MnO_3$ sample has relatively low Z' and Z'' compared to other two samples. The EIS plot of $La_{0.7}Sr_{0.3}MnO_3$ was fitted with Z-view software and presented in Figure 6D. Corresponding equivalent circuit is represented as an inset of Figure 6D. The Bode magnitude plot (|Z| vs log f) of $La_{0.7}Sr_{0.3}MnO_3$ (not shown) was used to calculate the contribution of specific capacitance due to double-layer formation by using $|Z| = 1/C_{dl}$ (at $\omega = 1$) relation.[47] The C_{dl} value obtained from the plot was 37.24 F g^{-1}, which agrees well with the value predicted from Trasatti plot. We could calculate the low-frequency specific capacitance of the electrode material ($La_{0.7}Sr_{0.3}MnO_3$) using the relation $C_{sp} = \frac{1}{(2\pi f Z_{im})}$, where Z_{im} refers to the imaginary impedance at lowest frequency.[47,48] The estimated C_{sp} value was 298.67 F g^{-1}, which is lower than the values estimated from CV or GCD analysis of the sample. High electrolyte ion density and high ion transfer resistance of the solution result in

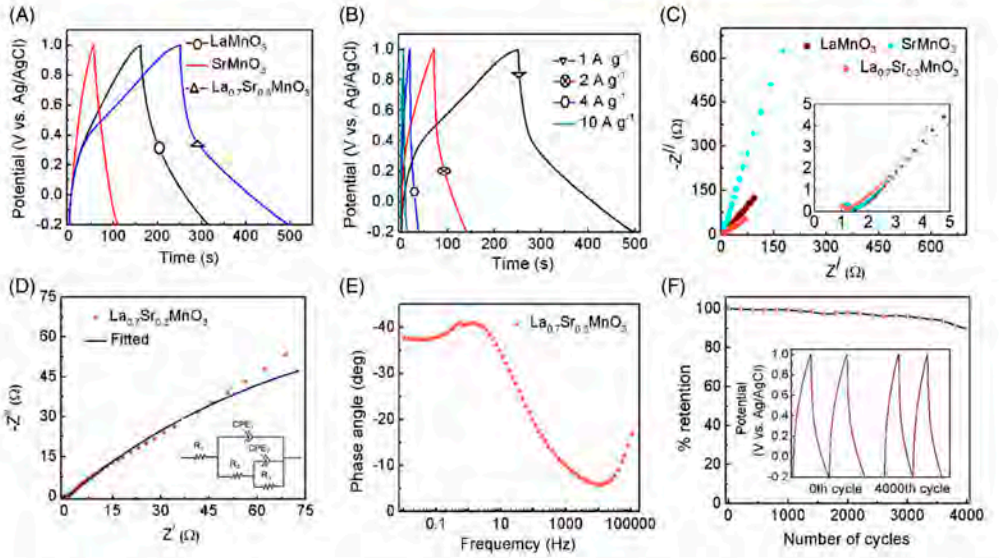

FIGURE 6 A, GCD curves of $LaMnO_3$, $SrMnO_3$, and $La_{0.7}Sr_{0.3}MnO_3$ at current density 1 A g^{-1}; B, GCD curves of $La_{0.7}Sr_{0.3}MnO_3$ at different current densities; C, Nyquist plots of all three samples in 1 M Na_2SO_4 electrolyte (*inset*) in high-frequency region; D, EIS plot of $La_{0.7}Sr_{0.3}MnO_3$ along with fitted curve and (*inset*) equivalent circuit; E, Bode phase plot for $La_{0.7}Sr_{0.3}MnO_3$ sample; and F, cyclic stability study of $La_{0.7}Sr_{0.3}MnO_3$ sample, (*inset*) GCD curves during 1st and 4000th cycle [Colour figure can be viewed at wileyonlinelibrary.com]

the decrease of specific capacitance.[48] From the Bode phase plot of $La_{0.7}Sr_{0.3}MnO_3$ presented in Figure 6E, it is possible to predict the charge storage mechanism in the device. For EDLC-type materials, the phase angle at low frequency, that is, 0.01 Hz, reaches to 90°, whereas, for pseudocapacitive materials the phase angle is 37.7°, which is much less than 90°. The low phase angle of $La_{0.7}Sr_{0.3}MnO_3$ indicates the pseudocapacitance mechanism is predominant in the charge storage process of the electrode.

Cyclic stability of the electrode material was studied by recording the GCD cycles of the working electrode over 4000 cycles at a fixed current density of 10 A g^{-1}. As can be seen in the retention vs cycle number plots presented in Figure 6F, the material retains about 89.6% of specific capacitance even after 4000 charge–discharge cycles. The nature of charge–discharge cycle remained almost same after 4000 GCD cycles, although there is a slight decrease in charging and discharging time. The 1st and 4000th GCD cycles are shown in the inset of the Figure. The material retains a Coulombic efficiency of 86% after 4000 charge–discharge cycles. This excellent long-term stability of the material along with excellent Coulombic efficiency demonstrates the nanostructured $La_{0.7}Sr_{0.3}MnO_3$ is an efficient electrode material for supercapacitors. To further explore the supercapacitive performance of the $La_{0.7}Sr_{0.3}MnO_3$ sample, a prototype ASC device was fabricated (schematic diagram and prototype ASC are shown in Figure 7A). Electrochemical performances of the device were tested by studying all three conventional electrochemical techniques, that is, CV, GCD, and EIS. The CV traces were recorded in a large potential window of 1.8 V (0-1.8 V). The CV plots of $La_{0.7}Sr_{0.3}MnO_3$//AC ASC at various scan rates are presented in Figure 7B. The ASC exhibited undistorted CV curves even at elevated scan rates, which suggests an excellent reversibility. There was no indication of gas evolution from the electrode. The ASC exhibited a maximum specific capacitance of 192.6 F g^{-1} at the lowest scan rate of 2 mV s^{-1}. GCD study of the ASC was also been performed for current densities between 1 and 10 A g^{-1} (Figure 7C). The specific capacitance decreased from 197 to 125.6 F g^{-1} with the increase of current density from 1 to 10 A g^{-1}, which suggests an outstanding rate capability of the $La_{0.7}Sr_{0.3}MnO_3$//AC ASC. At the same time, the Coulombic efficiency increased from 85.15% to 90.4%, indicating a rapid intercalation/deintercalation of

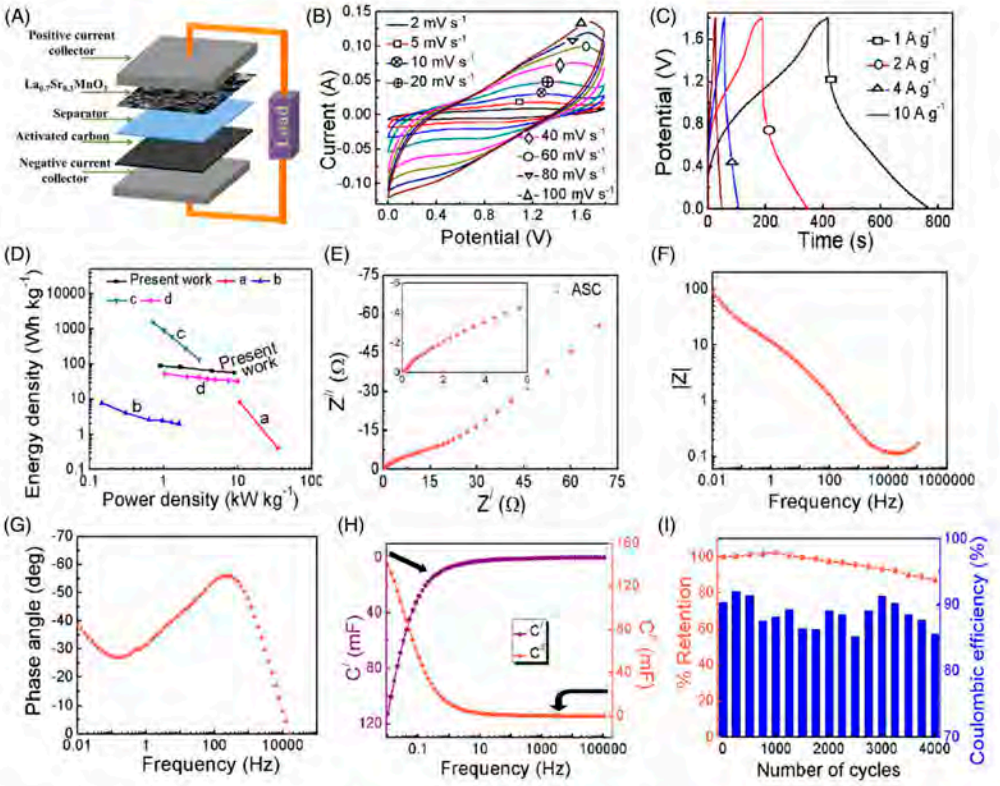

FIGURE 7 A, Schematic of prototype of $La_{0.7}Sr_{0.3}MnO_3$//AC ASC; B, CV plots of ASC at different scan rates; C, GCD plots at different current densities within the same window; D, Ragone plot [a-,[52] b-,[15] c-,[53] d-[54]]; E, Nyquist plot of impedance, (*inset*) high-frequency region; F, Bode magnitude plots; G, Bode phase plots; H, real and imaginary component of capacitance vs frequency plot; and I, long term stability plot for 4000 cycles, (*inset*) Coulombic efficiency plots for 4000 cycles [Colour figure can be viewed at wileyonlinelibrary.com]

TABLE 1 Various parameters of $La_{0.7}Sr_{0.3}MnO_3$//AC ASC

Current density (A g^{-1})	Charge time (s)	Discharge time (s)	Specific capacitance (F g^{-1})	Coulombic efficiency (%)	Specific energy (Wh kg^{-1})	Specific power (kW kg^{-1})
1	416.4	354.6	197	85.2	88.7	0.9
2	189.6	162.8	180.9	85.9	81.2	1.7
4	57.6	50.8	141.1	88.2	63.5	4.5
10	25.0	22.6	125.6	90.4	56.5	9.0

electrolyte ions into the electrochemically active sites. The $La_{0.7}Sr_{0.3}MnO_3$//AC ASC exhibited a highest specific energy of 88.7 Wh kg^{-1} at a power density of 0.9 kW kg^{-1} and 56.5 Wh kg^{-1} at a higher power density of 9 kW kg^{-1} (Table 1). The Ragone plot of the $La_{0.7}Sr_{0.3}MnO_3$//AC ASC along with some other reported results is shown in Figure 7D. As can be seen, the $La_{0.7}Sr_{0.3}MnO_3$//AC ASC has moderate energy and power densities. The energy

efficiency of the ASC has also been calculated using the relation[49]:

$$\text{Energy efficiency}\,(\%) = \frac{\text{energy density}_{(\text{discharge})}}{\text{energy density}_{(\text{charge})}} \times 100(\%) \quad (8)$$

The energy efficiency of the supercapacitor was approximately 90% at current density 10 A g^{-1}, and it reduces to 85% for a current density of 1 A g^{-1}.

The Nyquist plot of the ASC is shown in Figure 7E. From the high-frequency region (inset of Figure 7E), it is clear that there is almost zero or negligible series resistance and relatively low charge transfer resistance (~7 Ω). At the low-frequency region, the curve is inclined to the *x*-axis with an angle of approximately 45°, which suggests the presence of diffusion-controlled Warburg element. The EIS data were further utilized to characterize the device. Typical Bode magnetic and Bode phase plots of $La_{0.7}Sr_{0.3}MnO_3$//AC ASC are shown in Figure 7F, G. At a lower frequency such as 0.01 Hz, the phase angle reached to −38.3°, clearly suggesting the pseudocapacitive nature of the device. On the other hand, the figure of merit of a supercapacitor can be estimated from its relaxation time. The relaxation time was calculated using the equivalence $\tau_0 = \frac{1}{2\pi f_0}$, where, f_0 is the frequency at the phase angle −45° (where the contribution of capacitive and resistive impedance are identical).[50] The time constant obtained from the Bode phase plot was 8.7 ms. This small value of the time constant facilitates quick ion transport during the electrochemical process.

The variation of real (C') and imaginary (C'') components of the $La_{0.7}Sr_{0.3}MnO_3$//AC ASC device with frequency was estimated and shown in Figure 7H. The real part of capacitance depends on the nature of electrolyte, porosity, and the active mass of electrode material. However, the imaginary component is directly related to energy dissipation.[51] From the curves, it is clear that the resistive behavior of $La_{0.7}Sr_{0.3}MnO_3$ at the high-frequency region changes to capacitive at lower frequencies due to ion migration. The long-term stability of the $La_{0.7}Sr_{0.3}MnO_3$//AC ASC was further investigated by performing 4000 GCD cycles at a fixed current density of 10 A g^{-1} (Figure 7i). As can be noticed, about 87.2% of the specific capacitance retained even after 4000 GCD cycles, suggesting excellent stability of the device. The Coulombic efficiency of the $La_{0.7}Sr_{0.3}MnO_3$//AC ASC device was also measured over 4000 cycles, which varied in-between 90.4% and 85.6%. The results obtained in the present study suggest that nanostructured $La_{0.7}Sr_{0.3}MnO_3$ is an excellent electrode material for supercapacitor applications.

4 | CONCLUSIONS

In summary, we demonstrated the possibility of synthesizing strontium (Sr)-doped $LaMnO_3$ ($La_{0.7}Sr_{0.3}MnO_3$) perovskite nanostructures through ball-milling assisted solid-state reaction. XRD study confirmed the ABO_3-type rhombohedral structure of $La_{0.7}Sr_{0.3}MnO_3$. N_2 adsorption–desorption study confirmed the mesoporous texture of the nanostructures. Electrochemical performances of the $La_{0.7}Sr_{0.3}MnO_3$ nanostructures studied in neutral aqueous electrolyte (1 M Na_2SO_4) revealed a maximum specific capacitance of 393.5 F g^{-1}. Pseudocapacitive mechanism was seen to be responsible for charge storage in the material. Furthermore, the material has been utilized to fabricate asymmetric $La_{0.7}Sr_{0.3}MnO_3$//AC supercapacitors with the same neutral electrolyte. Asymmetric supercapacitors made of $La_{0.7}Sr_{0.3}MnO_3$ nanostructures as active electrode material operated within a potential window of 1.8 V and exhibited a highest specific capacitance of 197 F g^{-1}. Incorporation of Sr in $LaMnO_3$ nanostructures was seen to improve their electrochemical performance as well as their electrochemical stability. The results presented in this work clearly indicate that Sr-doped lanthanum magnetite perovskite nanostructures can be used as electrode material for fabricating supercapacitors with high energy density.

ACKNOWLEDGEMENTS

U.P. acknowledges CONACyT, Mexico for financial support (Grant # CB-A1-S-26720). S.D. is thankful to Jadavpur University for financial support through RUSA 2.0 (Ref No. R-11/281/19) research grant and Science and Engineering Research Board, Department of Science and Technology, Government of India for financial support through the "Core Research Grant" (File no #CRG/2019/001575). S.S. is thankful to CSIR, Govt. of India for financial support (File No.-09/096 (0898)/2017-EMR-I).

ORCID

Francisco Enrique Cancino-Gordillo https://orcid.org/0000-0001-8286-5734

Sachindranath Das https://orcid.org/0000-0002-6938-6701

REFERENCES

1. Chodankar NR, Dubal DP, Ji SH, Kim DH. Self-assembled nickel pyrophosphate-decorated amorphous bimetal hydroxides 2D-on-2D nanostructure for high-energy solid-state asymmetric supercapacitor. *Small*. 2019;15:1.
2. Dubal DP, Chodankar NR, Kim DH, Gomez-Romero P. Towards flexible solid-state supercapacitors for smart and wearable electronics. *Chem Soc Rev*. 2018;47:2065-2129.

3. Borenstein A, Hanna O, Attias R, Luski S, Brousse T, Aurbach D. Carbon-based composite materials for supercapacitor electrodes: a review. *J Mater Chem A*. 2017;5:12653-12672.
4. Tsai IL, Cao J, Le Fevre L, et al. Graphene-enhanced electrodes for scalable supercapacitors. *Electrochim Acta*. 2017;257:372-379.
5. Ramli NIT, Abdul Rashid S, Sulaiman Y, et al. Physicochemical and electrochemical properties of carbon nanotube/graphite nanofiber hybrid nanocomposites for supercapacitor. *Sources*. 2016;328:195-202.
6. Siddique AH, Butt R, Bokhari SW, Raj DV, Zhou X, Liu Z. All graphene electrode for high-performance asymmetric supercapacitor. *Int J Energy Res*. 2020;44:1244-1255.
7. Xia H, Shirley Meng Y, Yuan G, Cui C, Lu L. A symmetric RuO2/RuO2 supercapacitor operating at 1.6 V by using a neutral aqueous electrolyte. *Electrochem Solid St*. 2012;15:A60.
8. Iro ZS, Subramani C, Dash SS. A brief review on electrode materials for supercapacitor. *Int J Electrochem Sci*. 2016;11:10628.
9. Ray A, Roy A, Saha S, et al. Electrochemical energy storage properties of Ni-Mn-oxide electrodes for advance asymmetric supercapacitor application. *Langmuir*. 2019; acs.langmuir.9b00955.
10. Roy A, Ray A, Sadhukhan P, Saha S, Das S. Morphological behaviour, electronic bond formation and electrochemical performance study of V2O5-polyaniline composite and its application in asymmetric supercapacitor. *Mater Res Bull*. 2018;107:379-390.
11. Majumdar D, Maiyalagan T, Jiang Z. Recent Progress in ruthenium oxide-based composites for supercapacitor applications. *ChemElectroChem*. 2019;6:4343-4372.
12. Zhu H, Liu J, Zhang Q, Wei J. High electrochemical performance of metal azolate framework-derived ZnO/Co3O4 for supercapacitors. *Int J Energy Res*. 2020;44:8654-8665.
13. Chodankar NR, Rama Raju GS, Park B, et al. Potentiodynamic polarization assisted phosphorus-containing amorphous trimetal hydroxide nanofibers for highly efficient hybrid supercapacitors. *J Mater Chem A*. 2020;8:5721-5733.
14. Chodankar NR, Patil SJ, Rama Raju GS, et al. Two-dimensional materials for high-energy solid-state asymmetric pseudocapacitors with high mass loadings. *ChemSusChem*. 2020;13:1582-1592.
15. Mo H, Nan H, Lang X, et al. Influence of calcium doping on performance of $LaMnO_3$ supercapacitors. *Ceram Int*. 2018;44:9733-9741.
16. Cao Y, Lin B, Sun Y, Yang H, Zhang X. Synthesis, structure and electrochemical properties of lanthanum manganese nanofibers doped with Sr and Cu. *J Alloys Compd*. 2015;638:204-213.
17. Lu F, Xia T, Li Q, Wang J, Huo L, Zhao H. Heterostructured simple perovskite nanorod-decorated double perovskite cathode for solid oxide fuel cells: highly catalytic activity, stability and CO2-durability for oxygen reduction reaction. *Appl Catal Environ*. 2019;249:19-31.
18. Sharma AP, Pradhan DK, Xiao B, Pradhan SK, Bahoura M. Lead-free epitaxial ferroelectric heterostructures for energy storage applications. *AIP Adv*. 2018;8:125112.
19. Alexander CT, Mefford JT, Saunders J, Forslund RP, Johnston KP, Stevenson KJ. Anion-based pseudocapacitance of the perovskite library La1-xSrxBO3−δ(B = Fe, Mn, Co). *ACS Appl Mater Interfaces*. 2019;11:5084-5094.
20. Mefford JT, Hardin WG, Dai S, Johnston KP, Stevenson KJ. Anion charge storage through oxygen intercalation in LaMnO3 perovskite pseudocapacitor electrodes. *Nat Mater*. 2014;13:726-732.
21. Ruiz-Gonzalez L, Cortes-Gil R, Alonso JM, Gonzalez-Calbet JM, Vallet-Regi M. Revisiting the role of vacancies in manganese related perovskites. *Open Inorg Chem J*. 2007;1:37-46.
22. Laiho R, Lisunov KG, Lähderanta E, et al. Low-field magnetic properties of LaMnO3+δ with 0.065≤δ≤0.154. *J Phys Chem Solid*. 2003;64:2313-2319.
23. Cortés-Gil R, Arroyo A, Ruiz-González L, et al. Evolution of magnetic behaviour in oxygen deficient LaMnO3−δ. *J Phys Chem Solid*. 2006;67:579-582.
24. Wang XW, Zhu QQ, Wang XE, Zhang HC, Zhang JJ, Wang LF. Structural and electrochemical properties of La0.85Sr0.15MnO3 powder as an electrode material for supercapacitor. *J Alloys Compd*. 2016;675:195-200.
25. Zhong C, Deng Y, Hu W, Qiao J, Zhang L, Zhang J. A review of electrolyte materials and compositions for electrochemical supercapacitors. *Chem. Soc. Rev*. 2015;44:7484-7539.
26. Ramachandran R, Wang F. Electrochemical capacitor performance: Influence of Aqueous Electrolytes. *Supercapacitors - theoretical and practical solutions*. IntechOpen; 2016:51-68.
27. Wang G, Zhang L, Zhang J. A review of electrode materials for electrochemical supercapacitors. *Chem Soc Rev*. 2012;41:797-828.
28. Wang F, Xiao S, Hou Y, Hu C, Liu L, Wu Y. Electrode materials for aqueous asymmetric supercapacitors. *RSC Adv*. 2013;3:13059.
29. Liu Y, Dinh J, Tade MO, Shao Z. Design of perovskite oxides as anion-intercalation-type electrodes for supercapacitors: cation leaching effect. *ACS Appl Mater Interfaces*. 2016;8:23774-23783.
30. Guo J, Ma Y, Zhao K, et al. High-performance and ultra-stable aqueous supercapacitors based on a green and low-cost water-in-salt electrolyte. *ChemElectroChem*. 2019;6:5433-5438.
31. Nfoma EA. Structure and magnetic properties of lanthanum strontium ferrites nanopowders synthesized by thermal decomposition of mixed metal acetyl acetonates. *Int J Eng Res Technol*. 2015;4:907.
32. Ray A, Roy A, Ghosh M, et al. Study on charge storage mechanism in working electrodes fabricated by sol-gel derived spinel $NiMn_2O_4$ nanoparticles for supercapacitor application. *Appl Surf Sci*. 2019;463:513-525.
33. Ma Z, Shao G, Fan Y, Wang G, Song J, Shen D. Construction of hierarchical α-MnO2Nanowires@ultrathin δ-MnO2 nanosheets core-shell nanostructure with excellent cycling stability for high-Power asymmetric supercapacitor electrodes. *ACS Appl Mater Interfaces*. 2016;8:9050-9058.
34. Saha S, Maji P, Pethsangave DA, et al. Effect of morphological ordering on the electrochemical performance of MnO2-graphene oxide composite. *Electrochim Acta*. 2019;317:199-210.
35. Yang P, Qu X, Liu K, et al. Electrokinetic supercapacitor for simultaneous harvesting and storage of mechanical energy. *ACS Appl Mater Interfaces*. 2018;10:8010-8015.

36. Roy A, Ray A, Saha S, et al. NiO-CNT composite for high performance supercapacitor electrode and oxygen evolution reaction. *Electrochim Acta*. 2018;283:327-337.
37. Toby BH, Von Dreele RB. GSAS-II: the genesis of a modern open-source all purpose crystallography software package. *J Appl Cryst*. 2013;46:544-549.
38. Roy A, Ray A, Saha S, Das S. Investigation on energy storage and conversion properties of multifunctional PANI-MWCNT composite. *Int J Hydrogen Energy*. 2018;43:7128-7139.
39. Inagaki S, Fukushima Y, Kuruda K. Synthesis of highly ordered mesoporous materials from a layered polysilicate. *J Chem Soc Chem Commun*. 1993;680.
40. Das T, Uyama H, Nandi M. Pd-bound functionalized mesoporous silica as active catalyst for Suzuki coupling reaction: effect of OAc^-, PPh3 and Cl^- ligands on catalytic activity. *J Solid State Chem*. 2018;260:132-141.
41. Ortiz-Quiñonez JL, García-González L, Cancino-Gordillo FE, Pal U. Particle dispersion and lattice distortion induced magnetic behavior of $La_{1-x}Sr_xMnO_3$ perovskite nanoparticles grown by salt-assisted solid-state synthesis. *Mater Chem Phys*. 2020;246.
42. Conway BE. Transition from "Supercapacitor" to "Battery" behavior in electrochemical energy storage. *J Electrochem Soc*. 1991;138:1539-1548.
43. Augustyn V, Simon P, Dunn B. Pseudocapacitive oxide materials for high-rate electrochemical energy storage. *Energy Environ Sci*. 2014;7:1597.
44. Ardizzone S, Fregonara G, Trasatti S. "Inner" and "outer" active surface of RuO2 electrodes. *Electrochim Acta*. 1990;35:263-267.
45. Sankar KV, Selvan RK. The preparation of MnFe2O4 decorated flexible graphene wrapped with PANI and its electrochemical performances for hybrid supercapacitors. *RSC Adv*. 2014;4:17555.
46. Ray A, Roy A, Sadhukhan P, et al. Electrochemical properties of TiO2-V2O5 nanocomposites as a high performance supercapacitors electrode material. *Appl Surf Sci*. 2018;443:581-591.
47. Bai M-H, Liu T-Y, Luan F, Li Y, Liu X-X. Electrodeposition of vanadium oxide–polyaniline composite nanowire electrodes for high energy density supercapacitors. *J Mater Chem A*. 2014;2:10882-10888.
48. Islam DA, Chakraborty A, Roy A, Das S, Acharya H. Fabrication of graphene-oxide (GO)-supported sheet-like CuO nanostructures derived from a metal-organic-framework template for high-performance hybrid supercapacitors. *ChemSel*. 2018;3:11816-11823.
49. Eftekhari A. Energy efficiency: a critically important but neglected factor in battery research. *Sustain Energy Fuels*. 2017;1:2053-2060.
50. Zhang J, Zhao XS. On the configuration of supercapacitors for maximizing electrochemical performance. *ChemSusChem*. 2012;5:818-841.
51. Portet C, Taberna PL, Simon P, Flahaut E. Power J. Influence of carbon nanotubes addition on carbon–carbon supercapacitor performances in organic electrolyte. *Sources*. 2005;139:371-378.
52. Cao Y, Lin B, Sun Y, Yang H, Zhang X. Symmetric/asymmetric supercapacitor based on the perovskite-type lanthanum cobaltate nanofibers with Sr-substitution. *Electrochim Acta*. 2015;178:398-406.
53. Lang X, Mo H, Hu X, Tian H. Supercapacitor performance of perovskite La1−xSrxMnO3. *Dalt Trans*. 2017;46:13720-13730.
54. Shafi PM, Joseph N, Thirumurugan A, Bose AC. Enhanced electrochemical performances of agglomeration-free LaMnO3 perovskite nanoparticles and achieving high energy and power densities with symmetric supercapacitor design. *Chem Eng J*. 2018;338:147-156.

SUPPORTING INFORMATION

Additional supporting information may be found online in the Supporting Information section at the end of this article.

How to cite this article: Roy A, Cancino-Gordillo FE, Saha S, Pal U, Das S. Performance of asymmetric supercapacitor fabricated with perovskite-type Sr^{2+}-incorporated $LaMnO_3$ ($La_{0.7}Sr_{0.3}MnO_3$) nanostructures in neutral 1M Na_2SO_4 aqueous electrolyte. *Int J Energy Res*. 2021;45:14021–14033. https://doi.org/10.1002/er.6727

BUAP

Oficio No. IF-SACAD044/2023

Asunto: **Oficio de modalidad de titulación.**

MTRO. RICARDO VALDERRAMA VALDEZ
Director de Administración Escolar
Benemérita Universidad Autónoma de Puebla
Presente

El que suscribe, Director del Instituto de Física "Ing. Luis Rivera Terrazas", le informo que **FRANCISCO ENRIQUE CANCINO GORDILLO**, matrícula: 219570231, presentará y defenderá su examen de grado de **DOCTORADO EN CIENCIAS (EN LA ESPECIALIDAD DE CIENCIA DE MATERIALES)** en la **MODALIDAD DE PRESENTACIÓN DE TESIS**, cuyo título es: **"APLICACIÓN DE NANOPARTÍCULAS DE $Cu_2ZnSn_{1-x}Ge_xS_4$ COMO TRANSPORTADORES DE HUECOS EN CELDAS SOLARES DE PEROVSKITA BASADAS EN PLOMO"**, que se llevará a cabo el día **miércoles 19 de abril de 2023 a las 12:00 horas**, en el auditorio de este Instituto. El Jurado Examinador estará integrado por:

Dr. Eduardo Maximiano Sánchez Cervantes.	**Presidente** *-en línea-*
Dra. Hailin Zhao Hu.	**Secretaria** *-en línea-*
Dr. Gregorio Hernández Cocoletzi.	**Vocal**
Dr. Siva Kumar Krishnan.	**Vocal**
Dr. Umapada Pal.	**Vocal**

Sin otro asunto que el particular, aprovecho la ocasión para enviarle un cordial saludo.

A T E N T A M E N T E
"Pensar Bien, Para Vivir Mejor"
Puebla, Pue., a 24 de marzo de 2023

BENEMÉRITA UNIVERSIDAD AUTÓNOMA DE PUEBLA · INSTITUTO DE FÍSICA "LUIS RIVERA TERRAZAS" · 1578

DR. FELIPE PÉREZ RODRÍGUEZ
DIRECTOR

DR*FPR/DRA*MEGR/LAE*mhr

Instituto de Física
"Luis RiveraTerrazas"
Av. San Claudio esq. 18 Sur, Edif. IF1,
Ciudad Universitaria, Col. San Manuel
Puebla, Pue, C.P. 72570
01 (222) 229 55 00 Ext. 5610, 5611, 2008

BUAP

Oficio No. IF-SACAD045/2023

Asunto: Carta Aval

MTRO. ALFREDO AVENDAÑO ARENAZA
DIRECTOR GENERAL DE BIBLIOTECAS
BENEMÉRITA UNIVERSIDAD AUTÓNOMA DE PUEBLA
A QUIEN CORRESPONDA

El que suscribe, Director del Instituto de Física "Ing. Luis Rivera Terrazas" de la Benemérita Universidad Autónoma de Puebla, **AVALA** con base en los archivos que se encuentran en este Instituto que la tesis del **M.C. FRANCISCO ENRIQUE CANCINO GORDILLO**, matrícula: 219570231, cuyo título es: **"APLICACIÓN DE NANOPARTÍCULAS DE $Cu_2ZnSn_{1-x}Ge_xS_4$ COMO TRANSPORTADORES DE HUECOS EN CELDAS SOLARES DE PEROVSKITA BASADAS EN PLOMO"**, ha sido *revisada* y *aprobada* por el Comité respectivo para presentar su examen de grado de **DOCTORADO EN CIENCIAS (EN LA ESPECIALIDAD DE CIENCIA DE MATERIALES)** el próximo día 19 de abril de 2023 a las 12:00 horas en el auditorio del IFUAP. Dicho Comité está integrado por los siguientes profesores:

Dr. Eduardo Maximiano Sánchez Cervantes.	**Presidente**
Dra. Hailin Zhao Hu.	**Secretaria**
Dr. Gregorio Hernández Cocoletzi.	**Vocal**
Dr. Siva Kumar Krishnan.	**Vocal**
Dr. Umapada Pal.	**Vocal**

Se informa también que dicha tesis se encuentra lista para su impresión.

Sin otro asunto que el particular, reciba mi más alto reconocimiento.

A T E N T A M E N T E
"Pensar Bien, Para Vivir Mejor"
H. Puebla de Z., a 24 de marzo de 2023

DR. FELIPE PÉREZ RODRÍGUEZ
DIRECTOR

DR*FPR/DRA*MEBR/LAE*mhr

Instituto de Física "Luis Rivera Terrazas"
Av. San Claudio esq. 18 Sur, Edif. IF1, Ciudad Universitaria, Col. San Manuel Puebla, Pue. C.P. 72570
01 (222) 229 55 00 Ext. 5610, 5611, 2000